DISSERTATION

SYNTHETIC CONTROL OF MAGNETIC RESONANCE PROPERTIES TOWARDS METAL-BASED ELECTRON PARAMAGNETIC RESONANCE IMAGING

Submitted by

Anthony John Campanella

Department of Chemistry

In partial fulfillment of the requirements

For the Degree of Doctor of Philosophy

Colorado State University

Fort Collins, Colorado

Summer 2023

Doctoral Committee:

Advisor: Joseph Zadrozny

Matthew Shores
Jeff Bandar
Mingzhong Wu

ABSTRACT

SYNTHETIC CONTROL OF MAGNETIC RESONANCE PROPERTIES TOWARDS METAL-BASED ELECTRON PARAMAGNETIC RESONANCE IMAGING

Electron paramagnetic resonance imaging (EPRI) is the electron-spin analogue to conventional biological (nuclear) magnetic resonance imaging (MRI) whereby unpaired electron spins are probed in order to generate an image. The greater sensitivity of electron spins to their environment can thus be leveraged to capture detailed chemical information from the surroundings, producing an image of the local physiology that adds an extra dimension to the already powerful anatomical information gained from MRI. To move EPRI a step closer to common utilization, paramagnetic probes must be developed to sense the local environment using safe low-frequency microwaves at high (ca. 1.5 T) magnetic fields. Paramagnetic metal complexes are ideal candidates due to their electronic structures but have not been investigated for such purposes. The goal of this dissertation is to develop fundamental design principles to improve the utility of metal complexes as EPRI probes. Presented herein is the first comprehensive collection of experimental investigations to this end. Firstly, a method for improving signal sharpness is investigated, where exhaustive spectroscopic and computational studies suggest differences in relaxation dynamics as being a key factor in spectral linewidth (Chapters 2 and 3). A highly tunable clathrochelate structure is developed, inducing an unusual coordination geometry around the Ni(II) ion affording an 11 cm^{-1} control of zero-field splitting (Chapter 4). The temperature dependence of zero-field splitting is examined in a series of Mn(II) complexes where an unusually high temperature sensitivity is found in the solid state (Chapter 5). Finally, the utility of metal

complexes as environmental sensors is demonstrated with a pair of Mn(II) complexes showing that increasing magnetic anisotropy is a design strategy for enhancing microviscosity sensitivity (Chapter 6). The learned design principles will serve as a foundation for the design of metal-based EPRI agents towards improving the non-invasive diagnostic capabilities.

ACKNOWLEDGEMENTS

Over the course of five years, there are many I owe my thanks and acknowledgements to. It has been a long journey, (in the literal sense) moving 1560 miles from Swarthmore to Fort Collins, meeting new people, making discoveries, and finally seeing the light at the end of the tunnel as I write this document. It doesn't quite feel real yet, but perhaps that will change by the time this is finished.

First, I would like to thank my graduate advisor, Joe. From being the first professor to reach out to me upon my acceptance to CSU, he has always made me feel welcome and excited to be doing research. Molecular magnetism is a topic in chemistry that many consider quite intimidating, but his enthusiasm for the topic and ability to make it digestible to the common chemist made it something I wanted to spend the past five years banging my head against the wall for. Thank you for metaphorically lighting a fire under my butt when I need it and for your positive perspectives on seemingly failed experiments.

My interest in chemistry began in AP chemistry in my junior year of high school. Dina Dormer made the class interesting with her demos and immense enthusiasm for the subject. I consider my first "real" lab experience when she let myself and two other students perform an extraction of capsaicin at the end of the school year, an experiment that we researched, planned, and performed on our own.

My first research experience in a chemistry lab was in the lab of Eric Bloch. His guidance and ability to make working in a research lab cool and fun set me on the path towards graduate school. CSU may not have made it on my radar without him mentioning that a friend from graduate school (Joe) recently started a lab and that I should check out his work. His graduate student Dr.

Aeri Gosselin mentored me as an undergraduate researcher, bought me my first drinks as a 21-year-old, and most notably showed me how to have the patience to set up 96-vial shotgun crystallizations in order to get the best single-crystals.

Drs. Cassidy Jackson and Tyler Ozvat welcomed me into the Zadrozny lab as a "bright eyed" first year. Endearingly dubbing me "New Pleb", they taught me many of the lab skills I know, edited numerous papers and reports, and maybe most importantly showed me how to manage Joe. Being one year my senior, they served as examples of what to do (and not to do) as I progressed through graduate school. I owe a lot of my ability to communicate EPR effectively to Cassidy. Her skill of taking difficult concepts, like orientation dependence in EPR, and curating interesting analogies, like her toddler nephews using building blocks, is inspirational. Tyler set the bar for the quality of scientific figures and slide design to an extraordinary level, serving as the gold standard for presentation aesthetics. One of my fondest memories with Tyler is collecting EXAFS data at APS while playing Civilization VI between temperature points.

(Soon to be Dr.) Ian Moseley joined the Zadrozny lab at the same time as me and we shared similar research goals studying complexes with EPR, as well as becoming good friends. We pushed each other to be better researchers, kept each other (maybe a little too) humble, and made sure we had lives outside of lab with our climbing, hiking, and ski trips. Having someone to commiserate with when an instrument inevitably breaks made it a little less frustrating. I appreciated having someone who is always happy to get food at the Lake Street Market, LSC, MCHC, or elsewhere, even if he already packed a lunch.

I had many great conversations about research and proper glovebox techniques with Roxanna Martinez. Beyond that, she is an incredibly thoughtful person, making sure everyone's accomplishments were celebrated and occasionally bringing in pastries for the group. Drs. Okten,

Siyoung, AB, and Chun-Yi were awesome post-docs and each influenced me positively in their own way. I was fortunate to have overseen four undergraduate students throughout my time at CSU. Jeremiah, Jake, Fred, and Amanda were a pleasure to mentor and made meaningful contributions to my work and in the lab.

Many of the experiments I conducted would not have been possible without the support staff in the ARC. In particular Drs. Dan Bates, Indrani Bhowmick and Brian Newell helped maintain the EPR and troubleshoot it when it (inevitably) broke. Dr. Brian Newell also maintained the single crystal XRD and answered many of my questions about collecting crystal structures.

Profs. Sandy and Gareth Eaton, and their graduate student Willy were excellent collaborators, and I will fondly remember my trips to the University of Denver to use their L-band EPR spectrometer. Manh Nguyen, Jun Zhang, Malgorzata Makos, and Vanda Glezakou performed MD simulations for a number of the compounds I studied, resulting in two publications together. Their insight was invaluable, and our bi-weekly meetings were always interesting.

Beyond the people I interact with in a professional setting, there are many people behind the scenes that provide support that I am very thankful for. Firstly, David has been my best friend since we were 5. He helped me pack my car to the literal brim and drove with me to Colorado when this graduate school journey began, he flew back out to visit a few times, and would always make time to play video games from our childhood together. Steve was my roommate and my first (and closest) friend upon moving to Fort Collins. Having someone who is down to have a beer after a day of failed experiments, go skiing, camping, or on a long drive in the mountains, or celebrate 30 minutes of productive work with 2 hours of COD Zombies truly made this time in school memorable. To the “Brew Crew”, Cam, Steve, and Jeremy, maybe one day we will make a beer that we all agree tastes good.

My family has provided endless support from the beginning, and I would not be where I am without them. Their constant encouragement and not asking *too* often when I would be finished school was and still is always appreciated. And lastly, I would like to acknowledge Thor the cat for sitting by my side, blissfully unaware and peacefully sleeping. Beyond all the benefits having a pet brings, he served as an important reminder to take breaks (for treats and pets) and to not work too late, so as to make sure he gets his dinner at a reasonable hour.

Acknowledgements by Dissertation Chapter

Chapter 2 contains work reproduced from the journal article "Ligand Control of Low-Frequency Electron Paramagnetic Resonance Linewidth in Cr(III) Complexes" by Anthony J. Campanella, Manh-Thoung Nguyen, Jun Zhang, Thacien Ngendahimana, William E. Antholine, Gareth R. Eaton, Sandra S. Eaton, Vassiliki-Alexandra Glezakou and Joseph M. Zadrozny (*Dalton Trans.,* **2021**, 50, 5342–5350). Manh-Thoung Nguyen, Jun Zhang, and Vassiliki-Alexandra Glezakou performed molecular dynamics simulations and analyses. William E. Antholine maintained and oversaw the L-band EPR measurements. Thacien Ngendahimana, Gareth R. Eaton, and Sandra S. Eaton performed additional L-band EPR measurements. We thank Prof. Melissa Reynolds, Chris Allison, and Maddie Roach for the use of their mass spectrometer.

This research was performed with the support of Colorado State University (CSU) and the NIH (R21-EB027293). Part of the work described in this publication was performed at Pacific Northwest National Laboratory (PNNL), which is operated by Battelle for the United States Department of Energy (DOE) under Contract DE-AC05-76RL01830 and supported from the U.S. Department of Energy, Office of Science, Office of Basic Energy Sciences, Division of Chemical Sciences, Geosciences, and Biosciences. Computational resources were provided by the National

Energy Research Scientific Computing Center (NERSC), a U.S. Department of Energy Office of Science User Facility operated under Contract No. DEAC02-05CH11231 and PNNL's Research Computing.

Chapter 3 contains unpublished work from a manuscript in preparation titled "Structure and Dynamics of Ligands in Cr(III) Complexes for the Interpretation of EPR and Raman Spectral Lines" by Anthony J. Campanella, Malgorzata Z. Makos, Manh-Thoung Nguyen, George Sterbinsky, Vassiliki-Alexandra Glezakou, and Joseph M. Zadrozny. Anthony J. Campanella and Malgorzata Z. Makos contributed equally to this manuscript. Malgorzata Z. Makos, Manh-Thoung Nguyen, and Vassiliki-Alexandra Glezakou performed computational analyses of EPR, EXAFS and Raman spectra. George Sterbinsky performed EXAFS experiments at the Advanced Light Source and aided with data analysis. We thank Prof. Amber Krummel for access to a Raman spectrometer and Yusef Farah for experimental assistance.

This work received support from the US Department of Energy (DOE) Office of Science, Office of Basic Energy Science, Division of Chemical Sciences, Geosciences and Biosciences under FWP47319. Computer resources were provided by the National Energy Research Center (NERSC) located at LBNL and the PNNL Research Computing facility. Pacific Northwest National Laboratory is operated by Battelle for DOE under Contract DE-AC05-76RL01830. This work was also supported by the NIH (R21-EB027293).

Chapter 4 contains work reproduced from the journal article "Ligand Design of Zero-Field Splitting in Trigonal Prismatic Ni(II) Cage Complexes" by Anthony J. Campanella, Tyler M. Ozvat, and Joseph M. Zadrozny (*Dalton Trans.*, **2022**, 51, 3341-3348). Tyler M. Ozvat performed AILFT computations and analysis to support experimental findings. We thank Prof. Melissa Reynolds and Maddie Roach for use of their mass spectrometer. We also thank Prof. Garret

Miyake and Cameron Chrisman for their generous donation of ligand precursors. Lastly, we thank Ian P. Moseley for assistance with magnetometry measurements.

This work was performed with the support of Colorado State University (CSU) and the NIH (R21-EB027293). Magnetometry, EPR, and standard molecular characterization were performed at the CSU Analytical Resources Core, which is supported by an NIH-SIG award (1S10OD021814-01) and the CSU-CORES Program. Computational resources are enabled by the Catalysis Collaboratory for Light-activated Earth Abundant Reagent (C-CLEAR), which is supported by the National Science Foundation and the Environmental Protection Agency through the Networks for Sustainable Molecular Design and Synthesis (Grant CHE-1339674) at CSU, Fort Collins.

Chapter 5 contains unpublished work from a manuscript in preparation titled "Tailoring the Temperature Sensitivity of Zero-Field Splitting in Mn(II) Cage Complexes" by Anthony J. Campanella, Siyoung Sung, Cassidy E. Jackson, Roxanna Martinez, Andrew Ozarowski, and Joseph M. Zadrozny. Siyoung Sung synthesized the ligands and the complexes investigated. Cassidy E. Jackson and Roxanna Martinez performed high-field EPR analysis and were overseen by Andrew Ozarowski.

This work was performed with the support of Colorado State University (CSU), in part by the National Institutes of Health (R21-EB027293) and the Department of Energy (DE-SC0021259). Nuclear magnetic resonance experiments and standard molecular characterization were performed at the CSU Analytical Resources Core (Research Resource ID: SCR_021758), which is supported by an NIH-SIG award (1S10OD021814-01) and the CSU-CORES Program. A portion of this work was performed at the National High Magnetic Field Laboratory, which is

supported by National Science Foundation Cooperative Agreement No. DMR-1644779 and the State of Florida.

Chapter 6 contains unpublished work from a manuscript in preparation titled “Exploring Metal Complexes as Microviscosity Probes for EPR” by Anthony J. Campanella and Joseph M. Zadrozny. This work was performed with the support of Colorado State University (CSU), in part by the National Institutes of Health (R21-EB027293) and the Department of Energy (DE-SC0021259). Nuclear magnetic resonance experiments and standard molecular characterization were performed at the CSU Analytical Resources Core (Research Resource ID: SCR_021758), which is supported by an NIH-SIG award (1S10OD021814-01) and the CSU-CORES Program.

DEDICATION

To my family and friends

TABLE OF CONTENTS

CHAPTER 1 – Introduction

1.1. A Brief History of Magnetic Resonance Imaging

Magnetic resonance imaging (MRI) is an extremely useful and common medical diagnostic technique responsible for identifying ailments from tumors to a torn anterior cruciate ligament (ACL). This imaging technique was built on the same fundamental spin physics principles as nuclear magnetic resonance (NMR) spectroscopy, with Lauterbur initially proposing NMR could be used as a tool to form three-dimensional images in a 1973 publication,[1] and Mansfield describing how to selectively excite nuclear spins to form images.[2] In summary, magnetic field gradients allow for magnetic resonance signals from ^{1}H atoms to be differentiated spatially as they are probed with radiowaves to measure their relaxation dynamics. Image "slices" can thus be generated and combined into a three-dimensional image. These innovations were combined with a discovery by Damadian in 1971 that certain tissues and tumors in mice,[3] and later humans,[4] possess different ^{1}H relaxation times (T_1 and T_2), resulting in groundwork that made it clear that NMR could be leveraged for bioimaging. The first human head image was produced in 1978,[5] albeit nothing like the quality we are used to seeing today (**Figure 1.1**), and advances through the 80s and early 90s brought MRI to the point where over 10,000 were in use worldwide by 1996.[6] In one of the biggest recognitions that scientists can receive, Lauterbur and Mansfield received the Nobel prize in physiology or medicine for their discoveries related to MRI in 2003, illustrating how important MRI has become in medicine. Advances continue to be made, with the first image being generated in a 0.1 T magnetic field,[6] to most common MRI scanners operating at 1.5 or 3 T now,[6] a 7 T MRI scanner being approved by the FDA in 2020,[7] and a 11.7 T in development as of 2021.[8]

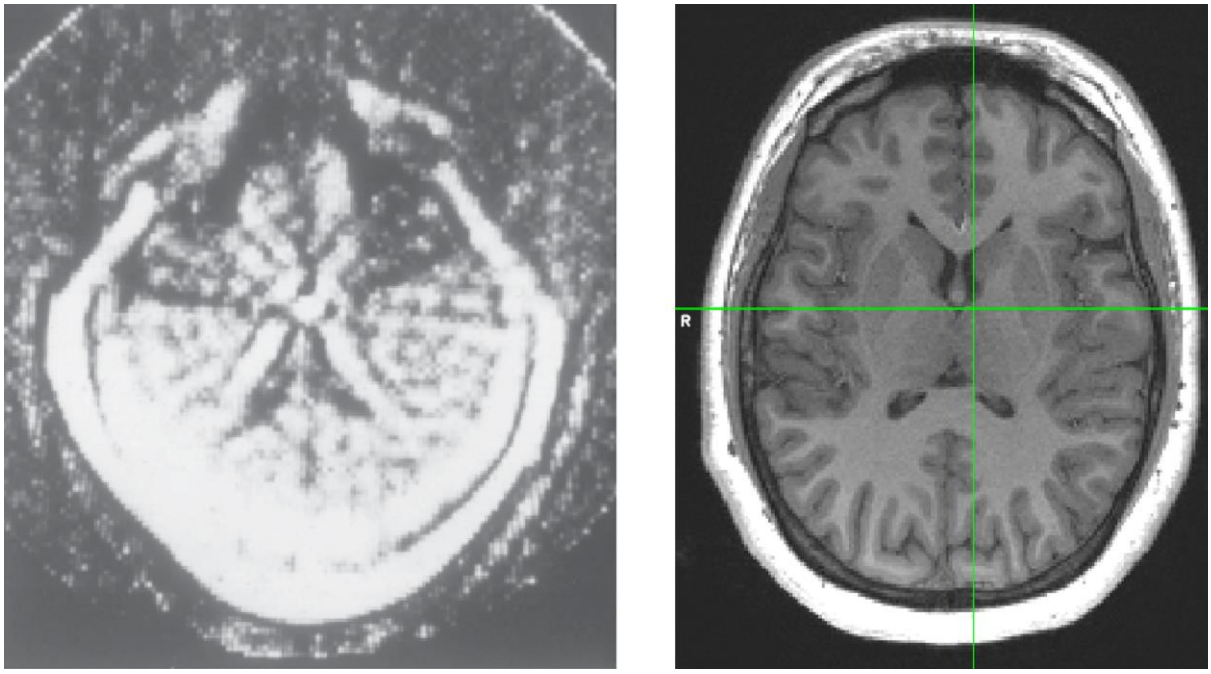

Figure 1.1. (Left) First MRI image of a human head from EMI Central Research Laboratories 1978. Image is used with permission from *MRI from Picture to Proton*. (Right) Recent MRI image of the head of Zadrozny Lab member Roxanna Martinez using a 3 T MRI scanner at the Colorado State University BRAiN Laboratory. Greater anatomical detail, such as folds in the brain tissue, can be resolved with current instrumentation technology. Image was obtained and used with permission from Roxanna Martinez.

1.2. Limitations of MRI and Electron Spin Advantages

As MRI has proven itself to be useful over the past 30 years, there is still a limited scope of what it can measure. ^{1}H nuclei, found most commonly in water and lipid molecules, make up 62% of atoms in the body,[9] and are the target of this imaging technique. The differences in the relaxation dynamics of these nuclei across tissue types are what is used to create a detailed anatomical image. For example, the ^{1}H nuclei on water molecules in normal breast tissue have an average T_1 time of 0.367 seconds, but a cancerous tumor in the same area has a T_1 time of 1.080 seconds as a result of the different cellular makeup.[4] This ability to determine tissue types is powerful, however, there is a lot of additional fundamental physiological information that is not detected. Indeed, contrast agents can improve sensitivity and make harder to visualize tissues

"brighter", but the detection of specific chemical signatures that could be evidence of biological disfunction are largely still in their infancy and limited in scope.[10] For example, physiological indicators like oxygen concentration,[11] local pH,[12] and redox stress[11] can be used as metrics to aid in the diagnosis of disease. Even beyond diagnosis capabilities, noninvasively imaging these chemical metrics would provide new fundamental insight into biochemical processes.[13]

Detailed chemical information can instead be obtained by taking a fundamentally different approach to magnetic-resonance-based imaging. ^{1}H, or more broadly nuclei, are not the only spin-bearing quantum objects that can be probed. Electron spins possess some differences that can be leveraged to produce a more sensitive imaging technique, known as electron paramagnetic resonance imaging (EPRI). Comparing these types of spins, an immediate major difference is the size their magnetic moments. The gyromagnetic ratio, which reflects the difference in the magnetic moments for nuclear and electron spins, is 42.5 **M**Hz/T for a nuclear spin and 28.0 **G**Hz/T for an electron spin. This nearly 700-fold difference implies that an electron spin can be thought of as a "big magnet" and a nuclear spin as a "small magnet". Having a "big magnet" in this case means one needs less of it in order to sense the environment and be detected by an instrument, which is reflected in the *nano*molar sensitivity of electron spins with current instrumentation, whereas nuclear spins have sensitivities on the order of *milli*molar.[14] EPRI techniques have been investigated over the past 25 years, showing promise for directly measuring important chemical markers like oxygenation,[11,15,16] pH,[17–19] redox stress,[20–22] and microviscosity.[23]

It is worth noting that EPRI should not replace MRI, as these techniques ultimately convey different information. However, these two techniques could work in tandem to produce a combination of anatomical and physiological images of the human body, ultimately providing an additional dimension of new information for medical professionals to use. As such, the ideal

scenario would be to take MRI and EPRI images nearly simultaneously, perhaps using some shared instrumentation. Much of the work to implement EPRI as described still needs to be developed. However, to set this technique up for ultimate future success, researchers must fundamentally design and optimize EPRI towards this ultimate goal. Some of that groundwork is described in this dissertation.

1.3. Current EPRI Probes

A question one might ask is: Why is EPRI not in widespread use when there are such clear uses for it? Importantly, it relies on paramagnetic material (a stable radical molecule or paramagnetic metal ion) to be detected in order to produce a signal. The human body does not naturally contain enough paramagnetic species to be detected with EPRI, relative to the abundance of ^{1}H in water, and as a result, a paramagnetic probe molecule has to be introduced.[14] Historically, that probe has been a "stable" organic radical, like a tri-aryl methyl radical or a nitroxide radical with ground state spins of $S = {}^{1}/_{2}$.[16,24] Though these molecules often have long relaxation times and sharp linewidths,[25,26] they are also relatively reactive and require high frequency microwave radiation to be addressed at the magnetic fields of typical MRI. Specifically at 1.5 T, those electron spins would need microwaves on the order of 40 GHz to be spectroscopically detected (**Figure 1.2 Left**). Radiation in this frequency regime is readily absorbed by water, precluding deep tissue measurements,[27] and can result in tissue heating.[28] As measurements beyond skin level are desired and microwave-induced heating would pose a safety hazard to patients, EPRI utilizing organic radicals is currently not viable in an MRI scanner. The frequency of the EPR transition for an $S = {}^{1}/_{2}$ system scales directly with magnetic field, meaning a low (safe) frequency regime can only be achieved at very low magnetic field, wherein 1H MRI resolution would be limited. To design a

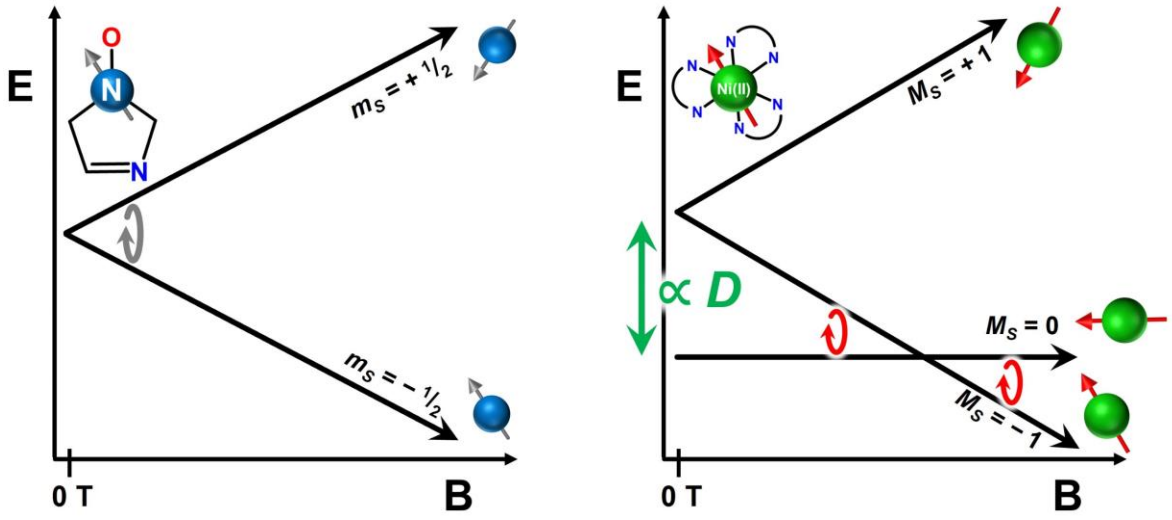

Figure 1.2. (Left) Zeeman diagram of a typical organic radical with $S = {}^1/_2$. The gray arrow illustrates where low-frequency spin transitions will occur in these systems. (Right) Zeeman diagram of a typical $S = 1$ octahedral Ni(II) complex with positive ZFS. The red arrows show where low-frequency spin transitions will occur between $M_S = 0$ and $M_S = -1$ levels, which are at higher magnetic fields in these systems.

useful probe to merge EPRI and MRI, new frequency dependences need to be discovered that enable low frequency analyses at high field. However, the diagrams of the EPR transitions for *all* organic radicals look like those in **Figure 1.2 Left**. Hence, organic radicals can only be expected to require high frequency microwaves at higher fields. Thus, new probes built on non-organic radical spin systems need to be developed.

1.4. Metal Ions as EPRI Probes

Paramagnetic metal ions with $S > {}^1/_2$ present themselves as a possible solution to conducting low-frequency EPR at high magnetic fields. As a consequence of the higher spin quantum number and spin-orbit coupling that is present in these complexes, zero-field splitting (ZFS, D) splits the multiple $|M_S|$ levels at zero magnetic field (**Figure 1.2 Right**).[29,30] Importantly, the presence of ZFS uniquely results in some EPR transitions that *decrease* in energy with increasing magnetic field. An increasing the magnitude of D will push an EPR signal to occur at

higher magnetic fields, and since D can vary 100s of cm^{-1} in magnitude depending on the molecule,[31,32] it is possible to generate low-frequency EPR signals from 0 to 10s, if not 100s of T. Importantly, D is an extremely tunable aspect of metal ion electronic structure,[29,30] which in principle, would give the synthetic inorganic chemist the ability to control the low-frequency (biologically safe) EPR signal. Metal ions have typically been studied with high-frequency high-field EPR, so these studies represent a blind-spot in EPR. Indeed, the first report of metal ions being studied with low-frequency (L-band, 1-2 GHz) EPR was in 1992 by Utsumi and coworkers[33] where the spectra of aqueous Mn^{2+} and VO^{2+} ions were collected. This first study demonstrated the challenges presented by low-frequency EPR of metal ions, like resolving hyperfine splitting. Later in 2019, Antholine was able to resolve hyperfine splitting in a Co^{2+} ion in an aqueous environment,[34] which serves as a testament to the advances that have been made in low-frequency EPR instrumentation, which ultimately will allow for the better detection of $S > {}^1/_2$ metal complexes for EPRI.

However, there still remains hurdles to metal-ion implementation for EPRI. One of those hurdles is that metal ions typically exhibit broad spectral linewidths which could inhibit the resolution needed to detect subtle chemical changes. In addition, a robust coordination environment must be designed to sequester the metal ion to guarantee safety in *vivo*. That platform should be tunable for controlling the electronic structure of the embedded metal.

1.5. Dissertation Organization

The research described in this document is based on the author's own published and unpublished work during his doctoral research, which spans six first author manuscripts (including a review article), three having been published in peer-reviewed journals, and three in preparation.

As such, each chapter is organized like a journal article with its own abstract, introduction, description of experiments, discussion of results and conclusions. While each chapter can be a stand-alone publication, collectively they contribute to the broader knowledge advancing metal-based EPRI. The six manuscripts, lists of authors/contributors, and associated publication information are listed here:

Campanella, A. J.; Üngör, Ö.; Zadrozny, J. M. Quantum Mimicry With Inorganic Chemistry *Comment. Inorg. Chem*. **2023**. (DOI: 10.1080/02603594.2023.2173588)

Campanella, A. J.; Nguyen, M.-T.; Zhang, J.; Ngendahimana, T.; Antholine, W. E.; Eaton, G. R.; Eaton, S. S.; Glezakou, V.-A.; Zadrozny, J. M. Ligand Control of Low-Frequency Electron Paramagnetic Resonance Linewidth in Cr(III) Complexes. *Dalton Trans.* **2021**, *50*, 5342-5350. (DOI: 10.1039/D1DT00066G)

Campanella, A. J.; Makos, M. Z.; Nguyen, M.-T.; Sterbinsky, G. E.; Glezakou, V.-A.; Zadrozny, J. M. Structure and Dynamics of Ligands in Cr(III)-Complexes for the Interpretation of EPR and Raman Spectral Lines. *In Preparation*.

Campanella, A. J.; Ozvat, T. M.; Zadrozny, J. M. Ligand Design of Zero-Field Splitting In Trigonal Prismatic Ni(II) Cage Complexes. *Dalton Trans.* **2022**, 51, 3341-3348. (DOI: 10.1039/D1DT02156G)

Campanella, A. J.; Sung, S.; Jackson, C. E.; Martinez, R.; Ozarowski, A.; Zadrozny, J. M. Tailoring the Temperature Sensitivity of Zero-Field Splitting in Encaged Mn(II) Complexes. *In preparation*.

Campanella, A. J.; Zadrozny, J. M. Highly Sensitive Metal-Based EPR Spin Probe for Viscosity Sensing. *In preparation.*

Chapter 2 details the first L-band EPR investigation of the Cr(III) ion. In this study, a series of Cr(III) *tris*-diamine complexes were studied to understand how to use ligands to sharpen EPR signal linewidths. The results of this study suggested that minimizing bond-length distributions through structural distortions may be one mechanism for achieving sharp linewidths.

Chapter 3 follows up on the first L-band EPR study of the Cr(III) ion. EXAFS and Raman spectroscopies, as well as molecular dynamics simulations, were employed to deeply study how the ligand dynamics affect the vibrational and EPR spectra. The results of this study suggest that the observed spectral broadening is likely rooted in homogeneous broadening from differences in T_2 relaxation times.

Chapter 4 describes an investigation of five nickelous cage compounds in the exotic trigonal prismatic geometry. It was found that small changes at the periphery of the ligand resulted in large changes to ZFS, over an 11 cm^{-1} range. This study also highlighted the effects that molecular and electronic structure can have on the magnetic properties of molecules.

Chapter 5 provides an investigation into the temperature response of ZFS in three Mn(II) cage complexes, one of which exhibited a surprisingly large change in D upon cooling. This study provides an insight as to how the tunability of metal complexes can be leveraged to reach a desired sensing property, in this case the sensitivity of temperature.

Chapter 6 demonstrates the utility of metal complexes as viscosity-sensitive EPR probes. Two Mn(II) complexes were tested to assess their sensitivity to molecular tumbling as assessed by EPR. Comparable viscosity sensitivities were achieved by the tested metal complexes compared to the state-of-the-art organic radical sensor molecule, and a new design principle for increasing sensitivity by increasing magnetic anisotropy was discovered.

It should be noted that the numbering schemes for referencing the molecules discussed herein refer to *only* the chapter that they appear in. Thus, complex **1** in Chapter 2 may refer to a different molecule than complex **1** in Chapter 3.

References

(1) Lauterbur, P. C. Image Formation by Induced Local Interactions: Examples Employing Nuclear Magnetic Resonance. *Nature* **1973**, *242* (5394), 190–191.

(2) Garroway, A. N.; Grannell, P. K.; Mansfield, P. Image Formation in NMR by a Selective Irradiative Process. *J. Phys. C: Solid State Phys.* **1974**, *7* (24), L457.

(3) Damadian, R. Tumor Detection by Nuclear Magnetic Resonance. *Science* **1971**, *171* (3976), 1151–1153.

(4) Damadian, R.; Zaner, K.; Hor, D.; DiMaio, T. Human Tumors Detected by Nuclear Magnetic Resonance. *Proc. Natl. Acad. Sci.* **1974**, *71* (4), 1471–1473.

(5) Britain's Brains Produce First NMR Scans. *New Scientist*. November 23, 1978, p 588.

(6) McRobbie, D. W.; Moore, E. A.; Graves, M. J.; Prince, M. R. *MRI From Picture to Proton*, 2nd ed.; Cambridge University Press, 2006.

(7) *Bringing Ultra-High Field MR Imaging from Research to Clinical: SIGNA 7.0T FDA Cleared*. https://www.gehealthcare.com/about/newsroom/press-releases/bringing-ultra-high-field-mr-imaging-from-research-to-clinical-signa-70t-fda-cleared (accessed 2023-01-23).

(8) *World's most powerful MRI unveiled*. CERN Courier. https://cerncourier.com/a/worlds-most-powerful-mri-unveiled/ (accessed 2023-01-23).

(9) da Silva, J. J. R. F.; Williams, R. J. P. *The Biological Chemistry of the Elements: The Inorganic Chemistry of Life*; OUP Oxford, 2001.

(10) Wahsner, J.; Gale, E. M.; Rodríguez-Rodríguez, A.; Caravan, P. Chemistry of MRI Contrast Agents: Current Challenges and New Frontiers. *Chem. Rev.* **2019**, *119* (2), 957–1057.

(11) James, P. E.; Swartz, H. M. Simultaneous Detection of pO_2 and NO by Electron Paramagnetic Resonance. In *Methods in Enzymology*; Nitric Oxide, Part D: Oxide Detection, Mitochondria and Cell Functions, and Peroxynitrite Reactions; Academic Press, 2002; Vol. 359, pp 52–66.

(12) Zhang, X.; Lin, Y.; Gillies, R. J. Tumor pH and Its Measurement. *J. Nucl. Med.* **2010**, *51* (8), 1167–1170.

(13) Fujii, H.; Berliner, L. J. In Vivo EPR Evidence for Free Radical Adducts of Nifedipine. *Magn. Reson. Med.* **1999**, *42* (4), 691–694.

(14) Danhier, P.; Gallez, B. Electron Paramagnetic Resonance: A Powerful Tool to Support Magnetic Resonance Imaging Research. *Contrast Media Mol. Imaging* **2015**, *10* (4), 266–281.

(15) Swartz, H. M.; Flood, A. B.; Schaner, P. E.; Halpern, H.; Williams, B. B.; Pogue, B. W.; Gallez, B.; Vaupel, P. How Best to Interpret Measures of Levels of Oxygen in Tissues to Make Them Effective Clinical Tools for Care of Patients with Cancer and Other Oxygen-Dependent Pathologies. *Physiol. Rep.* **2020**, *8* (15), e14541.

(16) *EPR Imaging and in Vivo EPR*, 1st ed.; Gareth R. Eaton, Sandra S. Eaton, Keiichi Ohno, Eds.; CRC Press, 2018.

(17) Voinov, M. A.; Scheid, C. T.; Kirilyuk, I. A.; Trofimov, D. G.; Smirnov, A. I. IKMTSL-PTE, a Phospholipid-Based EPR Probe for Surface Electrostatic Potential of Biological Interfaces at Neutral pH: Effects of Temperature and Effective Dielectric Constant of the Solvent. *J. Phys. Chem. B* **2017**, *121* (11), 2443–2453.

(18) Voinov, M. A.; Polienko, J. F.; Schanding, T.; Bobko, A. A.; Khramtsov, V. V.; Gatilov, Y. V.; Rybalova, T. V.; Smirnov, A. I.; Grigor'ev, I. A. Synthesis, Structure, and X-Band (9.5 GHz) EPR Characterization of the New Series of pH-Sensitive Spin Probes: N,N-Disubstituted 4-Amino-2,2,5,5-Tetramethyl-3-Imidazoline 1-Oxyls. *J. Org. Chem.* **2005**, *70* (24), 9702–9711.

(19) Gallez, B.; Mader, K.; Swartz, H. M. Noninvasive Measurement of the pH inside the Gut by Using pH-Sensitive Nitroxides. An in Vivo EPR Study. *Magn. Reson. Med.* **1996**, *36* (5), 694–697.

(20) Caia, G. L.; Efimova, O. V.; Velayutham, M.; El-Mahdy, M. A.; Abdelghany, T. M.; Kesselring, E.; Petryakov, S.; Sun, Z.; Samouilov, A.; Zweier, J. L. Organ Specific Mapping of in Vivo Redox State in Control and Cigarette Smoke-Exposed Mice Using EPR/NMR Co-Imaging. *J. Magn. Reson.* **2012**, *216*, 21–27.

(21) Hyodo, F.; Murugesan, R.; Matsumoto, K.; Hyodo, E.; Subramanian, S.; Mitchell, J. B.; Krishna, M. C. Monitoring Redox-Sensitive Paramagnetic Contrast Agent by EPRI, OMRI and MRI. *J. Magn. Reson.* **2008**, *190* (1), 105–112.

(22) Epel, B.; Sundramoorthy, S. V.; Krzykowska-Serda, M.; Maggio, M. C.; Tseytlin, M.; Eaton, G. R.; Eaton, S. S.; Rosen, G. M.; Kao, J. P. Y.; Halpern, H. J. Imaging Thiol Redox Status in Murine Tumors In Vivo with Rapid-Scan Electron Paramagnetic Resonance. *J. Magn. Reson.* **2017**, *276*, 31–36.

(23) Halpern, H. J.; Chandramouli, G. V. R.; Barth, E. D.; Yu, C.; Peric, M.; Grdina, D. J.; Teicher, B. A. Diminished Aqueous Microviscosity of Tumors in Murine Models Measured with in Vivo Radiofrequency Electron Paramagnetic Resonance. *Cancer Res.* **1999**, *59* (22), 5836–5841.

(24) *In Vivo EPR (ESR): Theory and Application*; Berliner, L. J., Ed.; Biological Magnetic Resonance; Springer US, 2003.

(25) Burks, S. R.; Makowsky, M. A.; Yaffe, Z. A.; Hoggle, C.; Tsai, P.; Muralidharan, S.; Bowman, M. K.; Kao, J. P. Y.; Rosen, G. M. The Effect of Structure on Nitroxide EPR Spectral Linewidth. *J. Org. Chem.* **2010**, *75* (14), 4737–4741.

(26) Biller, J. R.; Meyer, V.; Elajaili, H.; Rosen, G. M.; Kao, J. P. Y.; Eaton, S. S.; Eaton, G. R. Relaxation Times and Line Widths of Isotopically-Substituted Nitroxides in Aqueous Solution at X-Band. *J. Magn. Reson.* **2011**, *212* (2), 370–377.

(27) Rinard, G. A.; Quine, R. W.; Eaton, S. S.; Eaton, G. R. Frequency Dependence of EPR Sensitivity. In *EPR: Instrumental Methods*; Berliner, L. J., Bender, C. J., Eds.; Biological Magnetic Resonance; Springer US: Boston, MA, 2004; pp 115–154.

(28) Hitchcock, R. T. *Radio-Frequency and Microwave Radiation*; AIHA, 2004.

(29) Griffith, J. S. *The Theory of Transition-Metal Ions*; Cambridge University Press, 1964.

(30) Figgis, B. N.; Hitchman, M. A. *Ligand Field Theory and Its Applications*; Special topics in inorganic chemistry; Wiley-VCH, 2000.

(31) Titiš, J.; Boča, R. Magnetostructural D Correlation in Nickel(II) Complexes: Reinvestigation of the Zero-Field Splitting. *Inorg. Chem.* **2010**, *49* (9), 3971–3973.

(32) Ruamps, R.; Maurice, R.; Batchelor, L.; Boggio-Pasqua, M.; Guillot, R.; Barra, A. L.; Liu, J.; Bendeif, E.-E.; Pillet, S.; Hill, S.; Mallah, T.; Guihéry, N. Giant Ising-Type Magnetic Anisotropy in Trigonal Bipyramidal Ni(II) Complexes: Experiment and Theory. *J. Am. Chem. Soc.* **2013**, *135* (8), 3017–3026.

(33) Hideo Utsumi; Takuji Tatebe; Akira Hamada. ESR Spectra of VO^{2+} and Mn^{2+} in Aqueous Solution at L-Band. *Chem. Lett.* **1992**, 277–280.

(34) Antholine, W. E. Resolved Hyperfine at L-Band for High-Spin CoEDTA, A Model for Co Sites in Proteins. *Int. J. Mol. Sci.* **2019**, *20* (10), 2385.

CHAPTER 2 – Ligand Control of Low-Frequency Electron Paramagnetic Resonance Linewidth in Cr(III) Complexes

2.1. Overview

Understanding how the ligand shell controls low-frequency electron paramagnetic resonance (EPR) spectroscopic properties of metal ions is essential if they are to be used in EPR-based bioimaging schemes. In this work, we probe how specific variations in the ligand structure impact L-band (1-2 GHz) EPR spectroscopic linewidths in the trichloride salts of five Cr(III) complexes $[Cr(\textit{RR}\text{-dphen})_3]^{3+}$ (*RR*-dphen = (1*R*,2*R*)-(+)-diphenylethylenediamine, **1**), $[Cr(en)_3]^{3+}$ (en = ethylenediamine, **2**), $[Cr(me\text{-}en)_3]^{3+}$ (me-en = 1,2-diaminopropane, **3**), $[Cr(tn)_3]^{3+}$ (tn = 1,3-diaminopropane, **4**) $[Cr(\textit{trans}\text{-chxn})_3]^{3+}$ (*trans*-chxn = *trans*-(±)-1,2-diaminocyclohexane, **5**). Spectral broadening varies in a nonintuitive manner across the series, showing the sharpest peaks for **1** and broadest for **5**. Molecular dynamics simulations provide evidence that the broadening is correlated to rigidity in the inner coordination sphere and reflected in ligand-dependent distribution of Cr–N bond distances that can be found in frozen solution.

2.2. Introduction

Electron paramagnetic resonance imaging (EPRI), the electron spin analogue of nuclear magnetic resonance imaging (colloquially referred to as MRI), could greatly augment the chemical sensing capabilities of MRI.[1–3] For example, EPRI can track redox status,[4–7] pH,[8–11] and oxygenation,[12–14] thereby delivering local biochemical information that conventional ^{1}H MRI has considerable difficulty in doing. Merging EPRI with MRI would potentially permit the development of new imaging methodologies that integrate detailed anatomical and chemical

information to produce comprehensive physiological maps. However, several key hurdles need to be overcome to mesh EPRI with MRI.

One of the main challenges of merging MRI and EPRI is that EPRI requires microwave radiation. The state-of-the-art EPRI probes are organic radicals with ground state spins of $S = {}^1/_2$.[1] These probes offer sharp linewidths (< 0.1 mT) and long relaxation times ($T_1 \sim 10^{-6}$ s),[15,16] but require high-frequency microwaves (*ca.* 40 GHz) in a typical MRI magnetic field (1.5 T). Microwaves of this frequency do not efficiently penetrate water-rich tissue and increased microwave power to overcome this challenge can cause local heating of the biological tissue,[17–19] thus limiting the utility of these probes in current MRI systems.

Metal complexes with electronic spins greater than ${}^1/_2$ may provide a solution to these challenges. These complexes typically exhibit zero-field splitting (ZFS),[20,21] which can produce low-frequency EPR transitions at high magnetic fields (**Figure 2.1**). When combined with the

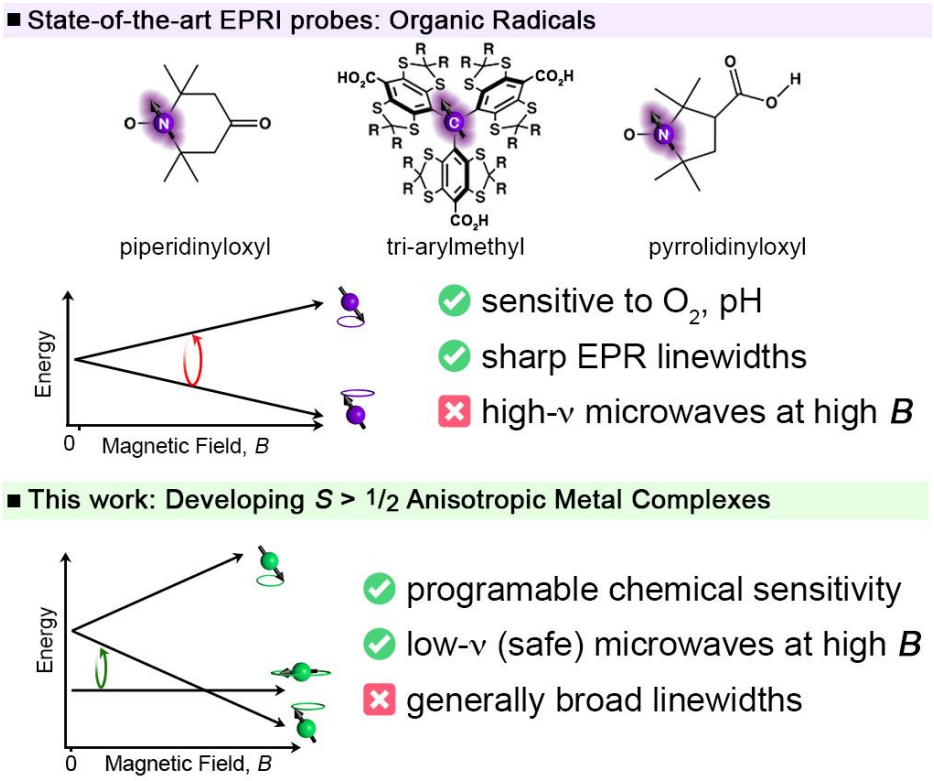

Figure 2.1. Overview of EPRI Probe classes and advantages.

widely tunable chemistry of metal ions,[20] it becomes clear that they may provide a highly versatile and useful EPRI probe class to develop novel imaging methodologies. To realize this vision, however, we need to understand structure-function relationships for metal complexes and EPR properties at low frequency. This region of electron spin dynamics is especially under-explored compared to higher frequency/higher field domains and constitutes a clear "blind spot" in the analysis of metal-ion complexes via magnetic resonance.

A particular challenge to harnessing metal ions for EPRI and related techniques is the extraordinary sensitivity of zero-field splitting to metal ion-electronic structure. A consequence of this sensitivity is a strong inhomogeneous broadening of EPR signals stemming from structural variations in solution.[22] In theory, these broad linewidths (typically greater than 1 mT) could prevent spectral resolution of subtle chemical changes. A broad linewidth would also necessitate large magnetic field gradients for the MRI scanner which presents an engineering barrier to implementation. Hence, understanding how to sharpen linewidths by molecular design is a pressing challenge. One path to sharpen linewidths is to install steric bulk in the coordination sphere of a metal ion and hence suppress inhomogeneous broadening due to structural distributions. This tactic is used in manipulating photophysical emission lifetimes[23–26] but has never been tested for manipulating low-frequency EPR linewidths.

Herein we present the first investigation of the ligand-dependence of the spectral broadening of the L-band (*ca.* 1.3 GHz) EPR spectra of a series of $S = {}^3/_2$ metal complexes. We specifically analyzed a series of Cr(III) *tris*-diamine complexes (**Figure 2.2**) $[Cr(RR\text{-dphen})_3]Cl_3$ (**1,** *RR*-dphen = (*1R,2R*)-(+)-1,2-diphenylethylenediamine), $[Cr(en)_3]Cl_3$ (**2**, en = ethylenediamine), $[Cr(me\text{-}en)_3]Cl_3$ (**3,** me-en = 1,2-diaminopropane), $[Cr(tn)_3]Cl_3$ (**4,** tn = 1,3-

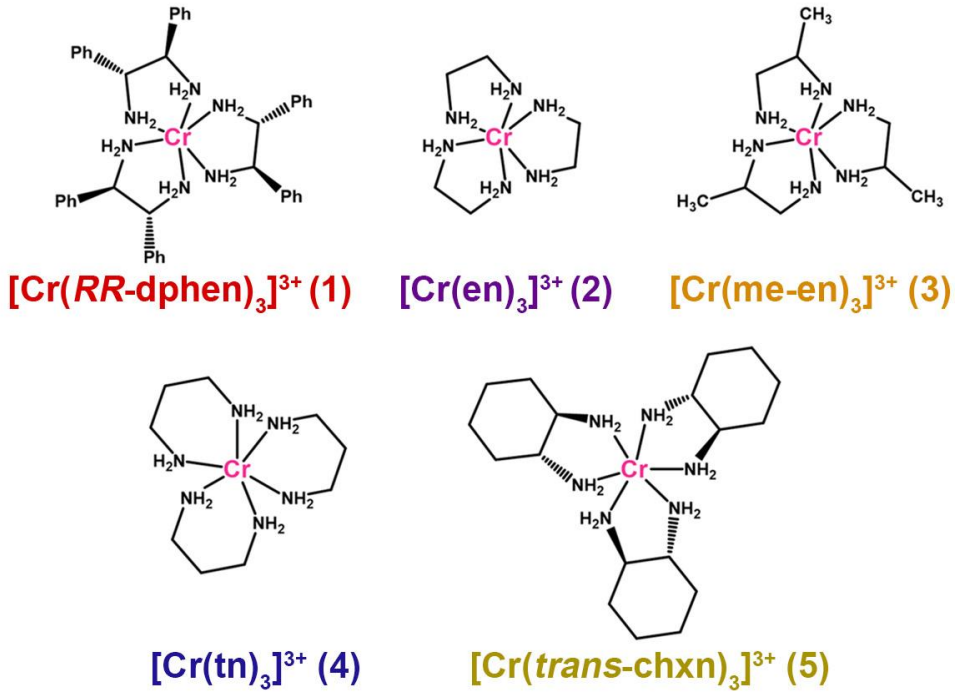

Figure 2.2. Bond-line structures of the $S = {}^3/_2$, Cr^{3+} complexes **1-5** used in this study. Cl^- counterions and most H-atoms are omitted for clarity. For complex **1**, the enantiopure (1*R*,2*R*)-(+)-1,2-diphenylethylenediamine ligand was used with the depicted geometry. For **5**, the racemic *trans*-(±)-1,2-diaminocyclohexane ligand was used and the *R,R* isomer is depicted.

diaminopropane), and $[Cr(trans\text{-chxn})_3]Cl_3$ (**5,** *trans***-**chxn = *trans*-(±)-1,2-diaminocyclohexane). In this series, the ligand backbones were selected to test how steric effects in the secondary coordination shell impact EPR linewidth. Our focus here lies on Cr(III) because of the half-integer spin and observable EPR signals for study, as well as the essential potential for low-frequency signals at higher magnetic fields (**Figure 2.3**). We also finally note that this ion might be a useful base for a functional agent due to its low toxicity, if an appropriate ligand scaffold were chosen.[27]

We hypothesized that the systems with the greatest steric congestion in the ligand shell (**1** and **5**) would exhibit the sharpest linewidths. Yet, diamino complexes are known to display multiple structural configurations[28–30] even when bound to the metal ion. Thus, we envisioned that steric congestion in the ligand scaffold, stemming from intramolecular repulsive interactions between ligand functional groups, would lessen the isomer distribution, consequently sharpening

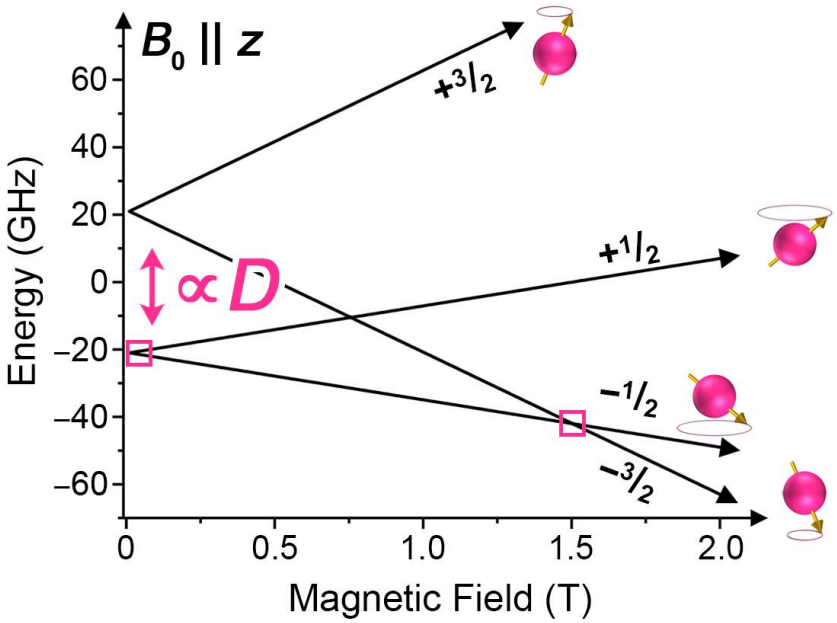

Figure 2.3. Calculated M_S-level diagram for an $S = {}^3/_2$ species with positive zero-field splitting ($D = +0.7$ cm^{-1}, $g = 2$) and field aligned with the molecular z-axis (approximately the viewing angle in **Figure 2.2**). Potential ground-state low-frequency transitions for these parameters occur near 0.05 T and 1.5 T and are highlighted with small pink boxes.

spectra. We did not observe a direct correlation between steric congestion on the ligand shell and EPR spectral sharpness. However, through spectral and molecular dynamics studies, we found that ligand-dependent distributions of Cr–N bond distances appear to correlate to spectral sharpness, underlining a new design strategy for affecting low-frequency EPR linewidths in these and future complexes.

2.3. Experimental Section

2.3.1. General Considerations

Reagents used throughout were purchased from commercial sources and used as received. Syntheses were adapted from a previously reported procedure.[31] All techniques were performed at atmospheric conditions unless otherwise specified. Elemental analyses were performed by Roberson Microlit Laboratories (Ledgewood, New Jersey, USA). Infrared spectra were recorded

on a Nicolet 6700 FTIR spectrometer using a diamond window ATR. Electronic absorption spectra of all complexes were recorded on aqueous with a Hewlett-Packard 8453 spectrophotometer using standard quartz cuvettes with a 1 cm path length. Mass spectral analyses were performed on an Agilent 6224 Accurate Mass TOF LC/MS in positive ion mode using direct injection. Peak assignment was on the basis of m/z, interpeak spacing, and isotopic distribution. Emission spectra were obtained on an Edinburgh FS5 Spectrofluorometer using a quartz cuvette with a 1 cm path length in a temperature-controlled sample holder. Samples were prepared as 30 mM solutions in water and held at 20 °C. Steady state emission spectra were obtained by exciting each sample at 460 nm with a 6.0 nm slit width and collecting from 480—800 nm. Spectra were averaged over three scans with a 0.5 s integration time. Time resolved emission spectra were obtained over a 500 ns time range with a repetition frequency of 2 MHz. Samples were excited with a 450 nm EPL picosecond pulsed diode laser and collected at 670 nm with a bandwidth of 20 nm.

2.3.2. Preparation of Compounds

Synthesis of [Cr(*RR*-dphen)$_3$]Cl$_3$•EtOH (**1**). In a 5 mL round-bottom flask, 160 mg of CrCl$_3$•6H$_2$O (0.602 mmol, 1 eq.) were added to 0.5 mL of DMSO and heated to 200°C with stirring. Upon reaching temperature, the mixture was cooled to 110°C. While that mixture cooled, 400 mg (1.88 mmol, 3.1 eq.) of (1*R,*2*R*)-(+)-1,2-diphenylethylenediamine were placed in a vial with ca. 0.5 mL of DMSO and warmed until dissolved. The diamine solution was added to the CrCl$_3$ solution, the temperature was raised to 150°C for 1 hour, then cooled to room temperature. A small amount of a dark yellow powder was visible. 1 mL of ethanol followed by 1 mL of ethyl ether were added to encourage precipitation. The solid was filtered, washed once with 5 mL of ethanol, then three times with 5 mL of ethyl ether, yielding a shiny, yellow-orange microcrystalline

powder. This solid was further purified by recrystallization from aqueous ethanol and dried under vacuum. The final yield was 125.7 mg (26%) of **1**. Crystals suitable for single-crystal x-ray diffraction were grown by the slow evaporation of a saturated methanol solution of **1**. IR (cm^{-1}, diamond ATR): 3032, 2905, 1579, 1497, 1455, 1401, 1310, 1238, 1180, 1076, 1024, 1000, 952, 915, 867, 764, 699. UV-vis (H_2O); λ_{max} (ε_M, $M^{-1}cm^{-1}$): 354 nm (85.7); 464 nm (94.5). LC-MS (m/z): positive ion mode: $\{[Cr(\textit{RR}\text{-dphen})_3Cl_2]\}^+$, 758.27; $\{[Cr(\textit{RR}\text{-dphen})_2Cl]\}^{++}$, 214.63. Elemental analysis for $C_{42}H_{48}Cl_3CrN_6 \bullet C_2H_6O$ calculated (found): %C: 62.82 (62.88), %H: 6.47 (6.39), %N: 9.99 (9.72).

Synthesis of $[Cr(en)_3]Cl_3$ (**2**). In a 50 mL round-bottom flask, 4 g of $CrCl_3 \bullet 6H_2O$ (15 mmol, 1 eq.) were added to 8 mL of DMSO and heated to 200°C with stirring. Upon reaching temperature, the mixture was cooled to 110°C. While that mixture cooled, 4 mL (60 mmol, 4 eq.) of ethylenediamine were placed in a vial with ca. 2 mL of DMSO and warmed. The diamine solution was added to the $CrCl_3$ solution and the temperature was raised to 150°C for 1 hour, then allowed to cool to room temperature. A small amount of a dark yellow powder was visible. 5 mL of ethanol and 2 mL of ethyl ether were added to encourage precipitation. The solid was filtered, washed several times with 10 mL of ethanol, then once with 10 mL of ethyl ether, yielding a shiny, yellow-orange microcrystalline powder. This solid was further purified by recrystallization from aqueous ethanol and dried under vacuum. The final yield was 4.63 g (91%) of **2**. IR (cm^{-1}, diamond ATR): 3180, 3121, 3066, 2984, 2950, 2938, 2898, 2890, 1575, 1560, 1537, 1459, 1364, 1331, 1304, 1275, 1214, 1158, 1141, 1121, 1059, 1010, 881, 867, 745. UV-vis (H_2O) spectra matches prior reports[31]; λ_{max} (ε_M, $M^{-1}cm^{-1}$): 351 nm (60.6); 458 nm (76.5). LC-MS (m/z): positive ion mode: $\{[Cr(en)_3Cl_2]\}^+$, 302.08; $\{[Cr(en)_2Cl_2]\}^+$, 242.01. Elemental analysis for $C_6H_{24}Cl_3CrN_6$ calculated (found): %C: 21.28 (21.26), %H: 7.14 (7.17), %N: 24.82 (24.47).

Synthesis of $[Cr(me\text{-}en)_3]Cl_3 \bullet 0.25H_2O$ (**3**). In a 50 mL round-bottom flask, 4 g of $CrCl_3 \bullet 6H_2O$ (15 mmol, 1 eq.) were added to 8 mL of dimethyl sulfoxide (DMSO) and heated to 200°C with stirring. Upon reaching temperature, the mixture was cooled to 110°C. While that mixture cooled, 5 mL (59 mmol, 3.9 eq.) of 1,2-propanediamine were placed in a vial with ca. 2 mL of DMSO and warmed. The diamine solution was added to the $CrCl_3$ solution and the temperature was raised to 150°C for 1 hour, then allowed to cool to room temperature. A small amount of a dark yellow powder was visible. 5 mL of ethanol and 2 mL of ethyl ether were added to encourage precipitation. The solid was filtered, washed three times with 10 mL of ethanol, then once with 10 mL of ethyl ether, yielding a yellow-orange powder. This solid was further purified by recrystallization from aqueous ethanol and dried under vacuum. The final yield was 2.98 g (58%) of **3**. IR (cm^{-1}, diamond ATR): 3163, 3054, 2965, 2938, 2880, 1538, 1456, 1393, 1372, 1343, 1310, 1236, 1126, 1101, 1042, 1015, 836, 730. UV-vis (H_2O) matches reported spectra[32]; λ_{max} (ε_M, $M^{-1}cm^{-1}$): 352 nm (59.5); 459 nm (74.1). LC-MS (m/z): positive ion mode: $\{[Cr(me\text{-}en)_3Cl_2]\}^+$, 344.13; $\{[Cr(me\text{-}en)_2Cl_2]\}^+$, 270.04. Elemental analysis for $C_9H_{30}Cl_3CrN_6 \bullet 0.25H_2O$ calculated (found): %C: 28.06 (28.21), %H: 7.98 (8.13), %N: 21.82 (21.65).

Synthesis of $[Cr(tn)_3]Cl_3$ (**4**). In a 50 mL round-bottom flask, 4 g of $CrCl_3 \bullet 6H_2O$ (15 mmol, 1 eq.) were added to 8 mL of dimethyl sulfoxide (DMSO) and heated to 200°C with stirring. Upon reaching temperature, the mixture was cooled to 110°C. While that mixture cooled, 8 mL (94 mmol, 6.2 eq.) of 1,3-diaminopropane were placed in a vial with ca. 2 mL of DMSO and warmed. The diamine solution was added to the $CrCl_3$ solution and the temperature was raised to 150°C for 1 hour, then allowed to cool to room temperature. A small amount of a dark yellow powder was visible. 5 mL of ethanol and 2 mL of ethyl ether were added to encourage precipitation. The solid was filtered, washed three times with 10 mL of ethanol, then once with 10 mL of ethyl ether,

yielding a shiny, yellow-orange microcrystalline powder. This solid was further purified by recrystallization from aqueous ethanol and dried under vacuum. The final yield was 2.53 g (49%) of **4**. Single crystals suitable for single-crystal X-ray diffraction were grown from layering ethanol onto an aqueous solution of **4**. IR (cm^{-1}, diamond ATR): 3277, 3129, 3072, 3032, 2960, 2942, 2946, 2887, 1596, 1568, 1546, 1479, 1464, 1444, 1401, 1390, 1352, 1303, 1285, 1259, 1228, 1218, 1186, 1171, 1034, 1025, 932, 917, 897, 877, 806, 731, 691, 673. UV-vis (H_2O) matches prior reports[31]; λ_{max} (ε_M, $M^{-1}cm^{-1}$): 355 nm (47.2); 464 nm (55.3). LC-MS (m/z): positive ion mode: $\{[Cr(tn)_3Cl_2]\}^+$, 344.13; $\{[Cr(tn)_2Cl_2]\}^+$, 270.04. Elemental analysis for $C_9H_{30}Cl_3CrN_6$ calculated (found): %C: 28.39 (28.36), %H: 7.94 (8.06), %N: 22.07 (21.89).

Synthesis of [Cr(*trans*-chxn)$_3$]Cl_3•0.25H_2O•0.25EtOH (**5**). In a 25 mL round-bottom flask, 1.5 g of $CrCl_3$•6H_2O (5.63 mmol, 1 eq.) were added to 4 mL of dimethyl sulfoxide (DMSO) and heated to 200°C with stirring. Upon reaching temperature, the mixture was cooled to 110°C. While that mixture cooled, 2.7 mL (22.5 mmol, 4 eq.) of *trans*-1,2-diaminocyclohexane were placed in a vial with ca. 1 mL of DMSO and warmed. The diamine solution was added to the $CrCl_3$ solution and the temperature was raised to 150°C for 1 hour, then allowed to cool to room temperature. A small amount of a dark yellow powder was visible. 4 mL of ethanol and 2 mL of ethyl ether were added to encourage precipitation. The solid was filtered, washed three times with 10 mL ethanol, then once with 10 mL ethyl ether, yielding a shiny, yellow-orange microcrystalline powder. This solid was further purified by recrystallization from aqueous ethanol and dried under vacuum. The final yield was 1.25 g (44%) of **5**. IR (cm^{-1}, diamond ATR): 3041, 2933, 2864, 1590, 1574, 1459, 1449, 1409, 1397, 1359, 1303, 1240, 1211, 1152, 1122, 1051, 1024, 946, 921, 859, 751. UV-vis (H_2O) match reported data[31]; λ_{max} (ε_M, $M^{-1}cm^{-1}$): 352 nm (55.9); 460 nm (71.1). LC-MS (m/z): positive ion mode: $\{[Cr(trans\text{-}chxn)_3Cl_2]\}^+$, 464.22; $\{[Cr(trans\text{-}chxn)_2Cl_2]\}^+$, 350.10; {[Cr(*trans*-

chxn)$_2$Cl]}$^{++}$, 214.63. Elemental analysis for $C_{18}H_{42}Cl_3CrN_6$•0.25H_2O•0.25C_2H_6O calculated (found): %C: 42.98 (42.90), %H: 8.58 (8.94), %N: 16.26 (16.53).

Synthesis of [Cr(*SS*-chxn)$_3$]Cl_3•H_2O (**5-*SS***). In a 25 mL round-bottom flask, 707 mg of $CrCl_3$•6H_2O (2.65 mmol, 1 eq.) were added to 2 mL of dimethyl sulfoxide (DMSO) and heated to 200°C with stirring. Upon reaching temperature, the mixture was cooled to 110°C. While that mixture cooled, 1 g (8.76 mmol, 3.3 eq.) of *(1S,2S)*-(+)-1,2-diaminocyclohexane were placed in a vial with ca. 1 mL of DMSO and warmed. The diamine solution was added to the $CrCl_3$ solution and the temperature was raised to 150°C for 1 hour, then allowed to cool to room temperature. A small amount of a dark yellow powder was visible. 2 mL of ethanol and 1 mL of ethyl ether were added to encourage precipitation. The solid was filtered, washed three times with 5 mL of ethanol, then once with 5 mL of ethyl ether, yielding a shiny, yellow-orange microcrystalline powder. This solid was further purified by recrystallization from aqueous ethanol and dried under vacuum. The final yield was 539 mg (40%) of **5-*SS***. Crystals suitable for single crystal x-ray diffraction were grown through the slow evaporation of a saturated aqueous solution of **5-*SS***. IR (cm^{-1}, diamond ATR): 3138, 3036, 2930, 2857, 1576, 1448, 1401, 1364, 1346, 1303, 1240, 1211, 1145, 1051, 1020, 948, 919, 862, 754. UV-vis (H_2O) match reported data[31]; λ_{max} (ε_M, $M^{-1}cm^{-1}$): 352 nm (65.7); 461 nm (83.6). LC-MS (m/z): positive ion mode: {[Cr(*SS*-chxn)$_3$$Cl_2$]}$^+$, 464.22; {[Cr(*SS*-chxn)$_2$$Cl_2$]}$^+$, 350.10; {[Cr(*SS*-chxn)$_2$Cl]}$^{++}$, 214.63. Elemental analysis for $CrC_{18}H_{42}Cl_3N_6$•H_2O calculated (found): %C: 41.66 (41.69), %H: 8.55 (8.88), %N: 16.19 (15.81).

Synthesis of [Cr(*RR*-chxn)$_3$]Cl_3•0.75H_2O•0.25EtOH (**5-*RR***). In a 25 mL round-bottom flask, 707 mg of $CrCl_3$•6H_2O (2.65 mmol, 1 eq.) were added to 2 mL of DMSO and heated to 200°C with stirring. Upon reaching temperature, the mixture was cooled to 110°C. While that mixture cooled, 1 g (8.76 mmol, 3.3 eq.) of *(1R,2R)*-(-)-1,2-diaminocyclohexane were placed in a

vial with ca. 1 mL of DMSO and warmed. The diamine solution was added to the $CrCl_3$ solution and the temperature was raised to 150°C for 1 hour, then allowed to cool to room temperature. A small amount of a dark yellow powder was visible. 2 mL of ethanol and 1 mL of ethyl ether were added to encourage precipitation. The solid was filtered, washed three times with 5 mL of ethanol, then once with 5 mL of ethyl ether, yielding a shiny, yellow-orange microcrystalline powder. This solid was further purified by recrystallization from aqueous ethanol and dried under vacuum. The final yield was 812 mg (60%) of **5-*RR***. Crystals suitable for single crystal x-ray diffraction were grown through the slow evaporation of a saturated aqueous solution of **5-*RR***. IR (cm^{-1}, diamond ATR): 3141, 3038, 2932, 2857, 1576, 1450, 1402, 1366, 1345, 1304, 1240, 1211, 1146, 1050, 1020, 949, 919, 862, 754. UV-vis (H_2O) match reported data[31]; λ_{max} (ε_M, $M^{-1}cm^{-1}$): 352 nm (74.5); 460 nm (93.0). Elemental analysis for $C_{18}H_{42}Cl_3CrN_6 \cdot 0.75H_2O \cdot 0.25C_2H_6O$ calculated (found): %C: 42.25 (42.26), %H: 8.62 (8.38), %N: 15.98 (15.98).

*2.3.3. X-ray Data Collection, Structure Solution and Refinement for **1**, **4**, **5-SS**, and **5-RR**.*

The diffraction data were collected at the X-Ray Diffraction facility of the Analytical Resources Core at Colorado State University. Data for **1, 4, 5-*SS*,** and **5-*RR*** were collected on a Bruker D8 Quest ECO single-crystal X-ray diffractometer equipped with Mo Kα (λ = 0.71073 Å). Data were collected and integrated using Bruker Apex 3 software. Absorption correction were applied using SADABS. Space group assignments were determined by examination of systematic absences, E-statistics, and successive refinement of the structures. Crystal structures were solved using SHELXT and refined with the aid of successive difference Fourier maps by SHELXL operated in conjunction with OLEX2 software.[33–35] None of the crystals demonstrated decay by X-ray radiation over the course of the experiment. Hydrogen atoms were placed in ideal positions

and refined using a riding model for all structures. In **1**, carbon atoms in their respective phenyl groups were restrained to be coplanar and C−C bond lengths were restrained to be within a standard error of 0.01 Å. In one of the methanol solvent molecules, disordered molecules freely modeling two positions yielded occupancies of 0.60(6) and 0.30(6). In one of the methanol solvent molecules, a disordered carbon freely modeling two positions yielded an occupancy of 0.62(4) and 0.38(4). In two methanol solvent molecules, disordered molecules were modeled with fixed occupancies of 0.50 and 0.50. In **4**, four 1,3-diaminopropane ligands were freely modeled over two positions yielding occupancies of 0.54(7) and 0.46(7), 0.51(6) and 0.49(6), 0.57(2) and 0.43(2), 0.66(4) and 0.34(4). In one ethanol solvent molecule, the disorder over two positions yielded occupancies 0.51(3) and 0.49(3). In two water solvent molecules, disordered molecules were modeled with fixed occupancies of 0.50 and 0.50. And finally, in one chloride counterion, disorder modeled over two positions yielded occupancies of 0.580(11) and 0.420(11). In **5-*RR***, two disordered water molecules free modeling two positions yielded occupancies of 0.687(20) and 0.313(9) for each. A disordered chloride counterion freely modeling two positions yielded occupancies of 0.684(9) and 0.316(9). Crystallographic information files for **1**, **4**, **5-*SS***, and **5-*RR*** are available in the CSD at accession numbers 2041467-2041470.

2.3.4. Electron Paramagnetic Resonance Measurements

EPR spectra collected herein were simulated using Easyspin[36] with the function pepper (frozen solution and solid) and were refined using the function "esfit" or simulations of the experimental data. All samples were prepared at atmospheric conditions as 30 mM aqueous solutions in ethylene glycol (1:1 v/v) the same day that the measurements took place. X-band CW EPR data were collected for all compounds on a Bruker ESR-300 spectrometer and was carried

out at 80 K using a liquid nitrogen cooled cryostat or at 77 K in a liquid nitrogen filled quartz finger dewar.

Perpendicular-mode L-band EPR spectra were performed on two different instruments. L-band CW EPR was performed on compounds **1, 2, 3, 4,** and **5** on a low-frequency spectrometer station assembled at the National Biomedical EPR Center at the Medical College of Wisconsin (Milwaukee, WI, USA). The station incorporates an in-house-built L-band (1–2 GHz) bridge, Varian V-7200 Electromagnet, Varian V-7700 Magnet Power Supply, and Bruker BH-15 Magnetic Field Controller. The 100 KHz field modulation and signal phase-sensitive detection were provided by a Varian E-109 System EPR console. EPR signals from the phase-sensitive detector were recorded on a PC with Windows 7 running a custom LabVIEW program. The program also controlled the BH-15 Field Controller and performed multiple-scan signal averaging, when needed. The L-band bridge in the spectrometer utilizes a low-phase-noise, mechanically and electronically tunable fundamental transistor oscillator capable of 50 mW power output to the sample resonator port at 0 dB main power attenuator setting. A cylindrical loop-gap resonator was used to collect sample measurements. The oscillator microwave frequency was locked to the sample resonator frequency by a 70 KHz automatic frequency control system in the bridge, operating through the electronic tuning port of the oscillator. A low-noise amplifier in the microwave signal receiver prior to signal mixing improved the overall bridge sensitivity. The measurements were taken at 112 K, which was the lowest temperature achieved by the cooling system consisting of a stream of nitrogen gas that was passed through a coil submerged in liquid nitrogen. Samples were placed in the center of the cavity.

Perpendicular mode L-band CW EPR analyses were also performed on ***5-SS*** on a locally-constructed 1-2 GHz spectrometer described in Quine et al., 1996.[37] Major changes include

collecting the signal in a Bruker Specjet digitizer, controlling the magnetic field with a BH15 field controller, and replacing a Varian power supply with a Bruker EMX080 power supply. The resonator was a Bruker ER4118L-MS5 splitring module mounted on an ER4118SPT Flexline probe head support. 4 or 5 mm diameter sample tubes can be used. The Flexline mounted resonator was in a Bruker/Oxford CF935 continuous flow cryostat, through which liquid nitrogen was passed to achieve the 112 K operating temperature. When sample size is kept constant and the frequency is lowered from X-band to L-band, sensitivity decreases by about a factor of 50 if the sample size and resonator size are kept constant.[38] Consequently, signal-to-noise at 1 GHz using standard 4 mm o.d. quartz sample tubes is very low relative to normal X-band CW EPR experience. The signal-to-noise specification for this resonator, if used with a Bruker bridge, was 300:1 for Bruker strong (not weak) pitch, using 6 G modulation amplitude.

2.3.5 Computational Details

The structures of complexes **1**, **2**, **4**, **5**, each micro-solvated by 20 water molecules were determined using NWPEsSe,[39] a global optimization method based on the artificial bee colony algorithm.[40,41] For each system, the search included 500 structures with the xTB method, and the lowest 10 structures were further optimized at the TPSSh+D3/def2-TZVP level of theory. The most stable one was taken as the minimum. These most-stable clusters are shown in **Figure A1.11**.

Using the most stable structures determined from the global optimization above, four simulation boxes were set up with the following contents. For **1**, the box contained [Cr(*RR*-dphen)$_3$]$^{3+}$, 3 × Cl$^-$ anions, and 300 H_2O molecules. For **2**, the box contained [Cr(en)$_3$]$^{3+}$, 3 × Cl$^-$ anions, and 150 H_2O molecules. For **4**, the box contained [Cr(tn)$_3$]$^{3+}$, 3 × Cl$^-$ anions, and 180 H_2O molecules. For **5**, the box contained [Cr(*trans*-chxn)$_3$]$^{3+}$, 3 × Cl$^-$ anions, and 180 H_2O molecules.

The boxes were first equilibrated under P = 1 atm and T = 300 K. The OPLS force fields[42] were used as implemented in the GROMACS program.[43] Following the NPT simulation, the cell parameter were fixed at 21.8 Å, (complex **1**), 17.1 Å (complex **2**), 18.1 Å, (complex **4**), and 19.2 Å, (complex **5**) and the four systems were equilibrated and allowed to run for about 10 ns in the NVT ensemble. These trajectories were used for the analysis of the results.

2.4. Results and Discussion

Compounds **1**-**5** were synthesized in a similar manner following a previously reported synthetic pathway of refluxing $CrCl_3 \cdot 6H_2O$ in DMSO, followed by the addition of 3.1 equivalents of the diamine.[31] In the case of **5**, we prepared two additional isomers of the $[Cr(chxn)_3]^{3+}$ complex, using enantiopure ligand starting materials, **5-*SS*** and **5-*RR***. The resulting powders for all syntheses were yellow-orange in color and the UV-visible absorbance spectra matched previous reports.[31,32]

Surprisingly, the crystal structures of **1**, **4**, **5-*SS***, and **5-*RR*** were unreported at the time of this study, despite the long history of diamine complexes of Cr(III).[31,44–48] We found that single

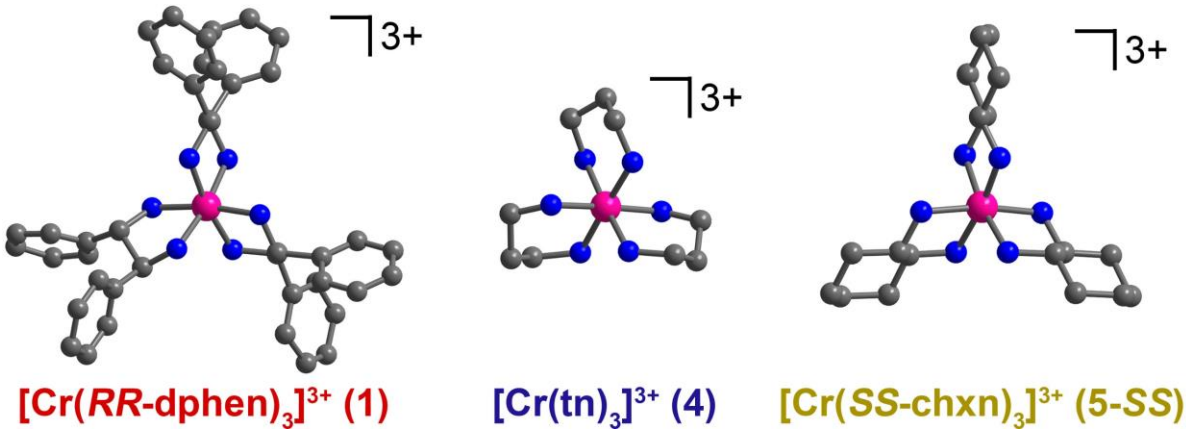

Figure 2.4. Molecular structures of $[Cr(dphen)_3]^{3+}$, $[Cr(tn)_3]^{3+}$, and $[Cr(SS\text{-chxn})_3]^{3+}$, as determined in the crystal structures of **1**, **4**, and **5-*SS***, respectively. Note that complex **5-*SS*** contains the enantiopure (1*S*,2*S*)-(+)-1,2-diaminocyclohexane) ligand. Pink, blue, and grey spheres represent Cr-, N-, and C-atoms, respectively. H-atoms and Cl^- counterions are omitted for clarity. Selected mean interatomic distances and angles can be found in **Table 2.1**.

crystals can be grown via the slow evaporation of a concentrated MeOH solution (**1**) or layering a concentrated aqueous solution with EtOH (**4**, **5-*SS***, and **5-*RR***) (**Figure 2.4**, **Tables A1.1-A1.4**).

Compounds **2** and **5** were identified some time ago.[49,50] Despite numerous attempts, however, we were unable to grow single crystals of **3** suitable for X-ray diffraction. A summary of structural parameters for **1**, **2**, **4**, and **5** are presented in Table 1. Compound **1** displayed Cr–N bond lengths between 2.057(7) and 2.090(7) Å with bite angles between 80.6(3)° and 82.4(3)°. The M–N lengths found were longer than the 1.968 Å bond lengths seen in the analogous Co(III) complexes.[51]

Complex $[Cr(tn)_3]^{3+}$ has been structurally characterized with $[Ni(CN)_5]^{3-}$ and $P_3O_9^{3-}$ counterions,[52–54] but not as the trichloride salt, which we present here. For **4**, we found Cr–N bond lengths ranging between 1.930(17) and 2.35(3) Å with bite angles between 90.3(9)° and 92.2(3)° (average values are given in **Table 2.1**). The M–N bond lengths are slightly longer for **4** than **1-3** and **5**, and N–Cr–N bond angles closer to 90˚ that **1-3** and **5**. Thus, the coordination geometry of **4** more closely resembles an octahedron than the other complexes in this study. These general observations match prior structures[52–54] and trends in analogous cobalt(III) complexes.[55–57]

Table 2.1. Mean structural bond distances (Å), angles (°), and shape-measure analyses from single-crystal diffraction experiments. [a]From ref 49. [b]Values computed from averaging **5** (from ref 50), **5-*SS***, and **5-*RR***. [c]Using N atoms on the same ligand. [d]Adjacent N atoms of different ligands. [e]Between N atoms that are *trans* to one another in the coordination shell. [f]Shape measure for octahedral geometry: $S(O_h) = 0$ indicates perfect octahedral CrN_6 structure.

	1	**2**[a]	**4**	**5**[b]
Cr−N	2.075(9)	2.078(17)	2.107(91)	2.0079(5)
N−Cr−N$_{Bite}$[c]	81.58(59)	82.66(48)	91.35(72)	82.29(28)
N−Cr−N$_{Adj}$[d]	93.0(2.2)	92.58(99)	89.9(4.4)	92.8(1.6)
N−Cr−N$_{Opp}$[e]	171(1.4)	173.1(9)	173(2.0)	172(1.1)
S(*O*$_h$)[f]	0.731	0.616	0.064	0.602

Finally, there does not appear to be substantial difference in bond distances and metrics for the Cr(III) ion in **5-*SS*** and **5-*RR***. These complexes were found to have Cr–N bond lengths between 2.077(5) and 2.085(5) Å for **5-*SS,*** and between 2.067(5) and 2.084(5) Å for **5-*RR***. Bite angles

were between 81.7(2)° and 82.4(2)° for **5-*SS*** and, 82.10(18)° and 82.77(19)° for **5-*RR***. The bond distances and angles for these two complexes fall closely in line with those of complex **5**.[50]

Continuous-Shape-Measurements (CSM) analysis using the SHAPE 2.0 software was performed on all complexes to quantitatively assess any geometric distortions from an idealized geometry.[58,59] We assessed each complex's geometry relative to those of an idealized octahedron and trigonal prism. A shape measure value, $S(O_h)$, of 0 corresponds to a perfect alignment with an octahedral geometry, whereas an $S(O_h)$, of 16.73 corresponds to a perfect trigonal prismatic geometry. These SHAPE measures for **1**, **2**, **4**, and **5** are in a tight range between 0.064 and 0.731 for an octahedral geometry (O_h) and above 12.00 for the trigonal prismatic geometry (D_{3h}) (**Tables 2.1**, **A1.5**). These results indicate that the ligands enforce a nearly octahedral environment around the Cr(III) center. Again, no substantial difference was observed between **5-*SS*** and **5-*RR***.

Continuous-wave (CW) EPR analyses of complexes **1**-**5** were carried out with L-band (1.3 GHz) and X-band (9.5 GHz) frequencies to directly elucidate spectral linewidths (Figs. 4, S1). The L-band CW-EPR spectra display two notable spectral features for each complex, appearing remarkably similar to X-band spectra for large-zero-field splitting Co(II) complexes.[60] For **1**, a large $g_{x,y}$ feature is observed at 25 mT and a small, but relatively sharp g_z feature at 50 mT. The basis of these peak assignments is discussed below. From complex **1** to **5**, these features become broader, with the spectrum of **5** much less well-resolved than for **1**. This qualitative trend is mirrored in the data collected at X-band frequency, where the spectra of complexes **1** to **5** were dominated by a sharp feature at 340 mT. While each possessed a large broad feature at 150 mT, this feature decreased in intensity, from very prominent in **1** to nearly unnoticeable in **5**.

EasySpin[36] was used to simulate the L-band EPR spectra, which enabled the determination of the spin Hamiltonian parameters as well as quantify the spectral broadening in **1**-**5**. Spectral fits

were achieved by simulations using the Spin Hamiltonian: $\widehat{\boldsymbol{H}} = g\mu_B \boldsymbol{B}\widehat{\boldsymbol{S}} + \widehat{\boldsymbol{S}}\boldsymbol{D}\widehat{\boldsymbol{S}}$. Here, g is an axial g-factor ($g_x = g_y \neq g_z$), μ_B is the Bohr magneton, $\boldsymbol{B}$ is the external applied magnetic field, $\widehat{\boldsymbol{S}}$ is the electronic spin, and $\boldsymbol{D}$ is the axial zero field splitting term. Since Cr has only a 9.5% natural abundance in the $I = {}^1/_2$ ^{53}Cr isotope,[61] hyperfine interactions (usually denoted with $\boldsymbol{A}$) between the $S = {}^3/_2$ spin and the nuclear spin were neglected. To account for the observed spectral broadening, we employed a model that explicitly averaged simulated spectra over a distribution of g_z and $g_{x,y}$ values. This model is relatively uncommon compared to typically applied isotropic broadening models or strains.[36,62]

As depicted in **Figures 2.5** and **A1.13**, the broadening model and spin Hamiltonian permitted high-quality simulations of the L-band spectra for **1**-**5**. The determined g values for **1**-**5**

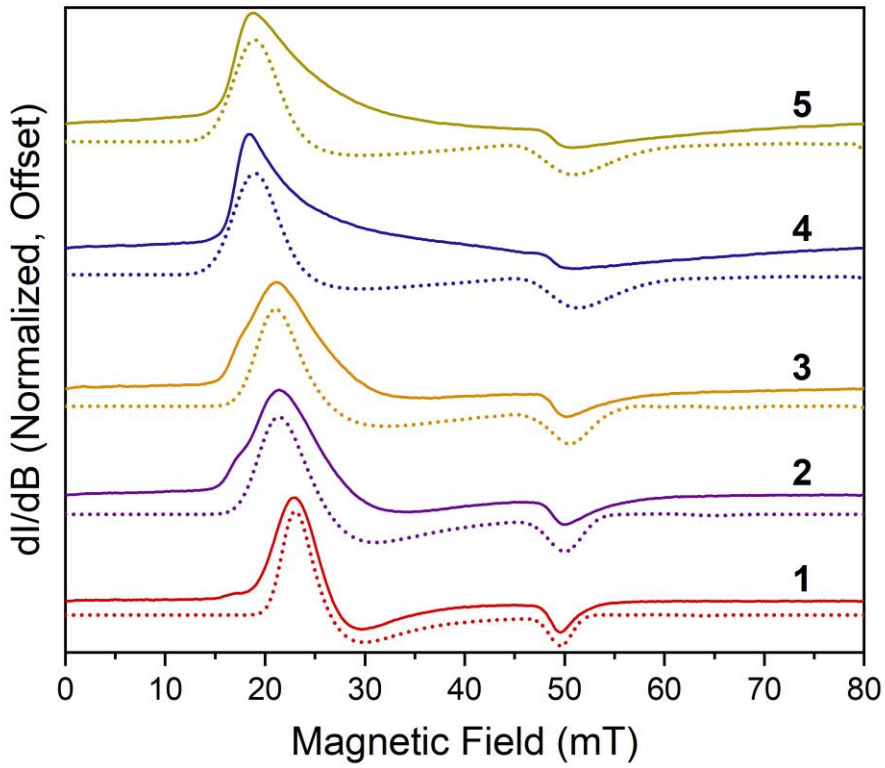

Figure 2.5. L-band (1.359 GHz) continuous wave EPR spectra for **1**-**5** in frozen glass solutions. Compounds were dissolved at 30 mM concentration in an ethylene glycol/water (1:1 v/v) solvent system and data collected at 112 K. Modulation amplitude was 0.8 mT, modulation frequency was 100 kHz, non-saturating power was used, and gain was 4×10^3 dB. Dotted lines are simulations that treat broadening with a distribution of g values, see main text for details.

are generally axial with $g_{x,y} > g_z$. The $g_{x,y}$ for **3** is the smallest of the series (1.985) and greatest for **4** and **5** (2.300). Across **1**-**5**, g_z varies significantly less, from 1.955 for **1** to 2.000 for **5**. The determined D values were all positive and *ca*. 3 GHz (roughly 0.1 cm^{-1}) for all complexes: 3.2(7), 3.0(3), 2.8(3), 2.9(7), and 2.9(4) GHz, for **1-5**, respectively (0.11(2), 0.10(1), 0.09(1), 0.09(2), and 0.09(1) cm^{-1} for **1-5** respectively). Here, errors are estimated by eye from inspection of simulation quality upon variation of D, since Easyspin does not determine uncertainties. Importantly, these g and D values are similar in magnitude and sign to prior analyses of Cr^{3+} diamine complexes.[63–65] Note that simulation quality was not improved by the inclusion of E though this parameter (while small relative to D) is expected to be present.[66–70] A full list of the parameters determined by the best simulations of each spectrum are tabulated in **Table A1.11**.

The spin Hamiltonian parameters from the simulations give insight into the nature of the observed transitions in the L-band spectrum (Fig. 5). The low-field transition involves levels of mixed identity that are mostly $M_S = \pm^1/_2$ character, but with a significant (*ca*. 8 %) $M_S = \pm^3/_2$ component, and stems from Cr^{3+} molecules aligned perpendicular to the applied magnetic field, B_0. The high-field transition (near 50 mT), in contrast, stems from molecules aligned parallel to B_0, and is a transition between unmixed $M_S = \pm^1/_2$ levels. Finally, the spin Hamiltonian values predict low-frequency transitions at fields beyond the range of the used instrument. For example, for **1**, crossing of the $M_S = -^3/_2$ and $M_S = -^1/_2$ levels at 237 mT means that EPR transitions below 1 GHz are possible within the 200 to 273 mT window.

The broadening model provides a direct way to quantitate the trend in spectral shape shown in **Figure 2.5**. Here, the changing signal shape from two resolved peaks in the first-derivative spectrum to the broadened signal can be quantified with the full width at half maximum (FWHM) of the distribution of each g value for **1**-**5**. For the L-band spectra, the g_z FWHM values are 0.01,

0.1, 0.8, 0.38, and 0.4, respectively, for **1**-**5**, generally increasing across the probed molecules (with **3** as the exception). For $g_{x,y}$, the FWHM of the parameter is considerably larger than g_z for all studied complexes. Indeed, the FWHM for $g_{x,y}$ varies, respectively, as 0.6, 0.8, 1.12, 3.80, and 4.0 for **1**-**5**. From these data, it appears that the broadening of $g_{x,y}$ is the most important feature in dictating the spectral shape, as it is this g factor that directly affects the energy of the low-field transition in **Figure 2.6**. Thus, these analyses suggest that the broadening of $g_{x,y}$ (and hence the low-field transition) is responsible for the trend in spectral shape.

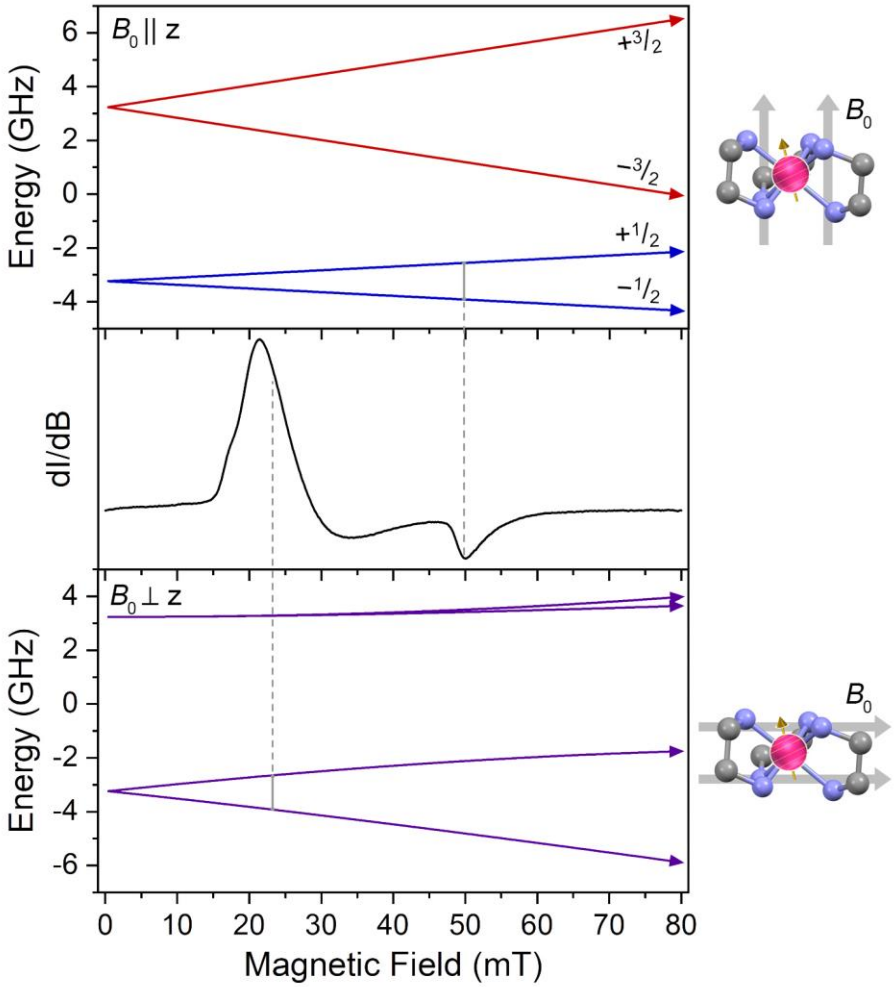

Figure 2.6. Spectral assignment for L-band EPR spectrum of **2**. The top- and bottom-most panels are M_S-level energies computed for B_0 parallel and perpendicular to the molecular C_3 axis, respectively. M_S-level energies were calculated with $g_{x,y}$ = 1.985; g_z = 1.960; D = +0.1 cm^{-1}, E = 0 cm^{-1}. Dashed lines correlate peaks to indicated transitions between levels. Energies and level compositions were computed with Easyspin.

On the basis of a superficial prediction of sharper linewidths from steric bulk on ligands, **1** and **5** were expected to yield the sharpest peaks. Instead, these ligands produced the sharpest (**1**) and broadest (**5**) spectra. Hence, we sought a more quantitative estimate of rigidity in the coordination shell of the Cr^{3+} metal ion. Tests of correlation between rigidity and ligand identity were pursued in a three-fold manner: by electronic absorption/emission spectroscopies, ligand isomer identity, and then, finally, molecular dynamics simulations.

Steady-state and time-resolved photoemission analyses of **1**-**5** were carried out as the first measure of quantifying rigidity in the ligand shell. Indeed, intense, long-lived emission is a sign of a rigid environment.[23,24,71] Complexes **1-5** are all emissive. Analyses of 30 mM aqueous solution of **1-5** with 460 nm excitation revealed a prominent emission generally near 675 nm (**Figure A1.8**). The shape and intensity of this emission peak varied, with **1**, **2**, and **5** having a relatively intense single peak, while **3** and **4** exhibited smaller peaks. The luminescence decays of these peaks were collected (**Figures A1.10-A1.11**) to provide the time constants of the decays (**Table A1.10**), which can serve as a quantitative measure for molecular rigidity.[23–26] The time-resolved emission data for **1-5** were best fit using either a bi- (**2-5**) or tri-exponential (**1**) decay model. Complexes **2**-**5** exhibit two starkly different relaxation emission decay times (τ): the first (τ_1) was on the order of 1 ns, and the second (τ_2) was on the order of 2 μs. Studies on similarly structured Cr(III) hexamine complexes indicate that the faster τ_1 corresponds to fluorescence, while τ_2 corresponds to a longer-lived phosphorescence.[72] For complex **1**, the tri-exponential decay yielded three lifetimes, τ_1 = 0.45(3), τ_2 = 38(5), and τ_3 = 1884(66) ns. Note that the free ligand (1*R*,2*R*)-(+)-1,2-diphenylethylenediamine in aqueous solution has an emission lifetime on the same order as τ_1 for **1** (**Figure A1.12**).[73] Hence we can conclude that the τ_2 from complex **1** is likely ligand-related, and τ_3 is metal-ion phosphorescence.

More importantly, our analysis suggests that emission as an indicator of rigidity appears to fail in describing the EPR broadening. Indeed, by the metric of the emission lifetimes, **2** is the most rigid complex with τ_1 = 1.40(5) ns, followed by **3** (τ_1 = 0.99(5) ns), **5** (τ_1 = 0.97(6) ns), **4** (τ_1 = 0.48(6) ns), and **1** (τ_1 = 0.45(3) ns). This ordering of rigidity does not correlate with the observed trend of **1** < **2** < **3** < **4** < **5** in the FWHM of g_{xy}. Emission lifetimes and rigidity can frequently be correlated directly with specific structural features like C–H v. C–D functionalization.[74] Thus, this work suggests that, at least for **1-5**, and possibly for other open-shell complexes, the specific "rigid" structural features that impact photophysics and EPR linewidth are not entirely coincident.

Our second and third tests of rigidity probed direct structural factors. First, note that *tris*-bidentate metal complexes exhibit stereochemistry that is influenced by the identity of the ligand backbone. Indeed, several previous studies of analogous *tris*-diamine metal complexes demonstrate that there are myriad isomers possible.[75,76] To test if the number of isomers influences EPR spectral linewidth, as these may each impose different *g* or *D* values (and thus broaden the signals), we synthesized and analysed **5-*SS***, a chemically identical complex to **5**, but using the enantiopure (1*S*,2*S*)-(+)-1,2-diaminocyclohexane, instead of racemic *trans*-(±)-1,2-diaminocyclohexane. The use of this ligand reduced the number of possible isomers from eight to two. We hypothesized that we would observe a sharper spectrum for complex **5-*SS*** compared to **5**, if the number of isomers dictates spectral broadness in this system.

Continuous-wave L-band EPR spectra were collected for **5-*SS*** in identical sample conditions to **5** and was subsequently modelled with EasySpin[36] to extract the spin Hamiltonian parameters (**Figure A1.13**, **Table A1.11**). There is a field offset because of differing experiment frequencies (1.360 GHz for **5** and 1.095 GHz for **5-*SS***). However, adequate simulations of both spectra could be achieved using the same simulation parameters. Furthermore, the FWHM of the

g_{xy} term was the same (4.0) in the analysis. This result indicates that EPR line broadening is likely not influenced by the number of isomers of a given species, and thus the differences in the possible number of isomers between **1**-**5** likely is not responsible for the observed trend in linewidth.

Systems **1**, **2**, **4**, and **5**, for which crystal structures are available in this work or others,[49,50] were further investigated by means of quantum chemical (QC) calculations and *ab initio* molecular dynamics (AIMD) simulations in explicit water. The purpose of these simulations is to test for correlations between mean atomic displacements in the first coordination shell (as a function of ligand) and the EPR spectral shape. The structures of **1**, **2**, **4**, and **5** micro-solvated by 20 water molecules were first optimized at the TPSSh+D3BJ/def2-TZVP level of theory using NWPEsSE (**Figure A1.14**).[39] The optimized structures were then used as initial structures in the following AIMD simulations in water boxes (**Figure A1.15**). Relevant structural parameters are listed in **Table 2.2**.

Table 2.2. Mean structural bond distances (Å) and angles (°) from Quantum chemical (QC) calculations and Ab initio molecular dynamics (AIMD) simulations.

	1	**2**	**4**	**5**
Cr−N (QC)	2.102	2.125	2.134	2.116
Cr−N (AIMD)	2.213	2.197	2.214	2.200
FWHM	0.120	0.229	0.128	0.123
N−Cr−N_{Bite} (QC)	80.7	80.9	89.5	80.9
N−Cr−N_{Bite} (AIMD)	79.8	81.0	89.4	80.9
N−Cr−N_{Adj} (QC)	93.1	94.0	90.1	93.8
N−Cr−N_{Adj} (AIMD)	93.2	92.6	89.5	92.6
N−Cr−N_{Opp} (QC)	171.3	170.9	178.6	170.6
N−Cr−N_{Opp} (AIMD)	166.2	169.2	173.8	168.9

Molecular dynamics (MD) simulations are commonly used for simulating EPR spectra in spin-labelled proteins,[77–79] or evaluating distances between metal complexes (either as spin labels[80] or aggregates[81]). Here we present, to the best of our knowledge, the first effort to use MD simulations to understand EPR spectral linewidth of $S > {}^1/_2$ metal complexes. Note that the

following structural analyses from AIMD simulations are obtained from solution-phase environments. These conditions are different than the frozen-glass solutions that produced the spectra in **Figure 2.5**. In the following analysis and discussion, we consider the spectra of the frozen glasses to provide a "snap-shot" of the distribution of possible geometries of the Cr^{3+} complexes in solution when frozen.

AIMD simulations were conducted using the CP2K package.[82] The potential energy surface was calculated at the PBE-D3 density functional[83] level of theory with Grimmes' correction for dispersion.[84] We adopted the Gaussian-Plane wave hybrid basis set scheme,[85] in which the Gaussian basis sets of the DVZP quality, in conjunction with a plane wave energy cut-off of 450 Ry, were used. MD simulations were performed within the NVT ensemble, with the temperature kept at 300 K with a velocity-rescaling thermostat.[86] For each simulation of a complex, the Cr(III) complex, three Cl^- counterions, and a box of water solvent molecules were initially equilibrated for at least 8 ps, followed with 10 ps production runs that were finally used for the computation of properties. Additional details for the simulations can be found in *Section 2.3.5*.

The structural parameters deduced from the AIMD simulations exhibit distributions in structural metrics but are otherwise similar to the crystalline structures. For example, all complexes are six-coordinate throughout the 10 ps time window, and distributions in observed Cr–N bond distances are all centered around 2.2 Å, which is close to the crystal structures. We note, however, that the full widths at half maxima of the Cr–N distributions change with the ligand: 0.120 Å for **1**, 0.118 Å for **2**, 0.128 Å for **4**, and 0.123 Å for **5**. The simulations also reveal that all complexes exhibit distributions in N–Cr–N angles, also close to the crystal structures.[49,50] For example, for **1**, **2**, and **5,** three peaks are exhibited in the distributions at ca. 79° (bite angle), 94° (adjacent N atoms on different ligands), and 170° (approximately *trans* N atoms). Complex **4**, in contrast, exhibits

only two peaks, one near 90° and one closer to 175°. Here, the sharpest two angles are relatively close in value, potentially encouraged by ligand strain, and consistent with solution-phase extended x-ray absorption fine-structure analyses of $[Co(tn)_3]^{3+}$.[87] The distributions of discussed parameters are depicted in **Figure 2.7**. We note that perfect agreement should not be expected for any structural parameter here since the crystalline environment is more rigid than the fluxional one in solution captured by molecular dynamics simulations.

The simulations also provided insights into the solvation structure of the complexes, by revealing the radial distribution function, g(r), that provides a measure of the average M•••O_{water}

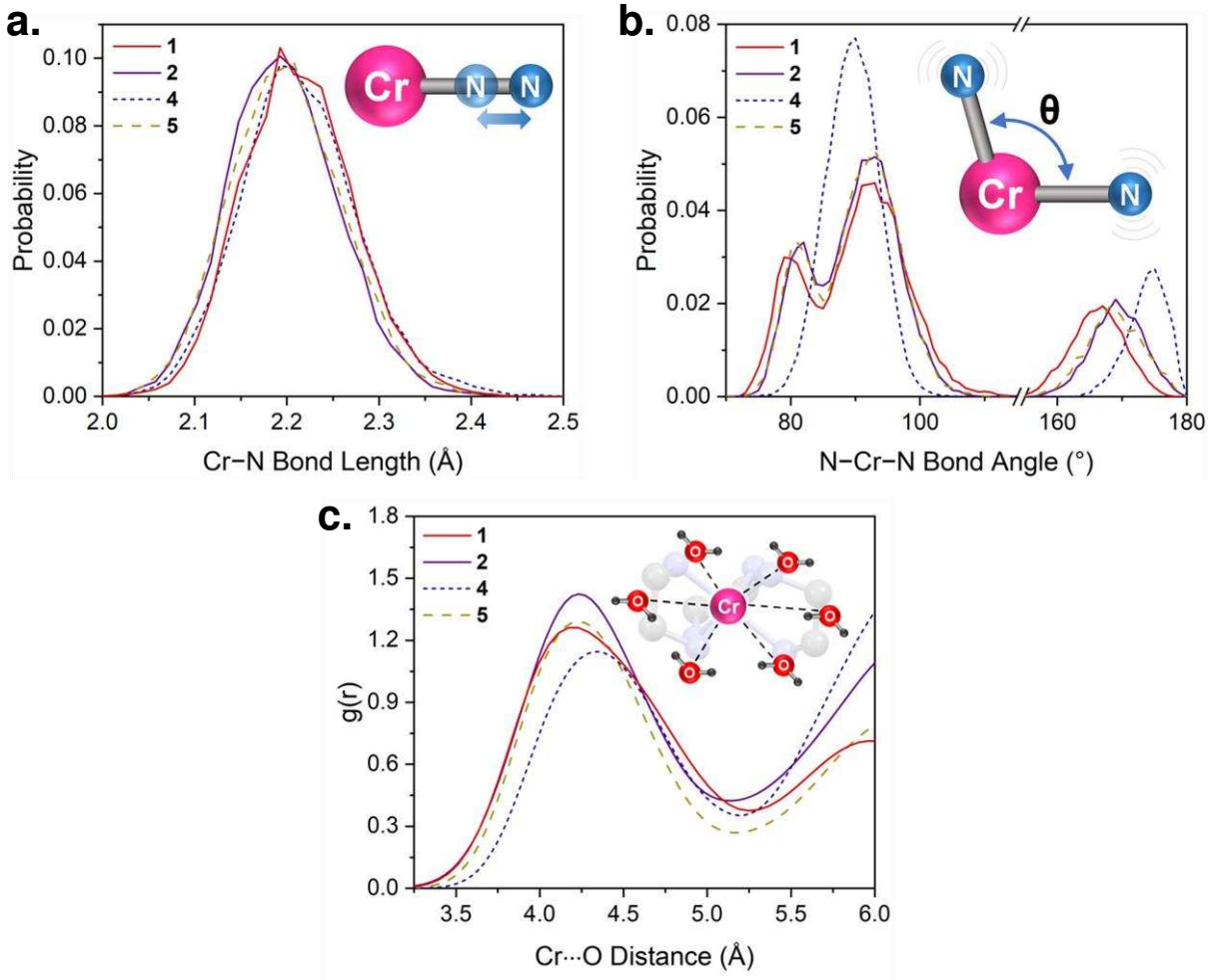

Figure 2.7. **(a)** Simulated distribution of Cr–N bond lengths for complexes **1**, **2**, **4**, and **5**. **(b)** Simulated distribution of N–Cr–N bond angles for complexes **1**, **2**, **4**, and **5**. **(c)** Simulated distribution of distances between Cr(III) metal centres and the oxygen atoms of surrounding water molecules for complexes **1**, **2**, **4**, and **5**.

distance and its fluctuation over the simulation period. For **1**, **2**, **4**, and **5**, the computed g(r) places the first solvent shell near 4.2 Å for all complexes: 4.17 Å for **1**, 4.23 Å for **2**, 4.34 Å for **4**, and 4.23 Å for **5**. Beyond 5 Å, a rise in g(r) is observed for all complexes, indicating the start of the second solvent shell in the 5.5-5.75 Å range.

The distributions of bond angles, bond distances, and solvent shell values were compared with the observed spectroscopic trends. We reasoned that the relative rigidity in the coordination shell correlates with the relatively tighter distributions of observed bond distances and angles from the 10 ps trajectory in solution for **1**, **2**, **4**, and **5**. The one parameter that approximately correlates to the observed spectral trend is the distribution in Cr–N bond distances. Complexes **1** and **2** have relatively sharper EPR spectra, smaller $g_{x,y}$ FWHM values, and slightly sharper distributions in the simulated Cr–N distances. Complexes **4** and **5**, in contrast, have slightly larger Cr–N distributions, which would broaden spectra by producing variation in electronic structure.[88,89] We tentatively speculate that **4** and **5** produce both broader distributions and spectra owing to more efficient structural trans-effect interactions between the N donor atoms. This effect results in larger M–L bond distances for donor atoms that are directly *trans* to another atom, which been observed with larger mean atomic displacements in crystal structures of other metal complexes.[90,91] Indeed, **4** and **5** are closest to O_h geometry (from the SHAPE measure analysis). Thus, the N–Cr–N the bond angles between *trans* N-donors in 4 and 5 are overall closer to 180°, enabling a stronger structural trans effect. If true, this idea suggests that geometries where the trans-effect is less operative (e.g. T_d or perhaps trigonal-prismatic coordination) are particularly promising for future molecules with sharper linewidths. Finally, we note that the observed difference between the distributions of **1**, **2**, **4**, and **5** is small, suggesting an extremely high sensitivity of spectral shape to ligand field.

Our calculations suggest variability in Cr–N bond lengths of *over* 0.2 Å (~10% based on *total* width of the distributions), which we infer leads to a large variation of *g*-values. We also suggest that the relative changes in the FWHM of these distributions, while small (e.g. 0.003 Å between **1** and **5**), are appreciably affecting relative linewidth. For this last point, literature evidence supports that relatively tiny changes can induce large changes to EPR spectra. For example, variable-pressure studies of Cr-doped solids (Al_2O_3:Cr and $Al_2(SO_4)_3$:Cr) show pressure dependence of zero-field splitting[92,93] and *g*-values[93], in some cases showing *ca*. 0.005 changes in *g* with 0.02 Å changes in Cr–O bond distances.[93,94] In a 1 GHz EPR spectrum at $g = 2.00$, a variation in *g* of ±0.15 would induce a 60 G span for the EPR peak, well within the width of the full spectra shown in **Figure 2.5**. Thus, these data suggest that the ligand-based distributions in observed Cr–N bond distances are affecting spectral shape, though quantitative correlation will likely need deeper studies of solution structure (e.g. by extended X-ray absorption fine structure spectroscopy), which are underway.

2.5. Conclusion

The foregoing study is the first analysis of low-frequency EPR linewidth as a function of ligand identity in $S > {}^1/_2$ metal complexes. Most importantly, our studies of *tris*-diamine Cr^{3+} complexes reveal three novel insights:

(1) Relatively minor changes in ligand identity can impact the L-band EPR spectral shape, which has important implications for, e.g., using tuneable ligand fields to image local chemistry via magnetic resonance.

(2) Our studies show that the same parameters that define "rigidity" in the sense of photochemical lifetimes do not correlate to EPR linewidth, suggesting more detailed approaches to rigidity design are necessary in this new field.

(3) Finally, our studies suggest that EPR linewidth in Cr^{3+} complexes can be correlated to variation in Cr–L bond distance variation in frozen solution.

This final outcome suggests that many tuneable aspects of metal complexes, e.g. donor atom, metal-ligand bond strength, and covalency, can all be harnessed to manipulate low-frequency EPR linewidth by controlling metal-ligand interactions. We note that the linewidths here (> 10 G) are still substantially larger than organic radicals under similar conditions (< 1G).[15] Thus, further tests of the effects of ligand shells on linewidth are clearly needed for functional metal-ion based EPRI molecular probes.

References

(1) In Vivo EPR (ESR): Theory and Application; Berliner, L. J., Ed.; Biological Magnetic Resonance; Springer US, 2003.

(2) Klare, J. P. Biomedical Applications of Electron Paramagnetic Resonance (EPR) Spectroscopy. *Biomed. Spectrosc. Imaging* **2012**, No. 1, 101–124.

(3) Colacicchi, S.; Ferrari, M.; Sotgiu, A. In Vivo Electron Paramagnetic Resonance Spectroscopy/Imaging: First Experiences, Problems, and Perspectives. *Int. J. Biochem.* **1992**, *24* (2), 205–214.

(4) Caia, G. L.; Efimova, O. V.; Velayutham, M.; El-Mahdy, M. A.; Abdelghany, T. M.; Kesselring, E.; Petryakov, S.; Sun, Z.; Samouilov, A.; Zweier, J. L. Organ Specific Mapping of in Vivo Redox State in Control and Cigarette Smoke-Exposed Mice Using EPR/NMR Co-Imaging. *J. Magn. Reson.* **2012**, *216*, 21–27.

(5) Mikuni, T.; He, G.; Petryakov, S.; Fallouh, M. M.; Deng, Y.; Ishihara, R.; Kuppusamy, P.; Tatsuta, M.; Zweier, J. L. In Vivo Detection of Gastric Cancer in Rats by Electron Paramagnetic Resonance Imaging. *Cancer Res.* **2004**, *64* (18), 6495–6502.

(6) Hyodo, F.; Murugesan, R.; Matsumoto, K.; Hyodo, E.; Subramanian, S.; Mitchell, J. B.; Krishna, M. C. Monitoring Redox-Sensitive Paramagnetic Contrast Agent by EPRI, OMRI and MRI. *J. Magn. Reson.* **2008**, *190* (1), 105–112.

(7) Epel, B.; Sundramoorthy, S. V.; Krzykowska-Serda, M.; Maggio, M. C.; Tseytlin, M.; Eaton, G. R.; Eaton, S. S.; Rosen, G. M.; Kao, J. P. Y.; Halpern, H. J. Imaging Thiol Redox Status in Murine Tumors In Vivo with Rapid-Scan Electron Paramagnetic Resonance. *J. Magn. Reson.* **2017**, *276*, 31–36.

(8) Voinov, M. A.; Scheid, C. T.; Kirilyuk, I. A.; Trofimov, D. G.; Smirnov, A. I. IKMTSL-PTE, a Phospholipid-Based EPR Probe for Surface Electrostatic Potential of Biological Interfaces at Neutral pH: Effects of Temperature and Effective Dielectric Constant of the Solvent. *J. Phys. Chem. B* **2017**, *121* (11), 2443–2453.

(9) Voinov, M. A.; Polienko, J. F.; Schanding, T.; Bobko, A. A.; Khramtsov, V. V.; Gatilov, Y. V.; Rybalova, T. V.; Smirnov, A. I.; Grigor'ev, I. A. Synthesis, Structure, and X-Band (9.5 GHz) EPR Characterization of the New Series of pH-Sensitive Spin Probes: N,N-Disubstituted 4-Amino-2,2,5,5-Tetramethyl-3-Imidazoline 1-Oxyls. *J. Org. Chem.* **2005**, *70* (24), 9702–9711.

(10) Gallez, B.; Mader, K.; Swartz, H. M. Noninvasive Measurement of the pH inside the Gut by Using pH-Sensitive Nitroxides. An in Vivo EPR Study. *Magn. Reson. Med.* **1996**, *36* (5), 694–697.

(11) Potapenko, D. I.; Foster, M. A.; Lurie, D. J.; Kirilyuk, I. A.; Hutchison, J. M. S.; Grigor'ev, I. A.; Bagryanskaya, E. G.; Khramtsov, V. V. Real-Time Monitoring of Drug-Induced Changes in the Stomach Acidity of Living Rats Using Improved pH-Sensitive Nitroxides and Low-Field EPR Techniques. *J. Magn. Reson.* **2006**, *182* (1), 1–11.

(12) *EPR Imaging and in Vivo EPR*, 1st ed.; Gareth R. Eaton, Sandra S. Eaton, Keiichi Ohno, Eds.; CRC Press, 2018.

(13) Demsar, F.; Walczak, T.; Morse, P. D.; Bačić, G.; Zolnai, Z.; Swartz, H. M. Detection of Diffusion and Distribution of Oxygen by Fast-Scan EPR Imaging. *J. Magn. Reson.* **1988**, *76* (2), 224–231.

(14) Swartz, H. M.; Flood, A. B.; Schaner, P. E.; Halpern, H.; Williams, B. B.; Pogue, B. W.; Gallez, B.; Vaupel, P. How Best to Interpret Measures of Levels of Oxygen in Tissues to Make Them Effective Clinical Tools for Care of Patients with Cancer and Other Oxygen-Dependent Pathologies. *Physiol. Rep.* **2020**, *8* (15), e14541.

(15) Burks, S. R.; Makowsky, M. A.; Yaffe, Z. A.; Hoggle, C.; Tsai, P.; Muralidharan, S.; Bowman, M. K.; Kao, J. P. Y.; Rosen, G. M. The Effect of Structure on Nitroxide EPR Spectral Linewidth. *J. Org. Chem.* **2010**, *75* (14), 4737–4741.

(16) Biller, J. R.; Meyer, V.; Elajaili, H.; Rosen, G. M.; Kao, J. P. Y.; Eaton, S. S.; Eaton, G. R. Relaxation Times and Line Widths of Isotopically-Substituted Nitroxides in Aqueous Solution at X-Band. *J. Magn. Reson.* **2011**, *212* (2), 370–377.

(17) Hitchcock, R. T. *Radio-Frequency and Microwave Radiation*; AIHA, 2004.

(18) Fuchs, J.; Herrling, T.; Groth, N. Detection of Free Radicals in Skin: A Review of the Literature and New Developments. In *Current Problems in Dermatology*; Thiele, J., Elsner, P., Eds.; Karger: Basel, 2000; Vol. 29, pp 1–17.

(19) Danhier, P.; Gallez, B. Electron Paramagnetic Resonance: A Powerful Tool to Support Magnetic Resonance Imaging Research. *Contrast Media Mol. Imaging* **2015**, *10* (4), 266–281.

(20) Griffith, J. S. *The Theory of Transition-Metal Ions*; Cambridge University Press, 1964.

(21) Figgis, B. N.; Hitchman, M. A. *Ligand Field Theory and Its Applications*; Special topics in inorganic chemistry; Wiley-VCH, 2000.

(22) Poole, C. P.; Farach, H. A. Line Shapes in Electron Spin Resonance. *Bull. Magn. Reson.* **1979**, *1* (4), 162–194.

(23) DeArmond, M. K. Relaxation of Excited States in Transition-Metal Complexes. *Acc. Chem. Res.* **1974**, *7* (9), 309–315.

(24) Roundhill, D. M. *Photochemistry and Photophysics of Metal Complexes*; Modern Inorganic Chemistry; Springer US, 1994.

(25) Rausch, A. F.; Murphy, L.; Williams, J. A. G.; Yersin, H. Improving the Performance of Pt(II) Complexes for Blue Light Emission by Enhancing the Molecular Rigidity. *Inorg. Chem.* **2012**, *51* (1), 312–319.

(26) Li, G.; Zhan, F.; Zheng, J.; Yang, Y.-F.; Wang, Q.; Chen, Q.; Shen, G.; She, Y. Highly Efficient Phosphorescent Tetradentate Platinum(II) Complexes Containing Fused 6/5/6 Metallocycles. *Inorg. Chem.* **2020**, *59* (6), 3718–3729.

(27) Vincent, J. B.; Lukaski, H. C. Chromium. *Adv. Nutr.* **2018**, *9* (4), 505–506.

(28) Matović, Z. D.; Meetsma, A.; Miletić, V. D.; van Koningsbruggen, P. J. Copper(II) Complexes with Unsymmetrical Pentadentate Ed3a-Type Diamino-Tricarboxylate Ligands. Crystal Structures, Configurational Analysis and DFT Study of Complexes. *Inorg. Chim. Acta.* **2007**, *360* (7), 2420–2431.

(29) Belošević, S.; Ćendić, M.; Djukić, M.; Vasojević, M.; Meetsma, A.; Matović, Z. D. Crystal Structure, Configurational and Density Functional Theory Analysis of Nickel(II) Complexes with Pentadentate 1,3-Pd3a-Type Ligands. *Inorg. Chim. Acta.* **2013**, *399*, 146–153.

(30) Noyori, R. Asymmetric Catalysis: Science and Opportunities (Nobel Lecture). *Angew. Chem. Int. Ed.* **2002**, *41* (12), 2008–2022.

(31) Pedersen, E. Preparation of Bis- and Tris(Diamine)Chromium(III) Complexes via Dimethyl Sulfoxide and Dimethylformamide Complexes. The Novel Series of Cis-Bis(Trimethylene-Diamine)- and Cis-Bis[(-)Trans-1,2-Cyclohexane-Diamine]Chromium(III) Complexes. *Acta Chem. Scand.* **1970**, *24*, 3362–3372.

(32) Gillard, R. D.; Mitchell, P. R.; Busch, D. H.; Sperati, C. R.; Jonassen, H. B.; Weston, C. W. Tris(Diamine)Chromium(III) Salts. *Inorg. Synth.* **2007**, *38*, 184–186.

(33) Sheldrick, G. M. SHELXT – Integrated Space-Group and Crystal-Structure Determination. *Acta Cryst. A,* **2015**, *71* (1), 3–8.

(34) Sheldrick, G. M. Crystal Structure Refinement with SHELXL. *Acta Cryst. C,* **2015**, *71* (1), 3–8.

(35) Sheldrick, G. M. A Short History of SHELX. *Acta Cryst. A,* **2008**, *64* (1), 112–122.

(36) Stoll, S.; Schweiger, A. EasySpin, a Comprehensive Software Package for Spectral Simulation and Analysis in EPR. *Journal of Magnetic Resonance* **2006**, *178* (1), 42–55.

(37) Quine, R. W.; Rinard, G. A.; Ghim, B. T.; Eaton, S. S.; Eaton, G. R. A 1–2 GHz Pulsed and Continuous Wave Electron Paramagnetic Resonance Spectrometer. *Rev. Sci. Instrum.* **1996**,

(38) Rinard, G. A.; Eaton, S. S.; Eaton, G. R.; Poole, C. P. J.; Farach, H. A. Sensitivity in EPR Measurements. In *Handbook of Electron Spin Resonance*; Poole, C. P. J., Farach, H. A., Eds.; Electron Spin Resonance; Springer-Verlag: New York, 1999; Vol. 2, pp 1–23.

(39) Zhang, J.; Glezakou, V.-A.; Rousseau, R.; Nguyen, M.-T. NWPEsSe: An Adaptive-Learning Global Optimization Algorithm for Nanosized Cluster Systems. *J. Chem. Theory Comput.* **2020**, *16* (6), 3947–3958.

(40) Zhang, J.; Dolg, M. ABCluster: The Artificial Bee Colony Algorithm for Cluster Global Optimization. *Phys. Chem. Chem. Phys.* **2015**, *17* (37), 24173–24181.

(41) Zhang, J.; Dolg, M. Global Optimization of Clusters of Rigid Molecules Using the Artificial Bee Colony Algorithm. *Phys. Chem. Chem. Phys.* **2016**, *18* (4), 3003–3010.

(42) Jorgensen, W. L.; Maxwell, D. S.; Tirado-Rives, J. Development and Testing of the OPLS All-Atom Force Field on Conformational Energetics and Properties of Organic Liquids. *J. Am. Chem. Soc.* **1996**, *118* (45), 11225–11236.

(43) Spoel, D. V. D.; Lindahl, E.; Hess, B.; Groenhof, G.; Mark, A. E.; Berendsen, H. J. C. GROMACS: Fast, Flexible, and Free. *J. Comput. Chem.* **2005**, *26* (16), 1701–1718.

(44) Niketic, S. R.; Rasmussen, K.; Woldbye, F.; Lifson, S.; Koskikallio, J. Conformational Analysis of Coordination Compounds. III. Tris-Diamine Cobalt(III) and Chromium(III) Complexes with Six-Membered Chelate Rings. *Acta Chem. Scand.* **1976**, *30a*, 485–497.

(45) Toftlund, H.; Pedersen, E. The Preparation and Optical Activity of the Isomers of the 1,2-Cyclopentanediamine Cobalt(III) and Chromium(III) Complexes. *Acta Chem. Scand.* **1972**, *26*, 4019–4030.

(46) Bear, J. L.; Wendlandt, W. W. The Thermal Decomposition of the Tris (Ethylenediamine) and Tris(1,2-Propylene-Diamine) Chromium (III) Chloride and Thiocyanate Complexes. *J. Inorg. Nuc. Chem.* **1961**, *17* (3), 286–294.

(47) Pfeiffer, P.; Haimann, M. Tripropylendiaminchromasalze. *Ber. Dtsh. Chem. Ges.* **1903**, *36* (1), 1063–1069.

(48) Pfeiffer, P. Über Chromiake. Abhandlung I. Trichlorotripyridinbrom Und Triäthylendiaminchromisalze. *Z. Für Anorg. Chem.* **1900**, *24* (1), 279–304.

(49) Whuler, A.; Brouty, C.; Spinat, P.; Herpin, P. Structure Du Complexe Actif Hydraté (+)-$Cr(en)_3Cl_3 \cdot 2H_2O$. Etude de La Configuration Absolue et Du Désordre Conformationnel. *Acta Cryst. B,* **1977**, *33* (9), 2877–2885.

(50) Kalf, I.; Calmuschi, B.; Englert, U. Chiral Cr(III) and Co(III) Complex Cations as Building Blocks for Ordered and Disordered Salts. *CrystEngComm,* **2002**, *4* (91), 548–551.

(51) Lewis, K. G.; Ghosh, S. K.; Bhuvanesh, N.; Gladysz, J. A. Cobalt(III) Werner Complexes with 1,2-Diphenylethylenediamine Ligands: Readily Available, Inexpensive, and Modular Chiral Hydrogen Bond Donor Catalysts for Enantioselective Organic Synthesis. *ACS Cent. Sci.* **2015**, *1* (1), 50–56.

(52) Spiro, T. G.; Terzis, A.; Raymond, K. N. Structure of $Ni(CN)_5^{3-}$. Raman, Infrared, and x-Ray Crystallographic Evidence. *Inorg. Chem.* **1970**, *9* (11), 2415–2420.

(53) Jurnak, F. A.; Raymond, K. N. Effect of Packing Forces on the Geometry of the Pentacyanonickelate(3-) Ion. Structures of Tris(1,3-Propanediamine)Chromium(III) Pentacyanonickelate(II) Dihydrate and Hexamminechromium(III) Pentacyanonickelate(II) Dihydrate. A Skew-Boat Conformation in a Six-Membered Metal Chelate Ring. *Inorg. Chem.* **1974**, *13* (10), 2387–2397.

(54) Sunatsuki, Y.; Miyahara, S.; Suzuki, T.; Kojima, M.; Nakashima, T.; Matsumoto, N.; Galsbøl, F. Homochiral Column Structure of Rac- and Λ-$[M^{III}(tn)_3]P_3O_9$ (M = Co, Cr; tn = 1,3-Diaminopropane; P_3O_9 = Cyclotriphosphate^{3-}) Produced by Multiple Hydrogen Bonds. *New J. Chem.* **2010**, *34* (12), 2777–2784.

(55) Nagao, R.; Marumo, F.; Saito, Y. The Crystal Structure of (−)589-Tris(1,3-Diaminopropane)Cobalt(III) Chloride Monohydrate, (−)589-$[Co(tn)_3]Cl_3 \cdot H_2O$. *Acta Cryst. B,* **1973**, *29* (11), 2438–2443.

(56) Saito, Y.; Iwasaki, H.; Ota, H. The Absolute Configuration of the Tris-*l*-Propylenediamine Cobalt (III) Ion, L-[Co *l*-Pn3]$^{3+}$. *Bull. Chem. Soc. Jpn.* **1963**, *36* (11), 1543–1544.

(57) Nomura, T.; Marumo, F.; Saito, Y. The Crystal Structure of (−)D-Tris(Trimethylenediamine)Cobalt(III) Bromide Monohydrate. *Bull. Chem. Soc. Jpn.* **1969**, *42* (4), 1016–1020.

(58) Alvarez, S.; Avnir, D.; Llunell, M.; Pinsky, M. Continuous Symmetry Maps and Shape Classification. The Case of Six-Coordinated Metal Compounds. *New J. Chem.* **2002**, *26* (8), 996–1009.

(59) Alvarez, S.; Alemany, P.; Casanova, D.; Cirera, J.; Llunell, M.; Avnir, D. Shape Maps and Polyhedral Interconversion Paths in Transition Metal Chemistry. *Coord. Chem. Rev.* **2005**, *249* (17), 1693–1708.

(60) Marts, A. R.; Greer, S. M.; Whitehead, D. R.; Woodruff, T. M.; Breece, R. M.; Shim, S. W.; Oseback, S. N.; Papish, E. T.; Jacobsen, F. E.; Cohen, S. M.; Tierney, D. L. Dual Mode EPR

Studies of a Kramers Ion: High-Spin Co(II) in 4-, 5- and 6-Coordination. *Appl. Magn. Reson.* **2011**, *40* (4), 501–511.

(61) *CRC Handbook of Chemstry and Physics*, 85th ed.; Lide, D. R., Ed.; CRC Press: Boca Raton, FL, 2004.

(62) Froncisz, W.; Hyde, J. S. Broadening by Strains of Lines in the *g* -parallel Region of Cu^{2+} EPR Spectra. *J. Chem. Phys.* **1980**, *73* (7), 3123–3131.

(63) Bonomo, R.; Riggi, F. EPR Investigation of Chromium (III) Complexes: Analysis of Their Frozen Solution and Magnetically Dilute Powder Spectra. *Chem. Phys.* **1991**, *151*, 323–333.

(64) McGarvey, B. R. Spin Hamiltonian for Cr III Complexes. Calculation from Crystal Field and Molecular Orbital Models and ESR Determination for Some Ethylenediammine Complexes. *The Journal of Chemical Physics* **1964**, *41* (12), 3743–3758.

(65) McGarvey, B. R. Spin Hamiltonian of Chromium (III) in a Cubic Field. *J. Chem. Phys.* **1962**, *37* (12), 3020–3021.

(66) Açıkgöz, M. A Semi-Empirical Analysis of ZFS Parameters for Transition Metal (TM) Ions (Cr^{3+} and Mn^{2+}) Centers in K_2MgF_4. *J. Phys. Chem. Solids* **2016**, *98*, 115–122.

(67) Açıkgöz, M. Investigation of the Cr3+ Centers in Rb2ZnF4, Rb2CdF4, and Rb2MgF4 Fluorine Compounds: A Semi-Empirical Analysis. *J. Fluor. Chem.* **2015**, *175*, 152–159.

(68) Žilić, D.; Androš Dubraja, L.; Krupskaya, Y.; Kataev, V.; Büchner, B. Magnetic Anisotropy of Cr(III) Ions in Polymeric Oxalate Complexes as Revealed by HF-ESR Spectroscopy. *Appl. Magn. Reson.* **2015**, *46*, 309–321.

(69) Kripal, R.; Yadav, A. K. EPR, Optical Absorption and Superposition Model Studies of Cr^{3+} Doped Dipotassium Stannic Chloride Monohydrate. *Chem. Phys. Lett.* **2014**, *612*, 245–250.

(70) Zangana, K. H.; Pineda, E. M.; Vitorica-Yrezabal, I. J.; McInnes, E. J. L.; Winpenny, R. E. P. Linking Cr_3 Triangles through Phosphonates and Lanthanides: Synthetic, Structural, Magnetic and EPR Studies. *Dalton Trans.* **2014**, *43* (35), 13242–13249.

(71) Su, D.; Teoh, C. L.; Wang, L.; Liu, X.; Chang, Y.-T. Motion-Induced Change in Emission (MICE) for Developing Fluorescent Probes. *Chem. Soc. Rev.* **2017**, *46* (16), 4833–4844.

(72) Comba, P.; Mau, A. W. H.; Sargeson, A. M. Excited-State Decay of the Macrobicyclic Hexaamine Chromium(III) Cage Complexes Cr(III)Sar^{3+} and Cr(III)$Diamsar^{3+}$. *J. Phys. Chem.* **1985**, *89* (3), 394–396.

(73) Santoro, A.; Kershaw Cook, L. J.; Kulmaczewski, R.; Barrett, S. A.; Cespedes, O.; Halcrow, M. A. Iron(II) Complexes of Tridentate Indazolylpyridine Ligands: Enhanced Spin-Crossover Hysteresis and Ligand-Based Fluorescence. *Inorg. Chem.* **2015**, *54* (2), 682–693.

(74) Hebbink, G. A.; Reinhoudt, D. N.; Veggel, F. C. J. M. van. Increased Luminescent Lifetimes of Ln^{3+} Complexes Emitting in the Near-Infrared as a Result of Deuteration. *Chem. Eur. J.* **2001**, *2001* (21), 4101–4106.

(75) Ehnbom, A.; Ghosh, S. K.; Lewis, K. G.; Gladysz, J. A. Octahedral Werner Complexes with Substituted Ethylenediamine Ligands: A Stereochemical Primer for a Historic Series of Compounds Now Emerging as a Modern Family of Catalysts. *Chem. Soc. Rev.* **2016**, *45* (24), 6799–6811.

(76) Jurnak, F. A.; Raymond, K. N. Conformations of Six-Membered Rings in Tris Metal Complexes. A Skew-Boat Conformation in $[Cr(NH_2CH_2CH_2CH_2NH_2)_3]^{3+}$. *Inorg. Chem.* **1972**, *11* (12), 3149–3152.

(77) Huang, Y.-W.; Chiang, Y.-W. Spin-Label ESR with Nanochannels to Improve the Study of Backbone Dynamics and Structural Conformations of Polypeptides. *Phys. Chem. Chem. Phys.* **2011**, *13* (39), 17521–17531.

(78) Martin, P. D.; Svensson, B.; Thomas, D. D.; Stoll, S. Trajectory-Based Simulation of EPR Spectra: Models of Rotational Motion for Spin Labels on Proteins. *J. Phys. Chem. B* **2019**, *123* (48), 10131–10141.

(79) Jeschke, G. DEER Distance Measurements on Proteins. *Annu. Rev. Phys. Chem.* **2012**, *63* (1), 419–446.

.

(80) Gamble Jarvi, A.; Sargun, A.; Bogetti, X.; Wang, J.; Achim, C.; Saxena, S. Development of Cu^{2+}-Based Distance Methods and Force Field Parameters for the Determination of PNA Conformations and Dynamics by EPR and MD Simulations. *J. Phys. Chem. B* **2020**, *124* (35), 7544–7556.

(81) Lockyer, S. J.; Nawaz, S.; Brookfield, A.; Fielding, A. J.; Vitorica-Yrezabal, I. J.; Timco, G. A.; Burton, N. A.; Bowen, A. M.; Winpenny, R. E. P.; McInnes, E. J. L. Conformational Flexibility of Hybrid [3]- and [4]-Rotaxanes. *J. Am. Chem. Soc.* **2020**, *142* (37), 15941–15949.

(82) Hutter, J.; Iannuzzi, M.; Schiffmann, F.; VandeVondele, J. Cp2k: Atomistic Simulations of Condensed Matter Systems. *WIREs Comput. Mol. Sci.* **2014**, *4* (1), 15–25.

(83) Perdew, J. P.; Burke, K.; Ernzerhof, M. Generalized Gradient Approximation Made Simple. *Phys. Rev. Lett.* **1996**, *77* (18), 3865–3868.

(84) Grimme, S.; Antony, J.; Ehrlich, S.; Krieg, H. A Consistent and Accurate Ab Initio Parametrization of Density Functional Dispersion Correction (DFT-D) for the 94 Elements H-Pu. *J. Chem. Phys.* **2010**, *132* (15), 154104.

(85) Lippert, G.; Hutter, J.; Parrinello, M. A hybrid Gaussian and plane wave density functional scheme. *Molecular Physics* **1997**, *92* (3), 477–488.

(86) Bussi, G.; Donadio, D.; Parrinello, M. Canonical Sampling through Velocity Rescaling. *J. Chem. Phys.* **2007**, *126* (1), 014101.

(87) Ozvat, T. M.; Sterbinsky, G. E.; Campanella, A. J.; Rappé, A. K.; Zadrozny, J. M. EXAFS Investigations of Temperature-Dependent Structure in Cobalt-59 Molecular NMR Thermometers. *Dalton Trans.* **2020**, *49*, 16380–16385.

(88) Abragam, A.; Bleaney, B. *Electron Paramagnetic Resonance of Transition Ions*; OUP Oxford, 2012.

(89) Dai, D.; Xiang, H.; Whangbo, M.-H. Effects of Spin-Orbit Coupling on Magnetic Properties of Discrete and Extended Magnetic Systems. *J. Comput. Chem.* **2008**, *29* (13), 2187–2209.

(90) Coe, B. J.; Glenwright, S. J. Trans-Effects in Octahedral Transition Metal Complexes. *Coord. Chem. Rev.* **2000**, *203* (1), 5–80.

(91) Elder, R. C.; Heeg, M. J.; Payne, M. D.; Trkula, M.; Deutsch, E. Trans Effect in Octahedral Complexes. 3. Comparison of Kinetic and Structural Trans Effects Induced by Coordinated Sulfur in Sulfito- and Sulfinatopentaaminecobalt(III) Complexes. *Inorg. Chem.* **1978**, *17* (2), 431–440.

(92) Bielecki, K. A High Pressure EPR Study of Cr^{3+} Doped Deuterated Potassium Aluminium Alum. *Phys. Stat. Sol. B* **1988**, *148* (1), K53–K56.

(93) Nelson, H. M.; Larson, D. B.; Gardner, J. H. Very High Pressure Effects upon the EPR Spectrum of Ruby. *J. Chem. Phys.* **1967**, *47* (6), 1994–1998.

(94) Finger, L. W.; Hazen, R. M. Crystal Structure and Compression of Ruby to 46 kbar. *J. Appl. Phys.* **1978**, *49* (12), 5823–5826.

CHAPTER 3 – Structure and Dynamics of Ligands in Cr(III) Complexes for the Interpretation of EPR and Raman Spectral Lines

3.1. Overview

Understanding how to control electron paramagnetic resonance (EPR) linewidth in metal complexes is a challenge. In this report we apply a combination of Extended X-ray Absorption Fine Structure (EXAFS) and Raman spectroscopies, as well as ab initio molecular dynamics (AIMD) and density functional theory (DFT) analyses to four Cr(III)-complexes, **1** $[Cr(en)_3]Cl_3$ (en = ethylenediamine), **2** $[Cr(tn)_3]Cl_3$ (tn = 1,3-diaminopropane), **3** $[Cr(\textit{trans}\text{-chxn})_3]Cl_3$ (*trans*-chxn = *trans*-(±)-1,2-diaminocyclohexane), and **4** $[Cr(\textit{RR}\text{-dphen})_3]Cl_3$ (*RR*-dphen = (1*R*,2*R*)-(+)-1,2-diphenylethylenediamine), with the aim of developing a valid model of inhomogeneous broadening for the interpretation of the EPR spectra of these species. We show that variations in bond lengths, strengths, vibrational level populations and vibration composition do not trend with linewidth. The results therefore provide numerous disproofs of inhomogeneous broadening as an important mechanism of spectral broadening and suggest homogenous broadening mechanisms related to spin relaxation are instead operative.

3.2. Introduction

The solution-phase structure of a metal complex can often differ greatly from the solid-state or crystal structure.[1,2] The disparities between these structures can impact electronic structures and all of the properties that stem from it, including reactivity,[3] optical spectra,[4] and magnetic resonance[5] or magnetic behaviors.[6] Of the latter class, a key magnetic resonance property is the line shape of the EPR spectrum.[7] The spectral shape directly stems from electronic structure,

which, for an $S > {}^1/_2$ metal ion, dictates magnetic parameters such as the g factor,[8] the zero-field splitting parameters (D and E)[9,10] and the distributions of these values. These parameters are often diagnostic for metal ion geometry,[11–13] oxidation state,[14–16] and identity,[17–19] and are thus of interest to the bioinorganic community and the study of metalloenzymes in non-crystalline conditions.[20] On the applied front, the spectral shape, specifically resonance location and sharpness, can reveal potential utility for applications as spin labels,[21] addressable molecular qubits,[22] or bioimaging techniques such as electron paramagnetic resonance imaging.[23]

For the foregoing reasons, simultaneously characterizing metal-complex solution structures *and* tying those structures to EPR linewidths is essential for developing a wide range of applications. Yet, this is a stark challenge as identifying solution-phase molecular structures with the same accuracy as single-crystal techniques is daunting, therefore multiple different techniques spanning solution spectroscopies and computational analyses are typically required. An additional complication is that structures in solution are dynamic, exhibiting distributions of structural parameters and thus electronic structures. In practice, these distributions *inhomogeneously* broaden the EPR linewidth.[23] Understanding how to minimize and control the effects of this broadening mechanism by molecular design is an important goal toward sharp transitions and applicability for any of the above applications. Indeed, such design principles also assume that inhomogenous broadening is the operative mechanism, and tests of the "truthiness" of that assumption are also necessary. Thus, the validation of new experimental/computational methods to elucidate the specific structural features contributing to this broadening mechanism is vital.

Quantum mechanical computation (DFT) and ab initio molecular dynamics (AIMD) simulations can assist in this effort. The g, D, and E parameters of an $S > {}^1/_2$ metal ion are directly tied to the d-orbital identities and energies of a metal complex,[24] and thus DFT can, in principle,

capture the molecular flexibilities along the AIMD trajectories that dictate distributions in *D* or *g,* and thus be used to model EPR spectral broadening. Instances of using DFT and AIMD simulations to model the EPR spectra of spin-labelled proteins,[25–27] and trinuclear metal complexes, where inter-spin interactions impact the spectra, demonstrate the power of modern computational methods.[28,29] Additionally, calculations of spin-Hamiltonian parameters for $S > ½$ metal ions based on single-crystal structure are also well trodden.[30,31] However, to the best of our knowledge, there are no tests of whether MD simulations can aid in understanding the spectral broadening mechanisms of $S > {}^1/_2$ metal ions, particularly those that arise from in-solution structural dynamics.

In this report, we use a battery of spectroscopic and computational techniques to aid in the connection of the solution-phase structures of a series of Cr(III) complexes with low-frequency (L-band, 1.3 GHz) EPR spectral shape. We tested four *tris*-diamino complexes as shown in **Figure 3.1**: $[Cr(en)_3]Cl_3$ (**1**, en = ethylenediamine), $[Cr(tn)_3]Cl_3$ (**2**, tn = 1,3-diaminopropane), and $[Cr(\textit{trans}\text{-chxn})_3]Cl_3$ (**3**, *trans*-chxn = *trans*-(±)-1,2-diaminocyclohexane), $[Cr(\textit{RR}\text{-dphen})_3]Cl_3$ (**4**, *RR*-dphen = (1*R*,2*R*)-(+)-1,2-diphenylethylenediamine). A prior report described the ligand-dependence of the L-band EPR linewidth for these species, which was posited to stem from relative distributions of Cr–N bond distances in solution.[7] In this manuscript, we further investigate correlating the structural distributions in MD simulations to EPR spectra with the assistance of frozen-solution EXAFS, Raman and local vibrational spectroscopies aiming for the following objectives:

(1) Determine spin-Hamiltonian parameters to characterize the molecular structure and detect bonding interactions relevant to those parameters;

(2) Assess the distribution of Cr−N bond lengths in frozen solutions and the solid-state spectroscopically and test specifically how that distribution affects spectral shape;

Elucidate the bonding character related to Cr-ligand modes and characterize the local components that contribute to enhanced intensity in the Raman spectra;

(3) Determine the intrinsic strength of the Cr-N bonds and whether correlation to spectral shape follows.

We found that the aggregate of these analyses yields new insight into the original reported analysis, and, in the process, provides a new toolkit for interpreting solution-phase EPR spectra of metal complexes.

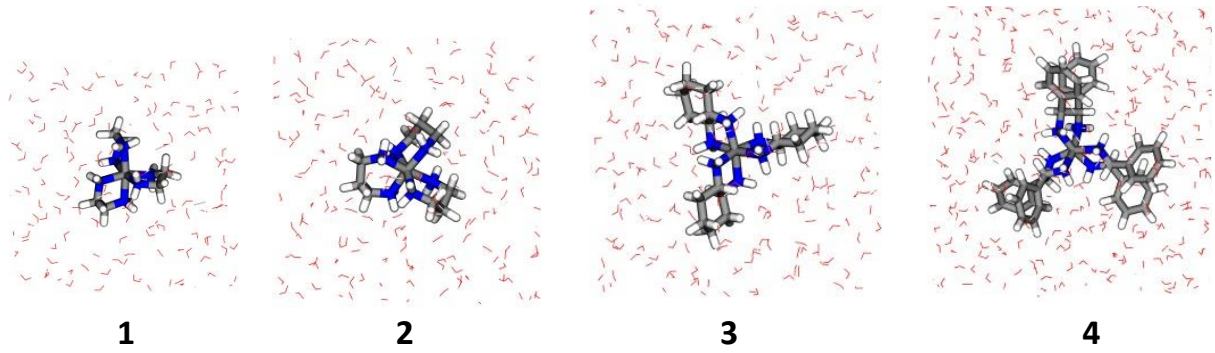

Figure 3.1. Structural depictions of the Cr(III) complexes **1**-**4** surrounded by water investigated by AIMD simulations. The complexes are $[Cr(en)_3]Cl_3$ (**1**, en = ethylenediamine), $[Cr(tn)_3]Cl_3$ (**2**, tn = 1,3-diaminopropane), and $[Cr(trans\text{-}chxn)_3]Cl_3$ (**3**, *trans*-chxn = *trans*-(±)-1,2-diaminocyclohexane), $[Cr(RR\text{-}dphen)_3]Cl_3$ (**4**, RR-dphen = (1*R*,2*R*)-(+)-1,2-diphenylethylenediamine).

3.3. Experimental Section

3.3.1 General Considerations

Compounds **1-4** were prepared following literature procedures.[7] Ethylene glycol and polyethylene glycol were purchased from commercial vendors and used as received. Water was purified through a Milli-Q system and sparged for 30 minutes prior to use.

3.3.2. Extended X-ray Absorption Spectroscopy

Samples were prepared in the solution phase and solid state. Frozen solutions for analyses were prepared at 30 mM in water and ethylene glycol (1:1 v/v), which forms a glass when frozen. These solutions were collected at 110 K. These conditions were selected to mirror those used for the L-band EPR data collection. Solid-state pellets were prepared by mixing polycrystalline samples of the respective Cr(III) complexes (4-6 mg) in polyethylene glycol (PEG, 25-30 mg) and finely grinding the mixture until homogeneous. The solid mixtures were then pressed into 7 mm diameter pellets and affixed to a 3D-printed sample holder with Kapton tape.

X-ray absorption fine structure (XAFS) spectroscopy measurements were carried out at beamline 9-BM of the Advanced Photon Source. The X-ray beam was focused to a roughly 1 mm diameter spot by a Rh-coated toroidal X-ray mirror, and X-ray energy was selected by a Si (111) double crystal monochromator. Liquid samples were injected into Teflon cells with Kapton windows. The cells were then loaded into a cryocooler and cooled to approximately 110 K during data collection. The XAFS spectra were obtained by detecting the Cr-$K\alpha$ fluorescence with a four-element silicon drift detector while scanning the energy through the Cr K-edge. Each experiment consisted of 8-12 collected scans per sample measurement.

EXAFS data were acquired from the raw XAS data in which the EXAFS regions were analyzed. Scans for each compound were averaged before rebinning the k^2-weighted EXAFS data. All data reduction and fits were made using the Demeter: XAS Data Processing and Analysis software using IFEFFIT. In the completed investigation of dynamic structural change between differing ligand compositions, the Fourier transform (FT) data of all solution-phase EXAFS spectra were fit against their respective crystal structures as each has been previously

reported.[7,32,33] Calculated scattering paths from these experimental solid-stated models were then used to construct fits elucidating the relative changes in bond lengths and degrees of atomic displacements between each solution-phase compound. The calculated scattering paths from the crystal-structure models were used to construct a complete fit for all spectra over k-range of 2-12 $Å^{-1}$. The magnitudes and real parts of the Fourier transform of $k^2c(k)$ along with the resulting fits are shown in **Figures A2.1-2.6**. All R-space fits were taken with k, k^2, and k^3-weighting from which S_0^2, E_0, ΔR, and σ^2 parameters were evaluated from the fitting software Artemis.[34] Atomic distances R were determined from ΔR of the fit, where $\Delta R = R - R_{eff}$ and R_{eff} is the atomic distance for a specified set of atoms in the reference model structure and was determined with the ATOMS function in Artemis, using the provided crystal structure data. All of the spectral fit parameters are summarized in **Tables A2.1-2.8**.

3.3.3. Computational Methods

EXAFS. Molecular trajectories reported in our previous work[7] were used to provide structures for EXAFS simulations and electronic structure analyses in the present work. Simulations were carried out using the FEFF software (v8.5).[35] For each compound, 20 evenly spaced AIMD frames were taken from a 10 ps trajectory. An ensemble average spectrum was then generated from all the frames.

EPR. Using density functional theory (DFT), g-tensor, hyperfine couplings, nuclear-quadrupole couplings, and the zero-field splitting tensors were calculated with the PBE exchange-correlation functional.[36] The all-electron scalar relativistic approach (ZORA)[37] and the EPR-III basis functions[38] were used to model the Cr-metal center, while the rest of the atoms are described using def2-TZVPP.[39] The spin-Hamiltonian parameters are shown in **Tables A2.9-2.12**. To

generate predicted EPR spectra that model the experimental frozen solution spectra, the spin Hamiltonian parameters were computed at using 50 frames extracted from 10 ps AIMD simulations.[7] A single spectrum is generated using the EasySpin function "Pepper" for each set of spin-Hamiltonian parameters. The individual spectra were weighted evenly and summed to produce a combined EPR spectra that accounted for the multitude of orientations found in solution.

Raman. Raman spectra of **1-4** were collected in H_2O samples at *ca*. 30 mM concentration. All samples were prepared in 1 dram (ca. 4 mL) volume vials and measured using a Horiba Scientific ONDAX IHR 550 Spectrometer equipped with a 785 nm near-IR laser. The collected spectral range was made over 100-1000 cm^{-1} and background subtracted from each sample's respective blank. Samples were collected for a 270 second acquisition time. A vial containing only deionized water was also collected under identical conditions for a blank and background subtraction upon data processing.

Raman calculations corresponding to gas and solvent phases of the Cr-complexes were also carried out using the PBE functional.[36] The Stuttgart−Dresden effective core potential (SDD)[40] was used for Cr and cc-pVTZ[41] for H, C, and N atoms. The PBE functional is reported as an effective choice for computing the vibrational modes of 3d transition metal complexes[42–44] and combined with SDD can achieve high accuracy.[45] Implicit solvent Raman spectra were obtained using CPCM[46] solvation model with a dielectric constant of 78.4 corresponding to water. Selected geometry parameters are shown in **Table A2.13**. The obtained Raman intensities and frequencies were plotted using Gaussian functions of constant width (σ = 6.5 and 10.0, respectively for **1-3** and **4** complexes).

Raman spectra, with a frequency below 1000 cm^{-1} were further characterized using local vibrational mode theory[47] to directly compare the vibrational spectra and determine the intrinsic

bond strength. Contrary to normal frequencies, local modes have the advantage of being independent of the choice of the coordinates used to describe the molecule in question and are independent of the atomic masses. Local modes are susceptible to differences in the electronic structure (e.g., caused by changing a ligand), and they capture only electronic effects. Therefore, they are an excellent choice to determine the bond strength in the transition metal complexes and evaluate the character of the spectra.[48–53] The local vibrational mode analysis was done using the LModeA software. All DFT calculations were done using ORCA package.[54]

3.4. Results and Discussion

Cr *K*-edge EXAFS spectroscopy was conducted to investigate the molecular structure of complexes **1**-**4** as frozen solutions and in the solid state. Our primary goal was to assess the distribution of Cr−N bond lengths in frozen solution to compare to solid-state structure and previously calculated MD simulation data, which initially suggested that the distributions of those bond lengths dictate EPR spectral broadening. Individual bond lengths are not determined by EXAFS, but the determination of the distributions of bond lengths is possible from the mean square of relative displacement parameter (σ^2) for the Cr−N scattering pathways. With this analysis, a larger σ^2 parameter would imply a larger distribution of Cr−N bond lengths.

For each complex in frozen solution, the Fourier transforms of the EXAFS spectra yield a large primary peak centered just above an apparent distance of 1.6 Å (1.66 Å for **1** and **2**, 1.63 Å for **3** and **4**) with several subsequent smaller peaks out to about 5 Å that vary with each complex (**Figure 3.2**). In the solid-state, a similar result is obtained (**Figure A2.3-2.6**), though the apparent distances are slightly shorter: 1.56, 1.59, 1.66, and 1.62 Å, respectively, for **1-4**. These results are consistent with the AIMD-EXAFS simulations for **1-4** in H_2O (**Figure 3.2b**), which produced

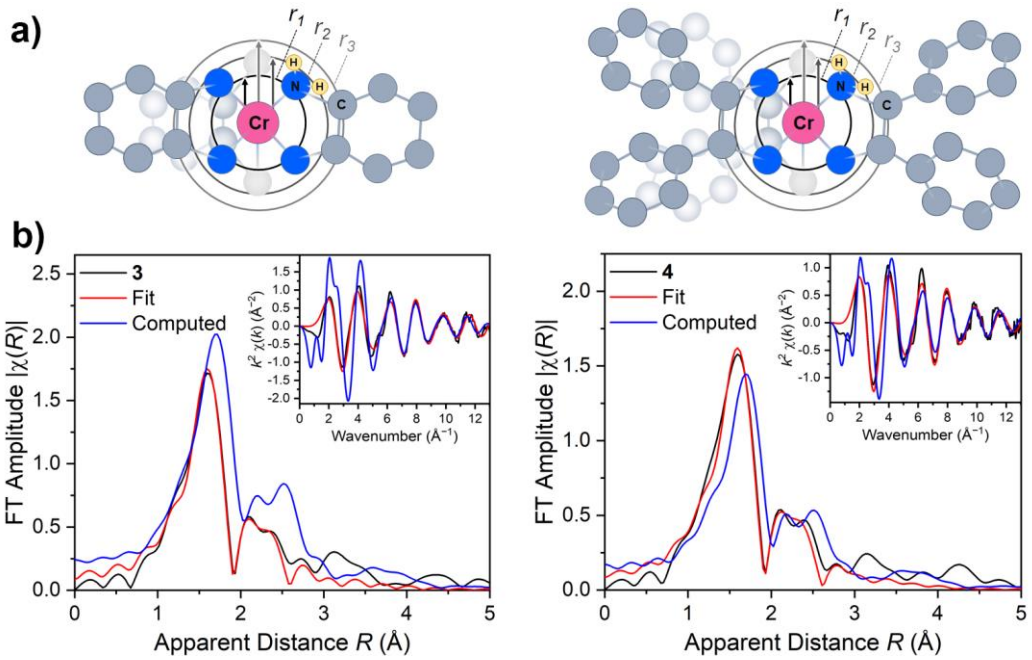

Figure 3.2. EXAFS analyses of **3** and **4**, which produce the broadest and sharpest EPR spectra, respectively. (**a**) Highlighted intramolecular atomic single scattering distances of **3** and **4** from the primary Cr–N_6 shell r_1, followed by second and third shells of ligand hydrogen and carbon atoms, r_2 and r_3, respectively. (**b**) Radial structure-function plot shown as Fourier Transform EXAFS data (Black) of **3** (left) and **4** (right), fit of experimental results (Red), and computed spectra from AIMD (Blue) with k^2-weighting over k-range of 2–12 $Å^{-1}$. Insets: k^2-weighted k-space plots and fits of **3** and **4**.

primary peaks centered at ~ 1.68 Å. The largest peak in each spectrum is likely attributable to scattering paths between the central Cr(III) ion and N atoms in the first coordination sphere. It is important to note that the center of this first peak, while stemming from the Cr–N bonding, should not directly match the Cr–N internuclear distance, as the scattering is triggered by electrons which also exist between the nuclei on the bond path. The smaller peaks at higher *R* likely originate from scattering paths between other atoms in the molecules, like the C-atoms of the ligand backbones. Overall, the collected spectra looked largely similar for **1-4,** regardless of the way they were collected, in frozen solution or the solid state.

The collected data were fit by modeling single-scattering-event pathways and starting with the reported crystal structures of **1-4**. For **1**, **3**, and **4**, for example, three distinct shells of scattering

atoms were included in the model (**Figure 3.2a**). The first shell included pathways between the Cr(III) center and the first coordination sphere N-atoms. The second shell included pathways between the Cr(III) center and the H-atoms connected to the coordinating N-atoms (N−H). Finally, the third shell included scattering pathways between the Cr(III) center and the first pair of C-atoms on the ligand backbone which are bound directly to the N-atoms. In complex **2**, all of the aforementioned scattering pathways were included, with one more: a single scattering path between the Cr(III) center and the third, central C-atom on that ligand backbone.

Fitting parameters appear to vary only slightly between the different phases. Focusing specifically on the parameters for the first coordination sphere, *R* values varied from 2.0796 Å for **4** to 2.0995 Å for **2** in frozen solution and 2.0704 Å for **2** to 2.0848 Å for **1** in the solid state. The *R* values indicate half of the total scattering path (from Cr to N, back to Cr), which can be thought of as analogous to the Cr−N atomic distance. These values can be compared to the crystallographically determined Cr−N bond lengths, which show good agreement, differing by less than 0.5% in both the solid and frozen solution phases.[7] Together, the EXAFS data indicate a high similarity between the CrN_6 coordination spheres from crystalline to solution phases.

The σ^2 values from the analysis of the first scattering path serve as the handle for the distribution of that scattering path length, and thus Cr−N bond length distributions. As shown in **Table 3.1**, extracted σ^2 values from the frozen solution and solid state imply that the greatest variation of Cr−N bond lengths occurs in complex **4**, followed by **1**, **2**, and **3** in solution. Whereas the greatest variation in Cr−N bond lengths in the solid state are found in complex **1**, followed by

Table 3.1. Relative displacement parameter (σ^2) for the Cr−N scattering pathways in Å^2.

σ^2	Frozen Solution	Solid State
1	0.00153 ± 0.00125	0.00410 ± 0.00243
2	0.00133 ± 0.00134	0.00406 ± 0.00242
3	0.00112 ± 0.00153	0.00183 ± 0.00174
4	0.00243 ± 0.00137	0.00353 ± 0.00197

2, **4**, and **3**. However, a closer inspection of the differences between each of the σ^2 values shows that those differences are smaller than the computed errors. For example, for **1** in frozen solution, the uncertainty of σ^2 is 0.00125 Å^2 when the value of σ^2 is 0.00153 Å^2. The resulting range, by extending the uncertainty in either direction around the principal value, includes the σ^2 values for the rest of the compounds measured. The same outcome is observed for **2**-**4.**

Based on the findings in our previous study,[7] we hypothesized the outcomes of this experiment would show that **1** and **4** would have the smallest σ^2, coincident with the sharpest EPR spectra and that **2** and **3** would have the largest σ^2 to match their broader spectra. Instead, the trend in σ^2 does not follow the observed broadening nor the variance in Cr−N bond lengths as determined by AIMD. Furthermore, a critical analysis of the error and parameter magnitudes suggests that the differences between the distributions of bond lengths may be below our ability to measure accurately. If that latter point is true, it is also possible that the bond distributions are too small to contribute significantly to EPR spectral broadening, disproving our prior hypothesis for linewidth control. Albeit this conclusion requires a conceptual leap between the determining that the differences in σ^2 are too small to measure and the reasoning that they may not contribute strongly to EPR spectral broadening, the results still indicate the need to test additional hypotheses to rule out other potential causes of the trend in linewidth. As such, we sought to investigate the role of metal-ligand vibrations to better understand the extent of its influence on EPR spectral broadening.

A growing body of work is showing the importance of Raman-active vibrational modes in governing spin-based properties, including spin-lattice relaxation for electron spins[55] and chemical-shift temperature sensitivity in ^{59}Co nuclear spins.[56] As such, we analyzed the Raman vibrational spectra of **1-4** to test the hypothesis that the EPR spectral shape may trend with specific vibrational characteristics. To conduct this analysis, we used a combination of the theoretical

Raman spectra calculated in implicit water as a solvent, which was corroborated with experimentally obtained Raman spectra collected in aqueous solutions in across a 200-1000 cm^{-1} frequency range.

As shown in **Figure 3.3**, the calculated spectra correctly reflect peaks and relative intensities of those observed experimentally. Complexes **1-3** possess strong bands in the 400-500 cm^{-1} region due to Cr–N stretching modes and in the 800-1000 cm^{-1} region due to Cr–N–C/H bending modes. A similar trend is seen in the gas phase, which is presented in **Figure A2.7**, and the Cr–N stretching is shown by the vibrational density-of-states (VDOS) obtained from the AIMD. **Figure A2.8** presents that the VDOS associated with stretching modes of Cr–N bonds

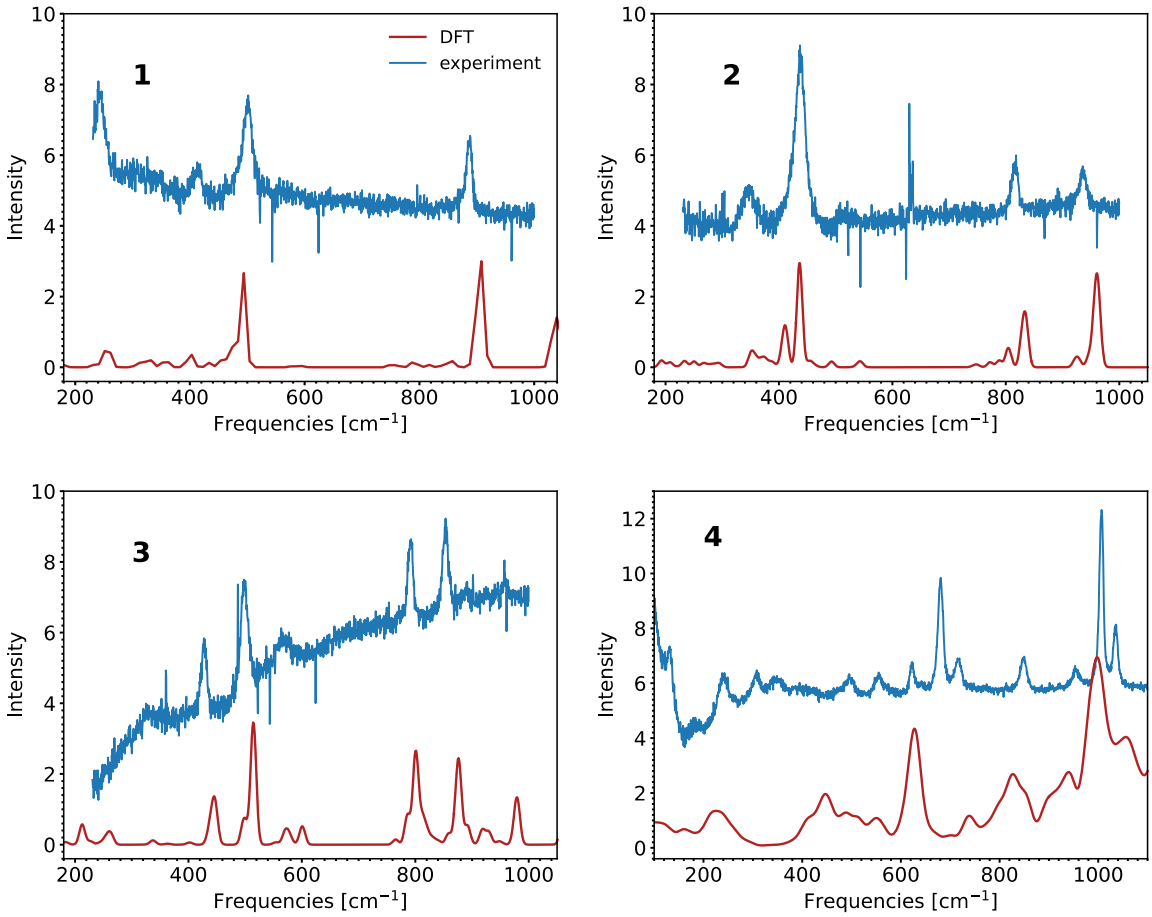

Figure 3.3. Experimental (Blue) and computed (DFT, Red) Raman spectra of solvated Cr-complexes (**1**-**4**). Spectra were collected in room temperature aqueous solutions at 30 mM concentrations.

appear in the same frequency as those observed in Raman spectroscopy. These results are all consistent with the quasi-octahedral coordination assigned to the Cr(III) complexes.[57]

The most striking difference between experiment and simulation is observed in complex **4**. However, a bulkiness of complex **4** can lead to the antisymmetric behavior of the vibrations.[58] Consequently, the enhancement at 450 cm^{-1} is observed due to Cr−N stretching, while high-frequency peaks are due to Cr−N−C/H bending and other coupling modes, which is explained in the next section.

We compared total vibrational partition functions for **1**-**4** using the computed Raman- and IR-active modes to test for correlations to linewidth. The total vibrational partition function (q_{total}) was calculated as the product of the partition function of each normal-mode given the equation $q = 1/(1 - e^{-E/k_B T})$, where E is the normal-mode energy, k_B is Boltzmann's constant, and T is the temperature. A higher q_{total} value would imply that the included modes are more populated at a given temperature, and, potentially, more possibility for structural variation and spectral broadening. However, comparison of observed linewidths simply with number of Raman modes failed to produce a meaningful correlation.

Owing to that lack of correlation, we sought to go a step deeper, acknowledging that a given normal mode in **1-4** is not a simple diatomic vibration but a complicated movement of multiple atoms in each molecule. We reasoned that we could therefore analyze the data by truncating the total vibrations to those that were "more localized" on the metal than those that were primarily focused on the ligands, which in this case corresponded to Cr–N stretches and N–Cr–N bends. Raman modes containing > 30% Cr−N stretch character were considered (**Figures 3.4**, **A2.9-2.12**), and the corresponding q_{total} values under these conditions yielded 1.16 (**1**), 1.27 (**2**), 1.18 (**3**), and 1.34 (**4**). These values do not follow the previously reported trend in broadening,

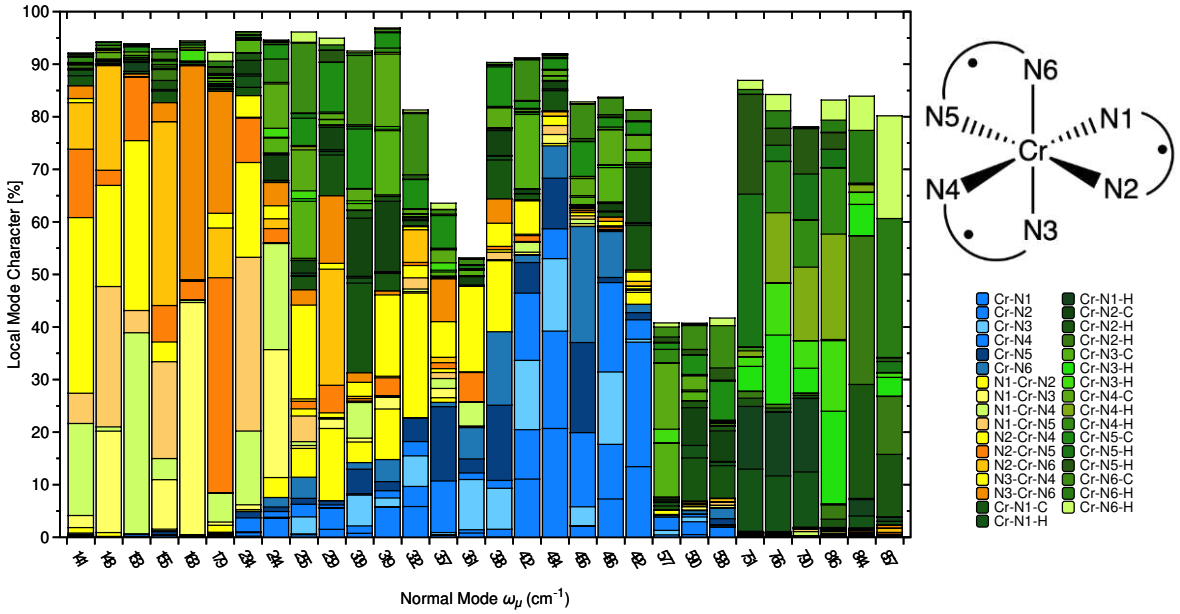

Figure 3.4. Decomposition of each normal vibrational mode of complex **1** into the local mode contributions. On the x-axis, the vibrational frequencies are given. The local modes are color-coded as defined in the legend: blue corresponds to Cr−N stretching contributions, yellow to N−Cr−N bending, green to Cr−N−C/H bending.

where **1** and **4** have the sharpest spectra. We further explored this point by assessing only modes that were primarily (> 30%) N−Cr−N bend in character, which also were generally low in energy. These comparisons yielded q_{total} values of 1.11 (**1**), 1.34 (**2**), 1.07 (**3**), and 8.48 (**4**), again standing in contrast to the observed trend in the EPR spectra shapes. We therefore conclude that simple numbers of low-energy symmetric Raman stretches do not guide EPR signal broadening as they do to other dynamic spin phenomena, at least under the conditions we measured.

Another possible explanation for the previously observed trend in spectral broadening relates to bond strength. In this hypothesis, a stronger Cr–N bond may produce a more rigid structure and therefore sharpen linewidth. To test this hypothesis, we applied local vibrational mode theory[47] to **1-4** to extract metal-ligand bond strengths and provide a comprehensive picture of the Raman spectra by decomposition of normal frequencies into local vibrational modes and contributions focusing on local parameters such as bonds and angles, as shown in **Figure 3.4**.

The bands between 402–486 cm^{-1} of complex **1** are attributed to all Cr−N stretches, which make up over 50% of each vibration and explain the peak broadening in the Raman spectra. The highest combination of all Cr−N stretches (75%) is observed at 434 cm^{-1}. The remaining 25% of this frequency consists of numerous N−Cr−N, Cr−N−C/H bends, and local vibrations that do not include the Cr atom. Frequencies below 234 cm^{-1} mainly consist of the various local modes associated with N−Cr−N stretches (yellow bars in **Figure 3.4**), while the frequencies above 751 cm^{-1} with Cr−N−C/H stretches (green bars). A similar trend is observed in complexes **2-4**, for which the local mode contributions are shown in **Figures A2.10-S12**.

Since the vibrational spectra are sensitive to the bond forces, the force constant is derived through local vibrational modes to determine the strength of the Cr-N bonds. We note that the information on the bond strength can be obtained from the relative displacement parameter (σ^2) shown in the EXAFS discussion above. However, the local stretching force constant, k^a, captures the pure electronic effects and provides a quantitative measure of the bond strength.[59]

As shown in **Table 3.2**, the strongest Cr−N bonds are calculated in complexes **3** and **4** with average force constants of 1.516 and 1.526 mdyn/Å, respectively. The weakest Cr−N bond is in complex **2** where the force constant is 1.373 mdyn/Å. A similar trend is observed in σ^2 measured by EXAFS in the solid state. In complexes **1**, **3**, and **4**, the Cr ion forms a five-membered ring with each bidentate ligand, which minimizes strain, optimizes overlap, and contributes to the electron donation towards the metal center, and strengthens the Cr–N bond. The triethylenediamine ligands

Table 3.2. Average of the Cr–N bond length, r_n, local force constant, k^a, and local vibrational frequency, ω^a.

	r_n (Å)	k^a (mdyn/Å)	ω^a (cm^{-1})
1	2.101	1.424	468
2	2.121	1.373	460
3	2.102	1.516	483
4	2.111	1.526	484

in complex **2** form six-membered rings with Cr and increase steric strain to weaken the Cr–N bond, in line with expectations.[60] Finally, we note that, like the other sections above, a comparison of k^a with linewidth broadening does not follow a trend, disproving the hypothesis that Cr–N bond strength is controlling the EPR linewidths of **1-4** in frozen solution.

Finally, we sought to compare the L-band EPR spectra determined from the spin-Hamiltonian parameters obtained via our computational methods to the experimentally determined EPR spectra. Computational tools for predicting EPR spectra were previously reported with connection to DFT, Hartree-Fock, and QM/MM methods.[61–63] With the aim of achieving a better understanding of the solvent dependence and electrostatic effects due to the polarity of the solvent, here the EPR spectra are predicted from AIMD, annealed to 110K, and compared to experimental values at the same temperature using the EasySpin software package.[64]

Experimental and two simulated EPR spectra of complexes **1-4** are displayed in **Figure 3.5**. The MD-simulated spectra were calculated as the average spectrum of the simulations of 50 different EPR spectra from 50 respective frames along the MD trajectory for that species. These simulations capture the changing orientations and geometries of each molecule in solution. The simulated EPR spectra were determined by fitting (by eye) the experimental spectra in EasySpin by modulating the spin-Hamiltonian parameters until a close match is achieved. Details for the latter fitting process are discussed at length in our previous report of these complexes.[7] For each complex, the MD-simulated EPR spectra produce an intense peak near 20 mT and a small dip that occurs between 50 and 70 mT. Hence, these simulated spectra capture the global features found in the experimentally obtained spectra, yet the simulations are not as smooth as the experimental data.

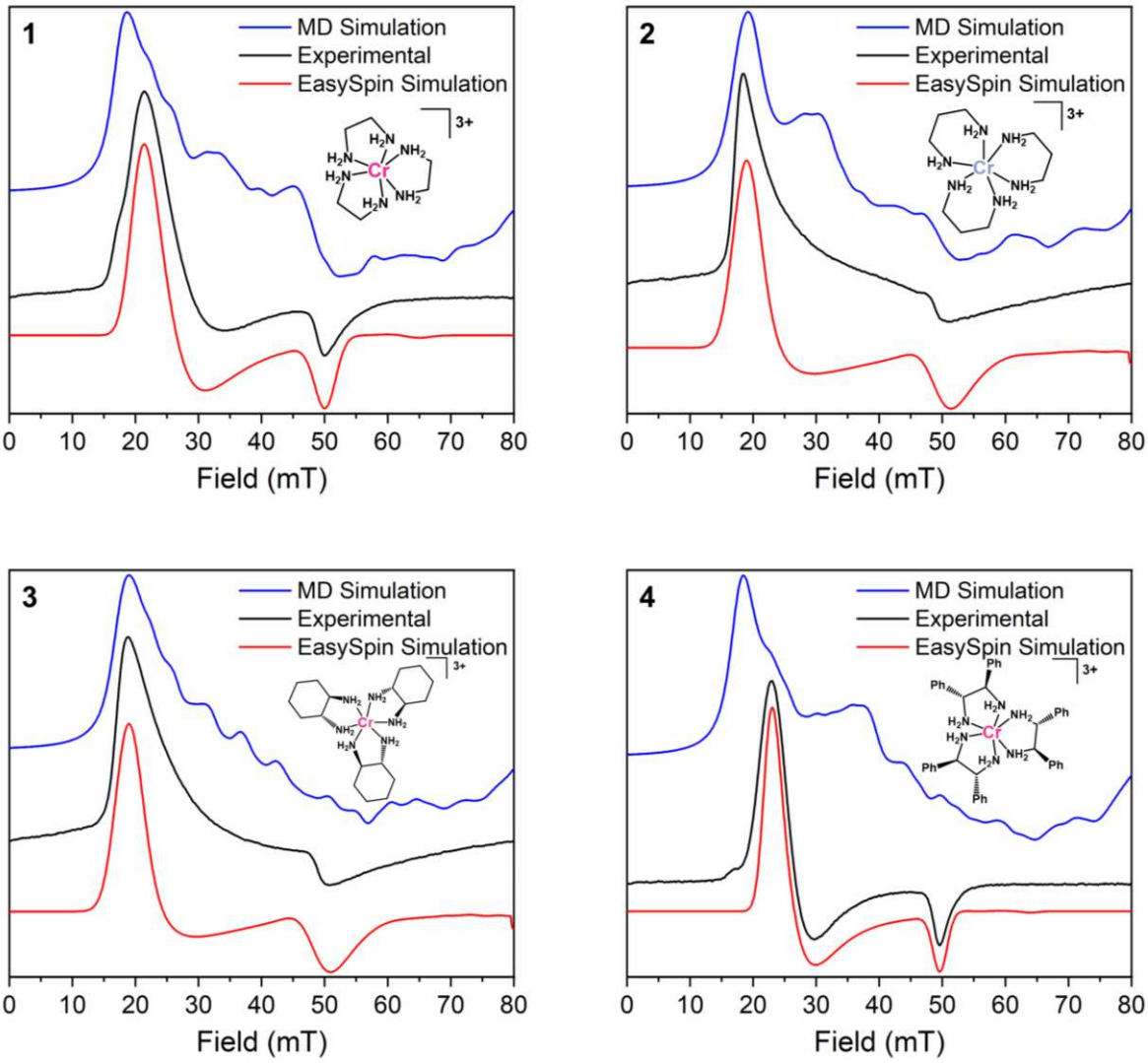

Figure 3.5. Experimental (Black), theoretical from the average of 50 snapshots in a 10 ps MD simulation (Blue), and simulated in EasySpin from inputted spin Hamiltonian parameters (Red) L-band EPR spectra of complexes **1-4**.

Table 3.3 shows the EPR parameters for complex **1**, and **2-3** are presented in **Tables A2.10-2.12**. The table includes anisotropic *g*-tensor components, g_x, g_y, g_z, an axial zero-field splitting interaction tensor, *D*, a hyperfine coupling constant, *A*, and *E*/*D* ratio, where *E* is the transverse zero-field splitting. The computed *g*-tensor components for both gas-phase and AIMD are in good agreement with experimental data. One can note that the *g*-tensor is nearly isotropic, suggesting weak polarity of the immediate surroundings, which is expected for a nearly octahedral

Table 3.3. EPR parameters for complex **1** of the data processing and calculation of the spin Hamiltonian parameters. For complexes **2-4**, see **Tables A2.10-2.12**.

	Gas Phase	**AIMD**	**Crystal Structure**	**Experiment (fitted)**
g_x	1.9938	1.9936	1.9944	1.985
g_y	1.9940	1.9937	1.9947	1.985
g_z	1.9942	1.9939	1.9950	1.960
D (cm^{-1})	–0.22	–0.08	–0.13	0.100
A (MHz)	27.10	27.45	26.98	0
E/D (cm^{-1})	0.05	0.03	0.10	0

CrN_6 coordination sphere. Axial g-values close to 1.99 are in line with octahedrally coordinated Cr(III) complexes,[65] thus, are satisfactory for obtaining optimal fit of experimental data in all four complexes. The AIMD-computed E/D ratios for all complexes are below 0.03, which is generally smaller than the value predicted from the crystal structures, where $E/D \sim 0.10$, resulting from small structural distortions from the ideal 3-fold rotational symmetry. The magnitude of E/D can sometimes correlate to molecular geometry: low E/D values are found for molecules with high axial symmetry and high E/D values for species with low molecular symmetry.[24] In this case, the predicted low values from AIMD, in conjunction with the results from the frozen-solution data, likely predict higher molecular symmetry for **1-4** in solution than in the solid state.

The foregoing results are illuminating of the viability of using AIMD and spectroscopy to understand solution structure and simulate low-frequency EPR spectroscopy. Indeed, to our knowledge, no previous attempts have been made to use computationally derived methods to predict L-band EPR spectra of metal complexes. Though the matches between the spectra derived from the MD simulations and the experimental spectra are not perfect, they are in reasonable agreement, capturing the major spectral features, which does suggest that this method can be a useful tool for predicting EPR spectra of frozen-solution phase molecules. This tool can be further

utilized for its predictive power in aiding the development of metal-based EPR imaging probes for future low-frequency/high-field spectroscopic studies.

Despite our application of multiple spectroscopies and AIMD analyses, the origin of the spectral broadening trend in **1-4** is not yet elucidated. However, Platt's method of strong inference[66] would argue the importance of these results as vital disproofs toward an understanding of the operative mechanism of broadening. First to the best of our evaluations here, variations on Cr–N bond distances or angles are likely not driving linewidth. Hence, we disproved one of the conclusions in our 2021 report. Second, we disproved that a Raman vibration population-based mechanism for broadening in **1-4** is active. Finally, third, we disproved that simple bond strengths and trends in spin Hamiltonian parameters are guiding the broadening. Each of these disproofs is important because they all reflect an assumption that the broadening is inhomogenous in nature.

In light of all the disproofs this report provides, the alternative explanation that comes up is related to *homogeneous* broadening. This mechanism is related to spin relaxation, namely, that the spin-spin relaxation time (T_2) of a spin is inversely proportional to the spectroscopic linewidth. In principle, this relaxation time could be slightly tweaked by two molecular features related to nuclear spin content.[67] First, changes in the solvent shell, governed by the ligand, could affect the proximity and number of protons, which in turn would influence T_2. Indeed, a preliminary plotting of the radial density distribution function of water molecules from the Cr(III) ions taken from the AIMD experiment (**Figure A2.13**) reveals a variable water content at distances out of 6 to 11 Å from the Cr(III) ion. Recent work by Stoll and coworkers[68,69] highlight protons in this region for their potency in causing T_2 to be short. Indeed complex **1** is predicted to have the fewest water molecules (and therefore protons) past the 6 Å, indicating that the lack of nuclear spin content in that region may play a role in the spectral sharpness. Hence, control of this solvent shell might be

integral to the linewidths of **1-4**. A second nuclear spin effect may be from those on the molecule itself, as these can affect T_2.[70–73] Ultimately, future studies utilizing pulsed EPR at low frequency are necessary to directly measure variations in T_2 and determine which factors strongly influence the relaxation dynamics, and thus homogeneous broadening. However, pulsed low-frequency EPR is an unusual capability and target for the magnetic resonance community,[74] and relaxation times often change with magnetic field/frequency,[75,76] so therefore simple extrapolation from common, higher-frequency experiments should be treated with caution. Instead, low-frequency instrumentation is necessary, and studies in this area will be reported in due course.

3.5. Conclusion

Understanding the EPR spectral shape of metal complexes, particularly in frozen solution, requires in depth studies of physical and electronic structures outside the comfortable confines of the single crystals. In this work, vibrational/X-ray absorption spectroscopies and modern DFT/AIMD methods allow for realistic modeling of the spectra *and* solution structures of Cr(III) complexes with *tris*-diamine ligands. As a result, we find the following as relevant to the frozen-solution EPR spectroscopic properties of the Cr(III) ions:

(1) The DFT-produced spin-Hamiltonian parameters, such as g, A, and E/D are in good agreement with those observed experimentally.

(2) The distribution of Cr−N bond lengths in frozen solution and solid state probed by Cr *K*-edge EXAFS spectroscopy and AIMD suggest that simple bond-length distributions do not contribute strongly to EPR spectral broadening.

(3) Analysis of the low-frequency Raman spectra via local-mode analysis for **1-4** enabled assignment of the observed vibrational modes and analysis of the thermal populations of these modes suggest that they are not a strong influence in EPR spectral broadening.

(4) Local force constant analysis revealed a trend in bond strengths for **1-4**, with **3** having the strongest and **1** the weakest Cr–N bonds. Importantly, the trend in this constant does not appear to follow the EPR results.

The aggregate insight afforded by the four conclusions above appears to be that homogeneous broadening could be driving the linewidth. This point then suggests design principles for spectral sharpness that do not depend on simple coordination chemistry principles like rigidity, but rather nuclear spin content, solvent-shell engineering, and more sophisticated design strategies based on magnetic effects. Future work exploring these ideas will be reported in due course.

References

(1) Braun, W.; Vasák, M.; Robbins, A. H.; Stout, C. D.; Wagner, G.; Kägi, J. H.; Wüthrich, K. Comparison of the NMR Solution Structure and the X-Ray Crystal Structure of Rat Metallothionein-2. *Proc. Natl. Acad. Sci.* **1992**, *89* (21), 10124–10128.

(2) Mah, V.; Jalilehvand, F. Cadmium(II) Complex Formation with Glutathione. *J. Biol. Inorg. Chem.* **2010**, *15* (3), 441–458.

(3) Benito-Garagorri, D.; Alves, L. G.; Puchberger, M.; Mereiter, K.; Veiros, L. F.; Calhorda, M. J.; Carvalho, M. D.; Ferreira, L. P.; Godinho, M.; Kirchner, K. Striking Differences between the Solution and Solid-State Reactivity of Iron PNP Pincer Complexes with Carbon Monoxide. *Organometallics* **2009**, *28* (24), 6902–6914.

(4) Shao, B.; Qian, H.; Li, Q.; Aprahamian, I. Structure Property Analysis of the Solution and Solid-State Properties of Bistable Photochromic Hydrazones. *J. Am. Chem. Soc.* **2019**, *141* (20), 8364–8371.

(5) Krzystek, J.; Yeagle, G. J.; Park, J.-H.; Britt, R. D.; Meisel, M. W.; Brunel, L.-C.; Telser, J. High-Frequency and -Field EPR Spectroscopy of Tris(2,4-Pentanedionato)Manganese(III): Investigation of Solid-State versus Solution Jahn−Teller Effects. *Inorg. Chem.* **2003**, *42* (15), 4610–4618.

(6) De, S.; Tewary, S.; Garnier, D.; Li, Y.; Gontard, G.; Lisnard, L.; Flambard, A.; Breher, F.; Boillot, M.-L.; Rajaraman, G.; Lescouëzec, R. Solution and Solid-State Study of the Spin-Crossover $[Fe^{II}(R\text{-bik})_3](BF_4)_2$ Complexes (R = Me, Et, Vinyl). *Eur. J. Inorg. Chem.* **2018**, *2018* (3–4), 414–428.

(7) Campanella, A. J.; Nguyen, M.-T.; Zhang, J.; Ngendahimana, T.; Antholine, W. E.; Eaton, G. R.; Eaton, S. S.; Glezakou, V.-A.; Zadrozny, J. M. Ligand Control of Low-Frequency Electron Paramagnetic Resonance Linewidth in Cr(III) Complexes. *Dalton Trans.* **2021**, No. 50, 5342–5350.

(8) Gast, P.; Groenen, E. J. J. EPR Interactions – g-Anisotropy. In *eMagRes*; John Wiley & Sons, Ltd, 2016; pp 1435–1444.

(9) Griffith, J. S. *The Theory of Transition-Metal Ions*; Cambridge University Press, 1964.

(10) Figgis, B. N.; Hitchman, M. A. *Ligand Field Theory and Its Applications*; Special topics in inorganic chemistry; Wiley-VCH, 2000.

(11) Churchill, M. R. Carbon-Hydrogen and Nitrogen-Hydrogen Distances Assumed in, and Determined from, Recent x-Ray Diffraction Studies on Inorganic Complexes. *Inorg. Chem.* **1973**, *12* (5), 1213–1214.

(12) Halcrow, M. A. Interpreting and Controlling the Structures of Six-Coordinate Copper(II) Centres – When Is a Compression Really a Compression? *Dalton Trans.* **2003**, No. 23, 4375–4384.

(13) Garribba, E.; Micera, G. The Determination of the Geometry of Cu(II) Complexes: An EPR Spectroscopy Experiment. *J. Chem. Educ.* **2006**, *83* (8), 1229.

(14) Burgdorf, T.; Löscher, S.; Liebisch, P.; Van der Linden, E.; Galander, M.; Lendzian, F.; Meyer-Klaucke, W.; Albracht, S. P. J.; Friedrich, B.; Dau, H.; Haumann, M. Structural and Oxidation-State Changes at Its Nonstandard Ni−Fe Site during Activation of the NAD-Reducing Hydrogenase from Ralstonia Eutropha Detected by X-Ray Absorption, EPR, and FTIR Spectroscopy. *J. Am. Chem. Soc.* **2005**, *127* (2), 576–592.

(15) Reaney, S. H.; Kwik-Uribe, C. L.; Smith, D. R. Manganese Oxidation State and Its Implications for Toxicity. *Chem. Res. Toxicol.* **2002**, *15* (9), 1119–1126.

(16) Yamada, H.; Hurst, J. K. Resonance Raman, Optical Spectroscopic, and EPR Characterization of the Higher Oxidation States of the Water Oxidation Catalyst, Cis,Cis-$[(Bpy)_2Ru(OH_2)]_2O^{4+}$. *J. Am. Chem. Soc.* **2000**, *122* (22), 5303–5311.

(17) Dutoit, C. E.; Binet, L.; Fujii, H.; Lattuati-Derieux, A.; Gourier, D. Nondestructive Analysis of Mummification Balms in Ancient Egypt Based on EPR of Vanadyl and Organic Radical Markers of Bitumen. *Anal. Chem.* **2020**, *92* (23), 15445–15453.

(18) Hunsicker-Wang, L.; Vogt, M.; DeRose, V. J. Chapter 16 - EPR Methods to Study Specific Metal-Ion Binding Sites in RNA. In *Methods in Enzymology*; Biophysical, Chemical, and Functional Probes of RNA Structure, Interactions and Folding: Part A; Academic Press, 2009; Vol. 468, pp 335–367.

(19) Hawkins, C. L.; Davies, M. J. Detection and Characterisation of Radicals in Biological Materials Using EPR Methodology. *Biochim. Biophys. Acta Gen. Subj.* **2014**, *1840* (2), 708–721.

(20) Brynda, M.; Britt, R. D. The Manganese-Calcium Cluster of the Oxygen-Evolving System: Synthetic Models, EPR Studies, and Electronic Structure Calculations. In *Metals in Biology: Applications of High-Resolution EPR to Metalloenzymes*; Hanson, G., Berliner, L., Eds.; Biological Magnetic Resonance; Springer: New York, NY, 2010; pp 203–271.

(21) Goldfarb, D. Gd^{3+} Spin Labeling for Distance Measurements by Pulse EPR Spectroscopy. *Phys. Chem. Chem. Phys.* **2014**, *16* (21), 9685–9699.

(22) von Kugelgen, S.; Krzyaniak, M. D.; Gu, M.; Puggioni, D.; Rondinelli, J. M.; Wasielewski, M. R.; Freedman, D. E. Spectral Addressability in a Modular Two Qubit System. *J. Am. Chem. Soc.* **2021**, *143* (21), 8069–8077.

(23) Abragam, A.; Bleaney, B. *Electron Paramagnetic Resonance of Transition Ions*; OUP Oxford, 2012.

(24) Gómez-Coca, S.; Aravena, D.; Morales, R.; Ruiz, E. Large Magnetic Anisotropy in Mononuclear Metal Complexes. *Coord. Chem. Rev.* **2015**, *289–290*, 379–392.

(25) Jeschke, G. DEER Distance Measurements on Proteins. *Annu. Rev. Phys. Chem.* **2012**, *63* (1), 419–446.

(26) Martin, P. D.; Svensson, B.; Thomas, D. D.; Stoll, S. Trajectory-Based Simulation of EPR Spectra: Models of Rotational Motion for Spin Labels on Proteins. *J. Phys. Chem. B* **2019**, *123* (48), 10131–10141.

(27) Huang, Y.-W.; Chiang, Y.-W. Spin-Label ESR with Nanochannels to Improve the Study of Backbone Dynamics and Structural Conformations of Polypeptides. *Phys. Chem. Chem. Phys.* **2011**, *13* (39), 17521–17531.

(28) Gamble Jarvi, A.; Sargun, A.; Bogetti, X.; Wang, J.; Achim, C.; Saxena, S. Development of Cu^{2+}-Based Distance Methods and Force Field Parameters for the Determination of PNA Conformations and Dynamics by EPR and MD Simulations. *J. Phys. Chem. B* **2020**, *124* (35), 7544–7556.

(29) Lockyer, S. J.; Nawaz, S.; Brookfield, A.; Fielding, A. J.; Vitorica-Yrezabal, I. J.; Timco, G. A.; Burton, N. A.; Bowen, A. M.; Winpenny, R. E. P.; McInnes, E. J. L. Conformational Flexibility of Hybrid [3]- and [4]-Rotaxanes. *J. Am. Chem. Soc.* **2020**, *142* (37), 15941–15949. https://doi.org/10.1021/jacs.0c06547.

(30) Jain, A. K.; Upreti, G. C. A Fast Computational Method of Determining Accurate Spin-Hamiltonian Parameters for Ions ($S > {}^1/_2$) in Crystals. *Mol. Phys.* **1977**, *34* (1), 273–285.

(31) Korkmaz, M.; Aktas, B. A Fast Computational Method to Obtain Spin-Hamiltonian Parameters of S and I = ${}^5/_2$ Ions. *Phys. Stat. Sol. B* **1985**, *132* (2), 573–579. https://doi.org/10.1002/pssb.2221320231.

(32) Kalf, I.; Calmuschi, B.; Englert, U. Chiral Cr(III) and Co(III) Complex Cations as Building Blocks for Ordered and Disordered Salts. *CrystEngComm* **2002**, *4* (91), 548–551.

(33) Whuler, A.; Brouty, C.; Spinat, P.; Herpin, P. Structure Du Complexe Actif Hydraté (+)-$Cr(en)_3Cl_3 \cdot 2H_2O$. Etude de La Configuration Absolue et Du Désordre Conformationnel. *Acta Cryst. B* **1977**, *33* (9), 2877–2885.

(34) Ravel, B.; Newville, M. ATHENA, ARTEMIS, HEPHAESTUS: Data Analysis for X-Ray Absorption Spectroscopy Using IFEFFIT. *J. Synchrotron. Rad.* **2005**, *12* (4), 537–541.

(35) Ankudinov, A. L.; Ravel, B.; Rehr, J. J.; Conradson, S. D. Real-Space Multiple-Scattering Calculation and Interpretation of x-Ray-Absorption near-Edge Structure. *Phys. Rev. B* **1998**, *58* (12), 7565–7576.

(36) Perdew, J. P.; Ernzerhof, M.; Burke, K. Rationale for Mixing Exact Exchange with Density Functional Approximations. *J. Chem. Phys.* **1996**, *105* (22), 9982–9985.

(37) van Lenthe, E.; Baerends, E. J.; Snijders, J. G. Relativistic Total Energy Using Regular Approximations. *J. Chem. Phys.* **1994**, *101* (11), 9783–9792.

(38) Hedegård, E. D.; Kongsted, J.; Sauer, S. P. A. Optimized Basis Sets for Calculation of Electron Paramagnetic Resonance Hyperfine Coupling Constants: Aug-Cc-PVTZ-J for the 3d Atoms Sc–Zn. *J. Chem. Theory Comput.* **2011**, *7* (12), 4077–4087.

(39) Weigend, F.; Ahlrichs, R. Balanced Basis Sets of Split Valence, Triple Zeta Valence and Quadruple Zeta Valence Quality for H to Rn: Design and Assessment of Accuracy. *Phys. Chem. Chem. Phys.* **2005**, *7* (18), 3297–3305.

(40) Dolg, M.; Wedig, U.; Stoll, H.; Preuss, H. Energy-adjusted Ab Initio Pseudopotentials for the First Row Transition Elements. *J. Chem. Phys.* **1987**, *86* (2), 866–872.

(41) Balabanov, N. B.; Peterson, K. A. Systematically Convergent Basis Sets for Transition Metals. I. All-Electron Correlation Consistent Basis Sets for the 3d Elements Sc–Zn. *J. Chem. Phys.* **2005**, *123* (6), 064107.

(42) Bensberg, M.; Neugebauer, J. Density Functional Theory Based Embedding Approaches for Transition-Metal Complexes. *Phys. Chem. Chem. Phys.* **2020**, *22* (45), 26093–26103.

(43) Janthon, P.; Luo, S.; Kozlov, S. M.; Viñes, F.; Limtrakul, J.; Truhlar, D. G.; Illas, F. Bulk Properties of Transition Metals: A Challenge for the Design of Universal Density Functionals. *J. Chem. Theory Comput.* **2014**, *10* (9), 3832–3839.

(44) Jensen, K. P.; Roos, B. O.; Ryde, U. Performance of Density Functionals for First Row Transition Metal Systems. *J. Chem. Phys.* **2007**, *126* (1), 014103.

(45) Bühl, M.; Reimann, C.; Pantazis, D. A.; Bredow, T.; Neese, F. Geometries of Third-Row Transition-Metal Complexes from Density-Functional Theory. *J. Chem. Theory Comput.* **2008**, *4* (9), 1449–1459.

(46) Barone, V.; Cossi, M. Quantum Calculation of Molecular Energies and Energy Gradients in Solution by a Conductor Solvent Model. *J. Phys. Chem. A* **1998**, *102* (11), 1995–2001.

(47) Kraka, E.; Zou, W.; Tao, Y. Decoding Chemical Information from Vibrational Spectroscopy Data: Local Vibrational Mode Theory. *WIREs Comput. Mol. Sci.* **2020**, *10* (5), e1480.

(48) Makoś, M. Z.; Freindorf, M.; Sethio, D.; Kraka, E. New Insights into Fe–H_2 and Fe–H^- Bonding of a [NiFe] Hydrogenase Mimic: A Local Vibrational Mode Study. *Theor. Chem. Acc.* **2019**, *138* (6), 76.

(49) Yannacone, S.; Sayala, K. D.; Freindorf, M.; Tsarevsky, N. V.; Kraka, E. Vibrational Analysis of Benziodoxoles and Benziodazolotetrazoles. *Physchem* **2021**, *1* (1), 45–68.

(50) Makoś, M. Z.; Freindorf, M.; Tao, Y.; Kraka, E. Theoretical Insights into [NHC]Au(I) Catalyzed Hydroalkoxylation of Allenes: A Unified Reaction Valley Approach Study. *J. Org. Chem.* **2021**, *86* (8), 5714–5726.

(51) Freindorf, M.; Yannacone, S.; Oliveira, V.; Verma, N.; Kraka, E. Halogen Bonding Involving I_2 and D_8 Transition-Metal Pincer Complexes. *Crystals* **2021**, *11* (4), 373.

(52) Kraka, E.; Freindorf, M. Characterizing the Metal–Ligand Bond Strength via Vibrational Spectroscopy: The Metal–Ligand Electronic Parameter (MLEP). In *New Directions in the Modeling of Organometallic Reactions*; Lledós, A., Ujaque, G., Eds.; Topics in Organometallic Chemistry; Springer International Publishing: Cham, 2020; pp 227–269.

(53) Oliveira, V.; Cremer, D. Transition from Metal-Ligand Bonding to Halogen Bonding Involving a Metal as Halogen Acceptor a Study of Cu, Ag, Au, Pt, and Hg Complexes. *Chemical Physics Letters* **2017**, *681*, 56–63.

(54) Neese, F. The ORCA Program System. *WIREs Comput. Mol. Sci.* **2012**, *2* (1), 73–78.

(55) Kazmierczak, N. P.; Mirzoyan, R.; Hadt, R. G. The Impact of Ligand Field Symmetry on Molecular Qubit Coherence. *J. Am. Chem. Soc.* **2021**, *143* (42), 17305–17315.

(56) Ozvat, T. M.; Rappé, A. K.; Zadrozny, J. M. Isotopomeric Elucidation of the Mechanism of Temperature Sensitivity in ^{59}Co NMR Molecular Thermometers. *Inorg. Chem.* **2022**, *61* (2), 778–785.

(57) Treiling, S.; Wang, C.; Förster, C.; Reichenauer, F.; Kalmbach, J.; Boden, P.; Harris, J. P.; Carrella, L. M.; Rentschler, E.; Resch-Genger, U.; Reber, C.; Seitz, M.; Gerhards, M.; Heinze, K. Luminescence and Light-Driven Energy and Electron Transfer from an Exceptionally Long-Lived Excited State of a Non-Innocent Chromium(III) Complex. *Angew. Chem. Int. Ed.* **2019**, *131* (50), 18243–18253.

(58) Albrecht, A. C. On the Theory of Raman Intensities. *J. Chem. Phys.* **1961**, *34* (5), 1476–1484.

(59) Zou, W.; Cremer, D. C2 in a Box: Determining Its Intrinsic Bond Strength for the $X_1\Sigma_g^+$ Ground State. *Chem. Eur. J.* **2016**, *22* (12), 4087–4099.

(60) Dalal, M. *A Textbook of Inorganic Chemistry – Volume 1*; Dalal Institute, 2017.

(61) Owenius, R.; Engström, M.; Lindgren, M.; Huber, M. Influence of Solvent Polarity and Hydrogen Bonding on the EPR Parameters of a Nitroxide Spin Label Studied by 9-GHz and 95-GHz EPR Spectroscopy and DFT Calculations. *J. Phys. Chem. A* **2001**, *105* (49), 10967–10977.

(62) Bernini, C.; Pogni, R.; Ruiz-Dueñas, F. J.; Martínez, A. T.; Basosi, R.; Sinicropi, A. EPR Parameters of Amino Acid Radicals in P. Eryngiiversatile Peroxidase and Its W164Y Variant Computed at the QM/MM Level. *Phys. Chem. Chem. Phys.* **2011**, *13* (11), 5078–5098.

(63) Roessler, M. M.; Salvadori, E. Principles and Applications of EPR Spectroscopy in the Chemical Sciences. *Chem. Soc. Rev.* **2018**, *47* (8), 2534–2553.

(64) Stoll, S.; Schweiger, A. EasySpin, a Comprehensive Software Package for Spectral Simulation and Analysis in EPR. *J. Magn. Reson.* **2006**, *178* (1), 42–55.

(65) Bonomo, R.; Riggi, F. EPR Investigation of Chromium (III) Complexes: Analysis of Their Frozen Solution and Magnetically Dilute Powder Spectra. *Chem. Phys.* **1991**, *151*, 323–333.

(66) Platt, J. R. Strong Inference: Certain Systematic Methods of Scientific Thinking May Produce Much More Rapid Progress than Others. *Science* **1964**, *146* (3642), 347–353.

(67) Jackson, C. E.; Moseley, I. P.; Martinez, R.; Sung, S.; Zadrozny, J. M. A Reaction-Coordinate Perspective of Magnetic Relaxation. *Chem. Soc. Rev.* **2021**, *50* (12), 6684–6699.

(68) Jahn, S. M.; Canarie, E. R.; Stoll, S. Mechanism of Electron Spin Decoherence in a Partially Deuterated Glassy Matrix. *J. Phys. Chem. Lett.* **2022**, *13* (24), 5474–5479.

(69) Canarie, E. R.; Jahn, S. M.; Stoll, S. Quantitative Structure-Based Prediction of Electron Spin Decoherence in Organic Radicals. *J. Phys. Chem. Lett.* **2020**, *11* (9), 3396–3400.

(70) Jackson, C. E.; Ngendahimana, T.; Lin, C.-Y.; Eaton, G. R.; Eaton, S. S.; Zadrozny, J. M. Impact of Counter Ion Methyl Groups on Spin Relaxation in $[V(C_6H_4O_2)_3]^{2-}$. *J. Phys. Chem. C* **2022**, *126* (16), 7169–7176..

(71) Lin, C.-Y.; Ngendahimana, T.; Eaton, G. R.; Eaton, S. S.; Zadrozny, J. M. Counterion Influence on Dynamic Spin Properties in a V(IV) Complex. *Chem. Sci.* **2019**, *10* (2), 548–555.

(72) Jackson, C. E.; Lin, C.-Y.; Johnson, S. H.; Tol, J. van; Zadrozny, J. M. Nuclear-Spin-Pattern Control of Electron-Spin Dynamics in a Series of V(IV) Complexes. *Chem. Sci.* **2019**, *10* (36), 8447–8454.

(73) Graham, M. J.; Yu, C.-J.; Krzyaniak, M. D.; Wasielewski, M. R.; Freedman, D. E. Synthetic Approach To Determine the Effect of Nuclear Spin Distance on Electronic Spin Decoherence. *J. Am. Chem. Soc.* **2017**, *139* (8), 3196–3201.

(74) Telser, J. Linewidth, Field, and Frequency in Electron Paramagnetic Resonance (EPR) Spectroscopy. *J. Biol. Inorg. Chem.* **2022**, *27* (7), 605–609.

(75) Eaton, S. S.; Eaton, G. R. Chapter Three - Multifrequency Pulsed EPR and the Characterization of Molecular Dynamics. In *Methods in Enzymology*; Qin, P. Z., Warncke, K.,

Eds.; Electron Paramagnetic Resonance Investigations of Biological Systems by Using Spin Labels, Spin Probes, and Intrinsic Metal Ions, Part A; Academic Press, 2015; Vol. 563, pp 37–58.

(76) Biller, J. R.; Elajaili, H.; Meyer, V.; Rosen, G. M.; Eaton, S. S.; Eaton, G. R. Electron Spin–Lattice Relaxation Mechanisms of Rapidly-Tumbling Nitroxide Radicals. *J. Magn. Reson.* **2013**, *236*, 47–56.

CHAPTER 4 – Ligand Design of Zero-Field Splitting in Trigonal Prismatic Ni(II) Cage Complexes

4.1. Overview

Complexes of encapsulated metal ions are promising potential metal-based electron paramagnetic resonance imaging (EPRI) agents due to zero-field splitting. Herein, we synthesize and magnetically characterize a series of five new Ni(II) complexes based on a clathrochelate ligand to provide a new design strategy for zero-field splitting in the encaged environment. UV-Vis and x-ray single-crystal diffraction experiments demonstrate slight physical and electronic structure changes as a function of the differing substituents. The consequence of these changes at the remote apical and sidearm positions of the encaging ligands is a zero-field splitting parameter (D) that varies over a range of 11 cm^{-1}. These results demonstrate a remarkable flexibility of the zero-field splitting and electronic structure in nickelous cages, giving a clear toolkit for modifying zero-field splitting in highly stable ligand shells.

4.2. Introduction

Electron paramagnetic resonance imaging (EPRI), the electron-spin analogue to conventional ^{1}H magnetic resonance imaging (MRI), is a potentially breakthrough technology[1–3] that can allow for non-invasive detection of various chemical markers (e.g. pH,[4–6] redox stress,[7–10] oxygenation[11–13]) indicative of biological distress and disease. Practical implementation of this technique requires low-frequency (< 1 GHz) microwaves to mitigate heating of water-rich biological tissue.[1,14] Thus, organic-radical based probes (the most common type)[1,11,15] require low magnetic fields for low-frequency analysis (**Figure 4.1 Top Left**). Integration of EPRI with MRI

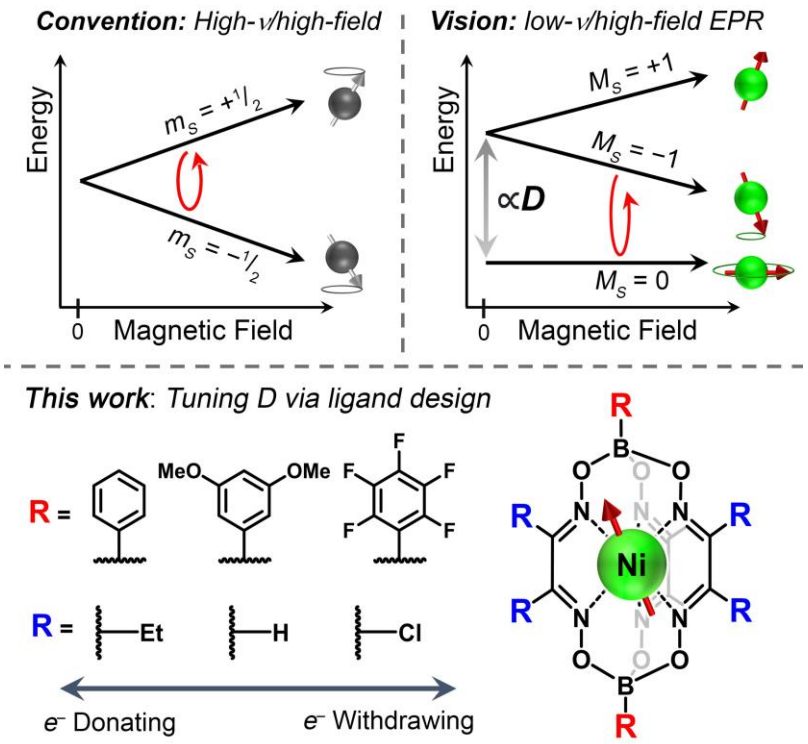

Figure 4.1. (**Top**) Depiction of low-frequency EPR transitions in an organic radical ($S = {}^1/_2$) system, compared to that in a metal complex ($S = 1$) system. (**Bottom**) Overview of new work presented in this study.

would enable mapping chemical and anatomical information, a transformative diagnostic capability. Yet, common MRI scanners operate at 1.5 T and above, where high frequency microwaves (ca. 35 GHz) are necessary for the function of organic radical probe systems (**Figure 4.1 Top Left**). Thus, new types of probes are needed if EPRI is to merge with high-field MRI.

Metal ions in encaging ligands are a promising yet unexplored alternative imaging probe platform, which could provide access to novel reactivities (relative to radicals),[16–20] high chemical stabilities,[21] and ultimately new, tunable magnetic properties. Centerpiece among such magnetic properties is the feature of zero-field splitting (ZFS, characterized by the zero-field splitting parameter D) for high electron spin systems ($S > {}^1/_2$), which can uniquely produce low-frequency EPR resonances at high magnetic fields. Zero-field splitting, which is ubiquitous in $S > {}^1/_2$ metal ions, can therefore potentially surmount a key challenge imposed by using organic radicals for

high-field EPRI (**Figure 4.1 Top Right**).[22–24] Furthermore, this property could be leveraged for chemical sensing: changes in ligand field (e.g. from ligand-based protonation reactions or changes in metal-ion redox state) can result in modification of ZFS and thus induce changes in EPR signal intensity or frequency.

If we are to realize a new generation of metal-complex-based EPRI probes, it is therefore imperative to understand how to control ZFS in ligands that impose high chemical stability for metal complexes. One class of such molecules are clathrochelates, which consist of a metal ion encaged with a macrocyclic ligand that imposes high molecular stability.[21] We note that there is an abundance of strategies for controlling aspects of the electronic structure and magnetic properties of coordination complexes.[25,26] However, clathrochelate ligand frameworks only typically permit functional group changes multiple chemical units away from the central metal, where impacts on D may be suppressed. Thus, it is important to understand the basic design principles for controlling ZFS in clathrochelates and how to maximize the tunability of this parameter.

Towards that understanding, herein we report a synthetic, spectroscopic, magnetic, and computational study of a series of five new Ni(II) complexes that test how specific clathrochelate ligand functional groups influence ZFS. We hypothesized that modifying the locations of the functional groups and electron donating/withdrawing capabilities of the ligand would modulate ZFS, with the remaining question being the whether the magnitude of change would be large or small. To test this hypothesis, we prepared and analyzed five novel complexes, NiL1 (**1**), NiL2 (**2**), NiL3 (**3**), NiL4 (**4**), and NiL5 (**5**) (**Figure 4.2**). The clathrochelate ligands (L1, L2, L3, L4, and L5) in this series vary the apical aryl rings and equatorial sidearms to test how the different groups affect the ZFS. We find that slight changes in the electronics and structure of the metal

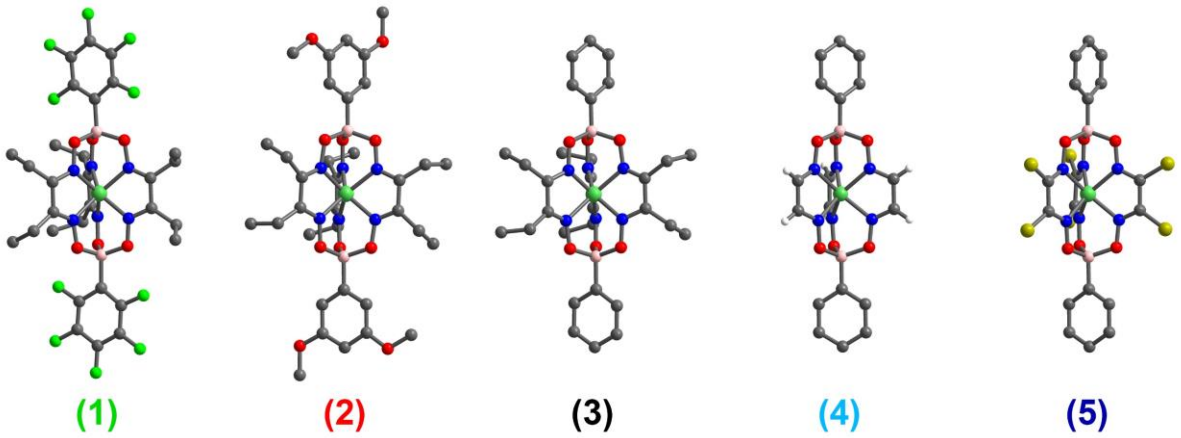

Figure 4.2. Molecular structures of **1**-**5** as determined from single crystal X-ray diffraction. Light green, gray, blue, red, pink, neon green, dark yellow, and white spheres correspond to Ni, C, N, O, B, F, Cl, and H atoms, respectively. Most hydrogen atoms (except the sidearms of **4**) and a solvent molecule (in **3**) were omitted for clarity.

complexes from these functional groups enable a high tunability of D, 11 cm^{-1} over **1-5**. These results demonstrate a high possible degree of tunability for D in clathrochelate complexes via synthetic design.

4.3. Experimental Section

4.3.1. General Considerations

Compounds **1**-**3** were synthesized using acetonitrile (MeCN) purified through a commercial solvent purification system from LC Technologies. Non-purified MeCN in atmospheric conditions was found to work as well for the syntheses of **1**-**3**, however, higher yields were obtained using MeCN from a solvent purification system under N_2. Nitromethane ($MeNO_2$) used in the synthesis of **4**-**5** was degassed via the freeze-pump-thaw method and stored over 3 Å molecular sieves for 3 days prior to use. Anhydrous nickelous chloride dimethoxyethane adduct ($NiCl_2$•DME) was synthesized following a literature procedure.[27] 3,4-hexanedione-dioxime,[28] glyoxime,[29] and dichloroglyoxime[29] were synthesized following their respective literature procedures. The aryl boronic acids used throughout were purchased from commercial sources and

used as received. Prior to the synthesis of **4** and **5**, excess moisture was removed from phenylboronic acid by heating the powder at 80°C under high vacuum for 12 hours. Elemental analyses were performed by Roberson Microlit Laboratories (Ledgewood, New Jersey, USA). Infrared spectra were recorded on a Nicolet 6700 FTIR spectrometer using a diamond window ATR. Electronic absorption spectra of all complexes were recorded on aqueous with a Hewlett-Packard 8453 spectrophotometer using standard quartz cuvettes with a 1 cm path length. Mass spectral analyses were performed on an Agilent 6224 Accurate Mass TOF LC/MS in positive ion mode using direct injection. Peak assignment was on the basis of m/z, interpeak spacing, and isotopic distribution.

4.3.2. Preparation of Compounds

Synthesis of Ni(L1)•0.5H_2O (**1**). In a 25 mL round-bottom flask, 202 mg (0.85 mmol, 1 eq.) of $NiCl_2$•6H_2O was dissolved in 10 mL of MeCN, followed by 367 mg (2.55 mmol, 3 eq.) of 3,4-hexanedione-dioxime, producing a maroon solution. This solution was heated at reflux for one hour under N_2, followed by the addition of 360 mg (1.70 mmol, 2 eq.) of pentafluorophenylboronic acid. The subsequent solution was then refluxed for four days, while remaining under N_2. After this time, a light green precipitant was observable in the reaction flask. The solution was cooled to room temperature and filtered open to air. The resulting light green powder was washed with MeCN (3 × 5 mL) followed by ethyl ether (3 × 10 mL) and dried overnight in a vacuum oven at 70°C. The final yield was 310 mg (43%) of **1**. Crystals suitable for single crystal x-ray diffraction were grown by layering a saturated chloroform solution of **1** with MeCN. IR (cm^{-1}, diamond ATR): 2984, 2944, 2880, 1645, 1609, 1467, 1293, 1129, 1106, 1058, 1032, 978, 919, 821, 752, 587. UV-vis (Methylene chloride); λ_{max} (ε_M, $M^{-1}cm^{-1}$): 770 nm (41.8). LC-MS (m/z): positive ion mode:

{H[Ni(L1)]}$^+$, 841.17. Elemental analysis for $C_{30}H_{40}B_2F_{10}N_6NiO_6$•0.5$H_2O$ calculated (found): %C: 42.40 (42.35), %H: 3.68 (3.97), %N: 9.89 (9.68).

Synthesis of Ni(L2)•1H_2O (**2**). In a 25 mL round-bottom flask, 178 mg (0.75 mmol, 1 eq.) of $NiCl_2$•6H_2O was dissolved in 10 mL of MeCN, followed by 324 mg (2.25 mmol, 3 eq.) of 3,4-hexanedione-dioxime, producing a maroon solution. This solution was heated at reflux for one hour under N_2, followed by the addition of 273 mg (1.50 mmol, 2 eq.) of 3,5-dimethoxyphenylboronic acid. The subsequent solution was then refluxed for two days, while remaining under N_2. After this time, a light green precipitant was observable in the reaction flask. The solution was cooled to room temperature and filtered open to air. The resulting light green powder was washed with MeCN (3 × 5 mL) followed by ethyl ether (3 × 10 mL) and dried overnight in a vacuum oven at 70°C. The final yield was 415 mg (69%) of **2**. Crystals suitable for single crystal x-ray diffraction were grown by layering a saturated methylene chloride solution of **2** with MeCN. IR (cm^{-1}, diamond ATR): 2978, 2946, 2932, 2832, 1583, 1456, 1410, 1331, 1284, 1245, 1198, 1171, 1148, 1106, 1062, 1025, 989, 900, 846, 816, 756, 710, 585. UV-vis (H_2O); λ_{max} (ε_M, $M^{-1}cm^{-1}$): 772 nm (62.3); 464 nm (94.5). LC-MS (m/z): positive ion mode: {H[Ni(L2)]}$^+$, 781.29. Elemental analysis for $C_{34}H_{48}B_2N_6NiO_{10}$•$H_2O$ calculated (found): %C: 51.10 (50.87), %H: 6.31 (6.05), %N: 10.52 (10.98).

Synthesis of Ni(L3) (**3**). In a 25 mL round-bottom flask, 119 mg (0.5 mmol, 1 eq.) of $NiCl_2$•6H_2O was dissolved in 10 mL of MeCN, followed by 216 mg (1.5 mmol, 3 eq.) of 3,4-hexanedione-dioxime, producing a maroon solution. This solution was heated at reflux for one hour under N_2, followed by the addition of 121 mg (1.0 mmol, 2 eq.) of phenylboronic acid. The subsequent solution was then refluxed for two days, while remaining under N_2. After this time, a light green precipitant was observable in the reaction flask. The solution was cooled to room

temperature and filtered open to air. The resulting light green powder was washed with MeCN (3 × 5 mL) followed by ethyl ether (3 × 10 mL) and dried overnight in a vacuum oven at 70°C. The final yield was 281 mg (85%) of **3**. Crystals suitable for single crystal x-ray diffraction were grown by layering a saturated methylene chloride solution of **3** with ethyl ether. IR (cm^{-1}, diamond ATR): 2976, 2940, 2876, 1612, 1461, 1433, 1218, 1179, 1105, 1055, 1016, 950, 899, 816, 745, 705, 651, 577, 492. UV-vis (H_2O); λ_{max} (ε_M, $M^{-1}cm^{-1}$): 772 nm (55.5); LC-MS (m/z): positive ion mode: $\{H[Ni(L3)]\}^+$, 661.25. Elemental analysis for $C_{30}H_{40}B_2N_6NiO_6$ calculated (found): %C: 54.51 (54.19), %H: 6.10 (5.92), %N: 12.71 (12.63).

Synthesis of Ni(L4)•2.5H_2O (**4**). In a N_2 glove box, 200 mg (0.91 mmol, 1 eq.) of $NiCl_2$•DME was dissolved in 10 mL of $MeNO_2$ in a 25 mL Schlenk flask, followed by 241 mg (2.73 mmol, 3 eq.) of glyoxime, and 221 mg (1.82 mmol, 2 eq.) of phenylboronic acid. The reaction vessel was removed from the glovebox and affixed to a Schlenk line under N_2. The solution was heated at reflux for four days. The solution was then cooled to room temperature and filtered open to air. The resulting light green powder was washed with MeOH (3 × 5 mL) followed by ethyl ether (3 × 10 mL) and dried overnight in a vacuum oven at 70°C. The final yield was 319 mg (65%) of **4**. Crystals suitable for single crystal x-ray diffraction were grown by vapor diffusion of ethyl ether into a saturated 1,4-dioxane solution of **4**. IR (cm^{-1}, diamond ATR): 3054, 3015, 2963, 2852, 1596, 1499, 1433, 1281, 1260, 1260, 1217, 1131, 1095, 943, 890, 847, 823, 754, 721, 700, 585. UV-vis (H_2O); λ_{max} (ε_M, $M^{-1}cm^{-1}$): 764 nm (29.2); LC-MS (m/z): positive ion mode: $\{H[Ni(L4)]\}^+$, 493.07. Elemental analysis for $C_{18}H_{16}B_2N_6NiO_6$•2.5H_2O calculated (found): %C: 40.21 (40.42), %H: 3.94 (3.55), %N: 15.63 (15.41).

Synthesis of Ni(L5) (**5**). In a N_2 glove box, 110 mg (0.5 mmol, 1 eq.) of $NiCl_2$•DME was dissolved in 10 mL of $MeNO_2$ in a 25 mL Schlenk flask, followed by 235 mg (1.5 mmol, 3 eq.) of

dichloroglyoxime, and 122 mg (1.0 mmol, 2 eq.) of phenylboronic acid. The reaction vessel was removed from the glovebox and affixed to a Schlenk line under N_2. The solution was heated at reflux for two days. The solution was then cooled to room temperature and filtered open to air. The resulting light green powder was washed with MeOH (3 × 5 mL) followed by ethyl ether (3 × 10 mL) and dried overnight in a vacuum oven at 70°C. The final yield was 326 mg (93%) of **5**. Crystals suitable for single crystal x-ray diffraction were grown by vapor diffusion of ethyl ether into a saturated dichloromethane solution of **5**. IR (cm^{-1}, diamond ATR): 3074, 3054, 3014, 1562, 1433, 1260, 1224, 1148, 1081, 959, 910, 883, 946, 761, 704, 657, 532. UV-vis (H_2O); λ_{max} (ε_M, $M^{-1}cm^{-1}$): 838 nm (44.2). Elemental analysis for $C_{18}H_{10}B_2N_6NiO_6$ calculated (found): %C: 30.62 (30.67), %H: 1.44 (1.33), %N: 12.02 (11.79).

*4.3.3. X-ray Data Collection, Structure Solution and Refinement for **1**-**5***

The diffraction data were collected at the X-Ray Diffraction facility of the Analytical Resources Core at Colorado State University. Data for **1-5** were collected on a Bruker D8 Quest ECO single-crystal X-ray diffractometer equipped with Mo Kα (λ = 0.71073 A). Data were collected and integrated using Bruker Apex 3 software. Absorption correction were applied using SADABS. Space group assignments were determined by examination of systematic absences, E7 statistics, and successive refinement of the structures. Crystal structures were solved using SHELXT and refined with the aid of successive difference Fourier maps by SHELXL operated in conjunction with OLEX2 software.[30–32] None of the crystals demonstrated decay by X-ray radiation over the course of the experiment. Hydrogen atoms were placed in ideal positions and refined using a riding model for all structures. In **1**, two disordered carbon atoms in one of the ethyl side-arms were modeled with fixed occupancies of 0.50 and 0.50, and 0.67 and 0.33.

Crystallographic information files for **1-5** are available in the CSD at accession numbers 2086087-2086091.

4.3.4. Magnetic Measurements

Magnetic data were collected on a Quantum Design MPMS SQUID magnetometer. Microcrystalline samples of **1**-**5** were pulverized and placed into a gelatin capsule then restrained with molten eicosane. Direct current (dc) measurements were obtained with 1000, 5000, 10000, and 30000 G applied fields with temperatures ranging from 1.8 to 300 K. All dc measurements were corrected for the diamagnetic contribution of the sample holder, as well as the restraining material and ligand framework (calculated using Pascal's constants).[33]

4.3.5. Computational Details

All computations were carried out using Orca 4.11 software package.[34] Experimental single crystal X-ray diffraction structures were used as the starting geometries for all computations with all C–H bonds modified to 1.09 Å. Initial orbital energies were generated via DFT (B3LYP functional)[35] using the SVP basis set,[36] RIJCOSX approximation,[37,38] and unrestricted natural orbitals (UNOs). With respect to the five 3d-orbitals and eight electrons of nickel(II), complete active space self-consistent field (CASSCF)[39,40] calculations were performed with the UNOs to yield zero-field splitting parameters, including D and g_{iso}. The %CASSCF block included triplet and singlet multiplets with 10 and 15 excitations, respectively. Additionally, calculations were completed including relativistic effects, spin-orbit coupling, and spin-spin coupling, and convergence followed using the SOSCF switchstep. Ab initio ligand field theory calculations

(AILFT)[41,42] were complete starting from successfully converged CASSCF outputs via MOREAD function and included NEVPT2[43–45] treatment.

4.3.6. Electron Paramagnetic Resonance Measurements

All samples were prepared at atmospheric conditions as 5 mM solutions in a glassing mixture of chloroform and toluene (1:1 v/v) the same day the measurements took place. X-band CW EPR data were collected on a Bruker ESR-300 spectrometer equipped with a ColdEdge liquid helium cryostat and the Bruker ER 4116DM dual-mode resonator. No signal that could be attributed to any of the nickel complexes studied was found under these conditions.

4.4. Results and Discussion

The encapsulating boron-capped tris-dioximate ligands in **1**-**5** were synthesized via a template reaction with a Ni(II) source. This ligand design was first realized for Co(II,III)[46,47] and later expanded to Fe(II),[48] Ru(II),[49] and Mn(II).[50] To the best of our knowledge, this is the first synthetic report of Ni(II) in this basic ligand structure, and only one other Ni(II) structure of a ligand of this type found in the CSD.[51] Complexes **1**-**3** were synthesized by combining $NiCl_2$•$6H_2O$ and 3,4-hexanedionedioxime in dry MeCN, resulting in a maroon solution, followed by the addition of the respective aryl boronic acid and refluxing for 2-4 days to give the product as a light green powder. Complexes **4** and **5** were synthesized similarly with $NiCl_2$•DME (DME = dimethoxyethane), glyoxime (for **4**) or dichloroglyoxime (for **5**), and phenylboronic acid. Dry $MeNO_2$ was used as a solvent in these latter two syntheses due to the higher boiling point, which offsets the reported lesser reactivity of glyoxime and dichloroglyoxime.[52]

The selected functional groups vary electron-donating and -withdrawing capabilities. Complexes **1**-**3** vary only the electron-withdrawing nature of the apical phenyl-borate unit and retain the same ethyl-sidearms. Complex **1** features perfluorinated phenyl rings and is the most electron-withdrawing system, followed by complex **2**, which bears axial phenyl groups with two methoxy groups in the 3- and 5-positions. Finally, **3** has no additional functional groups on the phenyl ring, suggesting that it is the least electron-withdrawing of the three. In complexes **3**-**5**, we instead vary the sidearms while keeping the apical phenyl group constant. Complex **3**, with ethyl groups, represents the most relative electron donating functional group in this series. In contrast, complex **4**, with hydrogen atoms and complex **5**, with chlorine atoms as sidearms, represent more electron-withdrawing systems. These qualitative assessments of the electron donating/withdrawing capabilities of the functional groups were made by comparing the appropriate Hammett constants for each substituent.[53]

All crystal structures indicate a nearly trigonal prismatic D_{3h} local symmetry for the NiN_6 coordination shell (**Figures 4.2, 4.3a-b,** and **Tables A3.1-A3.5**). Average Ni–N distances are in a

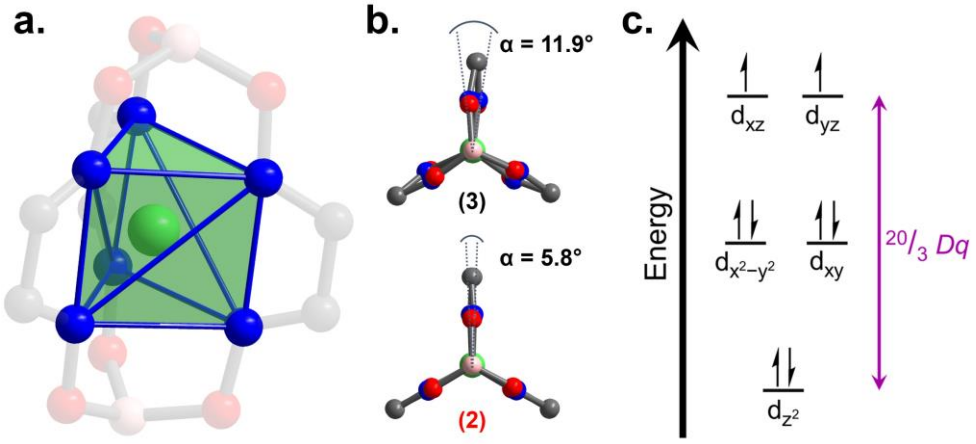

Figure 4.3. (**a**) Molecular structure of **2** highlighting the uncommon trigonal prismatic inner coordination geometry. Ethyl and phenyl groups were omitted for clarity. (**b**) Molecular structures of **2** and **3** viewed down the B–Ni–B axis showing the two extremes of the twist angle for **1**-**5** (denoted as α). Ethyl and phenyl groups were omitted for clarity. (**c**) 3*d*-orbital splitting diagram for a d^8 ion in an ideal trigonal prismatic geometry. $^{20}/_3Dq$ represents the energy gap between the top and bottom sets of orbitals.

tight range, increasing from 1.996(9) Å (**1**) to 2.019(12) Å (**5**) across the series. These are longer than those found in the analogous Fe(II)[54,55] (near 1.910 Å) and Co(II)[47] (near 1.970 Å) complexes. The N–Ni–N bite angles range from 76.0(7)° to 78.4(4)°. All compounds are close to ideal trigonal prisms with average distortion angles (α, **Figure 4.3b**) of 9.87(6)° (**1**), 5.83(8)° (**2**), 11.85(7)° (**3**), 11.63(8)° (**4**), and 6.60(2)° (**5**), where an ideal trigonal prism would have α = 0° and an octahedron would have α = 60°. Continuous-Shape-Measurement analysis using the SHAPE 2.0 software[56,57] quantitively assessed any geometric distortions from SHAPE score of 0 corresponds to perfect alignment with the tested geometry. For the trigonal prismatic D_{3h} geometry, SHAPE scores for complexes **1**-**5** range from 0.26 to 0.78, while scores for octahedral geometries are much higher, between 11.55 and 15.58. These results indicate that all five complexes presented closely resemble perfect trigonal prisms, a relatively uncommon geometry for first-row metals in six-coordinate environments.[58] As one final point, the closest intermolecular Ni···Ni distances range from 5.797(2) Å in **4** to 9.571(2) Å in **1**.

Electronic absorption spectra were collected to identify changes in the Ni(II) ligand field as a function of ligand tuning. A broad, low-intensity peak was observed near 13,000 cm^{-1} for **1**-**4** and near 12,000 cm^{-1} for **5**. A higher intensity shoulder peak was also observed between 22,000 cm^{-1} (**5**) and 22,300 cm^{-1} (**2**), (**Figure 4.4**). Peaks at energies above this latter set have been assigned as charge transfer bands in similar, isoelectronic Co(I) complexes.[52] Prior reports[59–61] of similar Ni(II) complexes in this geometry have made tentative assignments of the observed transitions, which enable comparisons between *Dq* values (where $^{20}/_{3}Dq$ for a trigonal prismatic complex is analogous to Δ_o, or $10Dq$, for O_h geometries, (**Figure 4.3c**) and ligand functional groups.[60]

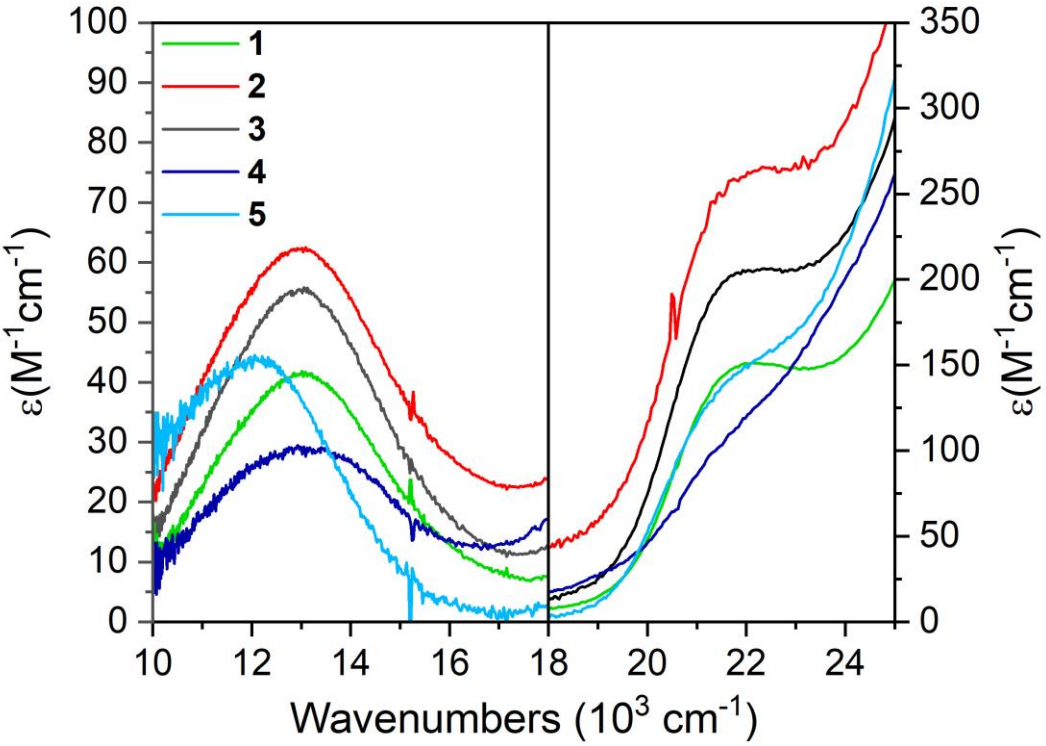

Figure 4.4. Electronic absorption spectra of complexes **1**-**5** collected in CH_2Cl_2 with focus on the regions with the *d*-*d* transitions. Energies of peak absorption are discussed in the main text. High energy charge transfer bands were omitted for clarity. The sharp features near 15,200 cm^{-1} and near 20,500 cm^{-1} are artifacts of the instrument.

For **1**-**5**, spectral deconvolution revealed two, low-energy peak in the absorbance spectra (**Figures A3.1-A3.6**). The peaks occurred at 11,400 and 13,100 cm^{-1} for **1**, 11,400 and 13,100 cm^{-1} for **2**, 11,600 and 13,200 cm^{-1} for **3**, 11,700 and 13,400 cm^{-1} for **4**, and 9900 and 12,400 cm^{-1} for **5**. Using a Tanabe-Sugano diagram for a d^8 trigonal prismatic system,[60] we assigned the lowest energy peak to the spin-forbidden $^3A_2' \rightarrow {}^1E'$ transition, owing to its significantly lower intensity compared to the higher energy peak, which was subsequently assigned to the spin-allowed $^3A_2' \rightarrow {}^3E'(P)$ transition. The computed $^{20}/_3Dq$ and B values are listed in **Table 4.1** and agree with those expected for species like **1-5**.[61]

For complexes **1**-**3** $^{20}/_3Dq$ decreased from 8,470 cm^{-1} (**3**), to 8,330 cm^{-1} (**1** and **2**) with the addition of more electron withdrawing ligand groups to the apical phenyl ring, implying a small

Table 4.1. UV-Vis spectroscopic and spin Hamiltonian parameters determined for **1**-**5** through experimental (top) and computational (bottom) methods. [a]In units of cm^{-1}. [b]Refined value is 2.5×10^{-6}.

	1	**2**	**3**	**4**	**5**
$^{20}/_{3}Dq^{a}$	8,330	8,330	8,470	8,530	7,250
B^{a}	779	776	788	799	740
g_{iso}	1.997(3)	2.166(1)	2.033(1)	2.111(1)	2.157(4)
D^{a}	19.1(1)	19.8(2)	25.2(1)	29.4(4)	29.9(2)
$\lvert E \rvert^{a}$	1.3(1)	~0[b]	1.3(7)	6.2(1)	3.9(6)
$^{20}/_{3}Dq^{a}$	14,170	13,912	13,717	13,400	13,204
g_{iso}	2.176	2.183	2.176	2.177	2.192
D^{a}	33.6	47.7	27.2	30.7	39.5

decrease in the ligand field strength (**Figure 4.3c**). To quantify the degree to which this change correlates with the electron withdrawing properties of ligand in **1**-**3**, we compared these results with the ^{11}B-NMR chemical shifts from the free boronic acid ligands. Spectra obtained of phenylboronic acid, 3,5-dimethoxyphenylboronic acid, and pentafluorophenylboronic acid produced ^{11}B chemical shifts at 29.18, 29.05, and 18.98 ppm, respectively (**Figures A3.6-A3.9**). Though the trend is weak, we do see that an increase in the ^{11}B chemical shift of the free boronic acid is coupled with an increase in $^{20}/_{3}Dq$ between complexes **1**-**3**. These results illustrate how changing apical ligand electronics, which are relatively far away from the Ni ion, are still important in the ligand field for these encaging ligands.

In comparing **3**-**5**, where the sidearms were varied, we saw a more substantial change in $^{20}/_{3}Dq$, where it ranged from 7,250 cm^{-1} (**5**) to 8,530 cm^{-1} (**4**) and compound **3** fell in between at 8,470 cm^{-1}. These results imply that there is a substantial decrease in the 3*d*-orbital splitting energy by adding Cl groups to the sidearms when compared to adding ethyl- or hydro- groups. However, these findings do not follow a clear trend with the electron donating/withdrawing character of the sidearm functional groups generally based on Hammett constants.[53] We note that although Hammett parameters are typically applied towards aromatic systems, in this instance, they only serve as a qualitative handle to make comparisons between the electronic effects of the ligand

groups. We speculate the departure of the expected trend in **5** could be due to π-donation from the Cl groups into the conjugated binding units, an effect absent in the side-arms in **3** and **4**. In this picture, the π-donation may offset the changing σ-interactions accounted for when solely looking at the degree of electron withdrawing and donating ability.

Variable-temperature dc susceptibility data at 0.1, 0.5 1.0, and 3.0 T for **1**-**5** were analyzed to correlate changes in electronic structure to changes in zero-field splitting. Data collected at 1.0 T displayed as $\chi_M T$ vs. T revealed $\chi_M T$ values of 1.04, 1.07, 1.03, 1.11, and 1.15 cm^3K/mol at 300

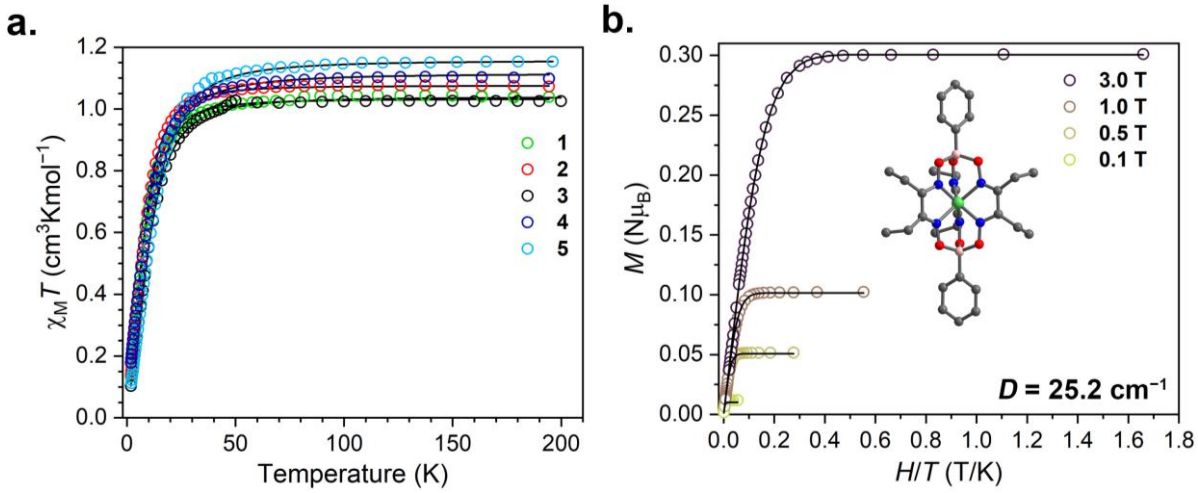

Figure 4.5. (**a**) Variable temperature dc susceptibility data under 1.0 T applied dc magnetic field for powder samples of **1**-**5**. Solid lines are simulated data using the parameters generated from fitting the reduced magnetization data. (**b**) Reduced magnetization data and molecular structure of complex **3**. Solid lines are fits for the data generated using PHI. The spin Hamiltonian parameters (**Table 4.1**) are discussed in the main text. See **Figures A3.6-A3.9** for the reduced magnetization plots of **1**-**2**, **4**-**5**.

K for **1**-**5**, respectively, (**Figure 4.5a**) close to the expected value for an S = 1 system (1.00 cm^3K/mol, g = 2.00). With decreasing temperature, $\chi_M T$ remains relatively constant until about 50 K, where it begins to decrease substantially. The decrease in $\chi_M T$ with temperature is likely from zero-field splitting in the measured complexes. The multi-field reduced magnetization data were fit with PHI[62] to the following spin Hamiltonian:

$$\hat{H} = g\mu_B \boldsymbol{B}\hat{\boldsymbol{S}} + D\left(\hat{S}_z^2 - \frac{1}{3}S(S+1)\right) + E(\hat{S}_x^2 - \hat{S}_y^2).$$

Here, g is an isotropic g-factor ($g_x = g_y = g_z$), μ_B is the Bohr magneton, $\boldsymbol{B}$ is the applied magnetic field, $\widehat{\boldsymbol{S}}$ is the electronic spin operator, D is the axial zero-field splitting parameter, and E is the rhombic zero-field splitting parameter. The values obtained from the fits are summarized in **Table 4.1**. As an additional measure of ZFS, we collected variable-field dc magnetometry on complexes **1**-**5** at 0.1 T, 0.5 T, and 3.0 T in temperatures ranging from 1.8 to 300 K (**Figure 4.5b**). Reduced magnetization data from these measurements were fit in PHI to obtain spin Hamiltonian parameters g and D. The fits were relatively insensitive to E in both magnitude and sign. The values of D were initially found to be 19.1(1) cm^{-1} (**1**), 19.8(2) cm^{-1} (**2**), 25.2(1) cm^{-1} (**3**), −29.4(4) cm^{-1} (**4**), and 29.9(2) cm^{-1} (**5**) and g values range from 1.997(3) to 2.166(1). The g values are within reported ranges of hexacoordinate Ni(II), however the D values are generally higher in magnitude than the typical –22 to +9.5 cm^{-1} range of O_h Ni(II) complexes.[63–67] To the best of our knowledge, this study represents the first experimental estimate of the tunability of D via ligand field modification in the D_{3h}, clathrochelate structure for Ni(II).

It stands out that **4** produced a fit with a negative sign for D. We note that fits of magnetic susceptibility data can give inaccuracies in D and E, particularly the signs of these parameters, where positive and negative D and E values can yield near-equal-quality data simulations.[68] Furthermore, as noted above, the susceptibility fits seemed insensitive to sign and magnitude of E. It is for these reasons that we report $|E|$ in **Table 4.1** rather than the sign.

Previous computational analyses of trigonal prismatic Ni(II) complexes,[69] as well as first-principle predictions based on the specific 3*d*-orbital excitations indicate that the sign of D should be positive.[70,71] This conclusion is also supported by $\chi_M T$ trending towards zero as the systems reach an $M_s = 0$ ground state. However, due to the possible inaccuracies in susceptibility determination of D, we pursued parallel-mode X-band EPR analyses of **1-5** to search for the ΔM_S

= ±1 intradoublet transition to provide additional experimental evidence to assign the sign of *D*. Analyses were conducted on **1-5** as 5 mM frozen glass solutions in a 1:1 (v/v) mixture chloroform and toluene at temperatures ranging from 4.5 K to 10 K. In the magnetic field of 0-600 mT, we failed to observe any signal that could be assigned to the complexes. At these lowest temperatures, observation of the intradoublet transition, with an intensity that increased with decreasing temperature, would have conclusively pinned the sign of *D* to be negative. Instead, there is no signal, even for **2**, which has a negligible *E* parameter. Owing to these spectroscopic and computational data, we confidently assign the zero-field splitting values as positive in **1-5** as noted in **Table 4.1**.

Ab initio calculations based on single crystal structures allowed theoretical assessment of the electronic structures of **1**-**5** for comparison to experimental results (see ESI). Predictions of molecular orbital energies via ab initio ligand field theory (AILFT)[41,42] were extracted from Complete Active Space Self Consistent Field (CASSCF)[39,40] and n-electron valence state perturbation theory (NEVPT2)[43–45] calculations. The complete active space chosen for these computations included eight electrons and the five *d* orbitals of the Ni(II) ions, denoted as CAS(8,5). Calculations included 10 triplet and 15 singlet states, of which the $^3A_{2g}$ triplet ground state was lowest in energy. AILFT analyses reveal values of $^{20}/_3Dq$ for **1**-**5** at 14170, 13912, 13717, 13400, 13204 cm^{-1}, respectively. The results trend in a decreasing order from **1** to **5** (**Figure 4.6**). For the series of apical-substituted groups (**1-3**), *reducing* the electron-withdrawing nature of the phenyl ring coincides with lower $^{20}/_3Dq$. Conversely, for the series of sidearm-substituted groups (**3-5**), *enhancing* the electron-withdrawing nature of the dioximates follows with lower $^{20}/_3Dq$. We note the overestimation of the calculated $^{20}/_3Dq$ relative to the experimental values stems from the

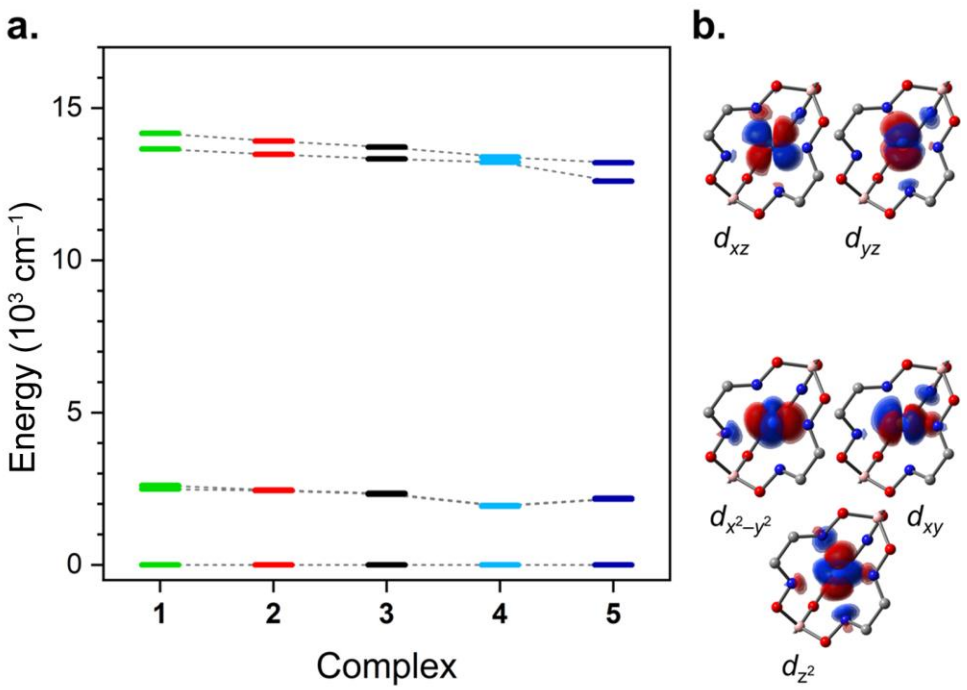

Figure 4.6. (**a**) Energies of the 3*d* orbitals in **1**-**5** determined via AILFT. (**b**) Surface plots of the 3*d* orbitals corresponding to their relative energy levels in the energy level diagram.

limited active space, however, the observed decrease in $^{20}/_{3}Dq$ is consistent with a progressively weaker σ-donating ligand resulting from the increased electron withdrawing ligand character on the side-arms, contributing to a weaker ligand field.[72] AILFT showed a steady decrease in $^{20}/_{3}Dq$ over the full series from **1**-**5** and specifically supports the experimental trend of decreasing $^{20}/_{3}Dq$ for **3**-**5**, driven by the electron-withdrawing capability of the ligand sidearm functional groups.

The foregoing electronic structures were also used to compute *D* for **1**-**5**. Results from CASSCF and NEVPT2 treatment gave all positive *D* values for **1**-**5** with magnitudes of 33.6, 47.7, 27.2, 30.7, and 39.5 cm^{-1}, respectively. No specific trend in *D* was accounted for by the apical substituents in series **1**-**3**. However, a notable increase in *D* in **3**-**5** matches the increased electron-withdrawing capabilities through the ligand sidearm.

The observed range of *D* in **1**-**5** stems from a range of contributions from the excited states. Of the 10 triplet states considered by CAS(8,5), only the four lowest-energy triplet excitations

(within 10,000 to 13,000 cm^{-1}) contribute significantly to *D* (**Table A3.6, Figures A3.13-A3.14**) For all five complexes, the first triplet excited states contribute to *D* with negative contributions that range from –2 to –12 cm^{-1}. The following three triplet excited states contribute positively to *D*, the largest of which range from +19 to +24 cm^{-1}. Strict consideration of triplet excitations showed mostly positive *D* contributions. Inclusion of singlet states was found to provide non-negligible contributions, despite the higher energies of these excitations (24,000 to 26,000 cm^{-1}). Of the 15 singlet states considered, only three affected *D* significantly, these being the second and third excited states (each near –5 cm^{-1}) and the fourth excited singlet state (between +15 to +19 cm^{-1}).

We note that the excited states are multiconfigurational, thus underlining the magnetic complexity of the zero-field splitting in these species (**Tables A3.7-A3.11**). Indeed, excitations between *d* orbitals of different $|m_l|$ value contribute to positive zero-field splitting magnitudes, whereas excitations within the same $|m_l|$ value are expected to contribute to a negative *D* (**Figure A3.15**).[73,74] The fact that some of the excitations deviate from this rule emphasizes their multiconfigurational nature and the not-at-all trivial origin of the magnetic anisotropy.

The experimental results do not follow the predicted $^{20}/_{3}Dq$ and *D* values which warrants further discussion. Restriction of the active space to just the 3*d* orbitals via CAS(8,5) likely fails to capture all of the complexities of the electronic structures in **1**-**5**. Indeed, with the delocalized, conjugated structures, it is possible that including orbitals with more ligand character would ultimately drive the experimental trend, as has been previously suggested for Ni(II) chelate complexes.[64] The present outcome, that a metal-only approach does not perfectly reproduce the series, thus underlines the potential tunability of electronic structures and ZFS in through clathrochelate modification.

An overarching analysis of the zero-field splitting trends in **1**-**5** and the spectroscopic/structural/computational data makes it challenging to assign the trend to a specific electronic or structural feature. For one, the trends in $^{20}/_{3}Dq$ seem to weakly suggest a stronger ligand field correlates to a higher ZFS in **1**-**3**, while the opposite is true in **3**-**5** (with **4** lying outside this trend), the latter being supported by our computations. In a more practical sense, that argument then suggests a more electron withdrawing group favors a larger *D* value when placed on the sidearm whereas an opposite effect is seen in the apical positions. The typical expectation for zero-field splitting is that it will be greatest with weakest ligand field splitting,[70] for which the trends from **1**-**3** seem to be in defiance of.

A complicating feature in the analysis of the *D* trend is that the changes to the coordination geometries with functional group are minor,[75] but may be significant for the zero-field splitting.[69] From **1** to **5**, an increase in *D* is observed with an increase in the average Ni–N distance across the series with **1** showing the shortest Ni–N distances (*ca*. 1.996 Å) and lowest *D* value, and **5** showing the highest Ni–N distances (*ca*. 2.019 Å) and highest *D* value, respectively. The Ni–N distances are likely reflective of the ligand-field consequences of the different functional groups, where electron withdrawing groups enforce weaker bonding, longer Ni–N distances, lower $^{20}/_{3}Dq$, and thus larger *D*. But, we also note that the apical functional groups could be inducing a change in the twist angle, a, of the trigonal prismatic ligand shell via steric forces around the congested B atom. Separate analyses suggest that a is the central parameter for affecting ZFS and electronic structure in similar complexes.[69,76] Yet there does not appear to be a correlation between α and *D* in our data. Owing to the foregoing points, it is thus challenging to attribute one sole feature to the modification of *D*, necessitating future studies to fully understand the variation.

Importantly, the variation in *D* that we observe here is dramatic for the relatively minor variations observed in the ligand shells of **1**-**5**. Large variations in *D* tend to result from substantial changes to the coordination shell. For example, large changes occur when donor atoms are directly swapped, as observed in the Co(II) complexes $[Co(EPh)_4]^{2-}$ (E = O, S, and Se), which vary 70 cm^{-1} in *D* as a function of E atom.[77] Second, large changes in geometry, e.g. changes in coordination number,[78] or conformation from square planar to tetrahedral,[79] can trigger high-amplitude modifications of *D*.[26] In the present system, we observe very slight change in bond distances (*ca.* 0.01 Å) and bond angles (*ca.* 5° for a), all within a nearly trigonal-prismatic, six-coordinate structure. Furthermore, these changes are imposed by varying function groups that are two and four bonds away from the Ni(II) ion, wherein any expected impact should be small. Yet, both experimental and computational evidence shows that these physical changes still exert a large effect on the zero-field splitting, even if the underlying electronic origin is still to be determined.

Finally, we used the spin-Hamiltonian parameters from **1** and **5** to calculate where safe, low-frequency transitions would potentially show up, because **1** and **5** are the two extremes of the series in terms of *D* (**Figure 4.7**). For molecules with the magnetic field aligned perpendicular to the B···Ni···B axis of the molecule, 1 GHz transitions appear at 19.0 T (for **1**) and 29.8 T (for **5**). This is nearly an 11 T range and demonstrates a remarkable degree of tunability of the low-frequency transition as a function of ligand identity. However, note that the resonant fields of these low-frequency EPR transitions are considerably larger than the typical fields used in MRI (*ca*. 1.5 T) and preclinical (*ca.* 7 T) scanners.[80] In order to have the desired low-frequency transitions in those field ranges for an $S = 1$ system, *D* would have to be near 1.5 cm^{-1} for the former case, and 6.6 cm^{-1} for the latter case. Thus, there is a need to design the low-frequency EPR transition for lower fields in Ni(II) systems, as well as taking the learned design strategies and applying them

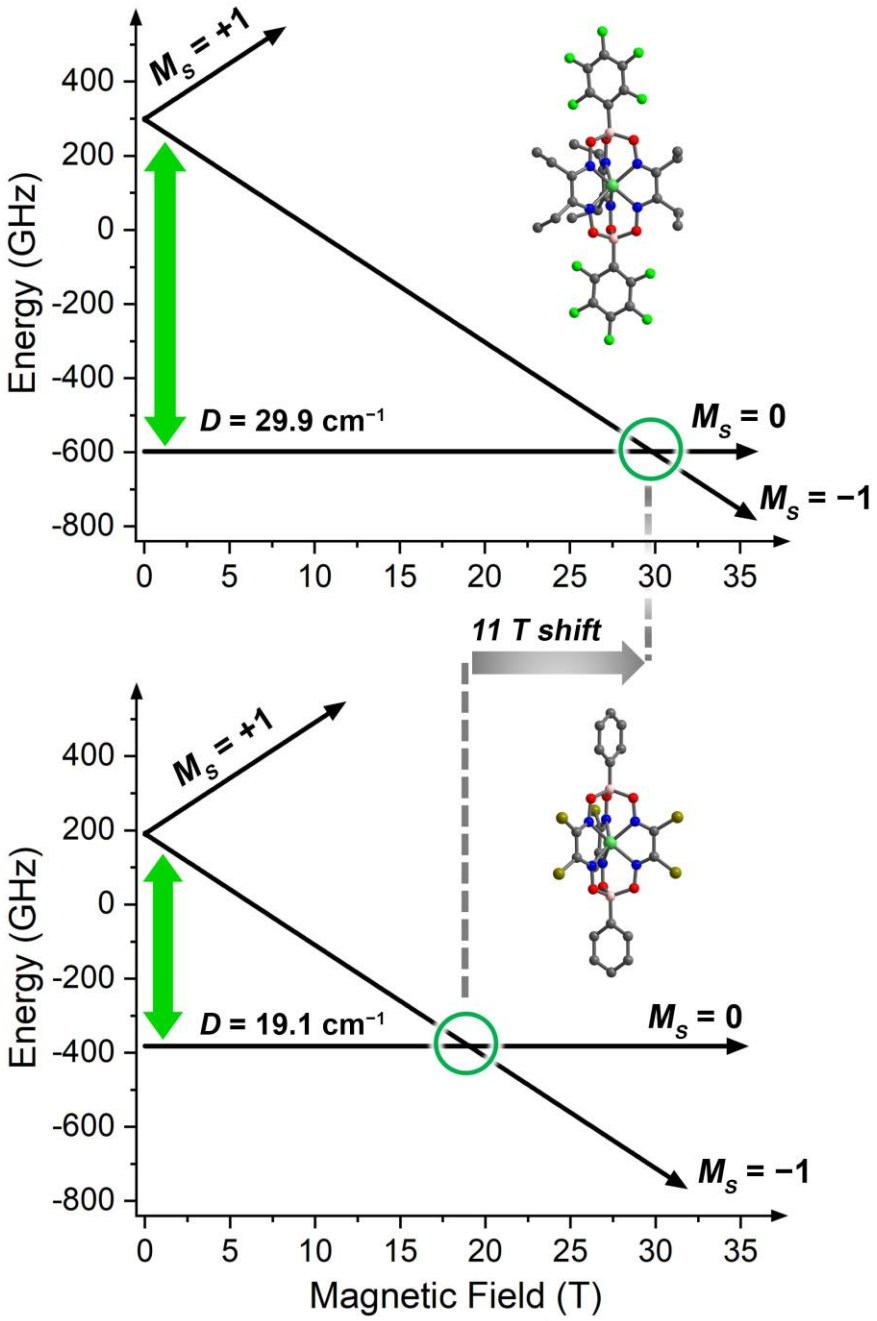

Figure 4.7. M_S-level energies for **1** and **5** (assuming magnetic field alignment with molecular *z* axis) showing the extent that *D* is tuned in this study. As a result of the change in *D*, the spin Hamiltonian parameters predict a *ca.* 11 T shift in the crossings of the $M_S = 0$ and $M_S = -1$ levels, demonstrating the tunability of fields for potential high-field/low-frequency EPR imaging studies.

towards other candidate EPRI molecular probes. Nevertheless, this striking degree of tunability suggests that will be possible with judicious ligand/metal selection.

4.5. Conclusion

In summary, we demonstrate a synthetic toolkit for finetuning the zero-field splitting in Ni(II) clathrochelate complexes. We found that judicious selection of axial and sidearm functional groups will modify ZFS over a relatively large, 11 cm^{-1} range. The significance of this range is underlined considering we do not directly modify the donor atom, but rather peripheral functional groups up to four bonds away from the metal. We note that there are several magnetostructural correlations for D and Ni(II),[63,65–68] but this study is, to the best of our knowledge, the first of its kind for the trigonal prismatic geometry.

The observations in this paper show that relatively tiny design changes to the encapsulating ligand shell can have dramatic impacts on ZFS, which has two important implications. First, the results highlight the possibility of engineering the operating field range for low-frequency EPR-based techniques by tuning D. A second implication of the sensitivity is that, if one engineered a pH-, redox- or other chemically responsive ligand field into a clathrochelate ligand, one could engender chemical sensitivity into any magnetic resonance spectroscopic property influenced by zero-field splitting. Toward applications of this type, including EPRI, we must first test whether the observed tunability carries over to the magnetic resonance properties of other metal ions and other spin states like $S = {}^3/_2$ Co(II) or $S = {}^5/_2$ Fe(III).

References

(1) *In Vivo EPR (ESR): Theory and Application*; Berliner, L. J., Ed.; Biological Magnetic Resonance; Springer US, 2003.

(2) Klare, J. P. Biomedical Applications of Electron Paramagnetic Resonance (EPR) Spectroscopy. *Biomed. Spectrosc. Imaging* **2012**, No. 1, 101–124.

(3) Colacicchi, S.; Ferrari, M.; Sotgiu, A. In Vivo Electron Paramagnetic Resonance Spectroscopy/Imaging: First Experiences, Problems, and Perspectives. *Int. J. Biochem.* **1992**, *24* (2), 205–214.

(4) Voinov, M. A.; Polienko, J. F.; Schanding, T.; Bobko, A. A.; Khramtsov, V. V.; Gatilov, Y. V.; Rybalova, T. V.; Smirnov, A. I.; Grigor'ev, I. A. Synthesis, Structure, and X-Band (9.5 GHz) EPR Characterization of the New Series of pH-Sensitive Spin Probes: N,N-Disubstituted 4-Amino-2,2,5,5-Tetramethyl-3-Imidazoline 1-Oxyls. *J. Org. Chem.* **2005**, *70* (24), 9702–9711.

(5) Voinov, M. A.; Scheid, C. T.; Kirilyuk, I. A.; Trofimov, D. G.; Smirnov, A. I. IKMTSL-PTE, a Phospholipid-Based EPR Probe for Surface Electrostatic Potential of Biological Interfaces at Neutral PH: Effects of Temperature and Effective Dielectric Constant of the Solvent. *J. Phys. Chem. B* **2017**, *121* (11), 2443–2453.

(6) Potapenko, D. I.; Foster, M. A.; Lurie, D. J.; Kirilyuk, I. A.; Hutchison, J. M. S.; Grigor'ev, I. A.; Bagryanskaya, E. G.; Khramtsov, V. V. Real-Time Monitoring of Drug-Induced Changes in the Stomach Acidity of Living Rats Using Improved pH-Sensitive Nitroxides and Low-Field EPR Techniques. *J. Magn. Reson.* **2006**, *182* (1), 1–11.

(7) Caia, G. L.; Efimova, O. V.; Velayutham, M.; El-Mahdy, M. A.; Abdelghany, T. M.; Kesselring, E.; Petryakov, S.; Sun, Z.; Samouilov, A.; Zweier, J. L. Organ Specific Mapping of in Vivo Redox State in Control and Cigarette Smoke-Exposed Mice Using EPR/NMR Co-Imaging. *J. Magn. Reson.* **2012**, *216*, 21–27.

(8) Mikuni, T.; He, G.; Petryakov, S.; Fallouh, M. M.; Deng, Y.; Ishihara, R.; Kuppusamy, P.; Tatsuta, M.; Zweier, J. L. In Vivo Detection of Gastric Cancer in Rats by Electron Paramagnetic Resonance Imaging. *Cancer Res.* **2004**, *64* (18), 6495–6502.

(9) Hyodo, F.; Murugesan, R.; Matsumoto, K.; Hyodo, E.; Subramanian, S.; Mitchell, J. B.; Krishna, M. C. Monitoring Redox-Sensitive Paramagnetic Contrast Agent by EPRI, OMRI and MRI. *J. Magn. Reson.* **2008**, *190* (1), 105–112.

(10) Epel, B.; Sundramoorthy, S. V.; Krzykowska-Serda, M.; Maggio, M. C.; Tseytlin, M.; Eaton, G. R.; Eaton, S. S.; Rosen, G. M.; Kao, J. P. Y.; Halpern, H. J. Imaging Thiol Redox Status in Murine Tumors In Vivo with Rapid-Scan Electron Paramagnetic Resonance. *J. Magn. Reson.* **2017**, *276*, 31–36.

(11) *EPR Imaging and in Vivo EPR*, 1st ed.; Gareth R. Eaton, Sandra S. Eaton, Keiichi Ohno, Eds.; CRC Press, 2018.

(12) Demsar, F.; Walczak, T.; Morse, P. D.; Bačić, G.; Zolnai, Z.; Swartz, H. M. Detection of Diffusion and Distribution of Oxygen by Fast-Scan EPR Imaging. *J. Magn. Reson.* **1988**, *76* (2), 224–231.

(13) Swartz, H. M.; Flood, A. B.; Schaner, P. E.; Halpern, H.; Williams, B. B.; Pogue, B. W.; Gallez, B.; Vaupel, P. How Best to Interpret Measures of Levels of Oxygen in Tissues to Make Them Effective Clinical Tools for Care of Patients with Cancer and Other Oxygen-Dependent Pathologies. *Physiol. Rep.* **2020**, *8* (15), e14541.

(14) Hitchcock, R. T. *Radio-Frequency and Microwave Radiation*; AIHA, 2004.

(15) Danhier, P.; Gallez, B. Electron Paramagnetic Resonance: A Powerful Tool to Support Magnetic Resonance Imaging Research. *Contrast Media Mol. Imaging* **2015**, *10* (4), 266–

(16) Voloshin, Y. Z.; Varzatskii, O. A.; Kron, T. E.; Belsky, V. K.; Zavodnik, V. E.; Strizhakova, N. G.; Nadtochenko, V. A.; Smirnov, V. A. Encapsulation of Ruthenium(II) with Macrobicyclic Dioxime-Functionalized Ligands: On the Way to New Types of DNA-Cleaving Agents and Probes. *J. Chem. Soc., Dalton Trans.* **2002**, No. 6, 1203–1211.

(17) Voloshin, Y. Z.; Varzatskii, O. A.; Kron, T. E.; Belsky, V. K.; Zavodnik, V. E.; Strizhakova, N. G.; Palchik, A. V. Triribbed-Functionalized Clathrochelate Iron(II) Dioximates as a New and Promising Tool To Obtain Polynucleating and Polynuclear Compounds with Improved Properties. *Inorg. Chem.* **2000**, *39* (9), 1907–1918.

(18) Voloshin, Y. Z.; Lebedev, A. Y.; Novikov, V. V.; Dolganov, A. V.; Vologzhanina, A. V.; Lebed, E. G.; Pavlov, A. A.; Starikova, Z. A.; Buzin, M. I.; Bubnov, Y. N. Template Synthesis, X-Ray Structure, Spectral and Redox Properties of the Paramagnetic Alkylboron-Capped Cobalt(II) Clathrochelates and Their Diamagnetic Iron(II)-Containing Analogs. *Inorg. Chim. Acta.* **2013**, *399*, 67–78.

(19) Planes, O. M.; Scopelliti, R.; Fadaei-Tirani, F.; Severin, K. Ligand Effects in Low-Valent Co(I) Clathrochelate Complexes. *Z. Anorg. Allg. Chem.* **2021**, *647* (10), 1065–1069.

(20) Cecot, G.; Doll, M. T.; Planes, O. M.; Ramorini, A.; Scopelliti, R.; Fadaei-Tirani, F.; Severin, K. Cages vs. Prisms: Controlling the Formation of Metallosupramolecular Architectures with Ligand Side-Chains. *Eur. J. Inorg. Chem.* **2019**, *2019* (25), 2972–2976.

(21) Voloshin, Y.; Belaya, I.; Krämer, R. Cage Metal Complexes. In *Cage Metal Complexes*; Springer International Publishing: Cham, 2017; pp 1–100.

(22) Griffith, J. S. *The Theory of Transition-Metal Ions*; Cambridge University Press, 1964.

(23) Figgis, B. N.; Hitchman, M. A. *Ligand Field Theory and Its Applications*; Special topics in inorganic chemistry; Wiley-VCH, 2000.

(24) Campanella, A. J.; Nguyen, M.-T.; Zhang, J.; Ngendahimana, T.; Antholine, W. E.; Eaton, G. R.; Eaton, S. S.; Glezakou, V.-A.; Zadrozny, J. M. Ligand Control of Low-Frequency Electron Paramagnetic Resonance Linewidth in Cr(III) Complexes. *Dalton Trans.* **2021**, No. 50, 5342–5350.

(25) Gómez-Coca, S.; Aravena, D.; Morales, R.; Ruiz, E. Large Magnetic Anisotropy in Mononuclear Metal Complexes. *Coord. Chem. Rev.* **2015**, *289–290*, 379–392.

(26) Frost, J. M.; Harriman, K. L. M.; Murugesu, M. The Rise of 3-d Single-Ion Magnets in Molecular Magnetism: Towards Materials from Molecules? *Chem. Sci.* **2016**, *7* (4), 2470–2491.

(27) Fowles, G. W. A.; Rice, D. A.; Walton, R. A. The Donor Properties of Simple Ethers—II[1]: Complexes of Manganese(II), Iron(II), Cobalt(II) and Nickel(II) Halides with Tetrahydrofuran and 1,2-Dimethoxyethane. *J. Inorg. Nuc. Chem.* **1969**, *31* (10), 3119–3131.

(28) Zaitsev, A. B.; Schmidt, E. Yu.; Vasil'tsov, A. M.; Mikhaleva, A. I.; Petrova, O. V.; Afonin, A. V.; Zorina, N. V. 1,2-Dioximes in the Trofimov Reaction. *Chem. Heterocycl. Compd.* **2006**, *42* (1), 34–41.

(29) Matsubara, R.; Ando, A.; Hasebe, H.; Kim, H.; Tsuneda, T.; Hayashi, M. Synthesis and Synthetic Application of Chloro- and Bromofuroxans. *J. Org. Chem.* **2020**, *85* (9), 5959–5972.

(30) Sheldrick, G. M. SHELXT – Integrated Space-Group and Crystal-Structure Determination. *Acta Cryst. A* **2015**, *71* (1), 3–8.

(31) Sheldrick, G. M. Crystal Structure Refinement with SHELXL. *Acta Cryst. C* **2015**, *71* (1), 3–8.

(32) Sheldrick, G. M. A Short History of SHELX. *Acta Cryst. A* **2008**, *64* (Pt 1), 112–122.

(33) Bain, G. A.; Berry, J. F. Diamagnetic Corrections and Pascal's Constants. *J. Chem. Educ.* **2008**, *85* (4), 532.

(34) Neese, F. The ORCA Program System. *WIREs Comput. Mol. Sci.* **2012**, *2* (1), 73–78.

(35) Neese, F. A Spectroscopy Oriented Configuration Interaction Procedure. *J. Chem. Phys.* **2003**, *119* (18), 9428–9443.

(36) Schäfer, A.; Horn, H.; Ahlrichs, R. Fully Optimized Contracted Gaussian Basis Sets for Atoms Li to Kr. *J. Chem. Phys.* **1992**, *97* (4), 2571–2577.

(37) Neese, F.; Wennmohs, F.; Hansen, A.; Becker, U. Efficient, Approximate and Parallel Hartree-Fock and Hybrid DFT Calculations. A 'Chain-of-Spheres' Algorithm for the Hartree-Fock Exchange. *Chem. Phys.* **2009**, *356*, 98–109.

(38) Izsák, R.; Neese, F. An Overlap Fitted Chain of Spheres Exchange Method. *J. Chem. Phys.* **2011**, *135* (14), 144105.

(39) Aquilante, F.; Pedersen, T. B.; Lindh, R.; Roos, B. O.; Sánchez de Merás, A.; Koch, H. Accurate Ab Initio Density Fitting for Multiconfigurational Self-Consistent Field Methods. *J. Chem. Phys.* **2008**, *129* (2), 024113.

(40) Malmqvist, P.-Å.; Roos, B. O. The CASSCF State Interaction Method. *Chem. Phys. Lett.* **1989**, *155* (2), 189–194.

(41) Singh, S. K.; Eng, J.; Atanasov, M.; Neese, F. Covalency and Chemical Bonding in Transition Metal Complexes: An Ab Initio Based Ligand Field Perspective. *Coord. Chem. Rev.* **2017**, *344*, 2–25.

(42) Atanasov, M.; Zadrozny, J. M.; Long, J. R.; Neese, F. A Theoretical Analysis of Chemical Bonding, Vibronic Coupling, and Magnetic Anisotropy in Linear Iron(II) Complexes with Single-Molecule Magnet Behavior. *Chem. Sci.* **2012**, *4* (1), 139–156.

(43) Angeli, C.; Cimiraglia, R.; Malrieu, J.-P. N-Electron Valence State Perturbation Theory: A Spinless Formulation and an Efficient Implementation of the Strongly Contracted and of the Partially Contracted Variants. *J. Chem. Phys.* **2002**, *117* (20), 9138–9153.

(44) Angeli, C.; Cimiraglia, R.; Malrieu, J.-P. N-Electron Valence State Perturbation Theory: A Fast Implementation of the Strongly Contracted Variant. *Chem. Phys. Lett.* **2001**, *350* (3), 297–305.

(45) Angeli, C.; Cimiraglia, R.; Evangelisti, S.; Leininger, T.; Malrieu, J.-P. Introduction of N-Electron Valence States for Multireference Perturbation Theory. *J. Chem. Phys.* **2001**, *114* (23), 10252–10264.

(46) Boston, D. R.; Rose, N. J. Encapsulation Reaction. Synthesis of the Clathro Chelate 1,8-Bis(Fluoroboro)-2,7,9,14,15,20-Hexaoxa-3,6,10,13,16,19-Hexaaza-4,5,11,12,17,18-Hexamethylbicyclo[6.6.6]Eicosa-3,5,10,12,16,18-Hexaenecobalt(III) Ion. *J. Am. Chem. Soc.* **1968**, *90* (24), 6859–6860.

(47) Lingafelter, E. C.; Zakrzewski, G. A.; Ghilardi, C. A. Structure of the Cobalt(III) and Cobalt(II) Complexes of the Cage Ligand 1,8-Bis(Fluoroboro)-2,7,9,14,15,20-Hexaoxa-3,6-10,13,16,19-Hexaaza-4,5,11,12,17,18-Hexamethylbicyclo[6.6.6]Eicosa-3,5,10,12,16,18-Hexaene. *J. Am. Chem. Soc.* **1971**, *93* (18), 4411–4415.

(48) Jackels, S. C.; Rose, N. J. Encapsulation Reactions. Synthesis and Characterization of Clathro Chelates Derived from Iron(II), Dimethylglyoxime and Boron Compounds. *Inorg. Chem.* **1973**, *12* (6), 1232–1237.

(49) Muller, J. G.; Takeuchi, K. J.; Grzybowski, J. J. Preparation and Characterization of Ruthenium(II) Clathrochelate Complexes. *Polyhedron* **1989**, *8* (11), 1391–1399.

(50) Hsieh, W.-Y.; Liu, S. Novel Biscapped and Monocapped Tris(Dioxime) Mn(II) Complexes: X-Ray Crystal Structure of the First Cationic Tris(Dioxime) Mn(II) Complex [$Mn(CDOH)_3$ BPh]OH (CDOH = 1,2-Cyclohexanedione Dioxime). *Inorg. Chem.* **2006**, *45* (13), 5034–5043.

(51) Yongteng Wei. *CSD Comm.* **2018**. https://doi.org/DOI: 10.5517/ccdc.csd.cc20mgjn.

(52) Voloshin, Y. Z.; Varzatskii, O. A.; Novikov, V. V.; Strizhakova, N. G.; Vorontsov, I. I.; Vologzhanina, A. V.; Lyssenko, K. A.; Romanenko, G. V.; Fedin, M. V.; Ovcharenko, V. I.; Bubnov, Y. N. Tris-Dioximate Cobalt(I,II,III) Clathrochelates: Stabilization of Different Oxidation and Spin States of an Encapsulated Metal Ion by Ribbed Functionalization. *Eur. J. Inorg. Chem.* **2010**, *34*, 5401–5415.

(53) Hansch, Corwin.; Leo, A.; Taft, R. W. A Survey of Hammett Substituent Constants and Resonance and Field Parameters. *Chem. Rev.* **1991**, *91* (2), 165–195.

(54) Voloshin, Y. Z.; Kostromina, N. A.; Nazarenko, A. Y. Macrobicyclic D-Metal Tris-Dioximates Obtained by Cross-Linking with p-Block Elements Part I. Template Synthesis and Properties of Macrobicyclic Boron-Containing Iron(II) Dioximates. *Inorg. Chim. Acta.* **1990**, *170* (2), 181–190.

(55) Novikov, V. V.; Ananyev, I. V.; Pavlov, A. A.; Fedin, M. V.; Lyssenko, K. A.; Voloshin, Y. Z. Spin-Crossover Anticooperativity Induced by Weak Intermolecular Interactions. *J. Phys. Chem. Lett.* **2014**, *5* (3), 496–500.

(56) Alvarez, S.; Alemany, P.; Casanova, D.; Cirera, J.; Llunell, M.; Avnir, D. Shape Maps and Polyhedral Interconversion Paths in Transition Metal Chemistry. *Coord. Chem. Rev.* **2005**, *249* (17), 1693–1708.

(57) Alvarez, S.; Avnir, D.; Llunell, M.; Pinsky, M. Continuous Symmetry Maps and Shape Classification. The Case of Six-Coordinated Metal Compounds. *New J. Chem.* **2002**, *26* (8), 996–1009.

(58) Cremades, E.; Echeverría, J.; Alvarez, S. The Trigonal Prism in Coordination Chemistry. *Chem. Eur. J.* **2010**, *16* (34), 10380–10396.

(59) Gillum, W. O.; Wentworth, R. A. D.; Childers, R. F. Hindered Ligand Systems. IV. Complexes of Cis,Cis-1,3,5-Tris(Pyridine-2-Carboxaldimino)Cyclohexane. Trigonal-Prismatic vs. Octahedral Coordination. *Inorg. Chem.* **1970**, *9* (8), 1825–1832.

(60) Wentworth, R. A. D. Trigonal Prismatic vs. Octahedral Stereochemistry in Complexes Derived from Innocent Ligands. *Coord. Chem. Rev* **1972**, *9* (1–2), 171–187.

(61) C. Knight, J.; Alvarez, S.; Angelo, J. A.; G. Edwards, P.; Singh, N. A Novel Bipyridine - Based Hexadentate Tripodal Framework with a Strong Preference for Trigonal Prismatic Co-Ordination Geometries. *Dalton Trans.* **2010**, *39* (16), 3870–3883.

(62) Chilton, N. F.; Anderson, R. P.; Turner, L. D.; Soncini, A.; Murray, K. S. PHI: A Powerful New Program for the Analysis of Anisotropic Monomeric and Exchange-Coupled Polynuclear d- and f-Block Complexes. *J. Comput. Chem.* **2013**, *34* (13), 1164–1175.

(63) Desrochers, P. J.; Sutton, C. A.; Abrams, M. L.; Ye, S.; Neese, F.; Telser, J.; Ozarowski, A.; Krzystek, J. Electronic Structure of Nickel(II) and Zinc(II) Borohydrides from Spectroscopic Measurements and Computational Modeling. *Inorg. Chem.* **2012**, *51* (5), 2793–2805.

(64) Charron, G.; Malkin, E.; Rogez, G.; Batchelor, L. J.; Mazerat, S.; Guillot, R.; Guihéry, N.; Barra, A.-L.; Mallah, T.; Bolvin, H. Unraveling σ and π Effects on Magnetic Anisotropy in Cis-NiA_4B_2 Complexes: Magnetization, HF-HFEPR Studies, First-Principles Calculations, and Orbital Modeling. *Chem. Eur. J.* **2016**, *22* (47), 16850–16862.

(65) Gómez-Coca, S.; Cremades, E.; Aliaga-Alcalde, N.; Ruiz, E. Huge Magnetic Anisotropy in a Trigonal-Pyramidal Nickel(II) Complex. *Inorg. Chem.* **2014**, *53* (2), 676–678.

(66) Schweinfurth, D.; Krzystek, J.; Schapiro, I.; Demeshko, S.; Klein, J.; Telser, J.; Ozarowski, A.; Su, C.-Y.; Meyer, F.; Atanasov, M.; Neese, F.; Sarkar, B. Electronic Structures of Octahedral Ni(II) Complexes with "Click" Derived Triazole Ligands: A Combined Structural, Magnetometric, Spectroscopic, and Theoretical Study. *Inorg. Chem.* **2013**, *52* (12), 6880–6892.

(67) Titiš, J.; Boča, R. Magnetostructural D Correlation in Nickel(II) Complexes: Reinvestigation of the Zero-Field Splitting. *Inorg. Chem.* **2010**, *49* (9), 3971–3973.

(68) Boča, R. Zero-Field Splitting in Metal Complexes. *Coord. Chem. Rev* **2004**, *248* (9–10), 757–815.

(69) Suaud, N.; Rogez, G.; Rebilly, J.-N.; Bouammali, M.-A.; Guihéry, N.; Barra, A.-L.; Mallah, T. Playing with Magnetic Anisotropy in Hexacoordinated Mononuclear Ni(II) Complexes, An Interplay Between Symmetry and Geometry. *Appl. Magn. Reson.* **2020**, *51* (11), 1215–1231.

(70) Dai, D.; Xiang, H.; Whangbo, M.-H. Effects of Spin-Orbit Coupling on Magnetic Properties of Discrete and Extended Magnetic Systems. *J. Comput. Chem.* **2008**, *29* (13), 2187–2209.

(71) Sarkar, A.; Dey, S.; Rajaraman, G. Role of Coordination Number and Geometry in Controlling the Magnetic Anisotropy in FeII, CoII, and NiII Single-Ion Magnets. *Chem. Eur. J.* **2020**, *26* (62), 14036–14058.

(72) Shao, F.; Cahier, B.; Guihéry, N.; Rivière, E.; Guillot, R.; Barra, A.-L.; Lan, Y.; Wernsdorfer, W.; Campbell, V. E.; Mallah, T. Tuning the Ising-Type Anisotropy in Trigonal Bipyramidal Co(II) Complexes. *Chem. Commun.* **2015**, *51* (92), 16475–16478.

(73) Ruamps, R.; Batchelor, L. J.; Maurice, R.; Gogoi, N.; Jiménez-Lozano, P.; Guihéry, N.; de Graaf, C.; Barra, A.-L.; Sutter, J.-P.; Mallah, T. Origin of the Magnetic Anisotropy in Heptacoordinate NiII and CoII Complexes. *Chem. Eur. J.* **2013**, *19* (3), 950–956.

(74) Ruamps, R.; Batchelor, L. J.; Guillot, R.; Zakhia, G.; Barra, A.-L.; Wernsdorfer, W.; Guihéry, N.; Mallah, T. Ising-Type Magnetic Anisotropy and Single Molecule Magnet Behaviour in Mononuclear Trigonal Bipyramidal Co(II) Complexes. *Chem. Sci.* **2014**, *5* (9), 3418–3424.

(75) Kubow, S. A.; Takeuchi, K. J.; Grzybowski, J. J.; Jircitano, A. J.; Goedken, V. L. Distortions from Trigonal Prismatic Geometry for Several Structurally Characterized Clathrochelate Complexes: Significance of π-Backbonding on Clathrochelate Coordination Geometry. *Inorg. Chim. Acta.* **1996**, *241* (2), 21–30.

(76) Ruamps, R.; Maurice, R.; Batchelor, L.; Boggio-Pasqua, M.; Guillot, R.; Barra, A. L.; Liu, J.; Bendeif, E.-E.; Pillet, S.; Hill, S.; Mallah, T.; Guihéry, N. Giant Ising-Type Magnetic Anisotropy in Trigonal Bipyramidal Ni(II) Complexes: Experiment and Theory. *J. Am. Chem. Soc.* **2013**, *135* (8), 3017–3026.

(77) Zadrozny, J. M.; Telser, J.; Long, J. R. Slow Magnetic Relaxation in the Tetrahedral Cobalt(II) Complexes $[Co(EPh)_4]^{2-}$ (E = O, S, Se). *Polyhedron* **2013**, *64*, 209–217.

(78) Lin, P.-H.; Smythe, N. C.; Gorelsky, S. I.; Maguire, S.; Henson, N. J.; Korobkov, I.; Scott, B. L.; Gordon, J. C.; Baker, R. T.; Murugesu, M. Importance of Out-of-State Spin–Orbit Coupling for Slow Magnetic Relaxation in Mononuclear Fe^{II} Complexes. *J. Am. Chem. Soc.* **2011**, *133* (40), 15806–15809.

(79) Lomjanský, D.; Rajnák, C.; Titiš, J.; Moncoľ, J.; Smolko, L.; Boča, R. Impact of Tetrahedral and Square Planar Geometry of Ni(II) Complexes with (Pseudo)Halide Ligands to Magnetic Properties. *Inorg. Chim. Acta.* **2018**, *483*, 352–358.

(80) *Magnetic Resonance Imaging: Methods and Biologic Applications*; Prasad, P. V., Ed.; Methods in Molecular Medicine; Humana Press: Totowa, NJ, 2006.

CHAPTER 5 – Tailoring the Temperature Sensitivity of Zero-Field Splitting in Mn(II) Cage Complexes

5.1. Overview

Controlling the temperature response of magnetic resonance properties is an essential step toward novel molecular thermometers or quantum sensing platforms. To date, however, demonstrations using molecular design to control the temperature dependence of zero-field splitting (*D*), a critical property that governs the electron paramagnetic resonance (EPR) response of open-shell molecules, are absent in the literature. Herein we demonstrate that ligand design can control the temperature dependence of *D*. To do so, we prepared and analyzed three different encapsulated Mn^{2+} complexes. High-field, high-frequency EPR spectroscopy reveals an EPR spectrum that varies in width as a function of temperature, indicating a change in *D* value. At high temperature, *D* values vary from 1400 to 650 MHz (300 MHz ≅ 0.01 cm^{-1}). With decreasing temperature, these values change, in one case by nearly an order of magnitude. Importantly, the *D* values increase with decreasing temperature for the ligand L1 and L3 and decrease with increasing temperature for L2. These results are the first demonstration of the ability to tune the variable-temperature nature of *D* via ligand selection in any complex, and the first for the Mn^{2+} metal ion.

5.2. Introduction

Controlling the temperature dependence of magnetic resonance signals in molecules is a step toward better understanding of environmental sensitivity of quantum objects, which will pave the way toward new quantum sensing platforms.[1,2] This is especially true in open-shell molecules, which are tunable and can be dissolved in solution, paving the way for potential spin-based,

electron-paramagnetic-resonance imaging technologies that embrace quantum controls. Long-term abilities afforded by this application could include noninvasive thermometry via EPR[3,4] or optically-detected magnetic resonance, the latter of which currently harnesses nitrogen-vacancy center qubits.[5,6]

The temperature dependence of EPR properties in $S > {}^1/_2$ metal complexes is particularly appealing for potential thermometric applications because of its potential effects on zero-field splitting. This property is prevalent in paramagnetic metal ions and depends on the ligand field, its magnitude. and symmetry.[7] Small, temperature-dependent changes to a metal ion's geometry that affect the ligand field, such as M–L bond distance expansions/contractions are thus expected to directly affect the zero-field splitting.[8,9] Indeed, analogous arguments are made for the temperature dependence of the nuclear magnetic properties of metal nuclei (e.g. ^{59}Co).[10] In addition, the zero-field splitting parameter directly affects the magnetic field, frequency, and number of observed EPR transitions.[11] Hence, controlling the temperature dependence of the zero-field splitting would provide valuable routes spin-based quantum sensing capabilities, if completely understood.

Beyond the surface-level bond-distance compression/expansion view of temperature-dependent zero-field splitting, little is known about how actual molecular identity governs the temperature dependence of zero-field splitting in metal complexes. Indeed, outside of spin crossover[12] and valence tautomerizations,[13] the general procedure for modeling temperature-dependent magnetic data in mononuclear complexes assumes that D and other general spin Hamiltonian parameters are constant with temperature,[14,15] creating a blind spot of understanding for a potentially useful phenomenon.

Herein we present the synthesis and investigation of a series of three Mn^{2+} complexes with cryptand-derivative ligands: [MnL1]$(PF_6)_2$ (**1**, L1 = 1,4,7,10,13,16,21,24-Octaazabicyclo[8.8.8]

hexacosa-4,6,13,15,21,23-hexaene), $[MnL2](PF_6)_2$ (**2**, L2 = 1,4,7,10,13,16,21,24-Octaazabicyclo[8.8.8]hexacosane), and $[MnL3](PF_6)_2$ (**3**, L3 = 17,20,25,28-Tetraoxa-1,14,31,32-tetraazatetracyclo[12.8.8.13,7.18,12]dotriaconta-3,5,7(32),8,10,12(31)-hexaene) (**Figure 5.1**). We anticipated that Mn^{2+} would exhibit relatively high changes in D with changes in T owing to the high-spin states and population of e_g* MOs, such that the excited state energies should be significantly affected by slight T-dependent changes to bond distances and angles. The focus on encaging ligands is because of the kinetic stability afforded by such ligands, and that environmental sensitivities imposed by these ligands may, in the long run, be leveraged for novel bioimaging applications that avoid toxicity from metal-ion release.

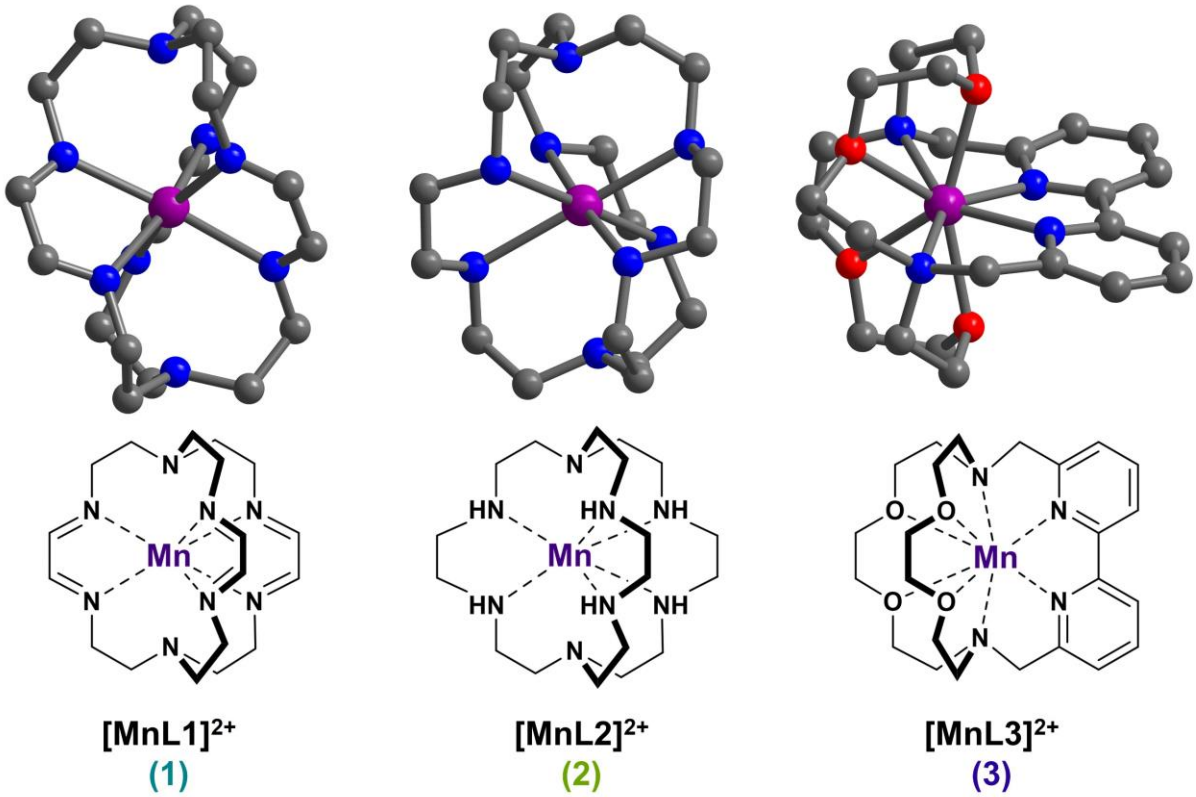

Figure 5.1. Crystal structures of $[MnL1]^{2+}$ (**1**), $[MnL2]^{2+}$ (**2**), and $[MnL3]^{2+}$ (**3**) determined from x-ray diffraction. Purple, red, blue, and gray spheres represent Mn-, O-, N-, and C- atoms, respectively. H-atoms, solvents, and PF_6^- counterions were omitted for clarity.

We find that there is a strong temperature dependence of the EPR spectra for **1-3** that can be modeled with a variable-temperature zero-field splitting. Excitingly, the observed temperature

dependences of *D* are all large for **1-3** and eclipse the magnetic resonance thermometry sensitivities of the prototypical NV center.[16,17] The variation in behavior across the complexes is likely dictated by ligand-counterion interactions, as nearly negligible changes are observed in solution, where complex-counterion interactions are expected to be suppressed. The results thus represent an important step in understanding what molecular features control temperature sensitivity of spin Hamiltonian parameters and therefore magnetic resonance spectra.

5.3. Experimental Section

5.3.1. General Considerations

L1, L2, and [NaL3]Br were synthesized following published procedures.[18–20] Methanol (MeOH), ethanol (EtOH), diethyl ether (Et_2O), acetonitrile (MeCN), NH_4PF_6, sucrose, and $MnCl_2 \cdot 4H_2O$ were all purchased commercially and used as received. Infrared spectra were recorded on a Bruker TENSOR II FTIR spectrometer. Mass spectral analyses were performed on an Agilent 6224 Accurate Mass TOF LC/MS in positive ion mode using direct injection. Peak assignment was on the basis of m/z, interpeak spacing, and isotopic distribution. UV-Vis spectra were collected on solutions of complexes with a Shimadzu UV-2600i UV-Vis-NIR spectrophotometer and standard quartz cuvettes of 1 cm path length. Emission spectra were obtained on an Edinburgh FS5 Spectrofluorometer using a quartz cuvette with a 1 cm path length in a temperature-controlled sample holder. Samples were prepared as 3.7-, 11.7-, and 0.23-mM solutions (**1**, **2**, and **3,** respectively) in MeCN and held at 20 °C. The differing concentrations were to give each complex roughly the same absorption. Steady state emission spectra were obtained by exciting each sample at 330 nm (**1** and **3**) and 220 nm (**2**) with a 5.0 nm slit width and collecting

from 350-750 nm (**1** and **3**) and 240-650 (**2**). Spectra were averaged over three scans with a 0.5 s integration time.

5.3.2. Preparation of Compounds

Synthesis of [MnL1]$(PF_6)_2$•H_2O (**1**). A solution of L1 (0.3087 g, 0.8611 mmol) in 5 mL EtOH was added dropwise to a solution of $MnCl_2$•$4H_2O$ (0.1713 g, 0.8656 mmol) in 5 mL EtOH and allowed to stir overnight, producing an intense orange solution and a small amount of precipitate. The mixture was evaporated to dryness, redissolved in a minimum amount (8 mL) of MeOH and filtered. The filtrate was placed in an Et_2O chamber and crystallized by vapor diffusion. The orange solid was collected and dissolved in a minimum amount (5 mL) of EtOH. This orange solution was then added to 5 mL of EtOH saturated in NH_4PF_6. An orange powder immediately precipitated, which was collected by vacuum filtration, washed with water, and dried under reduced pressure at 70˚C to yield **1** (0.2381 g, 0.3301 mmol, 38% yield). Single crystals suitable for single-crystal x-ray diffraction were grown by vapor diffusion of Et_2O into a concentrated MeCN solution of **1**. Combustion analysis, calculated for $C_{24}H_{30}N_8MnF_{12}P_2$•$H_2O$: 29.97 %C, 4.47 %H, 15.53 %N; found: 29.99 %C, 4.24 %H, 15.36 %N. IR (cm^{-1}, Diamond ATR): 2929, 2869, 2846, 1672, 1621, 1463, 1449, 1391, 1377, 1280, 1269, 1166, 1105, 1085, 1067, 1052, 999, 922, 825, 745, 622, 556, 544, 448, 423, 409. LC-MS (m/z), positive ion mode: $\{[Mn(L1)]PF_6\}^+$, 558.16. See **Figure A4.2** for UV-Vis characterization.

Synthesis of [MnL2]$(PF_6)_2$ (**2**). A colorless MeOH solution (5 mL) of $MnCl_2$•$4H_2O$ (0.1380 g, 0.6973 mmol) was added dropwise to a colorless methanol solution (5 mL) of L2 (0.2586 g, 0.6978 mmol). The pale orange reaction mixture was stirred at room temperature under ambient atmosphere overnight. The resulting solution was filtered through diatomaceous earth and the

resulting solution was crystallized via the slow evaporation of EtOH. The pale orange solid was then dissolved in a minimum amount (5 mL) of EtOH and this colorless solution was added to 5 mL of EtOH saturated in NH_4PF_6. A very pale orange powder immediately precipitated, which was collected by vacuum filtration, washed with water, and dried under reduced pressure to yield **2** (0.2126 g, 0.2971 mmol, 42% yield). Single crystals suitable for single-crystal x-ray diffraction were be grown by diffusion of Et_2O vapor into a concentrated MeCN solution of **2**. Combustion analysis, calculated for $C_{24}H_{36}N_8MnF_{12}P_2$: 30.22 %C, 5.92 %H, 15.66 %N; found: 30.47 %C, 5.94 %H, 15.68 %N. IR (cm^{-1}, Diamond ATR): 3336, 2980, 2928, 2877, 2841, 1472, 1452, 1376, 1360, 1304, 1269, 1158, 1100, 1067, 959, 936, 881, 833, 815, 798, 597, 556, 510, 426. LC-MS (m/z), positive ion mode: $\{[Mn(L2)]PF_6\}^+$, 570.25. See **Figure A4.2** for UV-Vis characterization.

Synthesis of $[MnL3](PF_6)_2$•0.5MeCN (**3**). A solution of $MnCl_2$•$4H_2O$ (0.2502 g, 1.2643 mmol) in 30 mL MeOH was added dropwise to a stirring 30 mL EtOH solution of [(L3)Na]Br (0.6672 g, 1.2232 mmol), and the reaction mixture was stirred at 60˚C overnight. Upon cooling, a small amount of white precipitant was filtered off. The filtrate was concentrated by rotary evaporation yielding a whitish-orange powder. The powder was then dissolved in minimum amount (10 mL) of EtOH and this solution was added to 10 mL of EtOH solution saturated in NH_4PF_6. A very pale orange powder immediately precipitated, which was collected by vacuum filtration and washed with EtOH to yield **3** (0.4058 g, 0.5023 mmol, 41% yield). Single crystals suitable for single-crystal x-ray diffraction were be grown by vapor diffusion of Et_2O into a concentrated MeCN solution of **3**. Combustion analysis, calculated for $C_{24}H_{34}N_4O_4MnF_{12}P_2$•$0.5C_2H_3N$: 30.22 %C, 5.92 %H, 15.66 %N; found: 30.47 %C, 5.94 %H, 15.68 %N. IR (cm^{-1}, Diamond ATR): 2962, 2898, 2857, 1599, 1578, 1468, 1439, 1264, 1243, 1177, 1131, 1088, 1058, 1040, 1012, 939, 908, 878, 830, 782, 739, 719, 649, 556, 434, 407. LC-

MS (m/z), positive ion mode: $\{[Mn(L3)]PF_6\}^+$, 642.16. See **Figure A4.2** for UV-Vis characterization.

*5.3.3. X-ray Data Collection, Structure Solution and Refinement for **1**-**3***

Single-crystal x-ray diffraction data were collected at the x-ray diffraction facility of the Analytical Resources Core at Colorado State University. Data for **1-3** were collected on a Bruker D8 Quest ECO single-crystal x-ray diffractometer equipped with Mo Kα (λ = 0.71073 Å) x-ray source. Data were collected and integrated using Bruker Apex 4 software. Absorption corrections were applied using SADABS. Space group assignments were determined by examination of systematic absences, E-statistics, and successive refinement of the structures. Crystal structures were solved using SHELXT[21] and refined with the aid of successive difference Fourier maps by SHELXL[22,23] operated in conjunction with OLEX2 software.[24] None of the crystals demonstrated decay by x-ray radiation over the course of the experiment. All non-hydrogen atoms were refined anisotropically. Hydrogen atoms were placed in ideal positions and refined using a riding model for all structures. The structure of **1** was slightly twinned with an initial Flack parameter near 0.5. We modeled twinned system with the TWIN Law (0, –1, 0, –1, 0, 0, 0, 0, –1), which improved the Flack parameter to 0.007.

5.3.4. Magnetic Measurements

Magnetic measurements were performed on polycrystalline samples of **1**-**3** using a Magnetic Property Measurement System MPMS3 (Quantum Design) equipped with a superconducting quantum interference device (SQUID) magnetometer. Direct-current (DC) magnetic susceptibility was measured in an applied magnetic field of 1000 Oe in the 2-300 K

temperature range, with a temperature sweep rate of 2 K/min. The data were corrected for the contribution from the sample holder and for intrinsic diamagnetism by using Pascal's constants.

5.3.5. EPR Measurements and Analyses

Variable magnetic field (up to 17 T) and high frequency (390 GHz) EPR spectra were recorded with a home-built spectrometer at the EMR facility of National High Magnetic Field Laboratory in Tallahassee, FL. The instrument has been described in detail elsewhere.[25] Briefly, the instrument is a transmission-type device in which waves are propagated in cylindrical light-pipes. The microwaves were generated by a phase-locked oscillator (Virginia Diodes) operating at a frequency of 8-20 GHz and generating its harmonics, of which the 4th, 8th, 12th, 16th, 24th and 32nd were available. A superconducting magnet (Oxford Instruments) capable of reaching a field of 17 T was employed. 390 GHz was selected as the frequency for EPR analysis based on signal-to-noise and peak-to-peak separation. Analyzed samples were solid, microcrystalline powders of **1**, **2**, and **3** ground with sucrose, loaded into a sample cup, then inserted into the spectrometer.

Samples for X-band EPR analyses of **1−3** were prepared by loading solutions of **1−3** in butyronitrile (5 mM) into a 4 mm outer diameter (OD) quartz EPR tube (Wilmad 707-SQ-250M) and placed into a Bruker ELEXSYS ESR-500 X-band EPR spectrometer (Bruker Biospin, Rheinstetten, Germany). The high-sensitivity probe was used, and temperatures were controlled via a Coldedge system for these measurements. All EPR spectra were analyzed via the program Easyspin[26] and modeled by the spin Hamiltonian and broadening mechanisms reported in the main text and **Tables A4.4-A4.9.**

5.4. Results and Discussion

Syntheses of the studied complexes proceeded via combination of the encapsulating ligands with $MnCl_2$ in ethanol. Counterion metathesis reactions with NH_4PF_6 yielded the PF_6^- salts of **1**, **2**, and **3** as yellow-orange compounds. These compounds were readily crystallized for single-crystal x-ray diffraction analyses (**Tables A4.1-A4.3**).

The Mn^{2+} ions in complexes **1-3** are of varying geometry (**Figure 5.1**). For **1** and **2**, the Mn ions are six-coordinate, bound to the side arms of the cryptand ligands and the apical N atoms are unbound, though seemingly oriented with the lone pairs pointing toward the Mn. For **3**, the Mn ion is eight-coordinate, bound to the two N and six O atoms of the ligand. For **1**, average Mn–N distances are 2.30(3) Å for bound N atoms and 3.12(8) Å for the apical N atoms. For **2**, the Mn–N distances expand slightly to 2.443(1) Å for bound N atoms but contract slightly, to 2.85(5) Å for the apical N–Mn distance. This particular change likely reflects the change in the metal-ligand interaction for *imino* N-donor atoms versus the *amino* N-donor atoms, which then distorts the total ligand geometry and shifts the apical N atoms. For **3**, there are two sets of Mn–N bonds, one set with the bipyridine group and the other are tertiary amines, with average Mn–N distances of 2.27(1) and 2.44(1) Å, respectively. For **3**, there are also Mn–O bonds, with an average distance of 2.39(6) Å. The local geometries of the Mn(II) ions in **1** and **2** are best described as axially compressed trigonal antiprismatic geometries, as the N–Mn–N bite angles are 71.92(3)° for **1** and 71.6(1)° for **2** (**Figure A4.1**). In contrast, the Mn(II) geometry in **3** is a distorted dodecahedral/square antiprismatic one, owing to the larger coordination number and three distinct types of donor atoms.

Solution phase UV-Vis spectroscopy analyses of **1**-**3** reveal peaks above 20,000 cm^{-1} with strong intensities indicative of charge transfer bands (**Figure A4.2**). Complex **1** exhibits the lowest

energy peak of the series, near 29,000 cm^{-1}. Complex **3** yields the next lowest energy peaks, near 33,000 and 40,000 cm^{-1}. Complex **2** yields the highest energy peak, near 45,000 cm^{-1}. The intensities of these transitions suggest that they are charge transfer transitions with the extended conjugated units in **1** and **3**. For **2**, however, which has no extended conjugation on the ligand shell, assignment of the high-energy transition is not as clear. These spectra are within expectation for Mn^{2+} as a high-spin, high-coordinate ion with half-filled shell, where any d-d transitions are forbidden, therefore weak or not observed.[27]

Complexes **1-3** also emit light when irradiated with light in the 300-220 nm window (**Figure A4.3**). The trend in highest emission intensity follows from **1** to **2** to **3**. Complex **1** emits at 22,000 cm^{-1}, **2** emits at 30,000 cm^{-1}, and then **3** yields even higher-energy emission, near 37,000 cm^{-1}. The ground state of the Mn(II) ions in **1-3** are all $^6A_1$, as indicated by the $S = {}^5/_2$ ground state (see magnetic analyses below). Inspection of the d^5 Tanabe-Sugano diagram[28] with the $^6A_1$ ground state in mind suggests the trend in emission energy could reflect a decreasing ligand-field strength from **3-1**, if the observed emission is from any of the lowest-three energy excited states ($^4T_2$, $^4T_1$, or $^2T_2$), with the $^2T_2 \rightarrow {}^6A_1$ emission being lowest in energy. These emissive characteristics are in agreement with observations of other Mn(II) complexes.[29,30]

Potential correlation of the electronic structures of **1**-**3** to zero-field splitting and other spin-Hamiltonian parameters was pursued by magnetic susceptibility and two EPR techniques. At 300 K, $\chi_M T$ values for **1**, **2**, and **3** are, respectively, 4.02, 4.28 and 4.32 cm^3K/mol (**Figure A4.3**). These values are close to the expected room temperature value of 4.38 cm^3K/mol for $S = {}^5/_2$ and $g = 2.00$. With decreasing temperature, $\chi_M T$ is relatively constant with little temperature dependence. Zero-field splitting values larger than 1-2 cm^{-1} will produce T-dependent $\chi_M T$ values below 50 K, hence, the absence of a strong T-dependence highlights a very small zero-field splitting (< 1 cm^{-1}).

The first EPR analysis we pursued was low-temperature (5 K), high-frequency (390 GHz), high-field EPR spectroscopy in the solid state (**Figure 5.2**). At high field and for most Mn^{2+} species (which often have positive D values < *ca.* 1 cm^{-1}) the EPR experiment proceeds in the so-called high-field limit, where the Zeeman interaction is the largest-energy term in the spin-Hamiltonian. As a result, one should expect five peaks corresponding to $|M_S = -5/2\rangle$ to $|M_S = -3/2\rangle$, $|M_S = -3/2\rangle$ to $|M_S = -1/2\rangle$, $|M_S = -1/2\rangle$ to $|M_S = +1/2\rangle$, $|M_S = +1/2\rangle$ to $|M_S = +3/2\rangle$, and $|M_S = +3/2\rangle$ to $|M_S = +5/2\rangle$ transitions. The resolution of these individual peaks at high frequency may be challenging owing to broadening from g strain or unresolved hyperfine interactions (e.g. with $I = 5/2$ ^{55}Mn or $I = 1$ ^{14}N and $I = 1/2$ ^{15}N donor atoms).[31] Nevertheless, the span of the peaks on the field axis should trend with the zero-field splitting magnitude for Mn^{2+} and display a greater width for a larger D magnitude.

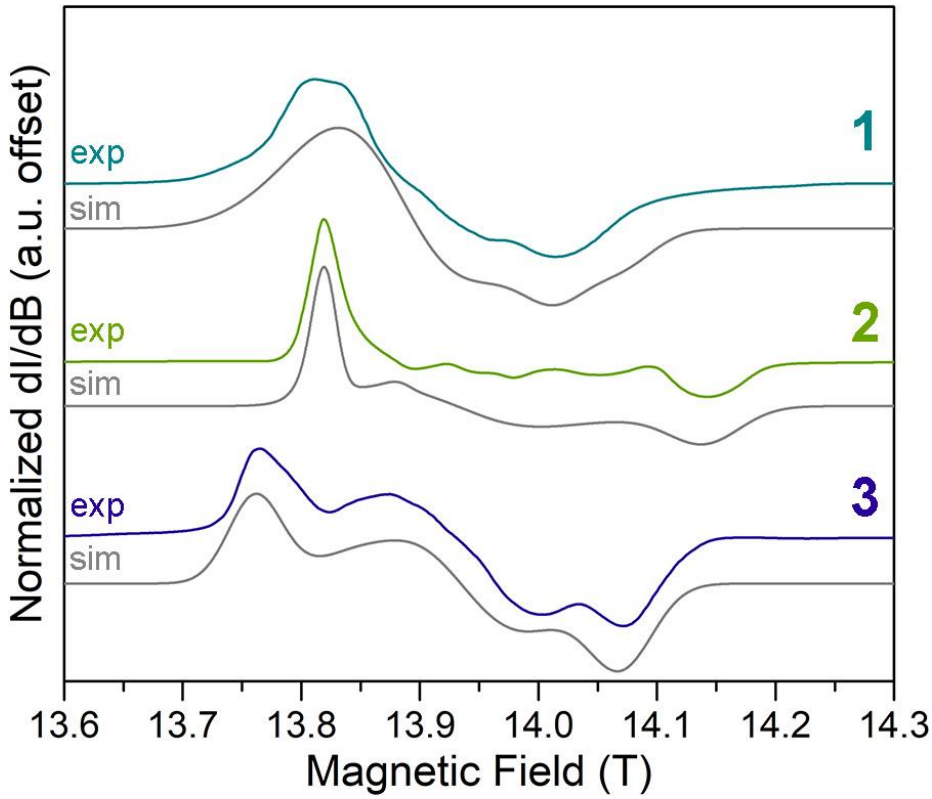

Figure 5.2. EPR spectra collected at 5 K and a frequency of 390 GHz for **1-3** in sucrose dispersions. Gray lines are fits using the spin-Hamiltonian parameters in **Tables A4.4-4.6**.

Simulations of the 390 GHz EPR spectra for **1-3** at 5 K (**Figures 5.2, A4.5-A4.6**) give a general trend in zero-field splitting magnitude of $|D|$ increasing from **1** to **2** to **3**. These values were determined from Easyspin,[26] which modeled the spectra using the following spin-Hamiltonian:

$$\hat{H} = \mu_B g \boldsymbol{BS} + D\hat{S}_z^2 + E(\hat{S}_x^2 - \hat{S}_y^2)$$

Here, μ_B is the Bohr magneton, g is the anisotropic g factor, $\boldsymbol{S}$ is the electronic spin operator, $\boldsymbol{B}$ is the applied magnetic field, D is the axial zero-field splitting, E is the transverse zero-field splitting, and $\hat{S}_i^2$ ($i = x$, y, and z) are the spin operators. Note that none of the 390 GHz spectra depict a clear six-line splitting that can be attributed to hyperfine coupling between the $S = {}^5/_2$ electronic spin and the $I = {}^5/_2$ ^{55}Mn nucleus, and it is likely that the hyperfine coupling is contained within the general broadening of the spectra we observe (see **Tables A4.4-A4.6** for simulation details). We specifically avoided the inclusion of hyperfine coupling because of the spectral absence of its effects and a desire to avoid overparameterization. Obtained values of D and E are, respectively, $D = +800$ and $E = +220$ MHz for **1**, $D = +900$ and $E = +220$ MHz for **2**, and $D = +1050$ and $E = +260$ MHz for **3**. The g values for all three are rhombic, hovering around average values of 2.004, 1.995, and 2.006, respectively, for **1**, **2**, and **3**. We note that comparison of simulations qualities with the signs of D and E appears diagnostic for these parameters, except for E in **3**.

The general magnitudes of D obtained here are consistent with expectations for the Mn(II) ion and our other magnetic data.[32–35] Indeed, the observed temperature independence of the $\chi_M T$ data suggest $|D| < 1$ cm^{-1}. The obtained signs of D and E are also consistent with the general expectations for $S = {}^5/_2$, Mn^{2+}.[36–38] Finally, we note that our use of MHz as an energy unit here is necessitated by the small magnitudes in D and E that we observe; for ease of comparison with other transition metal ions, wherein D and E are often much larger[7] (300 MHz ≅ 0.01 cm^{-1}). We note that the UV-Vis data suggested that most electronic states for the Mn^{2+} ions in **1**-**3** are at very

high energy. The inverse relationship between the zero-field splitting value and the energy separation between the ground and excited states suggests that these contributions should be small and consistent with the small *D* values we find from our extensive magnetic analyses here.

Next, we evaluated the temperature dependence of the spectra for evidence of ligand effects on the temperature sensitivity of *D* and *E*. For **1**, **2**, and **3**, the 390 GHz EPR spectra from 5 to 300 K reveal broad signals near $g = 2.00$ (13.9 T) with an overall width that varies with temperature in a unique way for each complex (**Figures 5.3**, **A4.5-A4.6**). For **1**, the width of the signal (peak-to-peak) is *ca*. 0.07 T at 300 K and widens slightly with decreasing temperature, but more dramatically below 30 K to 0.2 T at 5 K. For **2**, in contrast, the spectral width starts at 0.36 T at 300 K and decreases by only 0.04 T from 300 to 5 K. Finally, for **3**, the spectral width increases with decreasing temperature, from 0.07 T at 300 K to 0.3 T at 5 K. The shapes of the spectra change as well, in some cases appearing to be single, broad resonances with slight features to low/high field of the main peak. At low temperature, however, the shapes are far more distinct.

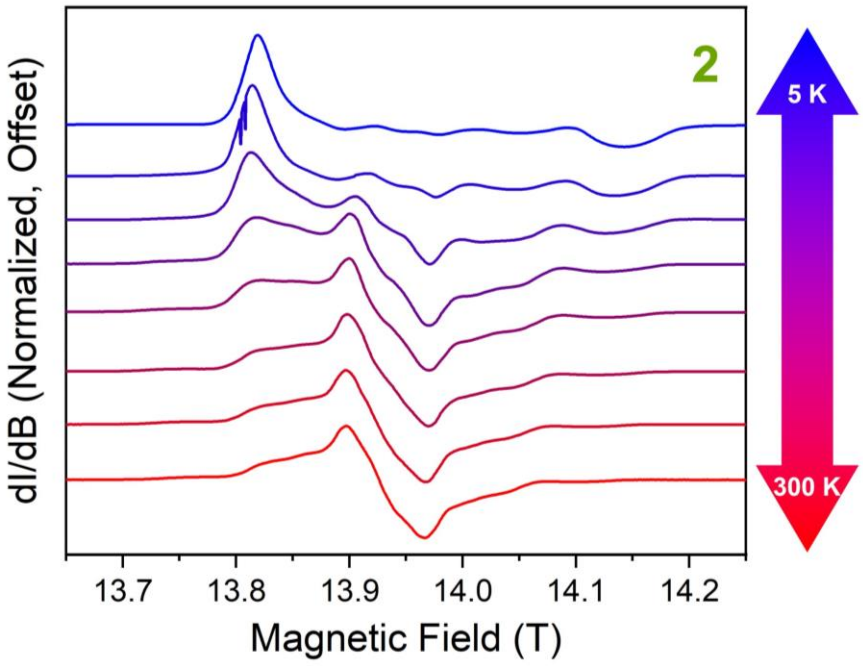

Figure 5.3. Selected variable temperature EPR spectra of **2** collected from 5-300 K at 390 GHz in sucrose dispersions. Spectra vary in width across this range as a result of the temperature sensitive ZFS. Spin-Hamiltonian parameters are found in **Table A4.5**.

The broadness and shapes of the collected 390 GHz variable-temperature spectra were modeled with the program Easyspin[26] to extract *g*, *D*, and *E* values for the studied complexes and their temperature dependence (**Figures 5.3, 5.4 and Tables A4.4-4.6**). For all complexes, *g* values hover close to 2.00 from 5 to 300 K with slight anisotropy that varies slightly with temperature. The obtained *D* and *E* values vary in a more noticeable way with temperature (**Figure 5.4**). For **1**,

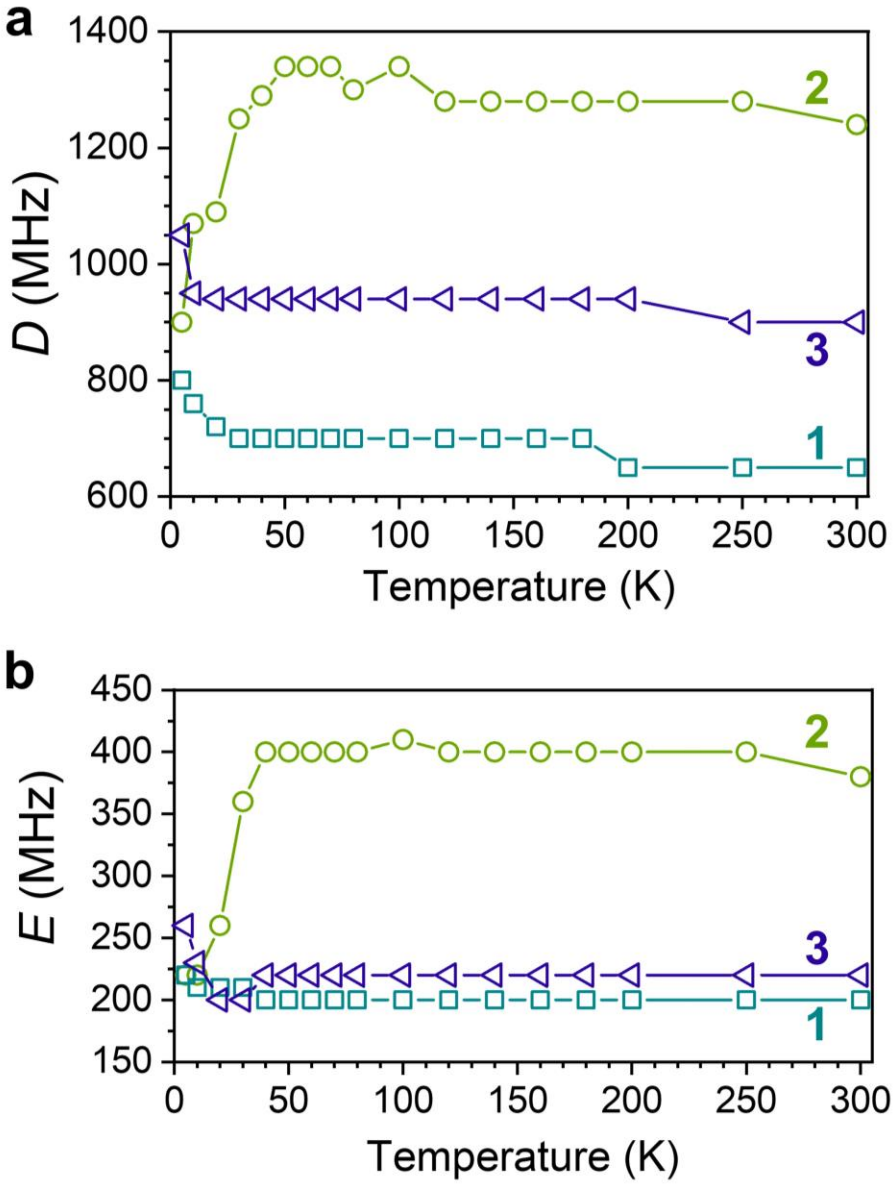

Figure 5.4. Temperature dependence of *D* and *E* from solid-state, 390 GHz analyses of **1**, **2**, and **3**. (**a**) Temperature dependence of *D* values. The uncertainty in each *D* values is *ca.* 10 MHz and evaluated by eye. (**b**) Temperature dependence of the *E* values for **1**, **2**, and **3**. Uncertainties in *E* are *ca.* 20 MHz. Solid lines in both **a** and **b** are guides for the eye.

D is 650 MHz at 300 K and increases slowly and only slightly with decreasing temperature to 700 MHz at 30 K. Below 30 K, *D* for **1** increases more substantially, reaching 800 MHz at 5 K. For **2**, *D* is relatively constant near 1300 MHz from 300 to 40 K, but decreases below 40 K to 900 MHz at 5 K. Finally, for **3**, *D* increases slightly from 900 to 940 MHz from 300 to 20 K, then more dramatically, reaching 1050 MHz at 5 K. The relative ranking of *D* values is generally **2** (1300 MHz) > **3** (900 MHz) > **1** (650 MHz), except at the lowest temperatures of analysis. The obtained *E* values are smaller than the *D* values and exhibit a smaller *T* sensitivity, showing the highest changes below 30 K, like *D*, but generally reflect the trends in *D* (*E* of **3** > *E* of **2** > *E* of **1**). The degree of rhombicity defined by *E*/*D* remained relatively constant for each complex, as an increase in *D* coincided with an increase in *E*, and vice versa.

The temperature sensitivities of the zero-field splitting are large. Taking the change in *D* for **1**, **2**, and **3** over the temperature range of 5 to 50 K, one finds 2.2, 9.8, and 2.2 MHz/K for the temperature sensitivity of *D*. For *E*, the temperature sensitivities are generally smaller over this window. For **1**, **2**, and **3**, $\Delta E/\Delta T$ values are 0.4 4 and 0.9 MHz/K. At higher temperatures, the changes are much smaller. From 50 to 300 K, $\Delta D/\Delta T$ values are 0.2, 0.4, and 0.2 MHz/K, respectively, and $\Delta E/\Delta T$ values are 0, 0.1, and 0 MHz/K for **1**, **2**, and **3**, also respectively.

The temperature sensitivities of the zero-field splitting parameters in **1-3** are significant in the greater context of what is known about *T*-dependent spin-Hamiltonian parameters. The temperature dependent values of *D* and *E* that we observe are, except for the $\Delta E/\Delta T$ values of **1** and **3**, all greater than the temperature sensitivity of the *D* value of the $S = 1$ nitrogen vacancy center in diamond (78 kHz/K),[39,40] several by orders of magnitude. These values are also among the highest temperature sensitivities for molecular systems and eclipse those of several other notable molecules. For example, the $\Delta D/\Delta T$ value of **2** eclipses the 5.7 MHz/K dependence on the

singlet-triplet EPR transition in $[Cu_2(tren)_2\text{-}(OCN)_2](BPh_4)_2$ (tren = tris(2-aminoethyl)amine),[41] a 2.4 MHz/K sensitivity for the $S = {}^5/_2$ $[Fe(DMSO)_6](NO_3)_3$ (DMSO = dimethyl sulfoxide),[42] the 2.3 MHz/K sensitivity for $[Cr(en)_3]^{3+}$ doped in $[Co(en)_3]Cl_3 \bullet 0.5NaCl \bullet 3H_2O$ (en = ethylenediamine),[43] and 1.5 MHz/K sensitivity of $[Cr(H_2O)_6]^{3+}$ in guanidinium aluminum sulfate hexahydrate.[44]

We also applied X-band EPR spectroscopy to frozen solutions of **1-3**, reasoning that the lower frequency may sharpen spectra sufficiently to enable the observation of hyperfine coupling and any associated *T*-dependence,[31] as well as providing a second measurement of the *T*-dependence of the zero-field splitting in a different phase than microcrystalline powder. The X-band EPR spectra were collected from 5.5 K (10 K in **2**) to 60 K in 5 mM butyronitrile solutions. They each exhibit intense peaks at *ca*. 3500 G with smaller features at lower and higher fields, as is typical for low-zero-field splitting (e.g. Mn(II)) complexes. Importantly, the strongest central peak and some of the minor peaks exhibit the six-fold pattern that is typical for Mn(II) with hyperfine coupling to the $I = {}^5/_2$ ^{55}Mn nucleus. At temperatures below 30 K, there were noticeable changes between each temperature point with small spectral features becoming more distinct as the temperature decreased, which was consistent between each molecule. Above 30 K, the spectra were largely similar to each other, with only very slight changes appearing in the baselines (**Figures 5.5**, **A4.10-11**).

To extrapolate how *D* varied with temperature for each of these complexes, spectral simulations were carried out in EasySpin[26] and the best fit spin-Hamiltonian parameters are listed in **Tables A4.7-4.9**. As the lower frequency experiment afforded a sharper spectrum with clear hyperfine peaks (relative to the high-frequency data), the hyperfine coupling energies (*A*) and their respective strains (*A*-strain) were included in these spectral simulations, along with *g*-values, *D* and *E* values. When assessing how *D* and *E* vary as a function of temperature, instead of finding a

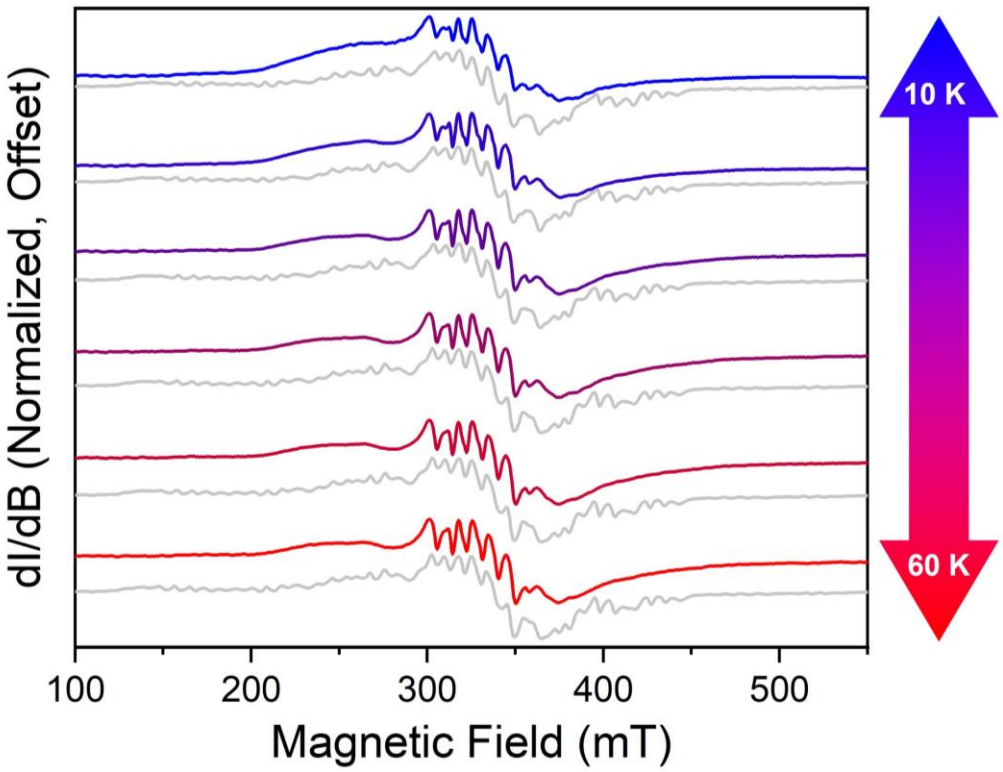

Figure 5.5. Variable temperature EPR spectra of complex **2** collected from 5.5 K to 60 K at 9.3 GHz in 5 mM butryonitrile solutions. Colored lines are the experimental data, and the gray lines are the spectral simulations. Spin-Hamiltonian are found in **Table A4.8**.

large temperature dependence in these values, as we had found in the high-frequency EPR experiments, the variations remained flat across the temperature range measured (**Figure 5.6**).

An initial survey of the relationships that govern the magnitude of D and E suggest that the temperature sensitivity should not vary with frequency or field strength.[45] Consequently, this result suggests that the high temperature sensitivity of the zero-field splitting is only present in the solid state, likely from changes to the crystalline structure as a function of temperature. We propose that butyronitrile, when used as a polar glassing solvent, affords an environment where there is little structural changes to the dissolved complexes that also disrupts counterion-complex interactions.

Finally, we think these data are an important note of caution for drawing structure-property relationships in systems with relatively small-magnitude spin-Hamiltonian parameters. Low-

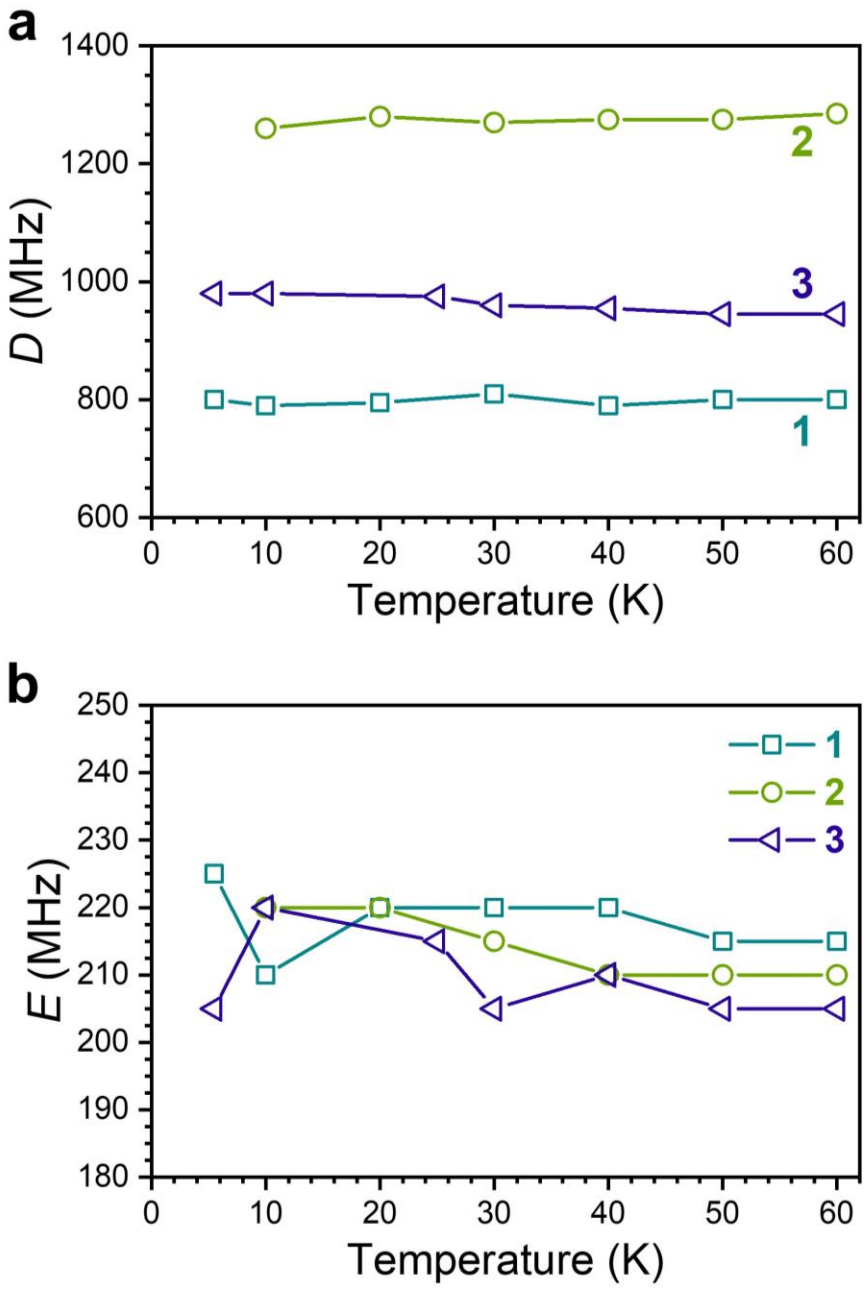

Figure 5.6. Temperature dependence of *D* and *E* from frozen solution, 9.3 GHz analyses of **1**, **2**, and **3**. (**a**) Temperature dependence of *D* values. The uncertainty in each *D* values is *ca.* 5 MHz and evaluated by eye. (**b**) Temperature dependence of the *E* values for **1**, **2**, and **3**. Uncertainties in *E* are *ca.* 10 MHz. Solid lines in both **a** and **b** are guides for the eye.

temperature high-field/frequency EPR measurements are often performed to determine the signs of *D* and *E* for high-spin complexes, though we did not need to apply that analysis here.[11] We think these data urge caution in comparing *D* values that are close between similar complexes,

particularly if the temperatures are different. Indeed, we see that the general trend in D magnitude switches from **1** < **2** < **3** at the lowest temperatures to **1** < **3** < **2** at the highest. We emphasize that the importance of this caution is largest when the general magnitudes of D, g, E, etc. are relatively small, as they are here. For example, a compound with a D value greater than 5 cm^{-1} is likely to yield spectra attributable to a greater-than-5 cm^{-1} D-value complex at low and high temperature, even with a 1000 MHz shift in spin Hamiltonian parameters, because that 1000 MHz shift is relatively small compared to the total magnitude of D (300 MHz ≅ 0.01 cm^{-1}). A complex with a *ca*. 500 MHz D value will in contrast yield spectra that appear much different.

5.5. Conclusion

The foregoing data illustrate that relatively simple transition metal complexes of Mn(II) can exhibit large temperature-dependent spin Hamiltonian parameters that eclipse the sensitivity of the NV center. In principle, understanding how to design this temperature sensitivity could be applied to developing novel means of sensing temperature through EPR imaging or optically-detected magnetic resonance. We note that the exceptional temperature sensitivities we observe are restricted to the solid state and absent in solution. These observations point toward complex-cation interactions in the crystalline state as a key driving force for engineering future, higher temperature dependences, and ligand design is likely a key part of that. To further elucidate the source of this temperature dependence, x-ray diffraction studies at low temperatures will be conducted to directly measure any changes to the molecular structure.

References

(1) Yu, C.-J.; von Kugelgen, S.; Laorenza, D. W.; Freedman, D. E. A Molecular Approach to Quantum Sensing. *ACS Cent. Sci.* **2021**, *7* (5), 712–723.

(2) Degen, C. L.; Reinhard, F.; Cappellaro, P. Quantum Sensing. *Rev. Mod. Phys.* **2017**, *89* (3), 035002.

(3) Klare, J. P. Biomedical Applications of Electron Paramagnetic Resonance (EPR) Spectroscopy. *Biomed. Spectrosc. Imaging* **2012**, No. 1, 101–124.

(4) *In Vivo EPR (ESR): Theory and Application*; Berliner, L. J., Ed.; Biological Magnetic Resonance; Springer US, 2003.

(5) Schirhagl, R.; Chang, K.; Loretz, M.; Degen, C. L. Nitrogen-Vacancy Centers in Diamond: Nanoscale Sensors for Physics and Biology. *Annu. Rev. Phys. Chem.* **2014**, *65* (1), 83–105.

(6) Kucsko, G.; Maurer, P. C.; Yao, N. Y.; Kubo, M.; Noh, H. J.; Lo, P. K.; Park, H.; Lukin, M. D. Nanometre-Scale Thermometry in a Living Cell. *Nature* **2013**, *500* (7460), 54–58.

(7) Gómez-Coca, S.; Aravena, D.; Morales, R.; Ruiz, E. Large Magnetic Anisotropy in Mononuclear Metal Complexes. *Coord. Chem. Rev.* **2015**, *289–290*, 379–392.

(8) Zheng, W.-C.; Wu, S.-Y. Theoretical Studies of the Temperature Dependence of Zero-Field Splitting of Cr^{3+} Centers in Ruby. *Phys. Rev. B* **1996**, *54* (2), 1117–1122.

(9) Xiong, Q.; Bai, G.; Zhao, M. A Theory for Pressure Dependence of Electron Paramagnetic Resonance Zero-field Splitting of $NiSiF_6 \cdot 6H_2O$. *J. Appl. Phys.* **1985**, *57* (8), 3739–3739.

(10) Üngör, Ö.; Ozvat, T. M.; Grundy, J. V.; Zadrozny, J. M. Transition Metal NMR Thermometry. In *Reference Module in Chemistry, Molecular Sciences and Chemical Engineering*; Elsevier, 2022.

(11) Krzystek, J.; Ozarowski, A.; Telser, J. Multi-Frequency, High-Field EPR as a Powerful Tool to Accurately Determine Zero-Field Splitting in High-Spin Transition Metal Coordination Complexes. *Coord. Chem. Rev.* **2006**, *250* (17), 2308–2324.

(12) Real, J. A.; Gaspar, A. B.; Muñoz, M. C. Thermal, Pressure and Light Switchable Spin-Crossover Materials. *Dalton Trans.* **2005**, No. 12, 2062–2079.

(13) Tezgerevska, T.; Alley, K. G.; Boskovic, C. Valence Tautomerism in Metal Complexes: Stimulated and Reversible Intramolecular Electron Transfer between Metal Centers and Organic Ligands. *Coord. Chem. Rev.* **2014**, *268*, 23–40.

(14) Kahn, O. *Molecular Magnetism*; VCH, 1993.

(15) Mugiraneza, S.; Hallas, A. M. Tutorial: A Beginner's Guide to Interpreting Magnetic Susceptibility Data with the Curie-Weiss Law. *Commun. Phys.* **2022**, *5* (1), 1–12.

(16) Ivády, V.; Simon, T.; Maze, J. R.; Abrikosov, I. A.; Gali, A. Pressure and Temperature Dependence of the Zero-Field Splitting in the Ground State of NV Centers in Diamond: A First-Principles Study. *Phys. Rev. B* **2014**, *90* (23), 235205.

(17) Toyli, D. M.; de las Casas, C. F.; Christle, D. J.; Dobrovitski, V. V.; Awschalom, D. D. Fluorescence Thermometry Enhanced by the Quantum Coherence of Single Spins in Diamond. *Proc. Natl. Acad. Sci. U.S.A.* **2013**, *110* (21), 8417–8421.

(18) Redko, M. Y.; Huang, R.; Dye, J. L.; Jackson, J. E. One-Pot Synthesis of 1,4,7,10,13,16,21,24-Octaazabicyclo[8.8.8]Hexacosane - The Peraza Analogue of [2.2.2]Cryptand. *Synthesis* **2006**, *2006* (5), 759–761.

(19) Smith, P. H.; Barr, M. E.; Brainard, J. R.; Ford, D. K.; Freiser, H.; Muralidharan, S.; Reilly, S. D.; Ryan, R. R.; Silks, L. A. I.; Yu, W. H. Synthesis and Characterization of Two Nitrogen-Donor Cryptands. *J. Org. Chem.* **1993**, *58* (27), 7939–7941.

(20) Alzakhem, N.; Bischof, C.; Seitz, M. Dependence of the Photophysical Properties on the Number of 2,2′-Bipyridine Units in a Series of Luminescent Europium and Terbium Cryptates. *Inorg. Chem.* **2012**, *51* (17), 9343–9349.

(21) Sheldrick, G. M. SHELXT – Integrated Space-Group and Crystal-Structure Determination. *Acta Cryst. A* **2015**, *71* (1), 3–8.

(22) Sheldrick, G. M. Crystal Structure Refinement with SHELXL. *Acta Cryst. C* **2015**, *71* (1), 3–8.

(23) Sheldrick, G. M. A Short History of SHELX. *Acta Cryst. A* **2008**, *64* (1), 112–122.

(24) Dolomanov, O. V.; Bourhis, L. J.; Gildea, R. J.; Howard, J. a. K.; Puschmann, H. OLEX2: A Complete Structure Solution, Refinement and Analysis Program. *J. Appl. Cryst.* **2009**, *42* (2), 339–341.

(25) Hassan, A. K.; Pardi, L. A.; Krzystek, J.; Sienkiewicz, A.; Goy, P.; Rohrer, M.; Brunel, L.-C. Ultrawide Band Multifrequency High-Field EMR Technique: A Methodology for Increasing Spectroscopic Information. *J. Magn. Reson.* **2000**, *142* (2), 300–312.

(26) Stoll, S.; Schweiger, A. EasySpin, a Comprehensive Software Package for Spectral Simulation and Analysis in EPR. *J. Magn. Reson.* **2006**, *178* (1), 42–55.

(27) Figgis, B. N.; Hitchman, M. A. *Ligand Field Theory and Its Applications*; Special topics in inorganic chemistry; Wiley-VCH, 2000.

(28) Tanabe, Y.; Sugano, S. On the Absorption Spectra of Complex Ions II. *J. Phys. Soc. Jpn.* **1954**, *9* (5), 766–779.

(29) Reid, H. O. N.; Kahwa, I. A.; White, A. J. P.; Williams, D. J. Intense Photosensitized Emission from Stoichiometric Compounds Featuring Mn^{2+} in Seven- and Eightfold Coordination Environments. *Inorg. Chem.* **1998**, *37* (15), 3868–3873.

(30) Hempel, J. C.; Palmer, R. A.; Yang, M. C. The Electronic Structure of Tris(Octamethylpyrophosphoramide)Manganese(II) Ion. Electronic Absorption, Emission, and Excitation Spectra of $Mn(OMPA)_3(ClO_4)_2$. *J. Chem. Phys.* **1976**, *64* (11), 4314–4320.

(31) Telser, J. Linewidth, Field, and Frequency in Electron Paramagnetic Resonance (EPR) Spectroscopy. *J. Biol. Inorg. Chem.* **2022**, *27* (7), 605–609.

(32) Pearson, T. J.; Fataftah, M. S.; Freedman, D. E. Enhancement of Magnetic Anisotropy in a Mn–Bi Heterobimetallic Complex. *Chem. Commun.* **2016**, *52* (76), 11394–11397.

(33) Jacobsen, C. J. H.; Pedersen, E.; Villadsen, J.; Weihe, H. ESR Characterization of Trans-Diacidatotetrakis(Pyridine)Vanadium and -Manganese Trans-$V^{II}(Py)_4X_2$ and Trans-$Mn^{II}(Py)_4X_2$ (X = NCS, Cl, Br, I; Py = Pyridine). *Inorg. Chem.* **1993**, *32* (7), 1216–1221.

(34) Azarkh, M.; Penkova, L. V.; Kats, S. V.; Varzatskii, O. A.; Voloshin, Y. Z.; Groenen, E. J. J. A Mononuclear Mn(II) Pseudoclathrochelate Complex Studied by Multi-Frequency Electron-Paramagnetic-Resonance Spectroscopy. *J. Phys. Chem. Lett.* **2014**, *5* (5), 886–889.

(35) L. Goodgame, D. M.; El Mkami, H.; M. Smith, G.; P. Zhao, J.; L. McInnes, E. J. High-Frequency EPR of Octahedral Mn(II) Compounds with Large Zero-Field Splittings. *Dalton Trans.* **2003**, *1*, 34–35.

(36) Duboc, C.; Collomb, M.-N.; Pécaut, J.; Deronzier, A.; Neese, F. Definition of Magneto-Structural Correlations for the Mn(II) Ion. *Eur. J. Chem.* **2008**, *14* (21), 6498–6509.

(37) Duboc, C. Determination and Prediction of the Magnetic Anisotropy of Mn Ions. *Chem. Soc. Rev.* **2016**, *45* (21), 5834–5847.

(38) Duboc, C.; Phoeung, T.; Zein, S.; Pécaut, J.; Collomb, M.-N.; Neese, F. Origin of the Zero-Field Splitting in Mononuclear Octahedral Dihalide Mn(II) Complexes: An Investigation by Multifrequency High-Field Electron Paramagnetic Resonance and Density Functional Theory. *Inorg. Chem.* **2007**, *46* (12), 4905–4916.

(39) Felton, S.; Edmonds, A. M.; Newton, M. E.; Martineau, P. M.; Fisher, D.; Twitchen, D. J. Electron Paramagnetic Resonance Studies of the Neutral Nitrogen Vacancy in Diamond. *Phys. Rev. B* **2008**, *77* (8), 081201.

(40) Simpson, D. A.; Ryan, R. G.; Hall, L. T.; Panchenko, E.; Drew, S. C.; Petrou, S.; Donnelly, P. S.; Mulvaney, P.; Hollenberg, L. C. L. Electron Paramagnetic Resonance Microscopy Using Spins in Diamond under Ambient Conditions. *Nat. Commun.* **2017**, *8* (1), 458.

(41) Duggan, D. Michael.; Hendrickson, D. N. Magnetic Exchange Interactions in Transition Metal Dimers. III. Nickel(II) Di-μ-Cyanato, Di-μ-Thiocyanato, and Di-μ-Selenocyanato Complexes and Related Outer-Sphere Copper(II) Complexes. *Inorg. Chem.* **1974**, *13* (12), 2929–2940.

(42) Solano-Peralta, A.; Saucedo-Vázquez, J. P.; Escudero, R.; Höpfl, H.; El-Mkami, H.; Smith, G. M.; Sosa-Torres, M. E. Magnetic and High-Frequency EPR Studies of an Octahedral Fe(III) Compound with Unusual Zero-Field Splitting Parameters. *Dalton Trans.* **2009**, No. 9, 1668–1674.

(43) Corzilius, B.; Michaelis, V. K.; Penzel, S. A.; Ravera, E.; Smith, A. A.; Luchinat, C.; Griffin, R. G. Dynamic Nuclear Polarization of ^{1}H, ^{13}C, and ^{59}Co in a Tris(Ethylenediamine)Cobalt(III) Crystalline Lattice Doped with Cr(III). *J. Am. Chem. Soc.* **2014**, *136* (33), 11716–11727.

(44) Misra, S. K.; Giguère, P.; Sharp, G. R. Electron Paramagnetic Resonance of Cr3+ in Guanidinium Aluminum Sulfate Hexahydrate. *J. Chem. Phys.* **1977**, *66* (4), 1758–1759.

(45) Dai, D.; Xiang, H.; Whangbo, M.-H. Effects of Spin-Orbit Coupling on Magnetic Properties of Discrete and Extended Magnetic Systems. *J. Comput. Chem.* **2008**, *29* (13), 2187–2209.

CHAPTER 6 – Exploring Metal Complexes as Microviscosity Probes for EPR

6.1. Overview

The biggest advantage of electron paramagnetic resonance imaging (EPRI) over conventional magnetic resonance imaging is its leveraging of the high sensitivity of the electron spin to the local environment. One important environmental aspect that can be detected effectively with EPRI is the microviscosity, or viscosity at the molecular level, as the rate of molecular tumbling directly affects the EPR spectrum. Herein, we present the first study measuring microviscosity with metal-based molecular probes, where we test a novel design strategy to improve the sensitivity by increasing the intrinsic magnetic anisotropy in the spin-Hamiltonian of the Mn(II) complexes [MnL1]Br_2 (**1**) and [MnL2]Br_2 (**2**). Solution-phase X-band EPR was utilized to assess the variation of rotational correlation time (τ_r) as a function of viscosity, where complex **1** produced an over two-fold increase in sensitivity over complex **2**. This study serves as a first of its kind to highlight the exciting potential of metal complexes as EPR viscosity sensing agents.

6.2. Introduction

Electron paramagnetic resonance imaging (EPRI) is the electron-spin analog of (nuclear) magnetic resonance imaging (MRI) whereby unpaired electrons are probed with low-frequency microwaves in a magnetic field in order to generate a biological image.[1–4] When comparing the two non-invasive techniques, EPRI affords greater chemical sensitivity to the local environment, having been used to detect chemical heralds of physiological dysfunction like pH,[5–7] tissue oxygenation,[2,8–10] redox status,[11–13] and microviscosity.[14–21] Combining the techniques of MRI and

EPRI would provide both anatomical and physiological images of a biological system, aiding in medical diagnostics and gaining an additional window to studying living biochemistry.

As there is a dearth of natural paramagnetic material in biological systems for EPRI, a probe species must be introduced.[1] In most cases, this exogenous probe is an organic radical, having a spin state $S = {}^1/_2$ from its one unpaired electron.[3] For these species, the large magnetic moment and the simplicity of the spin-Hamiltonian (where the Zeeman interaction is the strongest), high frequency microwaves (ca. 40 GHz), must be used to address these systems at the high magnetic fields typically used in MRI (1.5 T). As these high-frequency microwaves would be absorbed by water-rich biological tissue, causing heating and limiting penetration depth, the systems described would not be viable for implementation of EPRI with MRI.[1,22,23] To overcome this hurdle, metal complexes with multiple unpaired electrons ($S > {}^1/_2$) and zero-field splitting (ZFS, D) offer a more complex electronic structure that can produce low-frequency EPR transitions at high magnetic field.[24,25] The tunability of their electronic structures allows for optimizing metal complexes for specific sensing tasks, as well as controlling resonant field and other magnetic resonance properties. Investigations into low-frequency EPR at high magnetic field with these systems are few,[26] representing a fertile area for fundamental research.

As previously mentioned, EPRI can detect numerous environmental chemical signatures. In particular, intracellular viscosity is able to be tracked by other, well-studied spectroscopic methods like emission spectroscopy.[27–30] Though high sensitivities with fluorescent probes are possible, measuring viscosity by this technique is inherently invasive, as detecting visible-light photons requires direct imaging of the cells with no tissue in the path of the light. As a result, volumetric imaging of opaque tissue is impossible with emission spectroscopy and EPRI serves as a complimentary technique.

Measuring microviscosity via EPRI has been researched for over 20 years,[14] and many recent publications on the subject represent an increased interest in this application of EPR spectroscopy.[15,18–21] For such measurements, it becomes advantageous to conduct at lower frequencies, from both having less non-resonant absorption by water, and from the change in relaxation dynamics at lower frequencies. Under these conditions, the shorter T_1 relaxation times found by low frequency EPR measurements result in increased viscosity sensitivity, as the shortest correlation time that can be measured is limited by the electron spin's relaxation time.[16] In all of these studies, an organic radical molecule was the magnetic unit used to probe the microviscosity. The two classes of probes investigated are nitroxide radicals and isotopically enriched ^{13}C triaryl methyl (^{13}C-trityl) radicals. The former suffers from facile reduction in vivo to EPR silent hydroxylamines, and the latter requires expensive isotopically enriched starting materials to afford a measurable hyperfine interaction.[20,31] We propose that these two limitations could be easily addressed by developing metal complexes as the imaging probes.

Sensing microviscosity with EPR requires an anisotropic magnetic interaction to be present in the molecule in order to differentiate slow tumbling, where the directional dependences can be measured, and fast tumbling, where the anisotropies average out (**Figure 6.1**). Nitroxide radicals take advantage of the anisotropic hyperfine interaction between the unpaired electron and the ^{14}N nucleus (I = 1, A_x = 5.3 MHz, A_y = 9.6 MHz, A_z = 35.8 MHz), and anisotropic g-values (g_x = 2.0088, g_y = 2.0062, g_z = 2.0020).[21] Trityl radicals, on the other hand, typically have isotropic g-values (g_x = 2.0033, g_y = 2.0032, g_z = 2.00275) , and without enrichment of the methyl carbon, have no measurable hyperfine interaction.[16] However, upon enrichment to the ^{13}C-trityl species, a strongly axial hyperfine interaction (A_x = 18 MHz, A_y = 18 MHz, A_z = 160 MHz) can be leveraged to measure molecular tumbling rate, and thus microviscosity.[15,16,18–20] In metal complexes, the

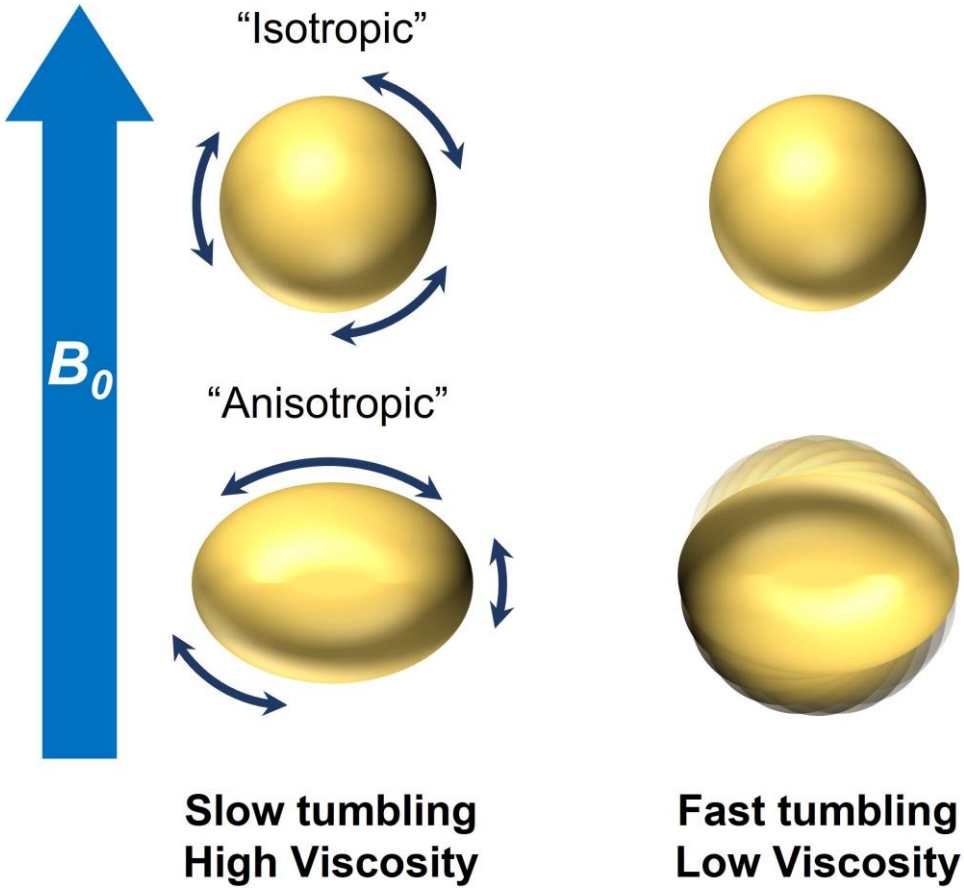

Figure 6.1. (Left) In a high viscosity system (slow molecular tumbling), an isotropic system (top, sphere) has identical EPR spectra from any orientation. An anisotropic system (bottom, prolate spheroid) has orientation dependence of its magnetic properties, resulting in EPR spectra that are different depending on the system's orientation. (Right) In a low viscosity system (fast molecular tumbling), the molecular orientations are averaged out. In the isotropic system, there is no change to the EPR spectra. In the anisotropic system, the spectra change, producing a viscosity dependent EPR spectra.

anisotropy of the *g*-values and the hyperfine interaction can be easily controlled via judicious ligand choice, one can envision it a simple task to have a complex that is sensitive to microviscosity. In fact, anisotropy in the *g*-tensor has been as great as $g_x = 0.53$, $g_y = 0.59$, and $g_z = 7.57$,[32] typical hyperfine anisotropy can be over a range of $A_x = 313$ MHz, $A_y = 363$ MHz, $A_z = 60$ MHz,[33] but get as high as 3,500 MHz.[34] In addition, the presence of axial and transverse zero-field splitting in $S > {}^1/_2$ systems presents another facet of magnetic anisotropy only found in metal complexes. As there are a multitude of air/water stable, paramagnetic oxidation states in first-row

transition metal ions (Cr^{3+}, Mn^{2+}, $Fe^{2/3+}$, Co^{2+}, Ni^{2+}, Cu^{2+}), as well as multiple elements with near 100% abundance of nuclear spin isotopes (^{51}V, ^{55}Mn, ^{59}Co, $^{63/65}Cu$), metal complexes are ideal candidates for this measurement technique (**Figure 6.2**).

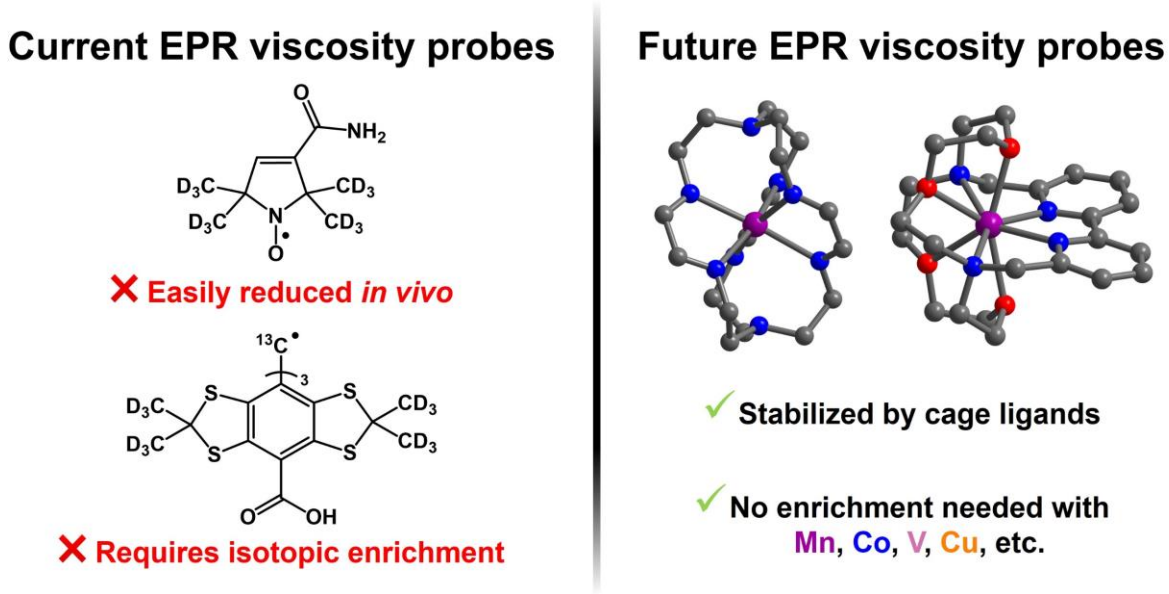

Figure 6.2. (Left) Depictions of two examples of state of the art EPRI viscosity probes (refs. 14 and 15). (Right) Depictions the two viscosity probe molecular complexes discussed in this chapter and their advantages over the traditional molecules on the left.

Towards this goal, we perform the first study of using metal complexes to measure solution microviscosity with EPR. We aimed to test 1) to what degree magnetic anisotropy plays a role in viscosity sensitivity and 2) if metal complexes can be as measurably sensitive as the state-of-the-art organic radical probes. Two Mn(II) clathrochelate complexes [Mn(L1)]Br_2 (**1**, L1 = 1,4,7,10,13,16,21,24-Octaazabicyclo[8.8.8]hexacosa-4,6,13,15,21,23-hexaene) and [Mn(L2)]Br2 (**2**, L2 = 17,20,25,28-Tetraoxa-1,14,31,32-tetraazatetracyclo [12.8.8.13,7.18,12] dotriaconta-3,5,7(32),8,10,12(31)-hexaene) were investigated where the inner coordination sphere geometry varied drastically (**Figure 6.3**). In **1**, relatively symmetric imino binding groups sequester the Mn(II) in the cage-like ligand, affording an apparent *less* anisotropic coordination sphere. Note that we do not assign this structure to be isotropic, as the coordination environment is not perfectly

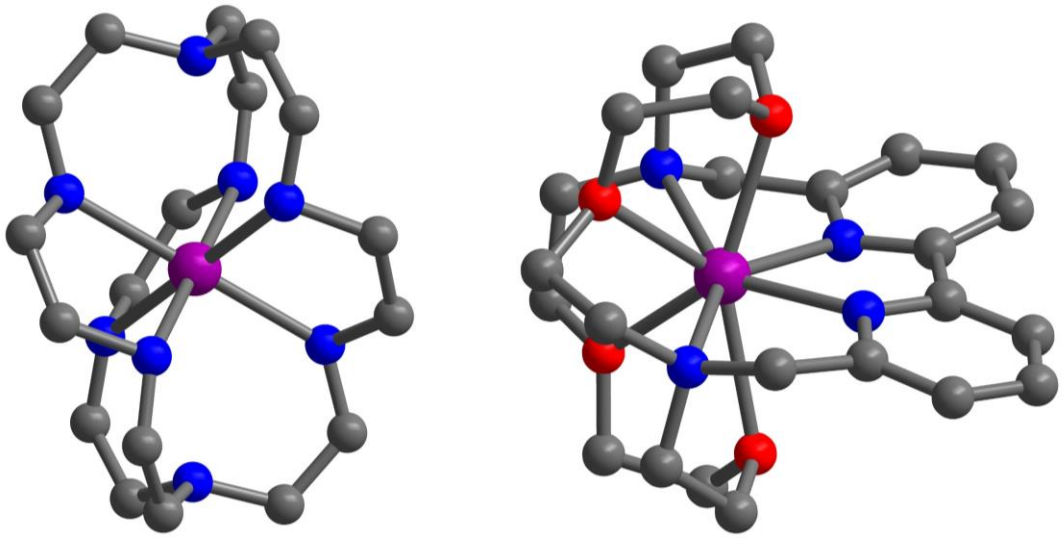

Figure 6.3. Crystal structures of $[MnL1]^{2+}$ (**1**) and $[MnL2]^{2+}$ (**2**) as determined from single-crystal x-ray diffraction. Purple, red, blue, and gray spheres represent Mn, O, N, and C atoms, respectively. Hydrogen atoms, solvents of crystallization, and Br^- counterions have been omitted for clarity.

symmetrical. In **2**, L2 provides a bipyridine binding unit, two tertiary amine groups, and four ether groups as potential binding units, which we anticipated would produce *more* anisotropic coordination sphere. Mn(II) ($S = {}^5/_2$) was picked as the metal ion due to its stability in ambient and aqueous conditions and the 100% abundance of the ^{55}Mn isotope ($I = {}^5/_2$) to produce a strong hyperfine interaction. We hypothesized that the more anisotropic coordination sphere in **2** would produce a more sensitive viscosity probe when measured with EPR.

6.3. Experimental Section

6.3.1. General Considerations

L1 and L2 were synthesized following published procedures.[35,36] Methanol (MeOH), ethanol, (EtOH), diethyl ether (Et_2O), acetone, $MnCl_2{\bullet}4H_2O$, and $MnBr_2{\bullet}4H_2O$ were purchased

and used as received. UV-Vis spectra were collected with a Shimadzu UV-2600i UV-Vis-NIR spectrophotometer and standard quartz cuvettes of 1 cm path length.

6.3.2. Preparation of compounds

Synthesis of [Mn(L1)]Br_2 (**1**). A solution of L1 (0.317 g, 0.888 mmol) in 10 mL of EtOH was combined with a solution of $MnBr_2$•$4H_2O$ (254 mg, 0.888 mmol) in 5 mL of EtOH and allowed to stir for 18 hours at room temperature. The pale yellow precipitant was filtered, dissolved in a minimum amount of MeOH, and recrystallized by vapor diffusion with Et_2O to yield **1** as a polycrystalline powder (485 mg, 0.846 mmol, 95% yield). Single crystals suitable for x-ray diffraction were achieved by the vapor diffusion of Et_2O into a concentrated methanol solution of **1** at −20 C. See **Figure A5.4** for UV-vis characterization.

Synthesis of [Mn(L2)]Br_2 (**2**). A solution of $MnCl_2$•$4H_2O$ (0.2502 g, 1.2643 mmol) in 30 mL of MeOH was combined with a 30 mL EtOH solution of [(L2)Na]Br (0.6672 g, 1.2232 mmol), and stirred at 60˚C overnight at room temperature. A small amount of white precipitant was filtered off. The filtrate was concentrated by rotary evaporator yielding a white powder. This was dissolved in a minimum amount (10 mL) of EtOH and added to 10 mL of an EtOH solution saturated with NH_4PF_6. A very pale orange powder immediately precipitated, which was collected by vacuum filtration and washed with EtOH. From the resulting PF_6^- salt, 140 mg was dissolved in 2 mL of acetone. In a separate vial, 2 mL of a concentrated tetrabutylammonium bromide solution in acetone was prepared, and they were combined. A colorless precipitant immediately formed, and was allowed to stir for 1 hour at room temperature. The suspension was filtered, washed with acetone, and dissolved in 4 mL of MeOH. Colorless-orange crystals of **2** were grown by the vapor

diffusion of the MeOH solution with Et_2O (84 mg, 0.128 mmol). See **Figure A5.4** for UV-vis characterization.

6.3.3. X-ray Data Collection, Structure Solution and Refinement for **1** and **2**.

Single-crystal x-ray diffraction data were collected at the x-ray diffraction facility in Analytical Resources Core at Colorado State University. Data for **1** and **2** were collected on a Bruker D8 Quest ECO single-crystal x-ray diffractometer with MoKα (λ = 0.71073 Å) radiation. Data were collected and integrated using Bruker Apex 4 software. Absorption corrections were applied using SADABS. Space group assignments were determined by examination of systematic absences, E-statistics, and successive refinement of the structures. Crystal structures were solved using SHELXT[37] and refined with successive difference Fourier maps by SHELXL[38,39] operated in conjunction with OLEX2 software.[40] None of the crystals demonstrated decay by x-ray radiation over the course of the experiment. All non-hydrogen atoms were refined anisotropically. Hydrogen atoms were placed in ideal positions and refined using a riding model for all structures. In **2**, a disordered methanol solvent molecule was modeled over a special position.

6.3.4. EPR Measurements and Analyses

Solutions for variable viscosity EPR measurements were prepared at a concentration of 5 mM in water/glycerol mixtures. Viscosity values were determined for room temperature solutions (293 K). A MATLAB function created by Volk[41] was used to calculate exact viscosity values based on the mass fractions of water and glycerol. Water was obtained from a Milli-Q system and sparged with nitrogen for 30 minutes. Glycerol was also sparged with nitrogen for 30 minutes prior to mixing. When samples of each complex were dissolved, they were loaded into 2 mm OD quartz

mark-tubes (Hilgenberg), sealed with high vacuum grease, and each tube was subsequently placed into a 5 mm OD quartz EPR tube for measurement. EPR spectra were collected with a Bruker ELEXSYS ESR-500 X-band EPR spectrometer (Bruker Biospin, Rheinstetten, Germany) equipped with the high-sensitivity probe. For frozen solution measurements, a helium cryostat was used (Oxford Coldedge). All spectra were analyzed with the program EasySpin[42] and modeled by the spin-Hamiltonian and broadening mechanisms reported in the main text.

6.4. Results and Discussion

Complex **1** was synthesized by the facile combination of $MnBr_2 \cdot 4H_2O$ and L1 in ethanol, affording a pale yellow precipitant that could be crystallized from methanol. The PF_6^- salt of complex **2** was utilized in a prior study (see Chapter 5) and a small amount was subsequently converted to the bromide salt via a salt metathesis reaction with tetrabutylammonium bromide. Interestingly, we found that when attempting to isolate these complexes as chloride salts, we instead isolated crystal structures of the $[MnCl_4]^{2-}$ salts. Owing to the presence of two possible sources of an EPR signal and potential convolution of subsequent EPR analyses, we instead isolated **1** and **2** as bromide salts, where we avoided the problem.

EPR analyses of **1** and **2** in varied-viscosity solutions were performed to assess each complex's ability to spectroscopically detect microviscosity through changes in their molecular tumbling rates. The 5 mM solutions of **1** and **2** were prepared ranging from 1 cP (100% H_2O, 0% glycerol) to 711 cP (2% H_2O, 98% glycerol) and measured as room temperature solutions using continuous wave X-band EPR spectroscopy. In low viscosity solutions, both complexes produced relatively symmetric six-line spectra that are typical of isotropic Mn^{2+} systems (**Figures 6.4, A5.1**). As the tumbling rate is fast in low viscosity solutions, any anisotropies in *g*-values, *A*-values, or

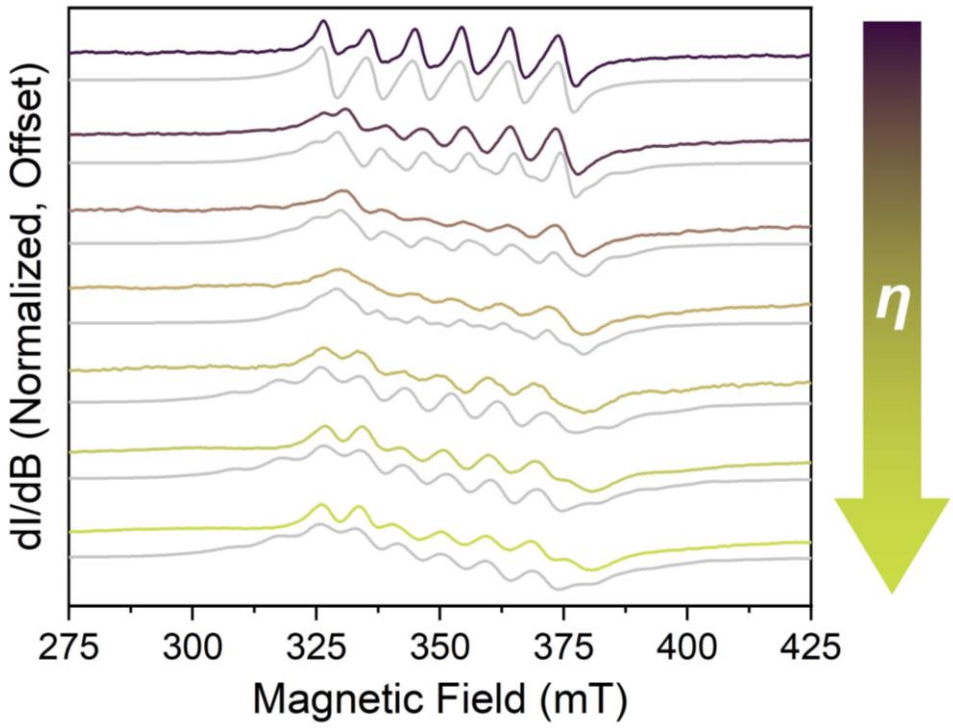

Figure 6.3. Viscosity dependent EPR spectra of **1** collected at X-band (9.8 GHz). Viscosities varied from 1 cP (top) to 711 cP (bottom). Experimental spectra are colored, and the spectral simulations are in gray. Simulation parameters are found in **Table A5.3**.

zero-field splitting (D) are averaged. As the viscosity of the solutions is increased, new features become more apparent, in particular the peak-to-peak spacing decreases and a seventh peak appears at the high-field end of the spectra, both are likely arising from the anisotropies in the spin-Hamiltonian becoming apparent from slower molecular tumbling.

To determine how viscosity effects the molecular tumbling rate, the EPR spectra were fit using the EasySpin[42] program. The function "chili" was used as it supports a wide range of correlation times and higher-spin ($S > {}^1/_2$) systems. The following spin-Hamiltonian was used to model the spectra:

$$\hat{H} = \mu_B g \boldsymbol{B}\hat{\boldsymbol{S}} + \hat{\boldsymbol{S}} D \hat{\boldsymbol{S}} + \hat{I} A \hat{\boldsymbol{S}}$$

Here, μ_B is the Bohr magneton, g is the anisotropic g factor, $\boldsymbol{B}$ is the applied magnetic field, $\hat{\boldsymbol{S}}$ is the electronic spin, D is the axial zero-field splitting, A is the hyperfine coupling constant, $\hat{I}$ is the

nuclear spin. Included in the simulation is the rotational correlation time (τ_r), which contributes to the overall spectral shape and broadness, and varies as a direct result of the solution microviscosity. The best fit simulation parameters are listed in **Tables A5.3-5.4** and fall in expected ranges consistent with other Mn(II) systems.[43–46]

As viscosity increased, τ_r also increased, implying that in solutions with higher viscosity, the molecules were tumbling at a slower rate. For **1**, τ_r was found to be 1000 ns in the 711 cP solution and fell to 0.562 ns in the 1.00 cP solution. Similarly, the τ_r for **2** fell from 298 ns to 0.891 ns. To quantify the sensitivity, we examined the relationship between τ_r and viscosity (**Figure 6.5**). Analysis of the data reveals that **1** has a sensitivity of 1.42 ns/cP and **2** has a sensitivity of 0.564 ns/cP, indicating that **1** is a more sensitive viscosity probe.

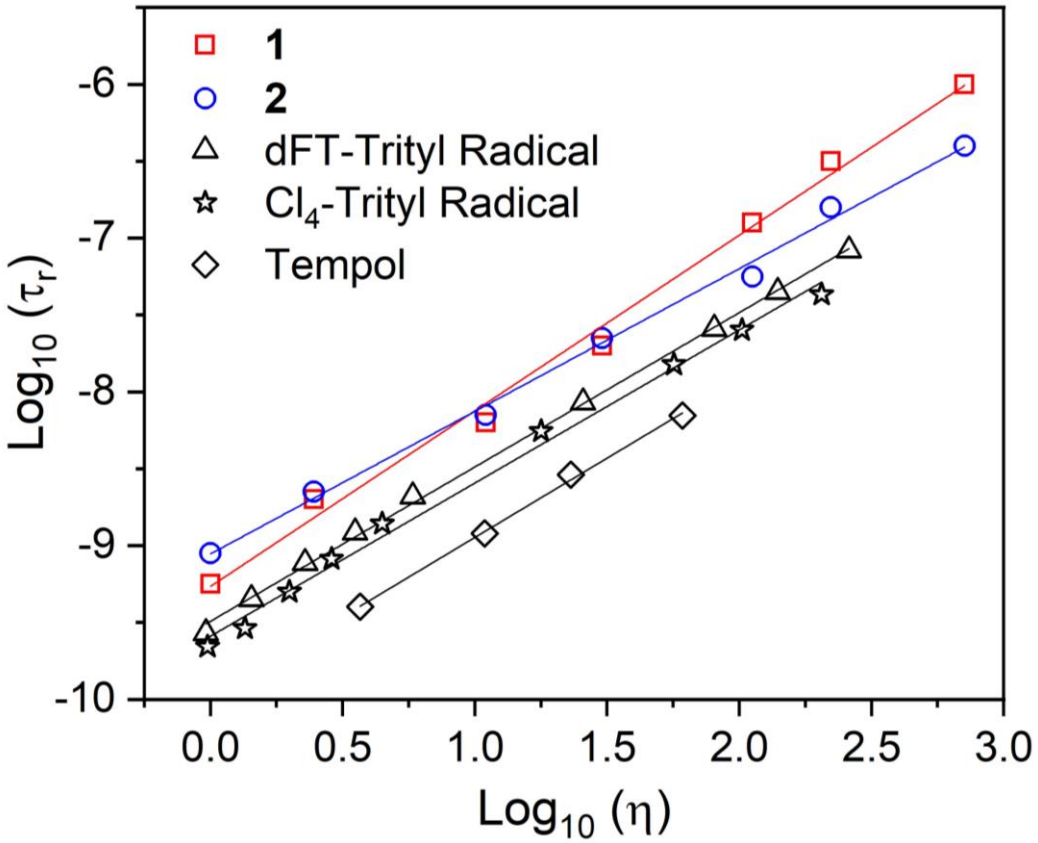

Figure 6.5. Plot of rotational correlation time (τ_r) as a function of solution viscosity (η) as determined from EPR for **1**, **2**, and selected radical EPR probes from previous studies. Slopes of the best-fit lines are discussed in the main text. It should be noted that the data are plotted on a Log-Log scale, where the differences in slope appear to be less than on a linear scale.

Upon initial inspection, **1** was predicted to be *less* sensitive to viscosity due to the fact it had a more "symmetrical" coordination environment. However, these results indicate that **1** is more sensitive, suggesting that the initial conception of a symmetrical coordination environment may not correlate with an isotropic spin-Hamiltonian. In order to quantify the degree of anisotropy in these complexes, EPR spectra were obtained in frozen glass solutions of **1** and **2** at 10 K (30% water, 70% glycerol). By measuring the complexes under these conditions, the degree of anisotropy can be determined as the molecules would not be moving, thus there would be no spectral averaging.

The frozen solution EPR spectra are displayed in **Figures A5.2-5.3**. Complex **1** produced a sharp seven-line spectra, consistent with the Mn(II) ion with zero-field splitting, whereas complex **2** produced a broader, six-line spectra, albeit the low field peak likely was the convolution of two smaller features akin to a seven-line spectra. Simulations in EasySpin were conducted to extrapolate the spin-Hamiltonian parameters. Since the spectra were frozen, the function "Pepper" was used, and the best fit parameters are found in **Table A5.5**. To assess the degree of anisotropy in the spin-Hamiltonian parameters, we can first consider the $|E/D|$ ratio, which is often used to quantify the degree of rhombic symmetry, where a greater ratio would imply a greater degree of anisotropy in the zero-field splitting.[47] This ratio is 0.28 for **1** and 0.22 for **2**, corroborating the results in relative viscosity sensitivity. As an additional measure, the range of *g*-values or *A*-values may also be useful metrics for assessing the degree of anisotropy these complexes. Here, the range of *g*-values is 0.029 for **1** and 0.007 for **2**, and the range of *A*-values is 30 MHz for **1** and 25 MHz for **2**, which both corroborate the results in relative viscosity sensitivity. Despite appearing more symmetrical by the initial inspection, complex **1** has a more anisotropic spin-Hamiltonian, and that larger anisotropy corresponds to an increased viscosity sensitivity.

Finally, we aimed to assess how the viscosity sensitivities of **1** and **2** compare to that of other known EPR probes from similar studies. Three additional radical-based probes were selected: the dFT-trityl radical,[15] Cl_4-trityl radical,[18] and the Tempol nitroxide radical.[21] The published data are plotted alongside the data from this study in **Figure 6.5**, where the sensitivities for the additional probes from the best-fit lines are 0.320, 0.215, and 0.115 ns/cP, respectively. Excitingly, our metal complex probes outperform all of these recent studies with their sensitivity values of 1.42 ns/cP for **1** and 0.564 ns/cP for **2**, demonstrating the potential metal complexes to be effective EPR probes for sensing microviscosity.

6.5. Conclusion

Herein, we describe the first investigation into the use of metal complexes as viscosity sensitive EPR probes, where we describe how increasing the anisotropy of the spin-Hamiltonian is an effective design strategy for increasing the sensitivity of EPR measurements to viscosity. Interestingly, the degree of anisotropy in the spin-Hamiltonian did not appear to correlate with the apparent molecular symmetry of the coordination sphere, suggesting that judiciously designing a ligand to maximize the asymmetry requires more than just having different types of binding groups to the metal. Computational insight may be required to definitively describe how L1 imparts a more anisotropic spin-Hamiltonian on the Mn(II) center. Broadly, these findings illustrate the potential for metal complexes to improve upon the viscosity sensitivity of the state-of-the-art radical systems. Future directions to improve these systems further will include increasing the size of the molecule, by designing similar ligand environments with long alkyl chains appended to the structure, to take advantage of the direct relationship between correlation time and molecular volume in the Stokes-Einstein equation.

References

(1) Danhier, P.; Gallez, B. Electron Paramagnetic Resonance: A Powerful Tool to Support Magnetic Resonance Imaging Research. *Contrast Media Mol. Imaging* **2015**, *10* (4), 266–281.

(2) *EPR Imaging and in Vivo EPR*, 1st ed.; Gareth R. Eaton, Sandra S. Eaton, Keiichi Ohno, Eds.; CRC Press, 2018.

(3) Lawrence J. Berliner; Sandra S. Eaton; Gareth R. Eaton. *Biological Magnetic Resonance: Distance Measurements in Biological Systems by EPR*; Springer US, 2001; Vol. 19.

(4) Gallez, B.; Swartz, H. M. In Vivo EPR: When, How and Why? *NMR Biomed.* **2004**, *17* (5), 223–225.

(5) Voinov, M. A.; Polienko, J. F.; Schanding, T.; Bobko, A. A.; Khramtsov, V. V.; Gatilov, Y. V.; Rybalova, T. V.; Smirnov, A. I.; Grigor'ev, I. A. Synthesis, Structure, and X-Band (9.5 GHz) EPR Characterization of the New Series of pH-Sensitive Spin Probes: N,N-Disubstituted 4-Amino-2,2,5,5-Tetramethyl-3-Imidazoline 1-Oxyls. *J. Org. Chem.* **2005**, *70* (24), 9702–9711.

(6) Voinov, M. A.; Scheid, C. T.; Kirilyuk, I. A.; Trofimov, D. G.; Smirnov, A. I. IKMTSL-PTE, a Phospholipid-Based EPR Probe for Surface Electrostatic Potential of Biological Interfaces at Neutral PH: Effects of Temperature and Effective Dielectric Constant of the Solvent. *J. Phys. Chem. B* **2017**, *121* (11), 2443–2453.

(7) Gallez, B.; Mader, K.; Swartz, H. M. Noninvasive Measurement of the PH inside the Gut by Using PH-Sensitive Nitroxides. An in Vivo EPR Study. *Magn. Reson. Med.* **1996**, *36* (5), 694–697.

(8) Demsar, F.; Walczak, T.; Morse, P. D.; Bačić, G.; Zolnai, Z.; Swartz, H. M. Detection of Diffusion and Distribution of Oxygen by Fast-Scan EPR Imaging. *J. Magn. Reson.* **1988**, *76* (2), 224–231.

(9) Subczynski, W. K.; Swartz, H. M. EPR Oximetry in Biological and Model Samples. In *Biomedical EPR, Part A: Free Radicals, Metals, Medicine, and Physiology*; Eaton, S. R., Eaton, G. R., Berliner, L. J., Eds.; Biological Magnetic Resonance; Springer US: Boston, MA, 2005; pp 229–282.

(10) James, P. E.; Swartz, H. M. Simultaneous Detection of PO2 and NO by Electron Paramagnetic Resonance. In *Methods in Enzymology*; Nitric Oxide, Part D: Oxide Detection, Mitochondria and Cell Functions, and Peroxynitrite Reactions; Academic Press, 2002; Vol. 359, pp 52–66.

(11) Caia, G. L.; Efimova, O. V.; Velayutham, M.; El-Mahdy, M. A.; Abdelghany, T. M.; Kesselring, E.; Petryakov, S.; Sun, Z.; Samouilov, A.; Zweier, J. L. Organ Specific Mapping of in Vivo Redox State in Control and Cigarette Smoke-Exposed Mice Using EPR/NMR Co-Imaging. *J. Magn. Reson.* **2012**, *216*, 21–27.

(12) Hyodo, F.; Murugesan, R.; Matsumoto, K.; Hyodo, E.; Subramanian, S.; Mitchell, J. B.; Krishna, M. C. Monitoring Redox-Sensitive Paramagnetic Contrast Agent by EPRI, OMRI and MRI. *J. Magn. Reson.* **2008**, *190* (1), 105–112.

(13) Epel, B.; Sundramoorthy, S. V.; Krzykowska-Serda, M.; Maggio, M. C.; Tseytlin, M.; Eaton, G. R.; Eaton, S. S.; Rosen, G. M.; Kao, J. P. Y.; Halpern, H. J. Imaging Thiol Redox Status in Murine Tumors In Vivo with Rapid-Scan Electron Paramagnetic Resonance. *J. Magn. Reson.* **2017**, *276*, 31–36.

(14) Halpern, H. J.; Chandramouli, G. V. R.; Barth, E. D.; Yu, C.; Peric, M.; Grdina, D. J.; Teicher, B. A. Diminished Aqueous Microviscosity of Tumors in Murine Models Measured with in Vivo Radiofrequency Electron Paramagnetic Resonance. *Cancer Res.* **1999**, *59* (22), 5836–5841.

(15) Poncelet, M.; Driesschaert, B. A ^{13}C-Labeled Triarylmethyl Radical as an EPR Spin Probe Highly Sensitive to Molecular Tumbling. *Angew. Chem. Int. Ed.* **2020**, *59* (38), 16451–16454.

(16) Owenius, R.; Eaton, G. R.; Eaton, S. S. Frequency (250MHz to 9.2GHz) and Viscosity Dependence of Electron Spin Relaxation of Triarylmethyl Radicals at Room Temperature. *J. Magn. Reson.* **2005**, *172* (1), 168–175.

(17) Shin, C. S.; Dunnam, C. R.; Borbat, P. P.; Dzikovski, B.; Barth, E. D.; Halpern, H. J.; Freed, J. H. ESR Microscopy for Biological and Biomedical Applications. *Nanosci. Nanotechnol. Lett* **2011**, *3* (4), 561–567.

(18) Huffman, J. L.; Poncelet, M.; Moore, W.; Eaton, S. S.; Eaton, G. R.; Driesschaert, B. Perchlorinated Triarylmethyl Radical 99% Enriched ^{13}C at the Central Carbon as EPR Spin Probe Highly Sensitive to Molecular Tumbling. *J. Phys. Chem. B* **2021**, *125* (27), 7380–7387.

(19) Velayutham, M.; Poncelet, M.; Eubank, T. D.; Driesschaert, B.; Khramtsov, V. V. Biological Applications of Electron Paramagnetic Resonance Viscometry Using a ^{13}C-Labeled Trityl Spin Probe. *Molecules* **2021**, *26* (9), 2781.

(20) Poncelet, M.; Ngendahimana, T.; Gluth, T. D.; Hoblitzell, E. H.; Eubank, T. D.; Eaton, G. R.; Eaton, S. S.; Driesschaert, B. Synthesis and Characterization of a Biocompatible $^{13}C_1$ Isotopologue of Trityl Radical OX071 for in Vivo EPR Viscometry. *Analyst* **2022**, *147* (24), 5643–5648.

(21) Clark, A.; Sedhom, J.; Elajaili, H.; Eaton, G. R.; Eaton, S. S. Dependence of Electron Paramagnetic Resonance Spectral Lineshapes on Molecular Tumbling: Nitroxide Radical in Water:Glycerol Mixtures. *Concepts Magn. Reson. Part A* **2016**, *45A* (5), e21423.

(22) Hitchcock, R. T. *Radio-Frequency and Microwave Radiation*; AIHA, 2004.

(23) Röschmann, P. Radiofrequency Penetration and Absorption in the Human Body: Limitations to High-Field Whole-Body Nuclear Magnetic Resonance Imaging: RF Penetration/Absorption Limitations on Whole-Body MRI. *Med. Phys.* **1987**, *14* (6), 922–931.

(24) Figgis, B. N.; Hitchman, M. A. *Ligand Field Theory and Its Applications*; Special topics in inorganic chemistry; Wiley-VCH, 2000.

(25) Griffith, J. S. *The Theory of Transition-Metal Ions*; Cambridge University Press, 1964.

(26) Campanella, A. J.; Üngör, Ö.; Zadrozny, J. M. Quantum Mimicry With Inorganic Chemistry. *Comments Inorg. Chem.* **2023**.

(27) Levitt, J. A.; Kuimova, M. K.; Yahioglu, G.; Chung, P.-H.; Suhling, K.; Phillips, D. Membrane-Bound Molecular Rotors Measure Viscosity in Live Cells via Fluorescence Lifetime Imaging. *J. Phys. Chem. C* **2009**, *113* (27), 11634–11642.

(28) Requena, S.; Ponomarchuk, O.; Castillo, M.; Rebik, J.; Brochiero, E.; Borejdo, J.; Gryczynski, I.; Dzyuba, S. V.; Gryczynski, Z.; Grygorczyk, R.; Fudala, R. Imaging Viscosity of Intragranular Mucin Matrix in Cystic Fibrosis Cells. *Sci. Rep.* **2017**, *7* (1), 16761.

(29) Kuimova, M. K.; Botchway, S. W.; Parker, A. W.; Balaz, M.; Collins, H. A.; Anderson, H. L.; Suhling, K.; Ogilby, P. R. Imaging Intracellular Viscosity of a Single Cell during Photoinduced Cell Death. *Nature Chem.* **2009**, *1* (1), 69–73.

(30) Puchkov, E. O. Intracellular Viscosity: Methods of Measurement and Role in Metabolism. *Biochem. Moscow Suppl. Ser. A* **2013**, *7* (4), 270–279.

(31) Bobko, A. A.; Kirilyuk, I. A.; Grigor'ev, I. A.; Zweier, J. L.; Khramtsov, V. V. Reversible Reduction of Nitroxides to Hydroxylamines: Roles for Ascorbate and Glutathione. *Free Radic. Biol. Med.* **2007**, *42* (3), 404–412.

(32) Bar, A. K.; Pichon, C.; Sutter, J.-P. Magnetic Anisotropy in Two- to Eight-Coordinated Transition–Metal Complexes: Recent Developments in Molecular Magnetism. *Coord. Chem. Rev.* **2016**, *308*, 346–380.

(33) Jackson, C. E.; Lin, C.-Y.; van Tol, J.; Zadrozny, J. M. Orientation Dependence of Phase Memory Relaxation in the V(IV) Ion at High Frequencies. *Chem. Phys. Lett.* **2020**, *739*, 137034.

(34) Kundu, K.; White, J. R. K.; Moehring, S. A.; Yu, J. M.; Ziller, J. W.; Furche, F.; Evans, W. J.; Hill, S. A 9.2-GHz Clock Transition in a Lu(II) Molecular Spin Qubit Arising from a 3,467-MHz Hyperfine Interaction. *Nat. Chem.* **2022**, *14* (4), 392–397.

(35) Smith, P. H.; Barr, M. E.; Brainard, J. R.; Ford, D. K.; Freiser, H.; Muralidharan, S.; Reilly, S. D.; Ryan, R. R.; Silks, L. A. I.; Yu, W. H. Synthesis and Characterization of Two Nitrogen-Donor Cryptands. *J. Org. Chem.* **1993**, *58* (27), 7939–7941.

(36) Alzakhem, N.; Bischof, C.; Seitz, M. Dependence of the Photophysical Properties on the Number of 2,2′-Bipyridine Units in a Series of Luminescent Europium and Terbium Cryptates. *Inorg. Chem.* **2012**, *51* (17), 9343–9349.

(37) Sheldrick, G. M. SHELXT – Integrated Space-Group and Crystal-Structure Determination. *Acta Cryst. A* **2015**, *71* (1), 3–8.

(38) Sheldrick, G. M. Crystal Structure Refinement with SHELXL. *Acta Cryst. C* **2015**, *71* (1), 3–8.

(39) Sheldrick, G. M. A Short History of SHELX. *Acta Cryst. A* **2008**, *64* (1), 112–122.

(40) Dolomanov, O. V.; Bourhis, L. J.; Gildea, R. J.; Howard, J. a. K.; Puschmann, H. OLEX2: A Complete Structure Solution, Refinement and Analysis Program. *J. Appl. Cryst.* **2009**, *42* (2), 339–341.

(41) Volk, A.; Kähler, C. J. Density Model for Aqueous Glycerol Solutions. *Exp. Fluids* **2018**, *59* (5), 75.

(42) Stoll, S.; Schweiger, A. EasySpin, a Comprehensive Software Package for Spectral Simulation and Analysis in EPR. *J. Magn. Reson.* **2006**, *178* (1), 42–55.

(43) Pearson, T. J.; Fataftah, M. S.; Freedman, D. E. Enhancement of Magnetic Anisotropy in a Mn–Bi Heterobimetallic Complex. *Chem. Commun.* **2016**, *52* (76), 11394–11397.

(44) Jacobsen, C. J. H.; Pedersen, E.; Villadsen, J.; Weihe, H. ESR Characterization of Trans-Diacidatotetrakis(Pyridine)Vanadium and -Manganese Trans-$V^{II}(Py)_4X_2$ and Trans-$Mn^{II}(Py)_4X_2$ (X = NCS, Cl, Br, I; Py = Pyridine). *Inorg. Chem.* **1993**, *32* (7), 1216–1221.

(45) Azarkh, M.; Penkova, L. V.; Kats, S. V.; Varzatskii, O. A.; Voloshin, Y. Z.; Groenen, E. J. J. A Mononuclear Mn(II) Pseudoclathrochelate Complex Studied by Multi-Frequency Electron-Paramagnetic-Resonance Spectroscopy. *J. Phys. Chem. Lett.* **2014**, *5* (5), 886–889.

(46) L. Goodgame, D. M.; El Mkami, H.; M. Smith, G.; P. Zhao, J.; L. McInnes, E. J. High-Frequency EPR of Octahedral Mn(II) Compounds with Large Zero-Field Splittings. *Dalton Trans.* **2003**, *0* (1), 34–35.

(47) Petasis, D. T.; Hendrich, M. P. Chapter Eight - Quantitative Interpretation of Multifrequency Multimode EPR Spectra of Metal Containing Proteins, Enzymes, and Biomimetic Complexes. In *Methods in Enzymology*; Qin, P. Z., Warncke, K., Eds.; Electron Paramagnetic Resonance Investigations of Biological Systems by Using Spin Labels, Spin Probes, and Intrinsic Metal Ions, Part A; Academic Press, 2015; Vol. 563, pp 171–208.

CHAPTER 7 – Summary

This dissertation describes five studies aimed at furthering the utility of metal-based probes for EPRI. Electron spins are extremely sensitive to their local environment, an attribute that can be leveraged for sensing local physiology and aiding in non-invasive medical diagnostics. Investigations over the past 30 years toward this goal have utilized molecular organic radicals as sensing probes. However, limitations of these systems, in particular their incompatibility with high magnetic field measurements, prove that new systems must be investigated. The unique electronic structures of paramagnetic metal complexes may allow for the combination of safe low-frequency EPR measurements at high magnetic fields. Yet, prior to the studies in this dissertation, there was little fundamental insight into the spectral behavior of metal complexes in this regime, and how that spectral behavior can be controlled through synthetic chemistry.

To illuminate this blind spot in magnetic resonance and bring metal complexes closer to implementation for EPRI, several aspects of molecular design were investigated. They were 1) *how to sharpen EPR spectral linewidths through judicious ligand choice*, 2) *how to control zero-field splitting through ligand functional group in robust clathrochelate complexes*, 3) *how molecular structure can afford a temperature sensitive electronic structure*, and 4) *how to improve environmental sensitivity through ligand structure changes*. Each one of these facets was explored and has provided novel insight for the magnetic resonance properties of metal complexes. Firstly, towards sharpening EPR spectral linewidth, our initial report suggested that a more distorted coordination environment favors a sharper spectrum. However, further experimental insight disproved this hypothesis. Several additional spectroscopic and computational studies were conducted, eliminating key alternative hypotheses. The results suggest that the second

coordination sphere or environmental nuclear spins may play a key role, and as further developments in low-frequency instrumentation are made, key experiments can be conducted to test this hypothesis. Second, a robust cage ligand was investigated to assess the degree that zero-field splitting is tunable from several bonds away from the metal center. This unique ligand enforced an unusual trigonal prismatic geometry and resulted in large changes in zero-field splitting with small chemical augmentations from multiple bonds away. Third, we explored how temperature sensitivity of the zero-field splitting varied as a function of ligand and the measurement environment, which was found to be greater than the nitrogen vacancy center. Further probing of this temperature sensitivity found that it was only present in the solid state, indicating temperature dependent structural changes are likely the cause behind the changes in zero-field splitting. Finally, sensing microviscosity with EPR and a metal complex probe is a key demonstration of the utility of these molecules towards the goal of bioimaging. We determined that increasing magnetic anisotropy results in increasing viscosity sensitivity, a key design principle that can be used going forward to design the next generation of metal-based EPR probes for viscosity.

This work is envisioned as laying a foundation for advancing metal-based EPR and its applications. Further research to study more pronounced structural distortions may lead to increased clarity as to the nature of spectral broadening, as the Cr(III) complexes initially investigated were rather similar. To explore additional tunable ligand systems that afford smaller zero-field splitting, the next robust ligand system that is of interest is the pentapyridyl ligand described by Zadrozny et. al in 2010. The open coordination site this ligand affords will allow for systematic studies of the electronic structure by varying the binding group at the open site. Lastly,

to explore environmental sensing, other chemical signatures, like pH, will be investigated to assess how the protonation state of the ligand affects the EPR properties of the metal center.

Appendix 1: Supporting Information for Chapter 2

Appendix Table 1.1. Crystallographic information for the structural refinement of **1**.

Empirical formula	$C_{96}H_{138}Cl_6Cr_2N_{12}O_9S_2$
Formula weight	1985.00 g/mol
Temperature	100.02 K
Crystal system	Monoclinic
Space group	$P2_1$
a	12.3901(5) Å
b	19.3151(8) Å
c	24.4122(11) Å
α	90°
β	104.287(2)°
γ	90°
Volume	5661.5(4) Å^3
Z	2
ρ_{calc}	1.164 g cm^{-3}
μ	0.424 mm^{-1}
F(000)	2104.0
Crystal color	Orange
Crystal size	0.224 × 0.151 × 0.086 mm^3
Radiation	MoKα (λ = 0.71073 Å)
2θ range for data collection	1.722 to 49.42°
Index ranges	$-14 \leq h \leq 14$, $-22 \leq k \leq 22$, $-28 \leq l \leq 28$
Reflections collected	151263
Independent collections	19288 [R_{int} = 0.0591, R_{sigma} = 0.0339]
Data/restraints/parameters	19288/762/1158
Goodness-of-fit on F^2	1.040
Final R indexes [$I \geq 2\sigma$ (I)]	R_1 = 0.0853, wR_2 = 0.2412
Final R indexes [all data]	R_1 = 0.1009, wR_2 = 0.2622
Largest diff. peak/hole	1.45/–1.19 e Å^{-3}
Flack parameter	0.044(6)

Appendix Table 1.2. Crystallographic information for the structural refinement of **4**.

Empirical formula	$C_{20}H_{74}Cl_6Cr_2N_{12}O_5$
Formula weight	879.61 g/mol
Temperature	154.01 K
Crystal system	Monoclinic
Space group	*Cc*
a	28.4948(19) Å
b	12.0595(7) Å
c	14.7903(8) Å
α	90°
β	121.059(3)°
γ	90°
Volume	4353.8(5) $Å^3$
Z	4
ρ_{calc}	1.342 g cm^{-3}
μ	0.910 mm^{-1}
F(000)	1878.5
Crystal color	Orange
Crystal size	0.253 × 0.136 × 0.103 mm^3
Radiation	MoKα (λ = 0.71073 Å)
2θ range for data collection	3.214 to 64.258°
Index ranges	$-42 \leq h \leq 42$, $-18 \leq k \leq 18$, $-22 \leq l \leq 22$
Reflections collected	69980
Independent collections	12060 [R_{int} = 0.0499, R_{sigma} = 0.0382]
Data/restraints/parameters	12060/9/394
Goodness-of-fit on F^2	1.116
Final R indexes [$I \geq 2\sigma(I)$]	R_1 = 0.0667, wR_2 = 0.1883
Final R indexes [all data]	R_1 = 0.0878, wR_2 = 0.2117
Largest diff. peak/hole	1.53/–1.78 e $Å^{-3}$
Flack parameter	0.021(7)

Appendix Table 1.3. Crystallographic information for the structural refinement of **5-*SS***.

Empirical formula	$C_{18}H_{52}Cl_3CrN_6O_5$
Formula weight	591.01 g/mol
Temperature	99.99 K
Crystal system	Hexagonal
Space group	$P6_1$
a	12.2492(5) Å
b	12.2492(5) Å
c	33.5991(16) Å
α	90°
β	90°
γ	120°
Volume	4365.9(4) $Å^3$
Z	6
ρ_{calc}	1.349 g cm^{-3}
μ	0.705 mm^{-1}
F(000)	1902.0
Crystal color	Orange
Crystal size	0.123 × 0.088 × 0.086 mm^3
Radiation	MoKα (λ = 0.71073 Å)
2θ range for data collection	3.84 to 50.024°
Index ranges	$-14 \leq h \leq 13$, $-14 \leq k \leq 13$, $-39 \leq l \leq 39$
Reflections collected	19578
Independent collections	5157 [R_{int} = 0.0509, R_{sigma} = 0.0504]
Data/restraints/parameters	5157/3/313
Goodness-of-fit on F^2	1.097
Final R indexes [$I \geq 2\sigma(I)$]	R_1 = 0.0560, wR_2 = 0.1362
Final R indexes [all data]	R_1 = 0.0650, wR_2 = 0.1472
Largest diff. peak/hole	1.84/–0.65 e $Å^{-3}$
Flack parameter	0.031(13)

Appendix Table 1.4. Crystallographic information for the structural refinement of **5-*RR***.

Empirical formula	$C_{18}H_{52}Cl_3CrN_6O_5$
Formula weight	591.01 g/mol
Temperature	100.0 K
Crystal system	Hexagonal
Space group	$P6_5$
a	12.2603(6) Å
b	12.2603(6) Å
c	33.2599(16) Å
α	90°
β	90°
γ	120°
Volume	4329.7(5) $Å^3$
Z	6
ρ_{calc}	1.360 g cm^{-3}
μ	0.711 mm^{-1}
F(000)	1902.0
Crystal color	Orange
Crystal size	0.121 × 0.104 × 0.079 mm^3
Radiation	MoKα (λ = 0.71073 Å)
2θ range for data collection	4.026 to 52.73°
Index ranges	$-15 \leq h \leq 15$, $-15 \leq k \leq 15$, $-41 \leq l \leq 41$
Reflections collected	171415
Independent collections	5914 [R_{int} = 0.0669, R_{sigma} = 0.0184]
Data/restraints/parameters	5914/112/330
Goodness-of-fit on F^2	1.081
Final R indexes [$I \geq 2\sigma(I)$]	R_1 = 0.0561, wR_2 = 0.1251
Final R indexes [all data]	R_1 = 0.0608, wR_2 = 0.1288
Largest diff. peak/hole	1.09/–0.88 e $Å^{-3}$
Flack parameter	0.020(6)

Appendix Table 1.5. Selected inner coordination sphere bond lengths and angles of **1**.

Atoms	Length (Å)	Atoms	Angle (°)
Cr01–N00C	2.087(7)	N00E–Cr01–N00G	82.0(3)
Cr01–N00E	2.078(7)	N00F–Cr01–N00H	82.3(3)
Cr01–N00F	2.050(8)	N00I–Cr01–N00C	82.0(3)
Cr01–N00G	2.078(7)	N00F–Cr01–N00E	171.0(3)
Cr01–N00H	2.073(7)	N00G–Cr01–N00C	169.8(3)
Cr01–N00I	2.080(7)	N00H–Cr01–N00I	169.6(3)
Cr02–N00K	2.083(8)	N00N–Cr02–N00V	81.6(3)
Cr02–N00N	2.070(8)	N00S–Cr02–N00K	80.8(3)
Cr02–N00P	2.097(7)	N01D–Cr02–N00P	81.0(3)
Cr02–N00S	2.083(9)	N00N–Cr02–N00P	171.0(3)
Cr02–N00V	2.075(8)	N00V–Cr02–N00K	172.4(3)
Cr02–N01D	2.068((9)	N01D–Cr02–N00S	173.7(3)

Appendix Table 1.6. Selected inner coordination sphere bond lengths and angles of **4**.

Atoms	Length (Å)	Atoms	Angle (°)
Cr01–N009	2.098(7)	N00Q–Cr01–N00K	91.2(6)
Cr01–N00C	2.096(7)	N00R–Cr01–N00K	87.6(5)
Cr01–N00I	2.078(7)	N1–Cr01–N009	89.0(5)
Cr01–N00J	2.138(16)	N00I–Cr01–N00J	85.6(5)
Cr01–N00K	2.089(7)	N00I–Cr01–N00C	90.5(3)
Cr01–N00Q	2.045(17)	N00C–Cr01–N00R	173.8(6)
Cr01–N1	2.078(17)	N00I–Cr01–N009	176.8(3)
Cr01–N00R	2.144(14)	N00K–Cr01–N00J	175.6(6)
Cr02–N00D	2.35(3)	N00Q–Cr01–N00C	174.8(8)
Cr02–N00E	1.930(17)	N1–Cr01–N00K	174.7(7)
Cr02–N00H	2.207(17)	N2AA–Cr02–N00V	94.6(6)
Cr02–N00U	2.18(2)	N00D–Cr02–N00U	80.6(9)
Cr02–N0AA	2.195(15)	N4AA–Cr02–N3AA	90.4(4)
Cr02–N1AA	2.029(13)	N0AA–Cr02–N1AA	90.8(6)
Cr02–N00V	2.074(13)	N00E–Cr02–N00H	92.2(7)
Cr02–N2AA	1.971(17)	N00E–Cr02–N00D	173.2(8)
Cr02–N3AA	2.117(8)	N1AA–Cr02–N4AA	173.1(5)
Cr02–N4AA	2.105(10)	N2AA–Cr02–N0AA	172.4(6)
		N3AA–Cr02–N00U	169.1(9)
		N4AA–Cr02–N00H	172.4(6)
		N00V–Cr02–N3AA	175.9(5)

Appendix Table 1.7. Selected inner coordination sphere bond lengths and angles of **5-*SS***.

Atoms	Length (Å)	Atoms	Angle (˚)
Cr01–N005	2.079(5)	N007–Cr01–N005	82.57(19)
Cr01–N006	2.083(5)	N008–Cr01–N006	82.14(19)
Cr01–N007	2.078(5)	N00A–Cr01–N00B	82.2(2)
Cr01–N008	2.081(5)	N005–Cr01–N006	170.96(19)
Cr01–N00A	2.065(5)	N00A–Cr01–N007	170.2(2)
Cr01–N00B	2.074(5)	N00B–Cr01–N008	172.5(2)

Appendix Table 1.8. Selected inner coordination sphere bond lengths and angles of **5-*RR***.

Atoms	Length (Å)	Atoms	Angle (˚)
Cr01–N005	2.088(6)	N006–Cr01–N007	81.7(2)
Cr01–N006	2.076(6)	N008–Cr01–N00A	82.4(2)
Cr01–N007	2.084(6)	N009–Cr01–N005	82.4(2)
Cr01–N008	2.080(6)	N006–Cr01–N005	170.8(2)
Cr01–N009	2.085(7)	N007–Cr01–N00A	172.2(2)
Cr01–N00A	2.086(6)	N008–Cr01–N009	170.2(2)

Appendix Table 1.9. Continuous-shape-measurement (CSM) results for **1**, **2**, **4**, **5**, **5-*SS***, **5-*RR***.

Complex	SHAPE analysis octahedral	SHAPE analysis trigonal prismatic
1	0.731	12.69
2	0.616	13.43
4	0.064	15.73
5	0.510	13.79
5-SS	0.661	12.54
5-RR	0.636	12.55

Appendix Table 1.10. Emission lifetimes for **1-5** obtained through bi-exponential decay (**2-5, 5-*SS*, and 5-*RR***) or tri-exponential decay (**1**) fits.

Complex	τ_1 (ns)	τ_2 (ns)	τ_3 (ns)
1	0.45 ± 0.033	37.9 ± 4.7	1884 ± 66
2	1.40 ± 0.049	1800 ± 37	-
3	0.99 ± 0.054	1830 ± 32	-
4	0.48 ± 0.062	1950 ± 29	-
5	0.97 ± 0.059	1910 ± 34	-
5-SS	0.72 ± 0.034	1550 ± 23	-
5-RR	0.58 ± 0.048	1590 ± 21	-

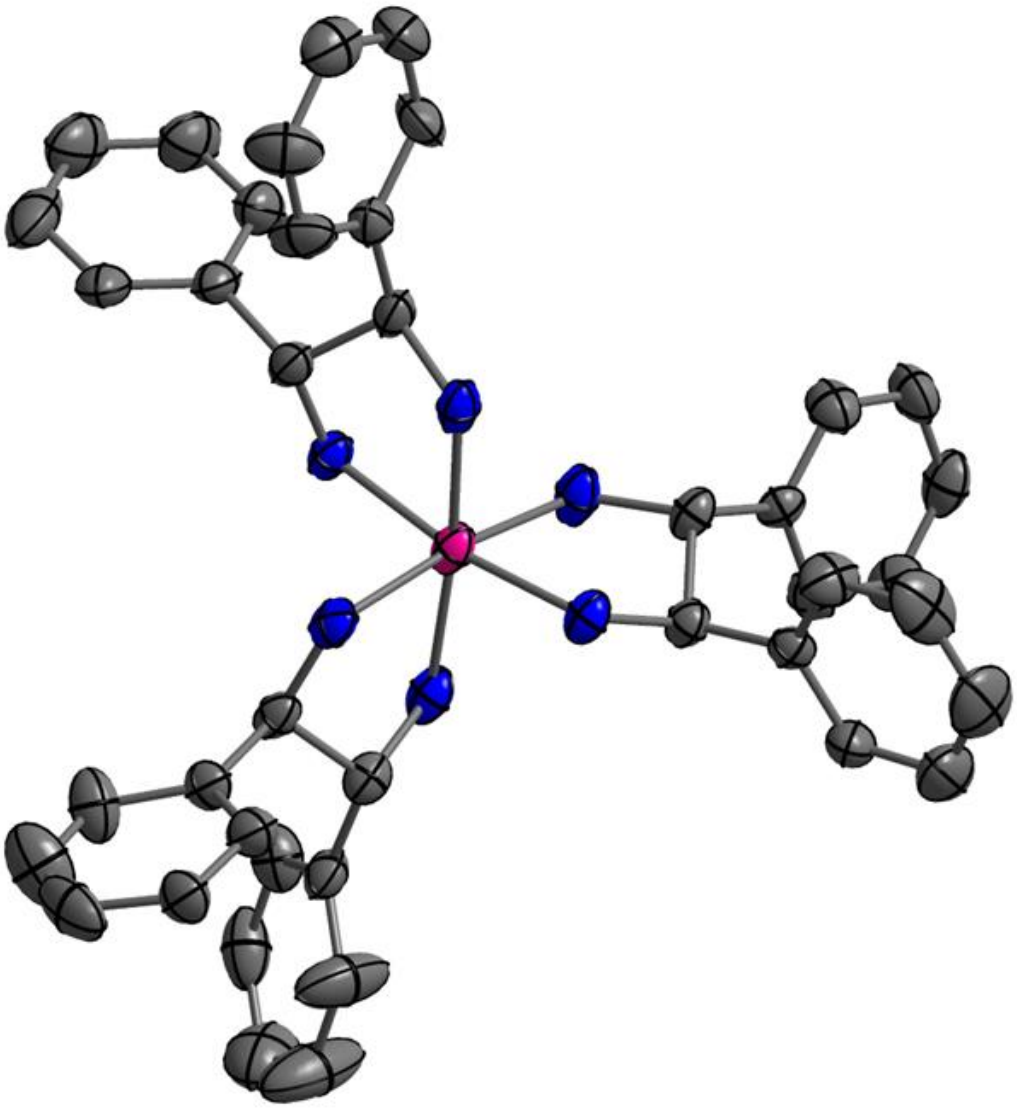

Appendix Figure 1.1. Thermal ellipsoid plot of **1** drawn at the 50% probability level. Hydrogen atoms, counterions, and solvent molecules were removed for clarity. Pink, blue, and grey ellipsoids correspond to chromium, nitrogen, and carbon, respectively.

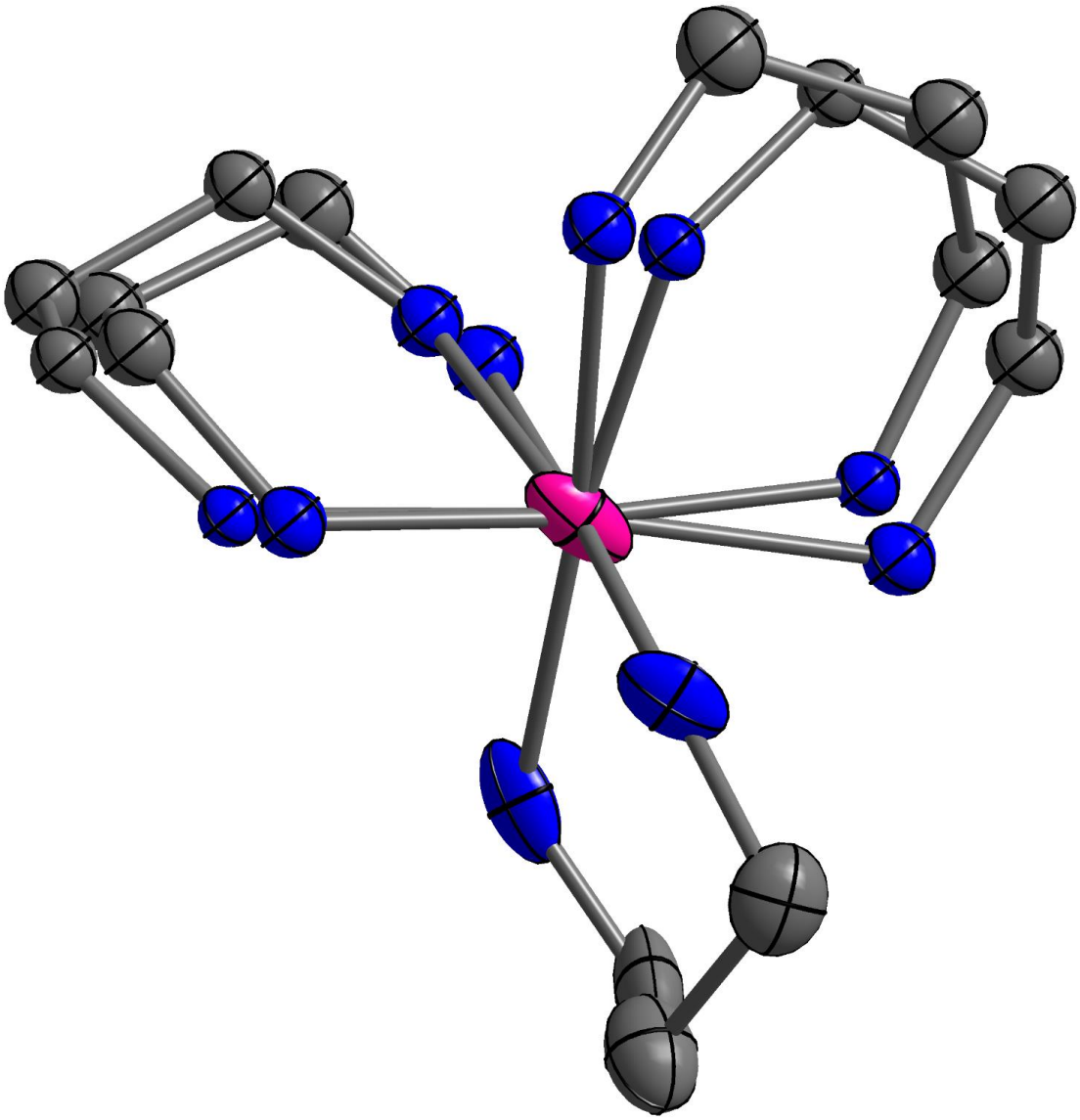

Appendix Figure 1.2. Thermal ellipsoid plot of **4** drawn at the 50% probability level. Disorder is illustrated for two of the 1,3-propanediamine arms, and the atoms here were modeled isotropically. Hydrogen atoms, counterions, and solvent molecules were removed for clarity. Pink, blue, and grey ellipsoids correspond to chromium, nitrogen, and carbon atoms, respectively.

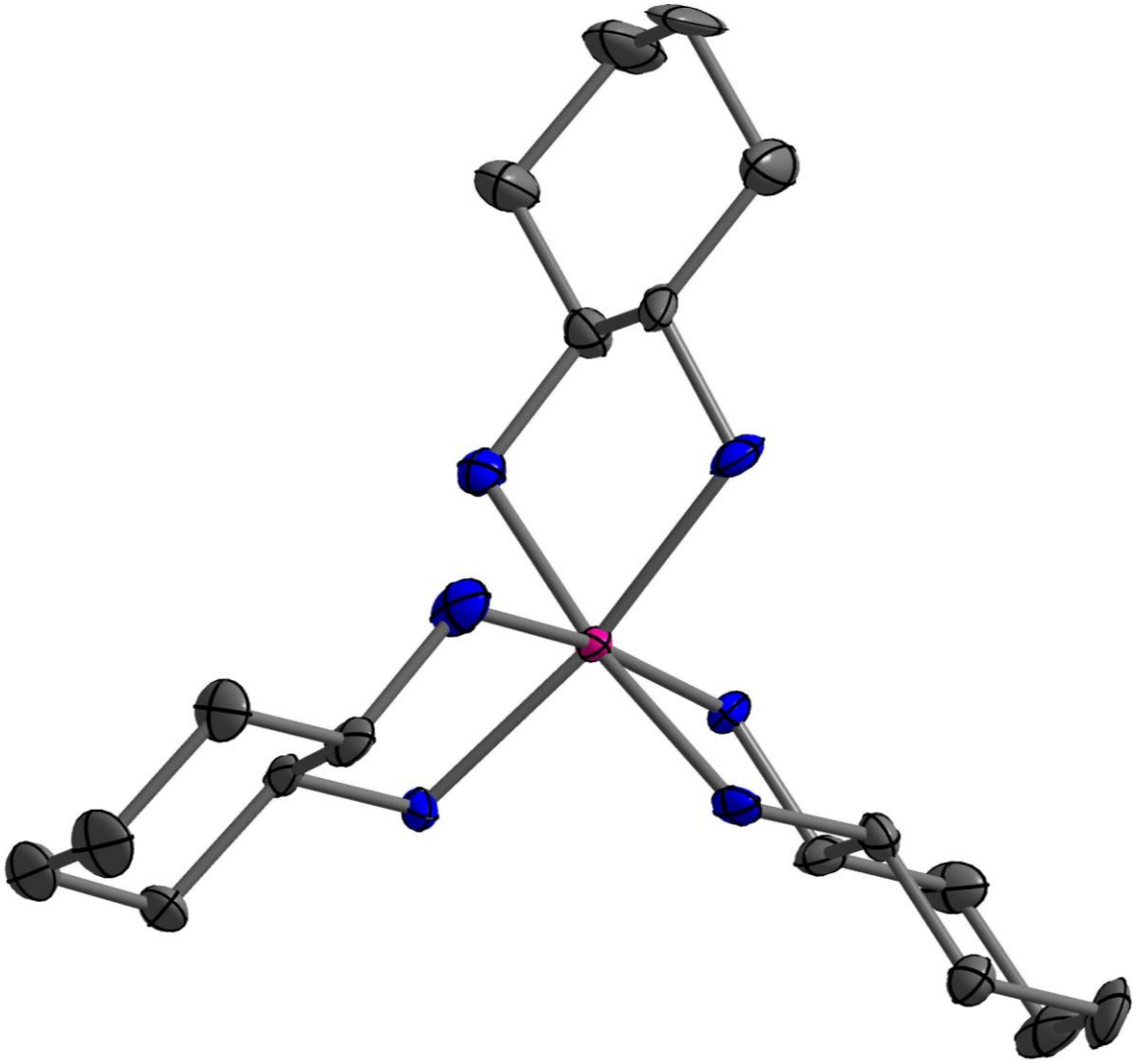

Appendix Figure 1.3. Thermal ellipsoid plot of **5-*SS*** drawn at the 70% probability level. Hydrogen atoms, counterions, and solvent molecules were removed for clarity. Pink, blue, and grey ellipsoids correspond to chromium, nitrogen, and carbon atoms, respectively.

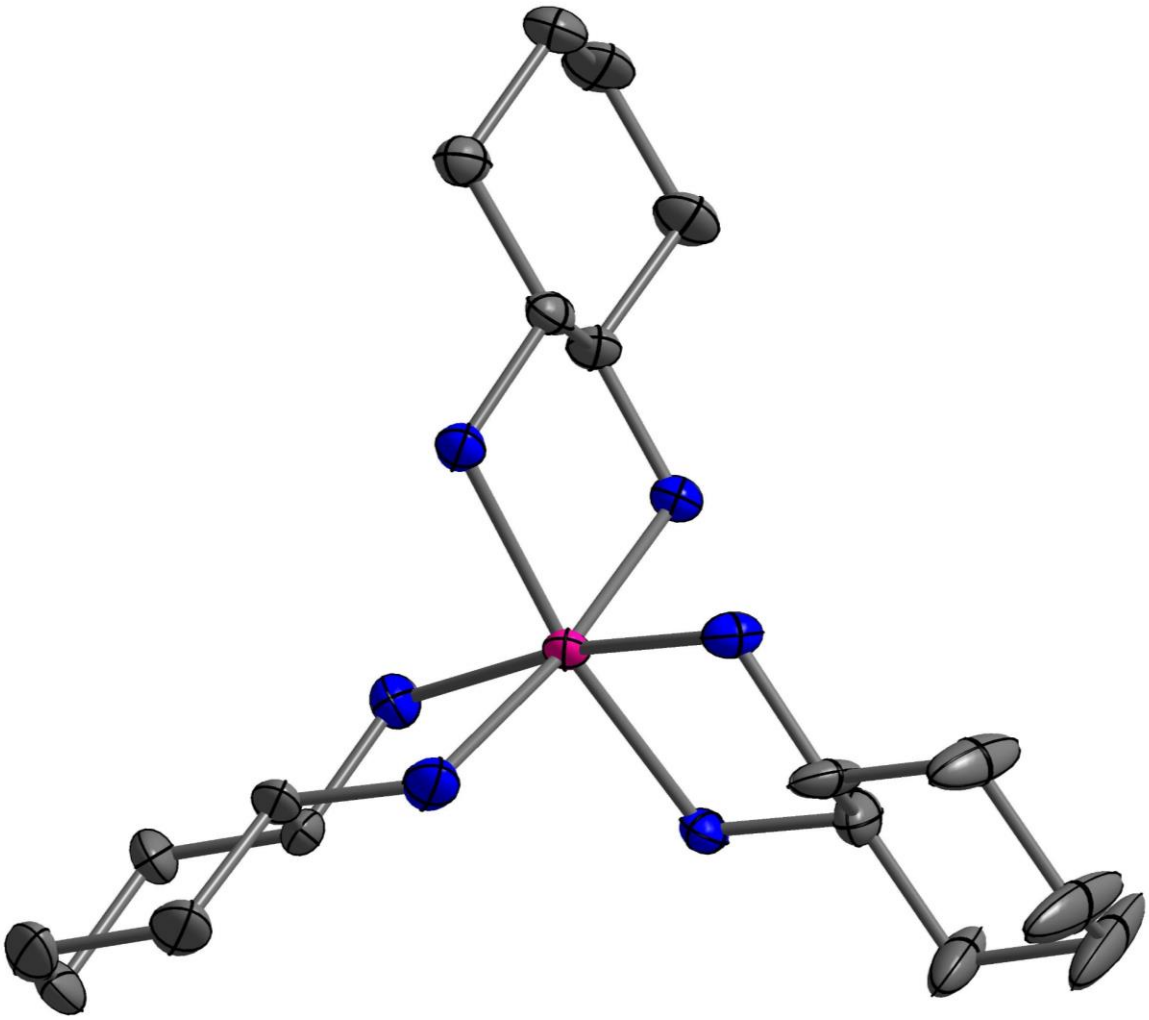

Appendix Figure 1.4. Thermal ellipsoid plot of **5-*RR*** drawn at the 50% probability level. Hydrogen atoms, counterions, and solvent molecules were removed for clarity. Pink, blue, and grey ellipsoids correspond to chromium, nitrogen, and carbon atoms, respectively.

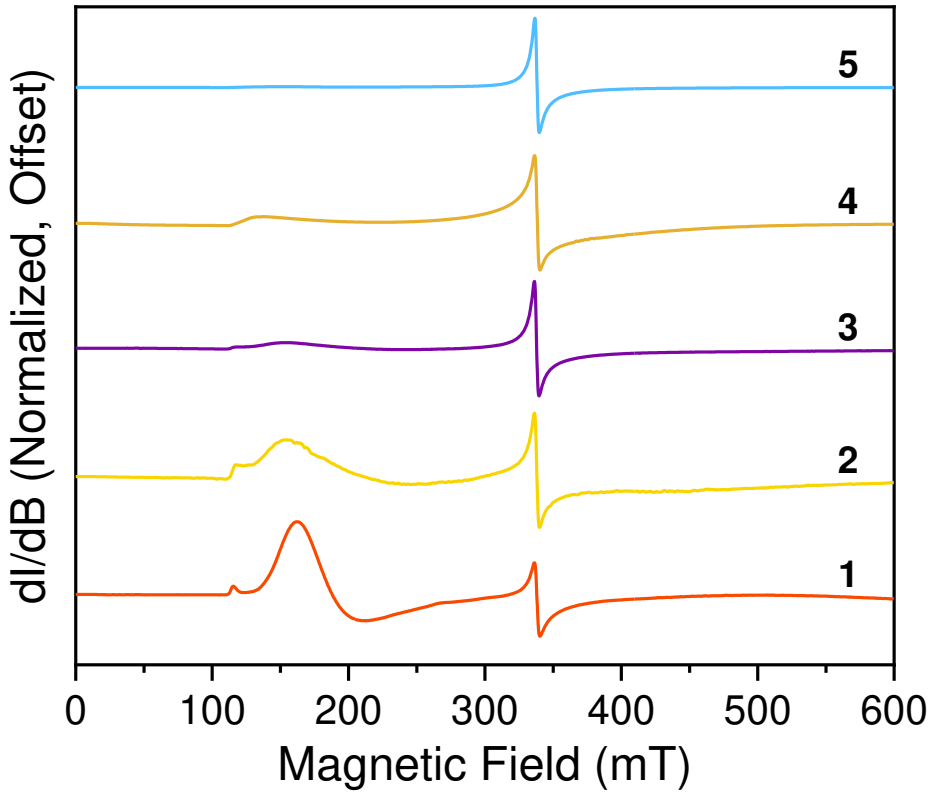

Appendix Figure 1.5. Continuous-wave X-band EPR spectra of **1**-**5** in ethylene glycol-water solutions (50:50 v/v) collected at 77 K.

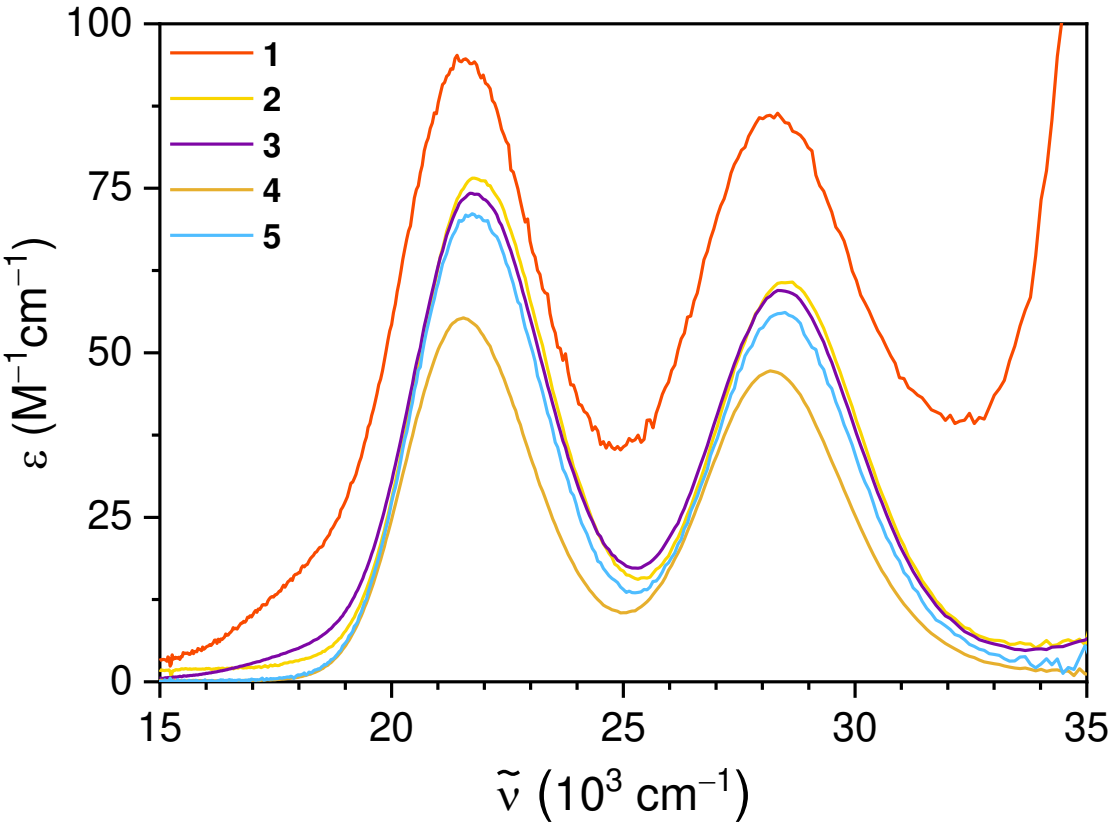

Appendix Figure 1.6. Electronic absorption spectroscopy data for complexes **1**-**5**. Solutions were prepared at ca. 1, 5, and 10 mM in deionized H_2O and spectra were collected at room temperature.

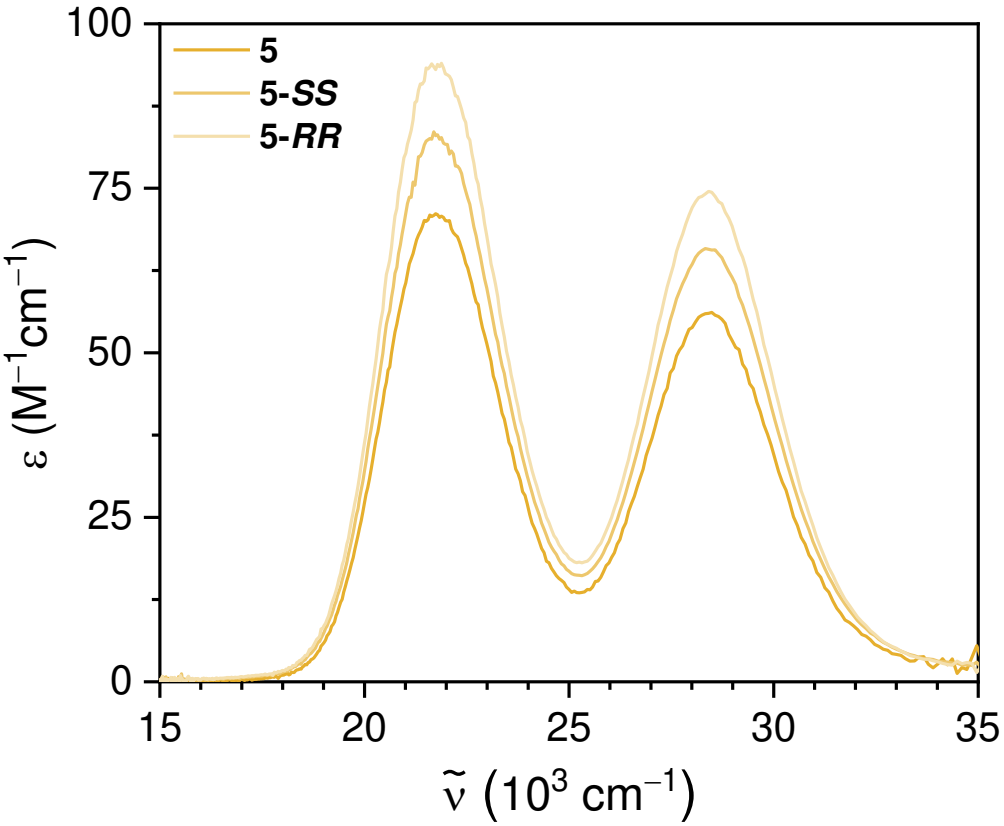

Appendix Figure 1.7. Electronic absorption spectroscopy data for complexes **5**, **5-*SS*,** and **5-*RR***. Solutions were prepared at ca. 1, 5, and 10 mM in deionized H_2O and spectra were collected at room temperature.

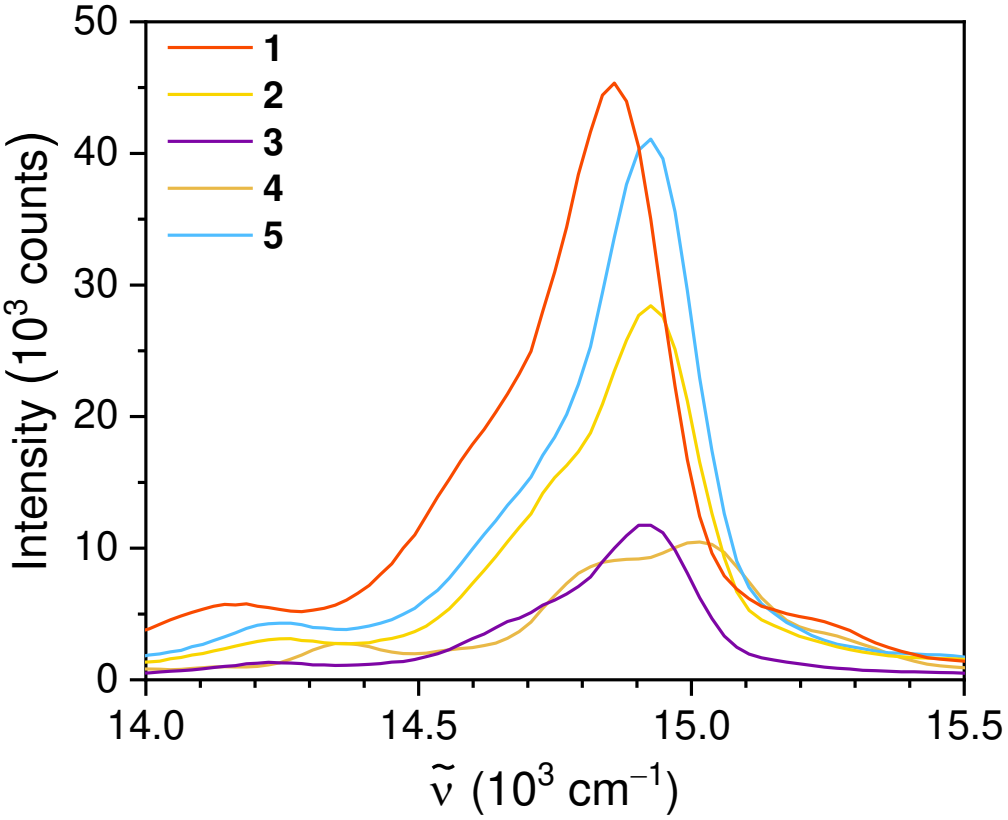

Appendix Figure 1.8. Steady-state emission spectroscopy data for **1**-**5**. Solutions were prepared at ca. 30 mM in deionized H_2O and spectra were collected at 20 °C.

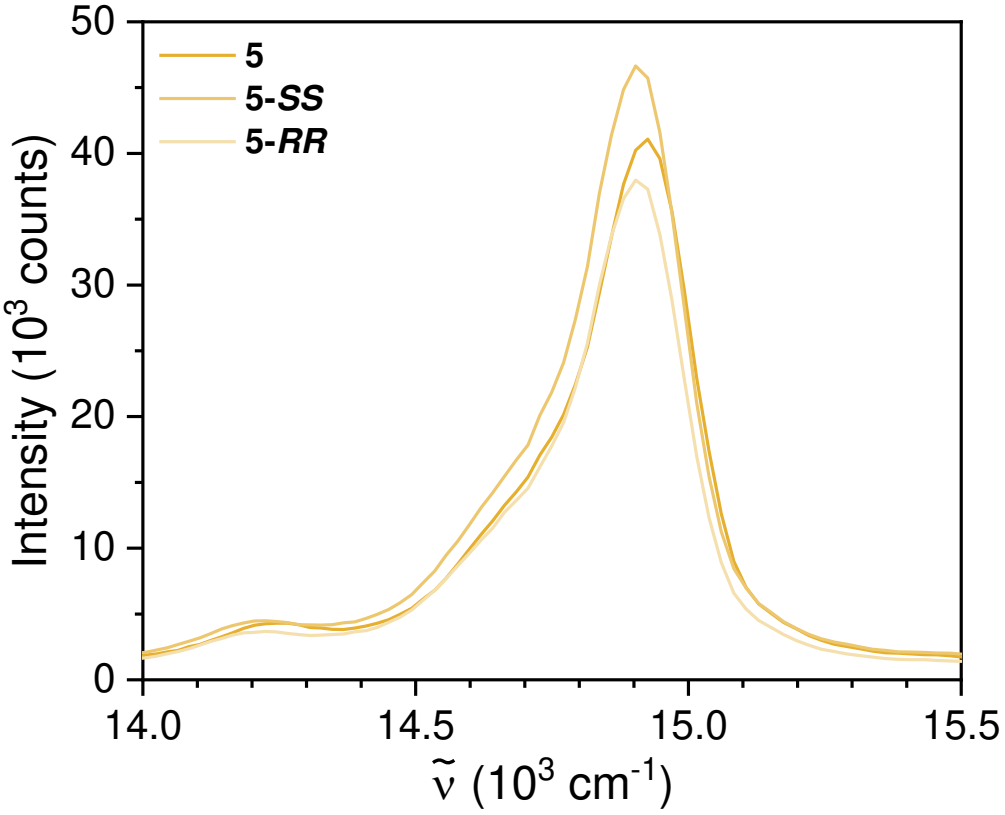

Appendix Figure 1.9. Steady-state emission spectroscopy data for **5**, **5-*SS*,** and **5-*RR***. Solutions were prepared at ca. 30 mM in deionized H_2O and spectra were collected at 20 °C.

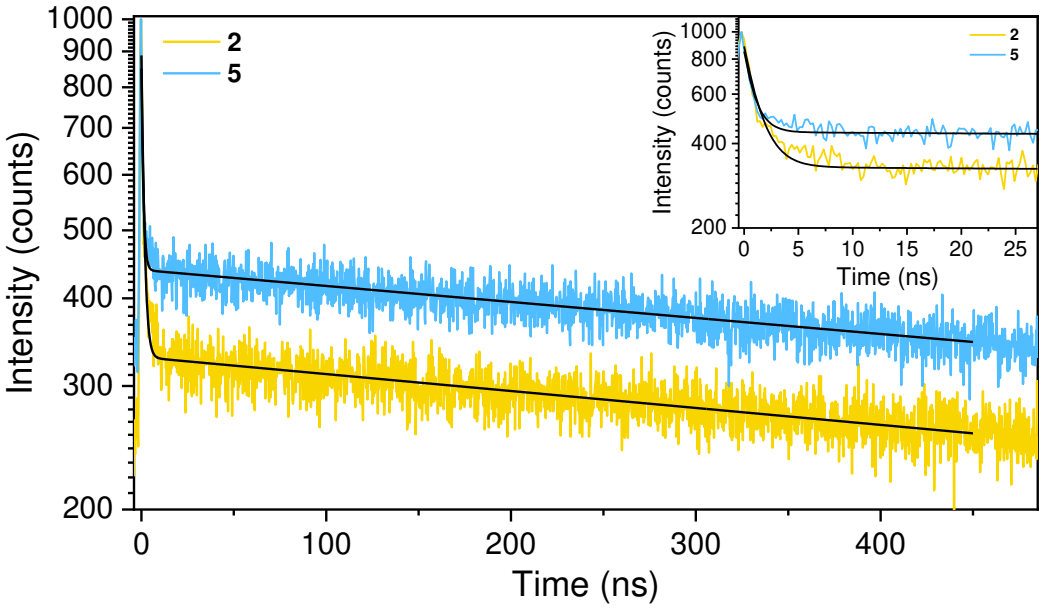

Appendix Figure 1.10. Time-resolved emission spectra for **2** and **5**. The solutions were prepared at ca. 30 mM in deionized H_2O and spectra were collected at 20 °C.

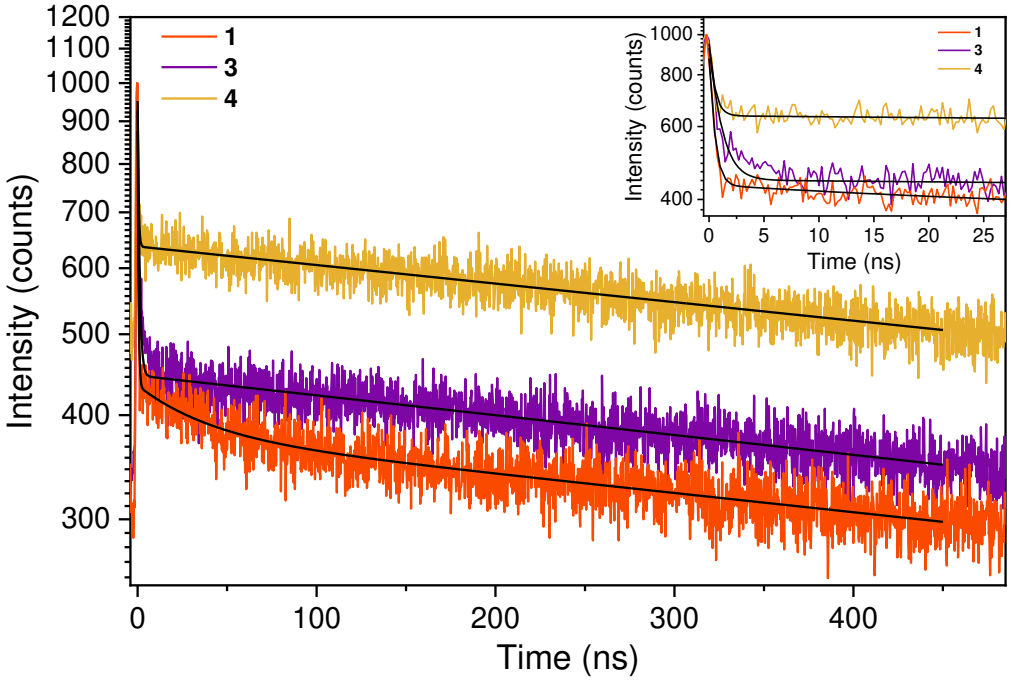

Appendix Figure 1.11. Time-resolved emission spectra for **1**, **3** and **4**. The solutions were prepared at ca. 30 mM in deionized H_2O and spectra were collected at 20 °C.

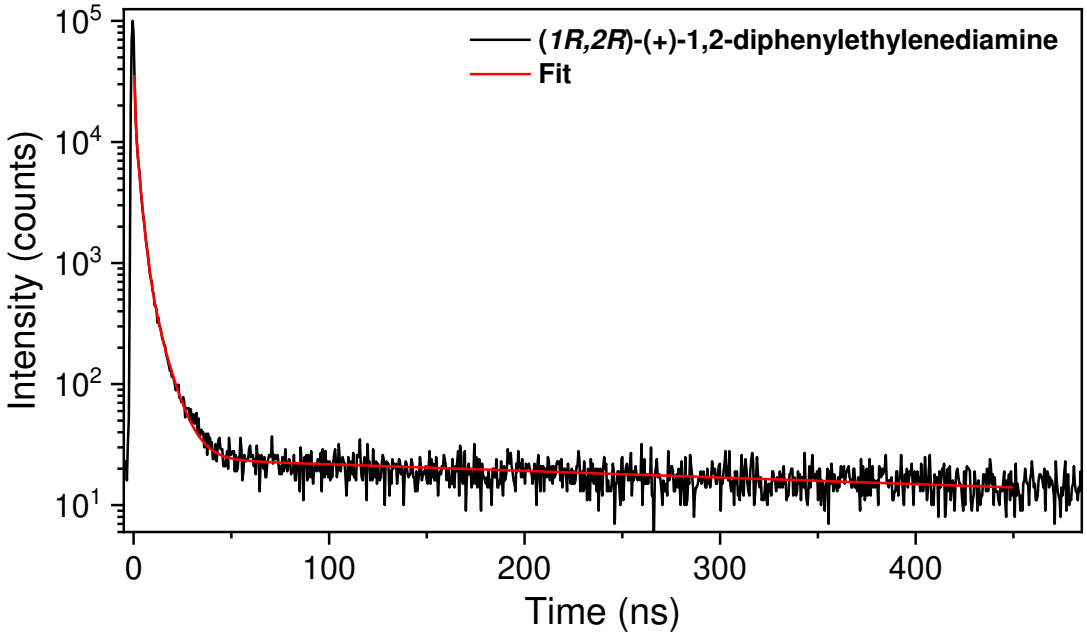

Appendix Figure 1.12. Time-resolved emission spectra for (1*R*,2*R*)-(+)-1,2-diphenylethylenediamine. The solution was prepared at ca. 30 mM in deionized H_2O and spectra were collected at 20 °C.

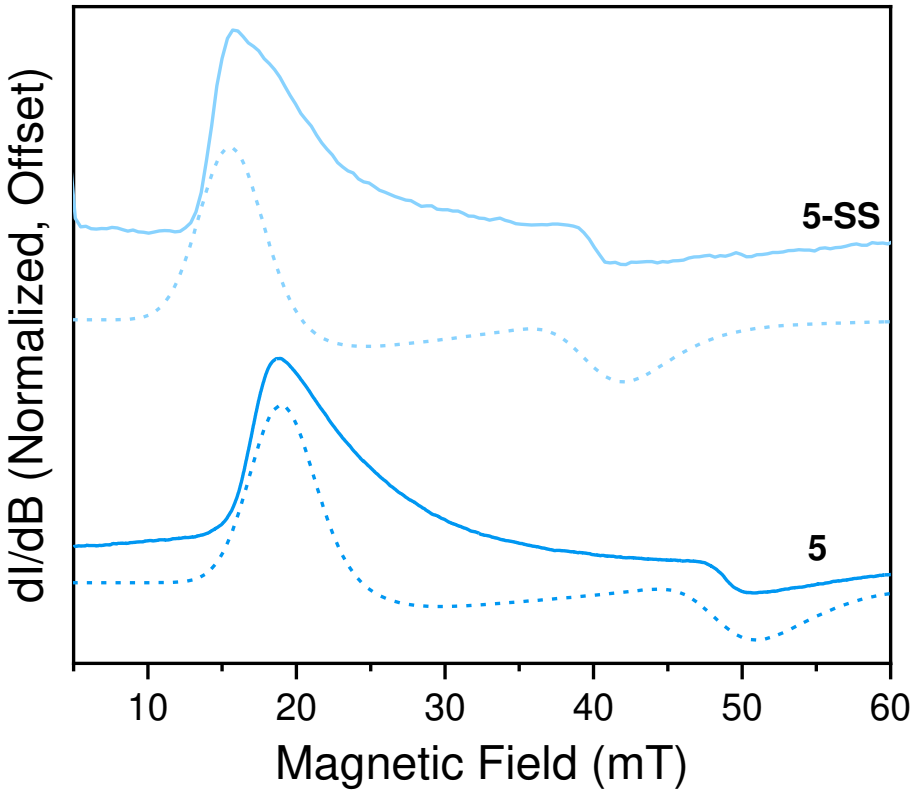

Appendix Figure 1.13. CW L-band EPR spectra of **5** and **5-*SS*** in 30 mM frozen glass solutions of an ethylene glycol/water (1:1 v/v) solvent system at 112 K. Dashed lines below each spectrum are the simulated spectra using the parameters from Table S7. Spectra appear offset due to slightly different tuning frequencies used in each experiment (1.095 GHz for **5-*SS*** and 1.360 GHz for **5**).

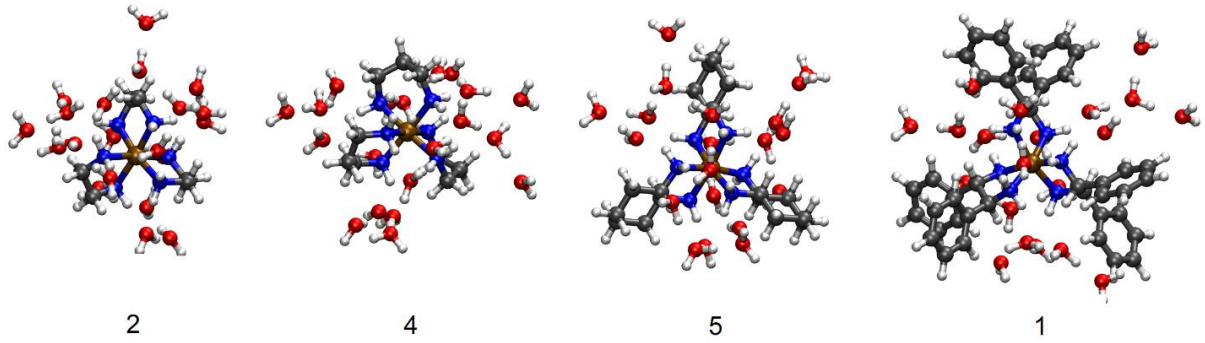

Appendix Figure 1.14. The putative global minima of the structures of the four Cr(III) complexes **1, 2, 4**, and **5** micro-solvated with 20 water molecules.

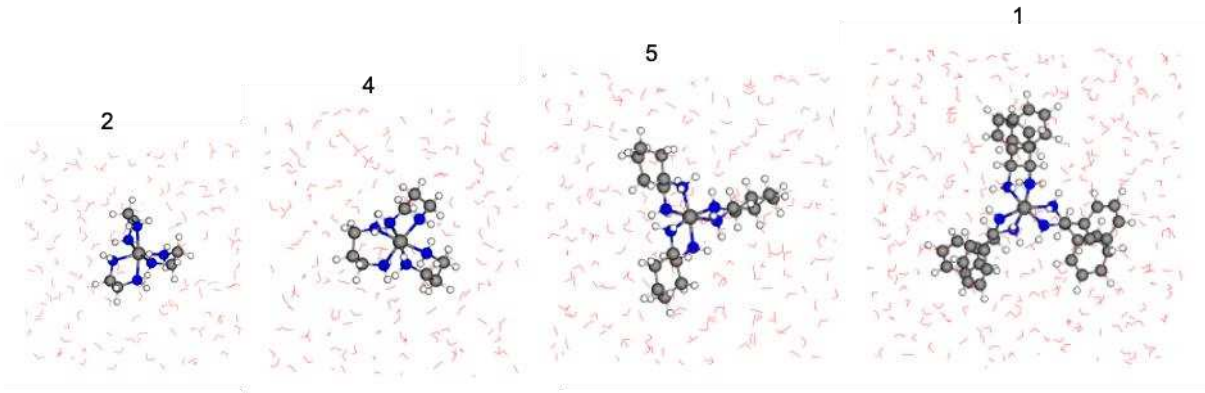

Appendix Figure 1.15. Molecular simulation boxes of the four Cr(III) complexes in water.

Appendix 2: Supporting Information for Chapter 3

Appendix Table 2.1. EXAFS parameters for complex **1** obtained from fitting the EXAFS spectra. Spectra were collected as 30 mM frozen solutions at 110 K.

	N	**C**	**H**
N	6	6	12
σ^2 (Å^2)	0.00153 ± 0.00125	0.00634 ± 0.00455	0.00192 ± 0.00575
***R* (Å)**	2.0822 ± 0.0089	2.9112 ± 0.0031	2.3875 ± 0.0453
S_0^2	0.645 ± 0.080		
E_0 (eV)	−0.550 ± 1.005		

Appendix Table 2.2. EXAFS parameters for complex **2** obtained from fitting the EXAFS spectra. Spectra were collected as 30 mM frozen solutions at 110 K.

	N	**C_1**	**C_2**	**H**
N	6	6	3	12
σ^2 (Å^2)	0.00133 ± 0.00134	0.00271 ± 0.00318	0.01073 ± 0.01668	0.00192 ± 0.00575
***R* (Å)**	2.0994 ± 0.0098	3.1142 ± 0.0252	3.5450 ± 0.0167	2.4430 ± 0.0532
S_0^2	0.665 ± 0.088			
E_0 (eV)	0.150 ± 1.144			

Appendix Table 2.3. EXAFS parameters for complex **3** obtained from fitting the EXAFS spectra. Spectra were collected as 30 mM frozen solutions at 110 K.

	N	**C**	**H**
N	6	6	12
σ^2 (Å^2)	0.00112 ± 0. 00153	0.00545 ± 0.00538	0.00218 ± 0.00793
***R* (Å)**	2.0813 ± 0.0109	2.9166 ± 0.0038	2.3941 ± 0.0607
S_0^2	0.696 ± 0.106		
E_0 (eV)	−1.097 ± 1.219		

Appendix Table 2.4. EXAFS parameters for complex **4** obtained from fitting the EXAFS spectra. Spectra were collected as 30 mM frozen solutions at 110 K.

	N	**C**	**H**
N	6	6	12
σ^2 (Å^2)	0.00243 ± 0. 00137	0.00691 ± 0.00498	0.00175 ± 0.00528
***R* (Å)**	2.0796 ± 0.0100	2.9472 ± 0.0328	2.3775 ± 0.0414
S_0^2	0.736 ± 0.092		
E_0 (eV)	−0.131 ± 1.076		

Appendix Table 2.5. EXAFS parameters for complex **1** obtained from fitting the EXAFS spectra. Spectra were collected as solid-state pellets at 30 K.

	N	**C**	**H**
N	6	6	12
σ^2 (Å^2)	0.00410 ± 0. 00243	0.01401 ± 0.01175	0.00219 ± 0.00641
***R* (Å)**	2.0622 ± 0.0159	2.8432 ± 0.0517	2.3368 ± 0.0631
S_0^2	0.813 ± 0.209		
E_0 (eV)	−1.843 ± 1.746		

Appendix Table 2.6. EXAFS parameters for complex **2** obtained from fitting the EXAFS spectra. Spectra were collected as solid-state pellets at 30 K.

	N	**C_1**	**C_2**	**H**
N	6	6	3	12
σ^2 (Å^2)	0.00406 ± 0.00242	0.00810 ± 0.00580	0.02108 ± 0.04337	0.01184 ± 0.01813
***R* (Å)**	2.0887 ± 0.0188	3.1026 ± 0.0535	3.4550 ± 0.280	2.3706 ± 0.146
S_0^2	0.839 ± 0.265			
E_0 (eV)	1.616 ± 3.262			

Appendix Table 2.7. EXAFS parameters for complex **3** obtained from fitting the EXAFS spectra. Spectra were collected as solid-state pellets at 30 K.

	N	**C**	**H**
N	6	6	12
σ^2 (Å^2)	0.00183 ± 0. 00174	0.00428 ± 0.00505	0.00659 ± 0.01494
***R* (Å)**	2.0853 ± 0.0137	2.9220 ± 0.0425	2.4155 ± 0.1015
S_0^2	0.689 ± 0.139		
E_0 (eV)	0.551 ± 2.017		

Appendix Table 2.8. EXAFS parameters for complex **4** obtained from fitting the EXAFS spectra. Spectra were collected as solid-state pellets at 30 K.

	N	**C**	**H**
N	6	6	12
σ^2 (Å^2)	0.00353 ± 0. 00197	0.00674 ± 0.00530	0.00526 ± 0.01014
R **(Å)**	2.0711 ± 0.0141	2.9586 ± 0.0405	2.3974 ± 0.0614
S_0^2	0.819 ± 0.171		
E_0 (eV)	−0.626 ± 2.020		

Appendix Table 2.9. Spin-Hamiltonian parameters of complex **1** computed with PBE/EPR-III(Cr)/ zora-def2-TZVPP level of theory.

	Gas Phase	**AIMD (0K)**	**Crystal Structure**	**Experiment (fitted)**
g_x	1.9938	1.9936	1.9944	1.985
g_y	1.9940	1.9937	1.9947	1.985
g_z	1.9942	1.9939	1.9950	1.960
D **(cm^{-1})**	−0.214472	−0.0787	−0.1323	0.100
A **(Mhz)**	27.0958	27.4458	26.9796	0
E/D	0.0504	0.0309	0.0991	0

Appendix Table 2.10. Spin-Hamiltonian parameters of complex **2** computed with PBE/EPR-III(Cr)/ zora-def2-TZVPP level of theory.

	Gas Phase	**AIMD (0K)**	**Crystal Structure**	**Experiment (fitted)**
g_x	1.9933	1.9928	1.9939	2.300
g_y	1.9934	1.9930	1.9941	2.300
g_z	1.9940	1.9936	1.9943	1.990
D **(cm^{-1})**	−0.084752	0.0918	0.1480	0.0967
A **(Mhz)**	28.0765	28.2721	27.7479	0
E/D	0.2510	0.2732	0.2490	0

Appendix Table 2.11. Spin-Hamiltonian parameters of complex **3** computed with PBE/EPR-III(Cr)/ zora-def2-TZVPP level of theory.

	Gas Phase	**AIMD (0K)**	**Crystal Structure**	**Experiment (fitted)**
g_x	1.9939	1.9937	1.9945	2.300
g_y	1.9943	1.9938	1.9949	2.300
g_z	1.9945	1.9939	1.9951	2.000
D **(cm^{-1})**	−0.097198	0.0765	−0.1621	0.0967
A **(Mhz)**	27.6673	27.7619	27.0174	0
E/D	0.1800	0.1272	0.1442	0

Appendix Table 2.12. Spin-Hamiltonian parameters of complex **4** computed with PBE/EPR-III(Cr)/ zora-def2-TZVPP level of theory.

	Gas Phase	**AIMD (0K)**	**Crystal Structure**	**Experiment (fitted)**
g_x	1.9941	1.9935	1.9945	1.995
g_y	1.9942	1.9937	1.9952	1.995
g_z	1.9944	1.9940	1.9955	1.955
D **(cm^{-1})**	−0.099732	0.0618	−0.1294	0.108
A **(Mhz)**	28.2944	27.8251	26.7759	0
E/D	0.2766	0.2614	0.1837	0

Appendix Table 2.13. Comparison of calculated geometry parameters in **1**-**4** in the gas phase and water solvation as determined by PBE/cc-pVTZ/SDD level of theory.

	1		**2**		**3**		**4**	
	Gas phase	Water	Gas phase	Water	Gas phase	Water	Gas phase	Water
Cr-N	2.15	2.10	2.14	2.12	2.15	2.10	2.20	2.11
N-Cr-N_{bite}	79.5	81.9	87.3	88.5	79.5	82.4	80.8	81.0
N-Cr-N_{adj}	93.7	92.9	90.9	90.6	93.6	92.8	93.2	93.3
N-Cr-N_{opp}	172.4	170.5	177.4	175	172.6	169.9	174.1	168.7

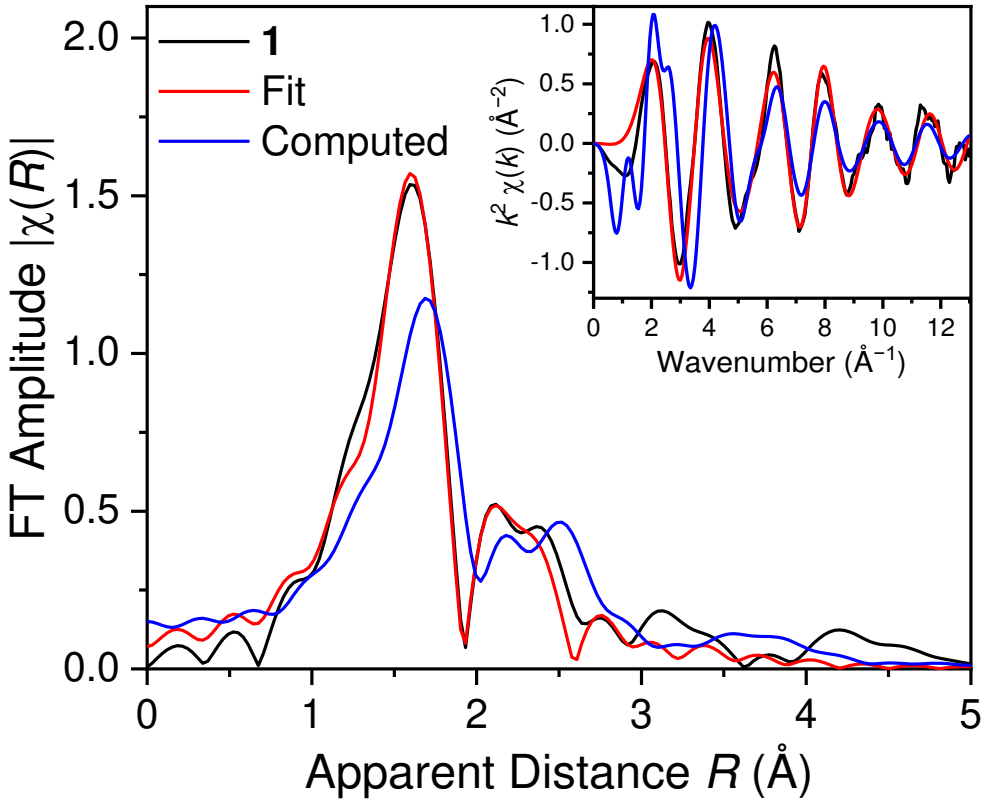

Appendix Figure 2.1. Radial structure function plot shown as Fourier Transform EXAFS data (Black) of **1** as a frozen solution, fit of experimental results (Red), and computed spectra from AIMD (Blue) with k^2-weighting over k-range of 2–12 Å^{-1}. Insets: k^2-weighted k-space plots and fits of **1**.

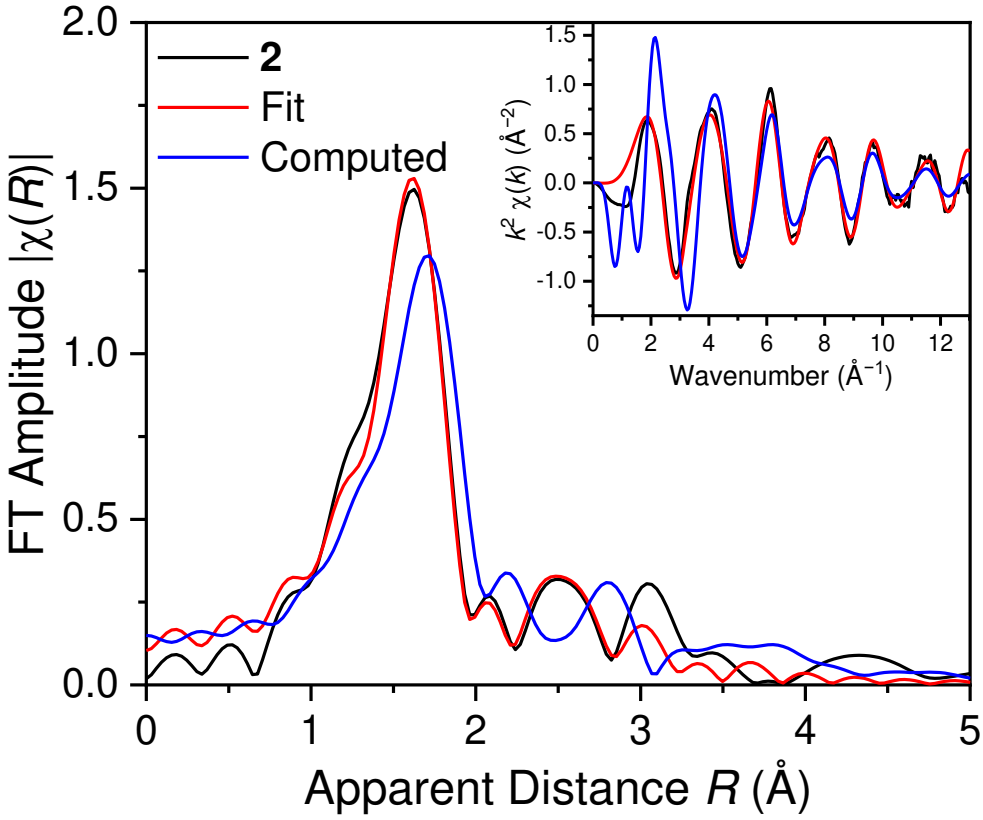

Appendix Figure 2.2. Radial structure function plot shown as Fourier Transform EXAFS data (Black) of **2** as a frozen solution, fit of experimental results (Red), and computed spectra from AIMD (Blue) with k^2-weighting over k-range of 2–12 Å^{-1}. Insets: k^2-weighted k-space plots and fits of **2**.

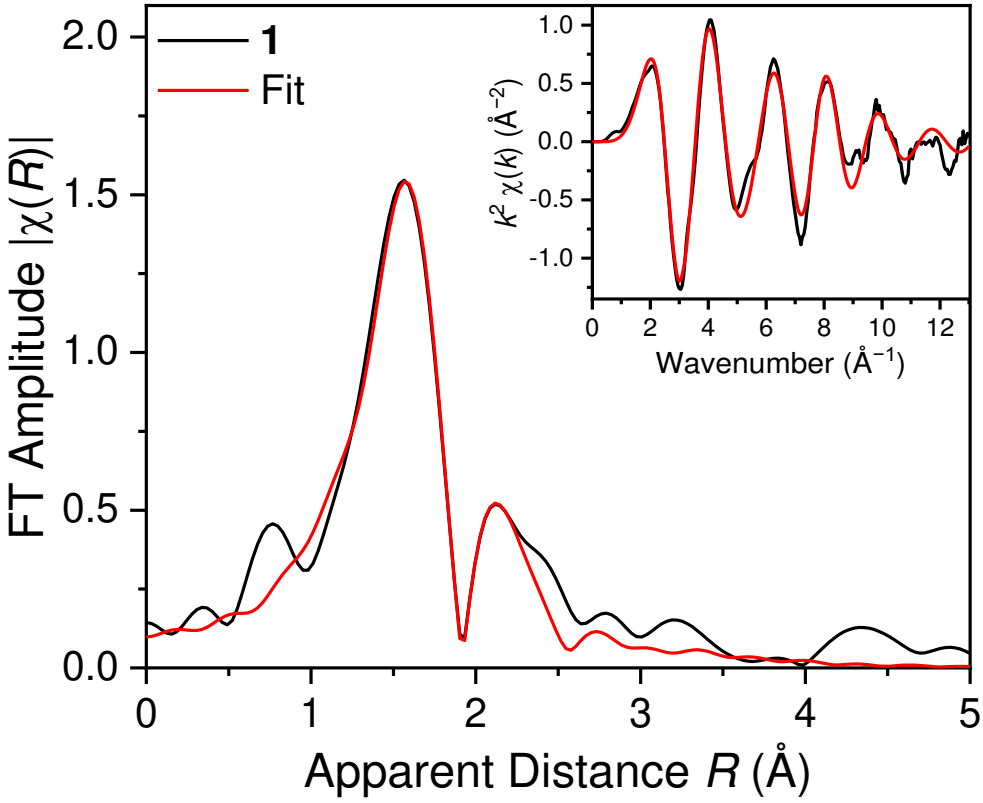

Appendix Figure 2.3. Radial structure function plot shown as Fourier Transform EXAFS data (Black) of **1** in the solid state and fit of experimental results (Red), with k^2-weighting over k-range of 2–12 Å^{-1}. Insets: k^2-weighted k-space plots and fits of **1**.

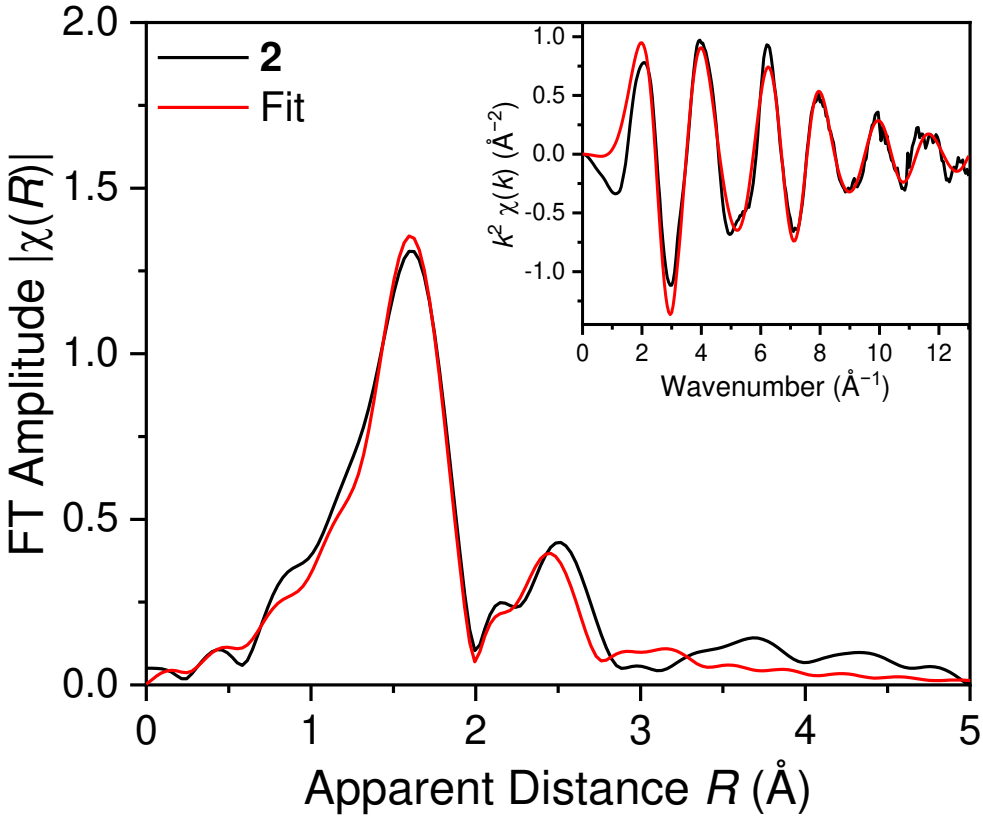

Appendix Figure 2.4. Radial structure function plot shown as Fourier Transform EXAFS data (Black) of **2** in the solid state and fit of experimental results (Red), with k^2-weighting over k-range of 2–12 Å^{-1}. Insets: k^2-weighted k-space plots and fits of **2**.

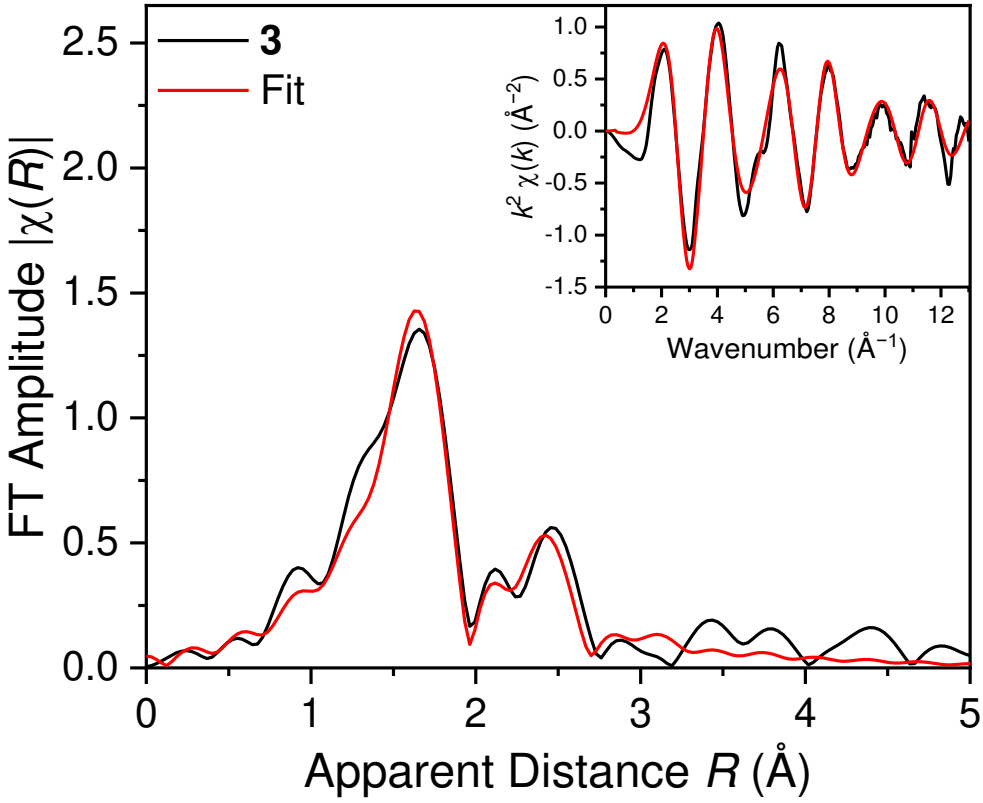

Appendix Figure 2.5. Radial structure function plot shown as Fourier Transform EXAFS data (Black) of **3** in the solid state and fit of experimental results (Red), with k^2-weighting over k-range of 2–12 Å^{-1}. Insets: k^2-weighted k-space plots and fits of **3**.

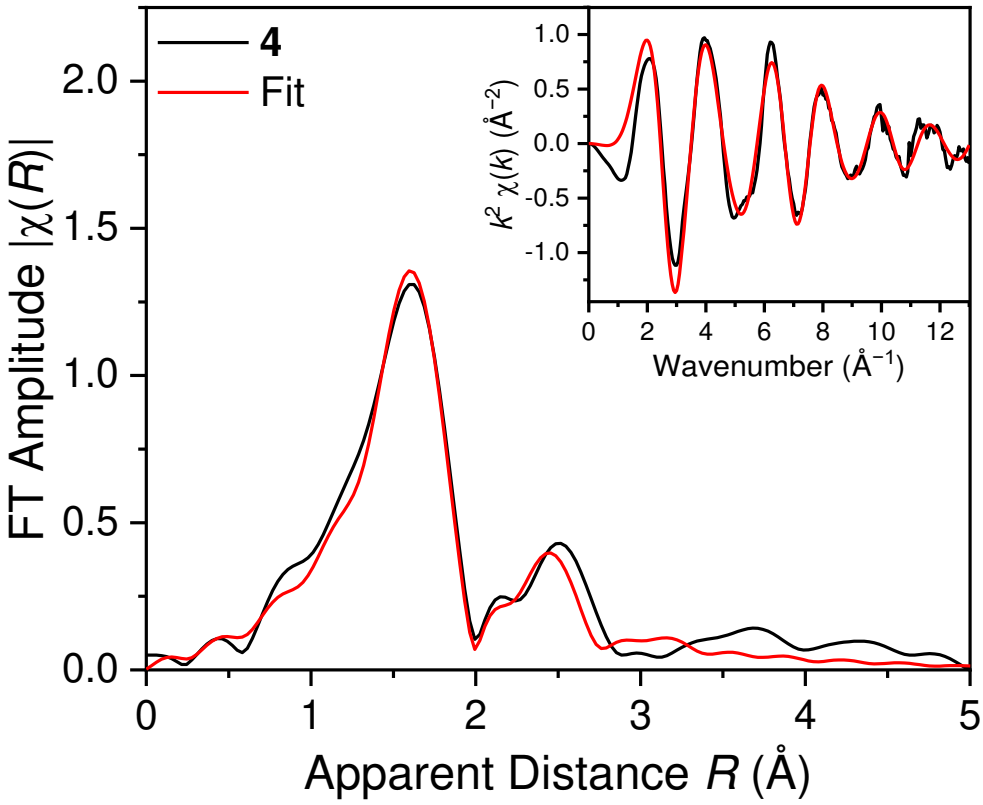

Appendix Figure 2.6. Radial structure function plot shown as Fourier Transform EXAFS data (Black) of **4** in the solid state and fit of experimental results (Red), with k^2-weighting over k-range of 2–12 Å^{-1}. Insets: k^2-weighted k-space plots and fits of **4**.

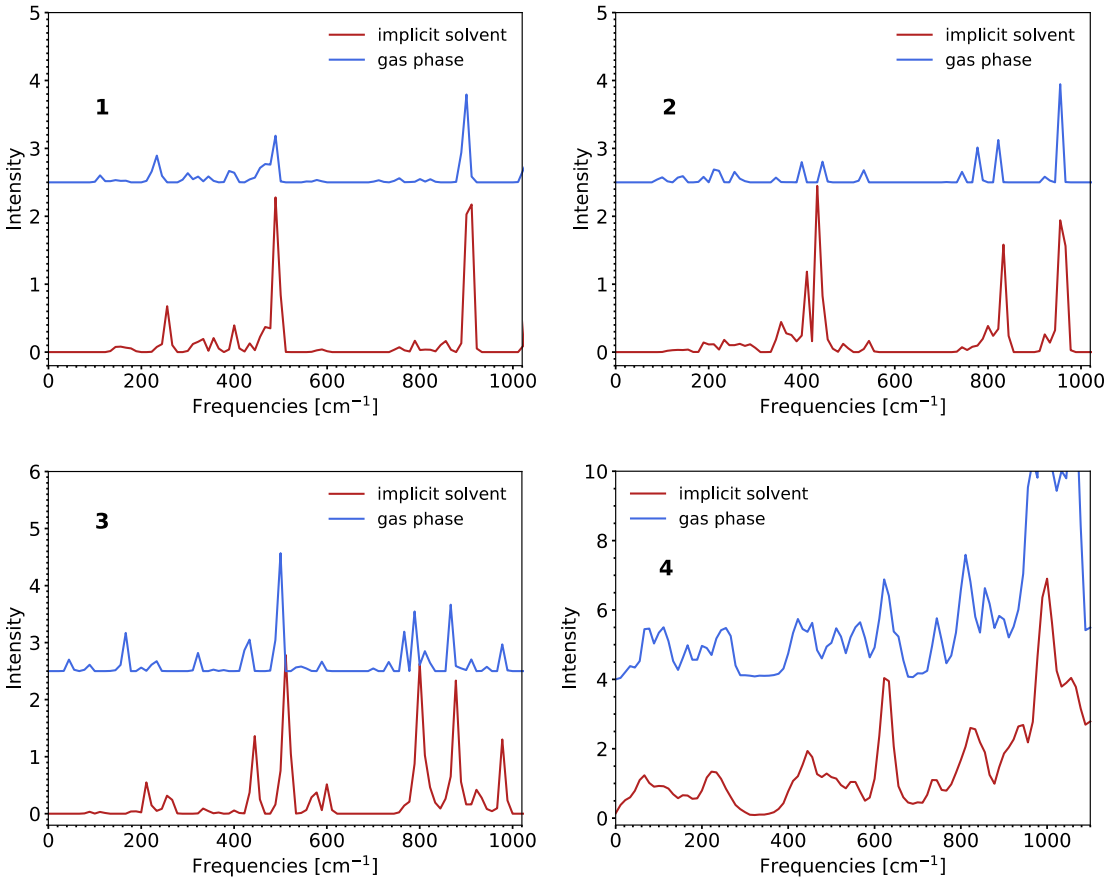

Appendix Figure 2.7. Calculated Raman spectra for Cr-complexes in water solvent and gas phase at PBE/cc-pVTZ/SDD level of theory.

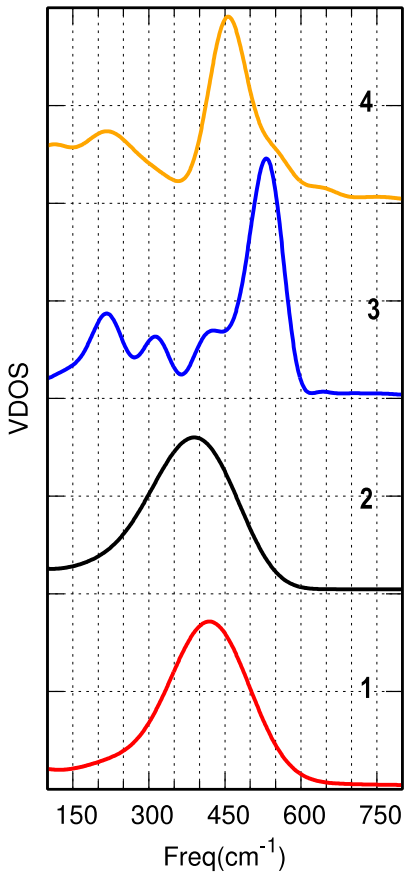

Appendix Figure 2.8. Vibrational density of states (VDOS) of Cr–N stretching modes. VDOS was calculated using the cosine transform of the autocorrelation function of corresponding internal coordinate. For example, the bond stretching mode was determined by:

$$VDOS(\omega) = \int_0^\infty d\tau \frac{\langle d(\tau)d(0)\rangle}{\langle d(0)d(0)\rangle}\cos(\omega\tau)$$

where $d(\tau)$ the time-dependent length of a given bond relative to its time-average value.

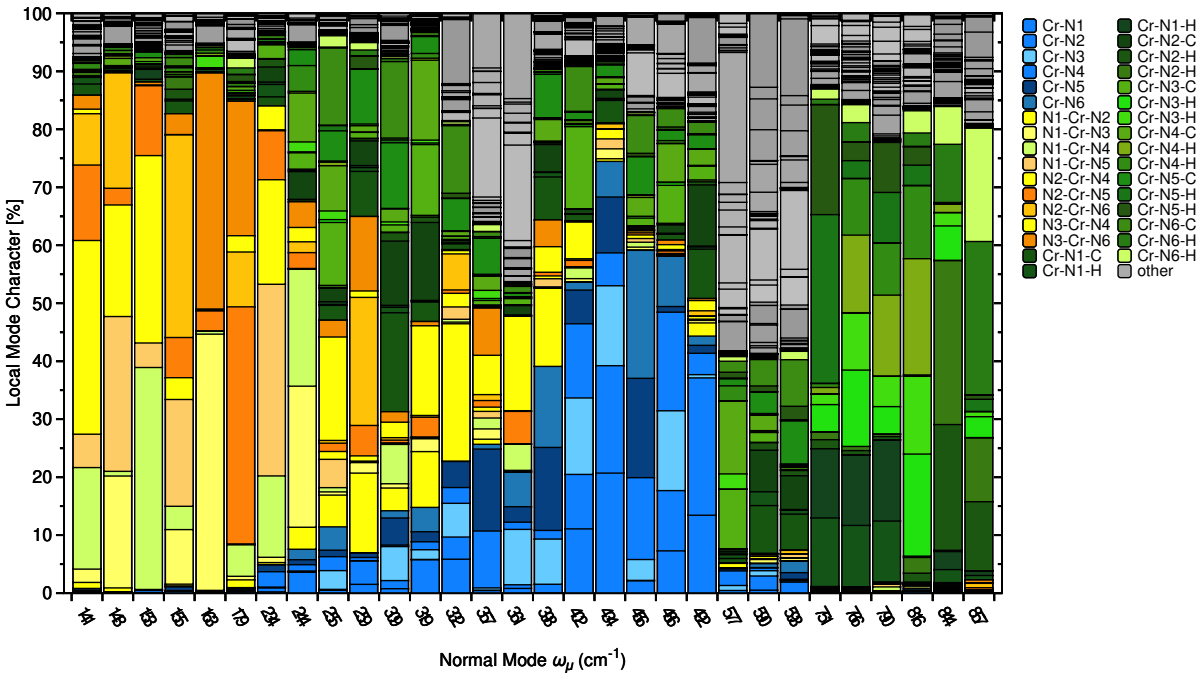

Appendix Figure 2.9. Decomposition of normal vibrational frequencies into % local vibrational mode contributions for complex **1**. In blues correspond to Cr−N stretching contributions, yellows to N−Cr−N bending, greens to Cr−N−C/H bending, greys to local modes without the Cr atom.

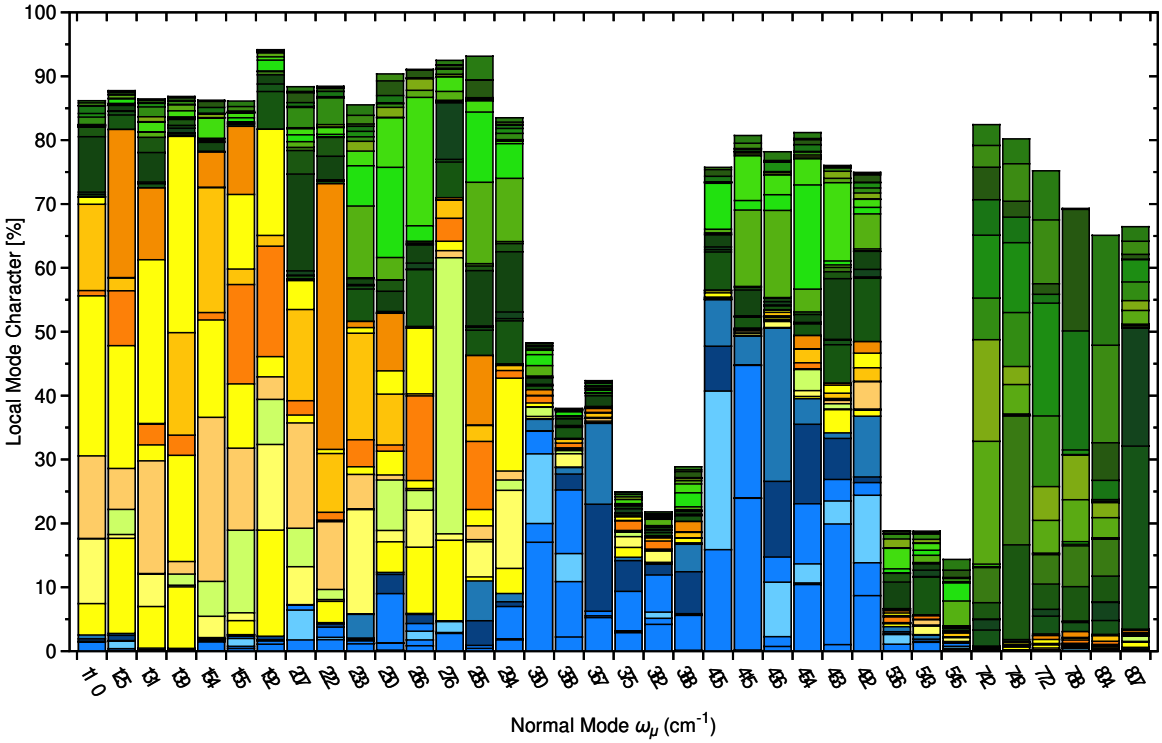

Appendix Figure 2.10. Decomposition of normal vibrational frequencies into % local vibrational mode contributions for complex **2**. In blues correspond to Cr–N stretching contributions, yellows to N–Cr–N bending, greens to Cr–N–C/H bending. Local modes without Cr are omitted for clarity.

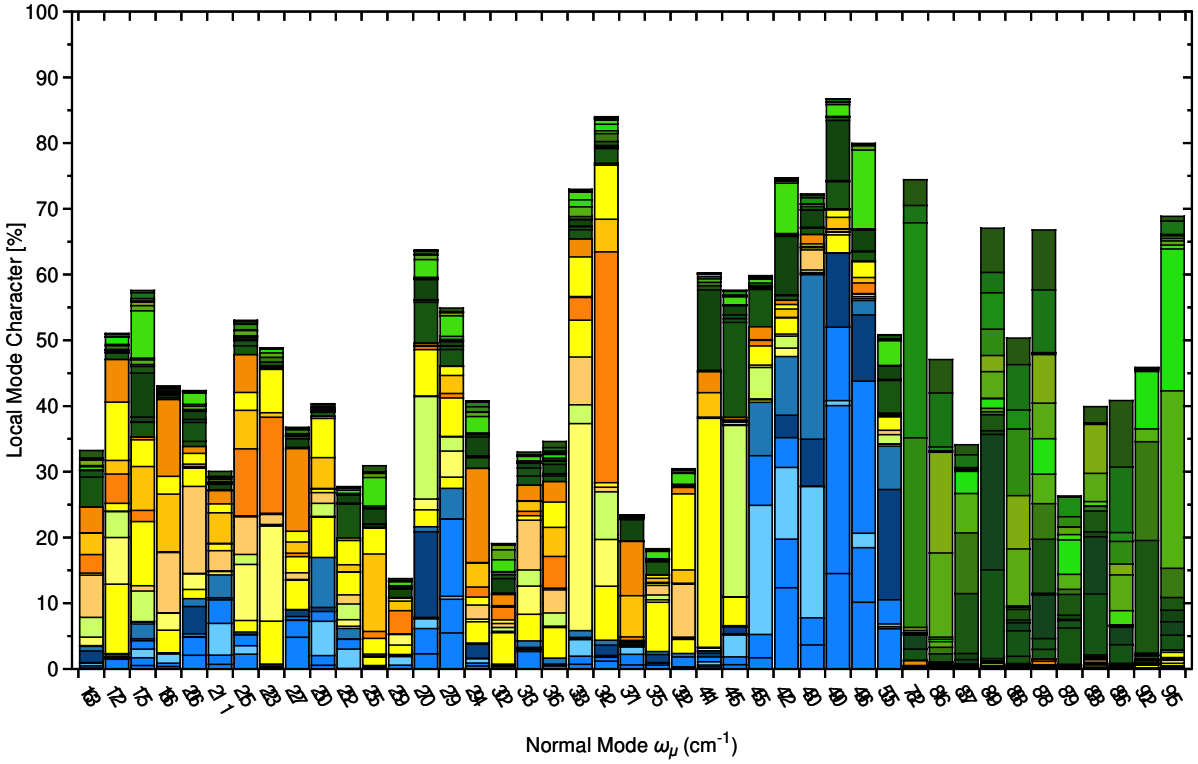

Appendix Figure 2.11. Decomposition of normal vibrational frequencies into % local vibrational mode contributions for complex **3**. In blues correspond to Cr−N stretching contributions, yellows to N−Cr−N bending, greens to Cr−N−C/H bending. Local modes without Cr are omitted for clarity.

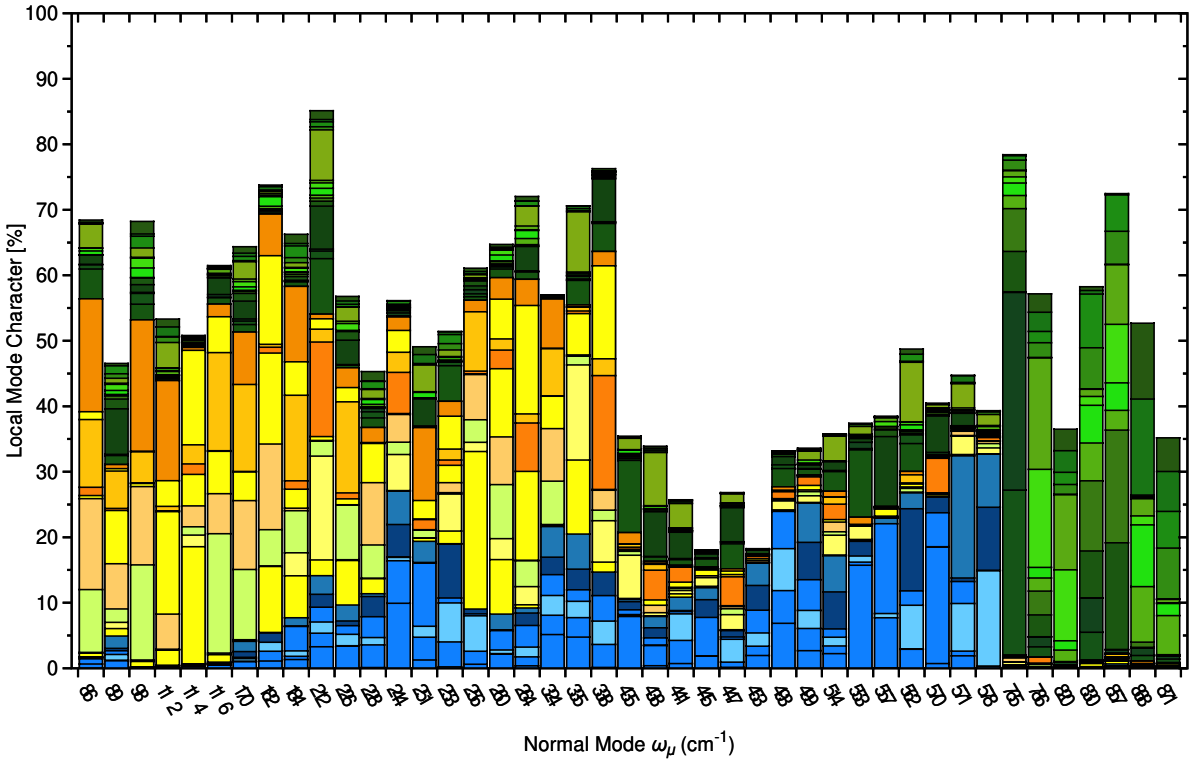

Appendix Figure 2.12. Decomposition of normal vibrational frequencies into % local vibrational mode contributions for complex **4**. In blues correspond to Cr−N stretching contributions, yellows to N−Cr−N bending, greens to Cr−N−C/H bending. Local modes without Cr are omitted for clarity.

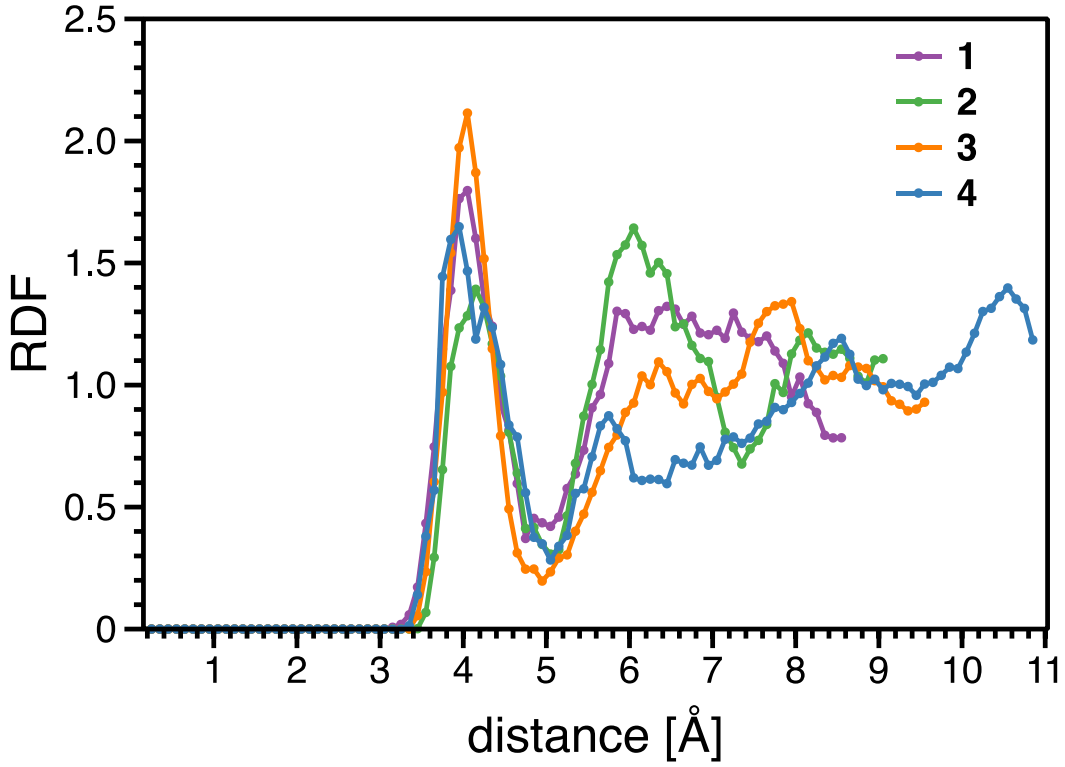

Appendix Figure 2.13. Radial distribution plot of Cr-water distances derived from AIMD.

Appendix 3: Supporting Information for Chapter 4

Appendix Table 3.1. Crystallographic information for the structural refinement of **1**.

Empirical formula	$C_{30}H_{30}B_2F_{10}N_6NiO_6$
Formula weight	840.96 g/mol
Temperature	104.13 K
Crystal system	Triclinic
Space group	*P*-1
a	11.7082(3) Å
b	12.2248(3) Å
c	13.9254(4) Å
α	67.6230(10)°
β	88.3260(10)°
γ	71.7290(10)°
Volume	1740.90(8) $Å^3$
Z	2
ρ_{calc}	1.604 g cm^{-3}
μ	0.663 mm^{-1}
F(000)	856.0
Crystal color	Green
Crystal size	0.138 × 0.061 × 0.031 mm^3
Radiation	MoKα (λ = 0.71073 Å)
2q range for data collection	3.18 to 52.74°
Index ranges	$-14 \leq h \leq 14$, $-15 \leq k \leq 15$, $-17 \leq l \leq 17$
Reflections collected	96824
Independent collections	7132 [R_{int} = 0.0783, R_{sigma} = 0.0276]
Data/restraints/parameters	7132/0/501
Goodness-of-fit on F^2	1.134
Final R indexes [I ≥ 2σ (I)]	R_1 = 0.0431, wR_2 = 0.1100
Final R indexes [all data]	R_1 = 0.0576, wR_2 = 0.1261
Largest diff. peak/hole	1.74/–0.67 e $Å^{-3}$

Appendix Table 3.2. Crystallographic information for the structural refinement of **2**.

Empirical formula	$C_{34}H_{46}B_2N_6NiO_{10}$
Formula weight	779.10 g/mol
Temperature	100.01 K
Crystal system	Monoclinic
Space group	*C*2/*c*
a	26.8983(12) Å
b	8.7226(4) Å
c	17.7343(7) Å
α	90°
β	117.800(2)°
γ	90°
Volume	3680.6(3) $Å^3$
Z	4
ρ_{calc}	1.406 g cm^{-3}
μ	0.592 mm^{-1}
F(000)	1640.0
Crystal color	Green
Crystal size	0.268 × 0.127 × 0.029 mm^3
Radiation	MoKα (λ = 0.71073 Å)
2q range for data collection	3.424 to 49.418°
Index ranges	$-31 \leq h \leq 31$, $-10 \leq k \leq 10$, $-20 \leq l \leq 20$
Reflections collected	45379
Independent collections	3142 [R_{int} = 0.1308, R_{sigma} = 0.0424]
Data/restraints/parameters	3142/0/245
Goodness-of-fit on F^2	1.109
Final R indexes [I ≥ 2σ (I)]	R_1 = 0.0673, wR_2 = 0.1695
Final R indexes [all data]	R_1 = 0.0899, wR_2 = 0.1899
Largest diff. peak/hole	1.55/–0.84 e $Å^{-3}$

Appendix Table 3.3. Crystallographic information for the structural refinement of **3**.

Empirical formula	$C_{31}H_{42}B_2Cl_2N_6NiO_6$
Formula weight	745.92 g/mol
Temperature	100.02 K
Crystal system	Triclinic
Space group	*P*1
a	8.7045(3) Å
b	12.6193(5) Å
c	16.8514(6) Å
α	108.029(2)°
β	91.507(2)°
γ	100.848(2)°
Volume	1721.60(11) $Å^3$
Z	2
ρ_{calc}	1.439 g cm^{-3}
μ	0.771 mm^{-1}
F(000)	780.0
Crystal color	Green
Crystal size	0.256 × 0.043 × 0.037 mm^3
Radiation	MoKα (λ = 0.71073 Å)
2q range for data collection	3.468 to 52.742°
Index ranges	$-10 \leq h \leq 10$, $-15 \leq k \leq 15$, $-21 \leq l \leq 21$
Reflections collected	49643
Independent collections	14052 [R_{int} = 0.0612, R_{sigma} = 0.0586]
Data/restraints/parameters	14052/3/877
Goodness-of-fit on F^2	1.098
Final R indexes [$I \geq 2\sigma(I)$]	R_1 = 0.0408, wR_2 = 0.0908
Final R indexes [all data]	R_1 = 0.0565, wR_2 = 0.1049
Largest diff. peak/hole	0.44/–0.57 e $Å^{-3}$
Flack parameter	0.387(6)

Appendix Table 3.4. Crystallographic information for the structural refinement of **4**.

Empirical formula	$C_{18}H_{16}B_2N_6NiO_6$
Formula weight	492.68 g/mol
Temperature	214.44 K
Crystal system	Monoclinic
Space group	$P2_1/c$
a	11.291(6) Å
b	11.251(4) Å
c	15.826(6) Å
α	90°
β	104.49(2)°
γ	90°
Volume	1946.5(15) $Å^3$
Z	4
ρ_{calc}	1.681g cm^{-3}
μ	1.051 mm^{-1}
F(000)	1008.0
Crystal color	Green
Crystal size	0.102 × 0.065 × 0.032 mm^3
Radiation	MoKα (λ = 0.71073 Å)
2q range for data collection	3.726 to 52.04°
Index ranges	$-13 \leq h \leq 13$, $-13 \leq k \leq 13$, $-19 \leq l \leq 19$
Reflections collected	74743
Independent collections	3824 [R_{int} = 0.0838, R_{sigma} = 0.0247]
Data/restraints/parameters	3824/0/298
Goodness-of-fit on F^2	1.222
Final R indexes [I ≥ 2σ (I)]	R_1 = 0.0306, wR_2 = 0.0813
Final R indexes [all data]	R_1 = 0.0442, wR_2 = 0.0995
Largest diff. peak/hole	0.61/–0.60 e $Å^{-3}$

Appendix Table 3.5. Crystallographic information for the structural refinement of **5**.

Empirical formula	$C_{18}H_{10}B_2Cl_6N_6NiO_6$
Formula weight	699.35 g/mol
Temperature	110.22 K
Crystal system	Triclinic
Space group	*P*-1
a	8.1747(10) Å
b	12.442(2) Å
c	13.2849(18) Å
α	96.637(7)°
β	103.105(9)°
γ	108.640(7)°
Volume	1220.8(3) $Å^3$
Z	2
ρ_{calc}	1.903 g cm^{-3}
μ	1.503 mm^{-1}
F(000)	696.0
Crystal color	Green
Crystal size	0.052 × 0.046 × 0.035 mm^3
Radiation	MoKα (λ = 0.71073 Å)
2q range for data collection	3.216 to 52.988°
Index ranges	$-10 \leq h \leq 10$, $-15 \leq k \leq 15$, $-16 \leq l \leq 16$
Reflections collected	52346
Independent collections	5031 [R_{int} = 0.1056, R_{sigma} = 0.0477]
Data/restraints/parameters	5031/0/352
Goodness-of-fit on F^2	1.044
Final R indexes [$I \geq 2\sigma(I)$]	R_1 = 0.0428, wR_2 = 0.0957
Final R indexes [all data]	R_1 = 0.0649, wR_2 = 0.1043
Largest diff. peak/hole	1.24/–0.40 e $Å^{-3}$

Appendix Table 3.6. Contributions to *D* respective of triplet (*T*) and singlet (*S*) excited states in each complex and their respective energies.

	1		**2**		**3**		**4**		**5**	
State	Contrib. to *D* (cm^{-1})	ΔE (cm^{-1})	Contrib. to *D* (cm^{-1})	ΔE (cm^{-1})	Contrib. to *D* (cm^{-1})	ΔE (cm^{-1})	Contrib. to *D* (cm^{-1})	ΔE (cm^{-1})	Contrib. to *D* (cm^{-1})	ΔE (cm^{-1})
T1	-7.38	11168.9	-1.94	10532.7	-12.12	11379.4	-11.96	11446.1	-6.49	10310.1
T2	18.84	12159.4	1.99	10829.0	18.17	12366.0	21.11	12227.3	19.69	10888.1
T3	17.54	12425.4	23.24	11584.8	19.63	12493.8	20.53	12326.7	19.33	11541.6
T4	3.17	12613.6	22.40	11620.7	0.66	13371	0.10	13062.2	5.89	11572.5
S2	-5.27	24777.8	-5.04	23927.6	-5.13	25323.2	-5.44	25081.5	-5.48	24368.1
S3	-5.10	25247.5	-4.96	24148.4	-5.32	25705.1	-5.37	25616.6	-5.02	24275.3
S4	16.73	25383.1	19.01	24151.3	15.30	25824.7	16.17	25670.4	17.41	24407.3

Appendix Table 3.7. Multiconfiguration coefficients for **1**. Configurations here are listed as occupancy of *d* orbitals, with increasing energy from left to right. For example, in the *T1* column above, "22211" indicates a configuration of $(d_{z2})^2(d_{x2-y2})^2(d_{xy})^2(d_{xz})^1(d_{yz})^1$, like depicted in Fig. 3c of the main text, and the "A" number of 0.226 indicates the contribution of that configuration to the *T1* state.

Excitation Configurations of **1**

T1		***T2***		***T3***		***T4***		***S2***		***S3***		***S4***	
A	*config.*	*A*	*config.*	*A*	*config.*	*A*	*config.*	*A*	*config.*	*A*	*config.*	*A*	*config.*
0.226	22211	0.614	12122	0.455	21212	0.476	22121	0.382	12122	0.139	22220	0.250	22211
0.153	22121	0.103	21212	0.159	11222	0.211	22211	0.160	22211	0.133	22022	0.172	22022
0.144	12212	0.088	12221	0.144	22121	0.105	12221	0.121	11222	0.125	21212	0.107	22121
0.139	21221	0.066	22111	0.109	12212	0.062	12122	0.111	22202	0.124	22121	0.101	12212
0.117	12122	0.055	11222	0.080	21221	0.057	11222	0.069	21221	0.098	12212	0.090	11222
0.100	22112	0.038	12212	0.024	12221	0.033	21122	0.054	22220	0.081	20222	0.074	21122
0.063	21212	0.024	22211	0.019	22112	0.020	12212	0.039	22121	0.075	02222	0.069	22202
0.052	21122	0.008	22121	0.009	22211	0.019	21221	0.036	21212	0.065	22112	0.037	12221
0.004	12221					0.015	21212	0.010	12221	0.059	21221	0.032	02222
								0.007	20222	0.055	12122	0.020	12122
								0.005	12212	0.024	12221	0.014	21212
								0.004	22112	0.011	21122	0.014	22220
										0.007	22211	0.011	22112
										0.004	11222	0.007	21221

Appendix Table 3.8. Multiconfiguration coefficients for **2**. Configurations here are listed as occupancy of *d* orbitals, with increasing energy from left to right. For example, at the top of the *T1* column above, "12122" indicates a configuration of $(d_{z2})^1(d_{x2-y2})^2(d_{xy})^1(d_{xz})^2(d_{yz})^2$, and the "A" number of 0.352 indicates the contribution of that configuration to the *T1* state.

Excitation Configurations of **2**

T1		*T2*		*T3*		*T4*		*S2*		*S3*		*S4*	
A	*config.*	*A*	*config.*	*A*	*config.*	*A*	*config.*	*A*	*config.*	*A*	*config.*	*A*	*config.*
0.352	12122	0.436	11222	0.476	21212	0.451	21221	0.554	11222	0.200	02222	0.324	21212
0.340	21212	0.198	22112	0.273	22121	0.275	12212	0.352	22211	0.178	20222	0.217	12221
0.247	12221	0.183	22211	0.249	12122	0.224	11222	0.073	22112	0.149	22022	0.213	12122
0.061	22121	0.104	12212			0.020	22112	0.014	21221	0.133	22202	0.176	20222
		0.054	21221			0.019	22211	0.007	12212	0.123	22121	0.041	22202
		0.025	21122			0.011	21122			0.109	21212	0.024	22220
										0.084	12221	0.004	22121
										0.023	12122		

Appendix Table 3.9. Multiconfiguration coefficients for **3**. Configurations here are listed as occupancy of *d* orbitals, with increasing energy from left to right. For example, at the top of the *T1* column above, "21221" indicates a configuration of $(d_{z2})^2(d_{x2-y2})^1(d_{xy})^2(d_{xz})^2(d_{yz})^1$ and the "A" number of 0.550 indicates the contribution of that configuration to the *T1* state.

Excitation Configurations of **3**

T1		*T2*		*T3*		*T4*		*S2*		*S3*		*S4*	
A	*config.*	*A*	*config.*	*A*	*config.*	*A*	*config.*	*A*	*config.*	*A*	*config.*	*A*	*config.*
0.550	21221	0.435	21212	0.531	12122	0.408	22121	0.146	12122	0.186	21212	0.373	21221
0.193	12122	0.245	12122	0.182	21221	0.234	12221	0.134	21221	0.143	12122	0.340	12122
0.136	12212	0.172	12221	0.149	21212	0.098	22211	0.131	21212	0.113	12221	0.100	02222
0.041	11222	0.086	22211	0.050	22211	0.088	11222	0.125	22121	0.107	22121	0.081	12212
0.036	22121	0.034	21122	0.030	12221	0.075	21122	0.110	22220	0.095	11222	0.063	20222
0.028	12221	0.014	21221	0.024	21122	0.068	21221	0.097	12221	0.086	22220	0.020	22112
0.007	21212	0.013	22112	0.018	12212	0.015	12212	0.068	02222	0.078	22211	0.012	22220
0.006	22112			0.010	22112	0.010	21212	0.059	22022	0.076	21221	0.003	12221
				0.005	22121			0.054	20222	0.043	22022		
								0.036	22211	0.025	22112		
								0.015	22112	0.017	21122		
								0.011	11222	0.013	02222		
								0.009	21122	0.011	20222		
								0.004	22202	0.007	22202		
								0.003	12212				

Appendix Table 3.10. Multiconfiguration coefficients for **4**. Configurations here are listed as occupancy of *d* orbitals, with increasing energy from left to right. For example, at the top of the *T1* column above, "21212" indicates a configuration of $(d_{z2})^2(d_{x2-y2})^1(d_{xy})^2(d_{xz})^1(d_{yz})^2$ and the "A" number of 0.277 indicates the contribution of that configuration to the *T1* state.

Excitation Configurations of **4**

T1		*T2*		*T3*		*T4*		*S2*		*S3*		*S4*	
A	*config.*	*A*	*config.*	*A*	*config.*	*A*	*config.*	*A*	*config.*	*A*	*config.*	*A*	*config.*
0.277	21212	0.415	12122	0.372	22211	0.374	22112	0.234	12122	0.320	21221	0.365	21212
0.236	12122	0.227	21212	0.281	11222	0.225	21212	0.216	22202	0.258	22112	0.161	22121
0.165	22112	0.119	12221	0.104	21122	0.143	12212	0.131	21222	0.200	12212	0.132	02222
0.113	11222	0.092	22211	0.062	22121	0.095	22121	0.078	22112	0.064	11222	0.103	12122
0.107	21221	0.040	22121	0.055	21221	0.089	11222	0.071	22022	0.047	22022	0.055	22202
0.069	22121	0.040	22112	0.051	12221	0.024	21122	0.068	22121	0.026	22202	0.052	22112
0.024	12221	0.032	12212	0.043	22112	0.021	21221	0.057	02222	0.024	22211	0.039	11222
0.005	22211	0.022	21122	0.026	21212	0.016	12221	0.041	11222	0.015	21212	0.034	12221
0.003	12212	0.007	21221	0.003	12212	0.015	12122	0.035	22211	0.015	12122	0.028	22022
		0.007	11222					0.034	12212	0.010	02222	0.010	20222
								0.012	21221	0.010	12221	0.007	21122
								0.009	12221	0.007	21122	0.005	22211
								0.009	21212	0.003	20222	0.004	12212
								0.005	22220			0.004	22220

Appendix Table 3.11. Multiconfiguration coefficients for **5**. Configurations here are listed as occupancy of *d* orbitals, with increasing energy from left to right. For example, in the *T1* column above, "21221" indicates a configuration of $(d_{z2})^2(d_{x2-y2})^1(d_{xy})^2(d_{xz})^2(d_{yz})^1$ and the "A" number of 0.681 indicates the contribution of that configuration to the *T1* state.

Excitation Configurations of **5**

T1		*T2*		*T3*		*T4*		*S2*		*S3*		*S4*	
A	*config.*	*A*	*config.*	*A*	*config.*	*A*	*config.*	*A*	*config.*	*A*	*config.*	*A*	*config.*
0.681	21221	0.606	22121	0.504	22112	0.689	21212	0.381	22121	0.430	21221	0.378	22202
0.272	22112	0.269	12221	0.289	12212	0.099	22121	0.337	21212	0.347	22112	0.251	22220
0.023	12212	0.055	22211	0.097	21221	0.084	12221	0.107	22211	0.100	12212	0.165	22022
0.016	11222	0.039	21212	0.046	21212	0.079	22211	0.101	12221	0.050	22220	0.159	20222
0.003	22211	0.023	12122	0.024	12122	0.019	22112	0.026	11222	0.028	22202	0.012	21212
0.003	21212	0.003	21221	0.013	22121	0.012	12212	0.011	21122	0.012	12122	0.009	21221
		0.003	21122	0.009	22211	0.010	21221	0.010	22112	0.007	22022	0.009	22121
				0.008	21122	0.004	12122	0.006	20222	0.007	22121	0.008	12212
				0.008	11222	0.003	11222	0.005	12212	0.006	11222	0.004	02222
				0.004	12221			0.004	21221	0.005	20222	0.004	22112
								0.004	02222	0.005	22211		
								0.003	22022	0.003	21212		
								0.003	12122				

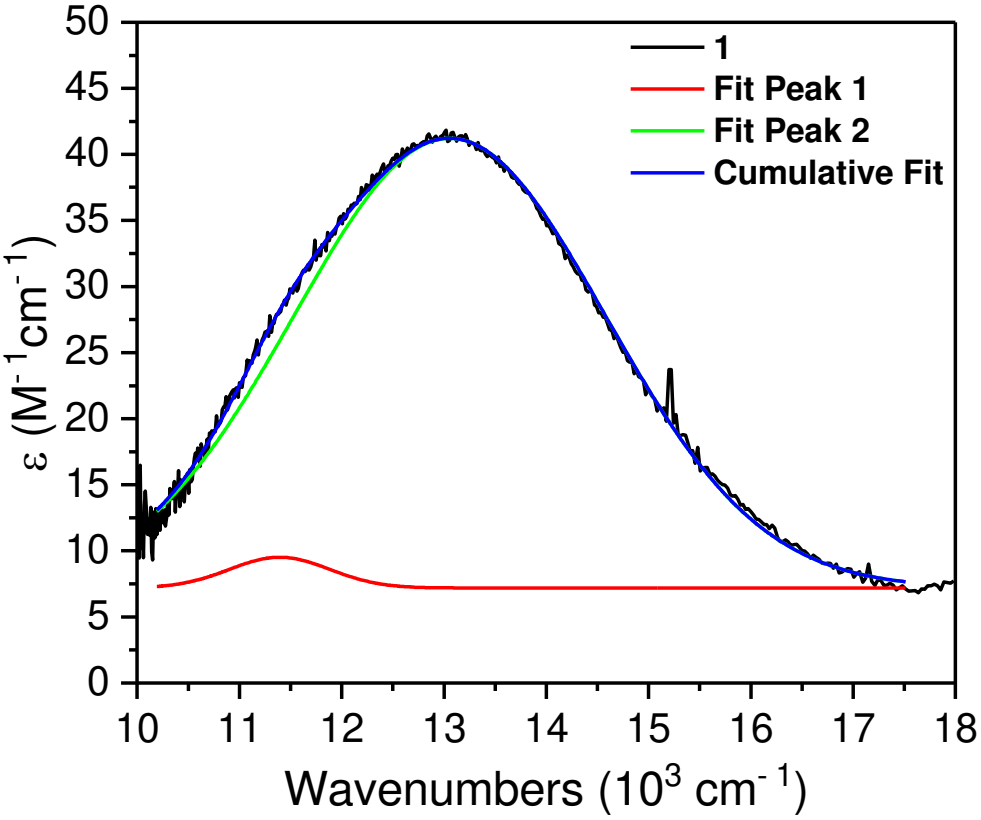

Appendix Figure 3.1. Deconvoluted electronic absorption spectra of **1**. Peak 1: 11406 cm^{-1}. Peak 2: 13071 cm^{-1}.

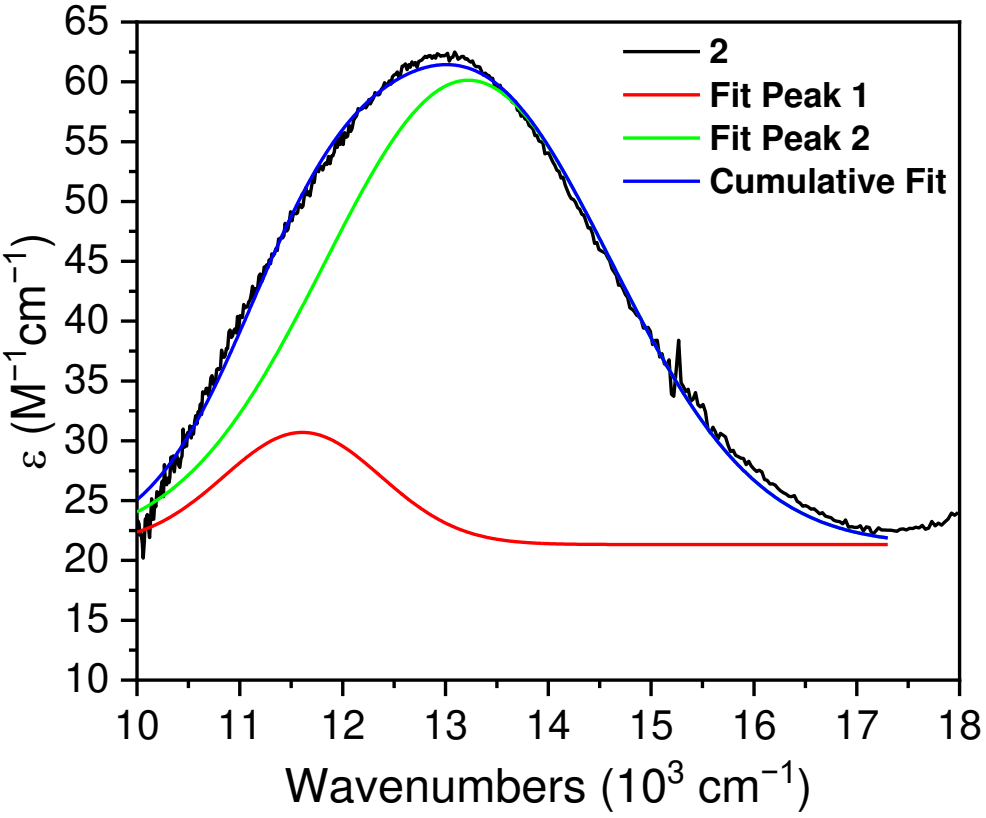

Appendix Figure 3.2. Deconvoluted electronic absorption spectra of **2**. Peak 1: 11397 cm^{-1}. Peak 2: 13053 cm^{-1}.

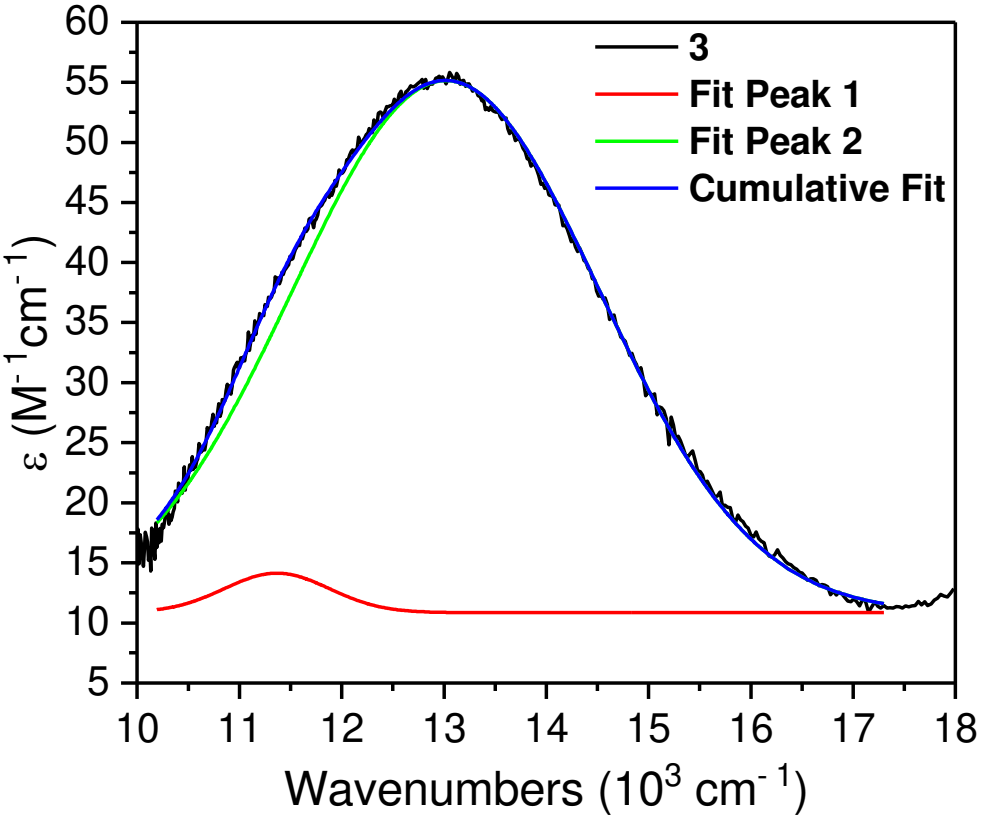

Appendix Figure 3.3. Deconvoluted electronic absorption spectra of **3**. Peak 1: 11608 cm^{-1}. Peak 2: 13222 cm^{-1}.

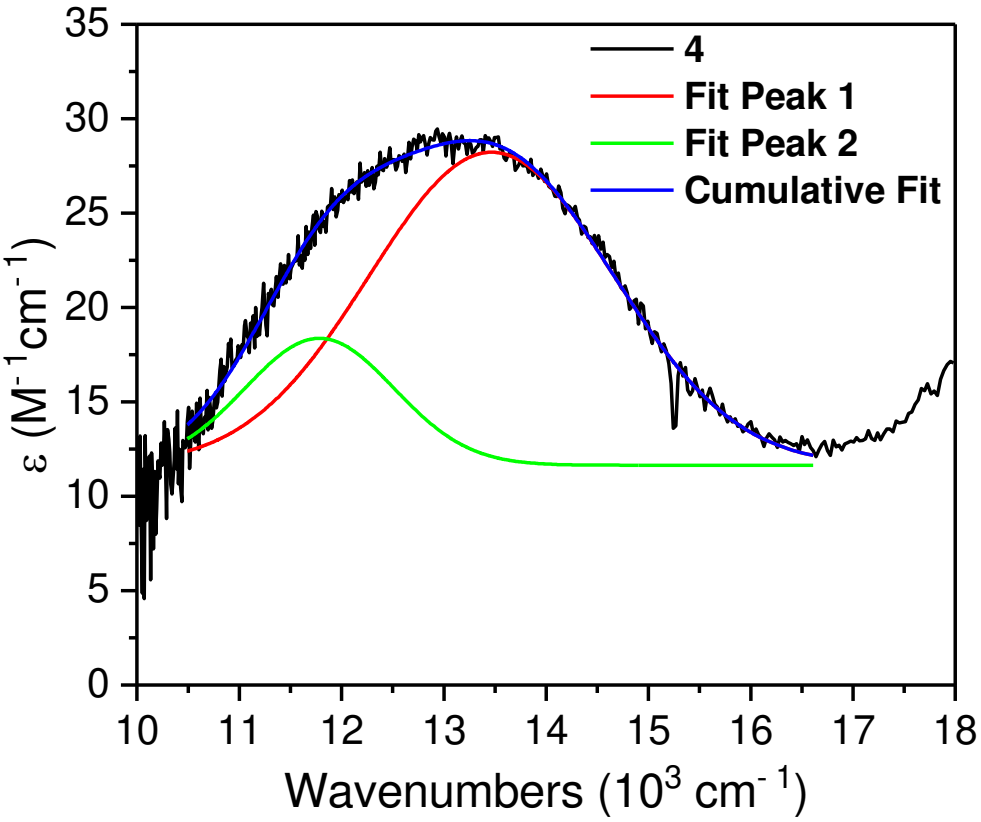

Appendix Figure 3.4. Deconvoluted electronic absorption spectra of **4**. Peak 1: 13412 cm^{-1}. Peak 2: 11703 cm^{-1}.

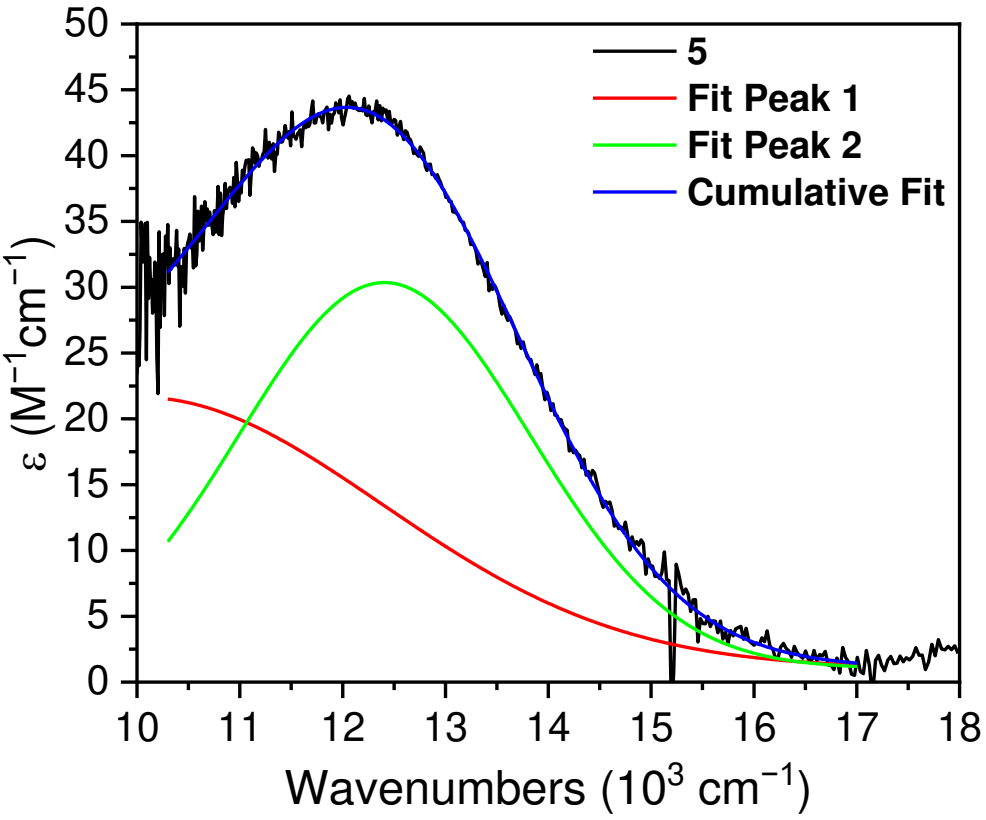

Appendix Figure 3.5. Deconvoluted electronic absorption spectra of **5**. Peak 1: 9903 cm^{-1}. Peak 2: 12396 cm^{-1}.

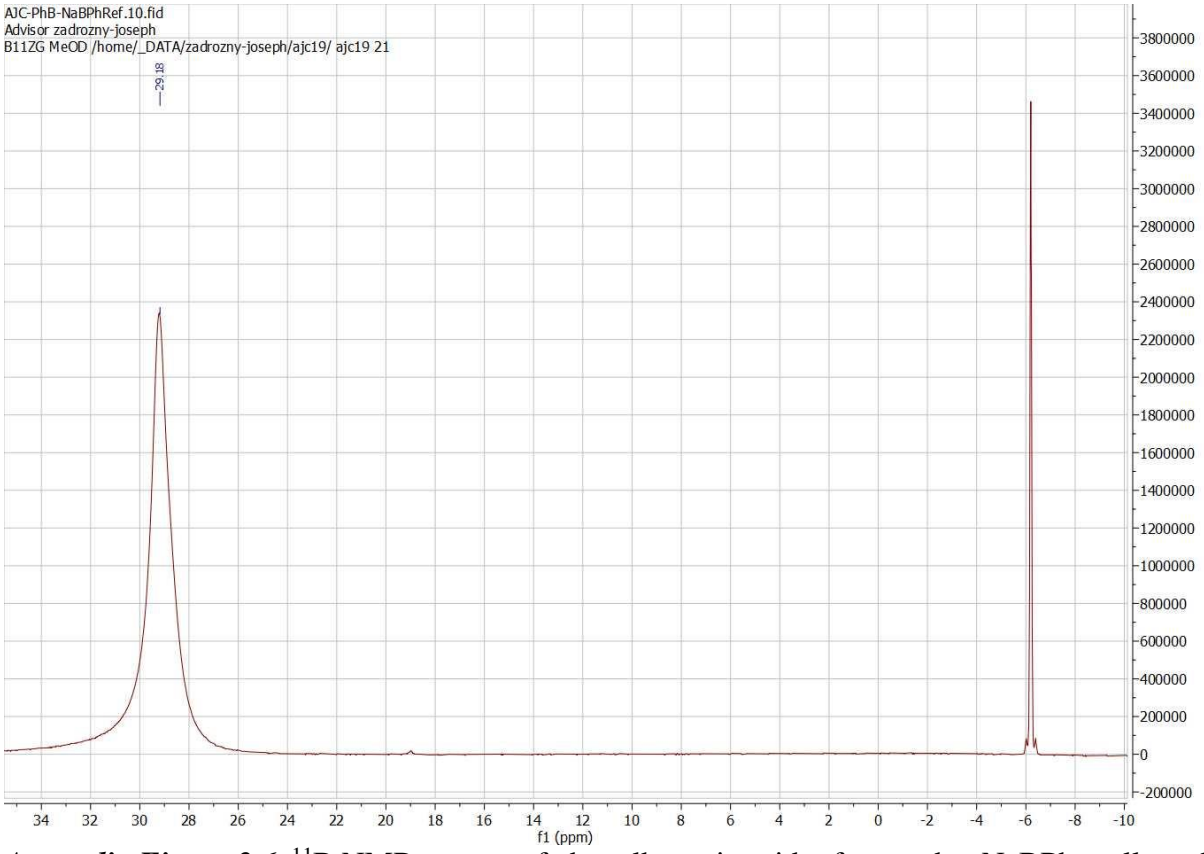

Appendix Figure 3.6. ^{11}B NMR spectra of phenylboronic acid referenced to $NaBPh_4$ collected in MeOH-d_4.

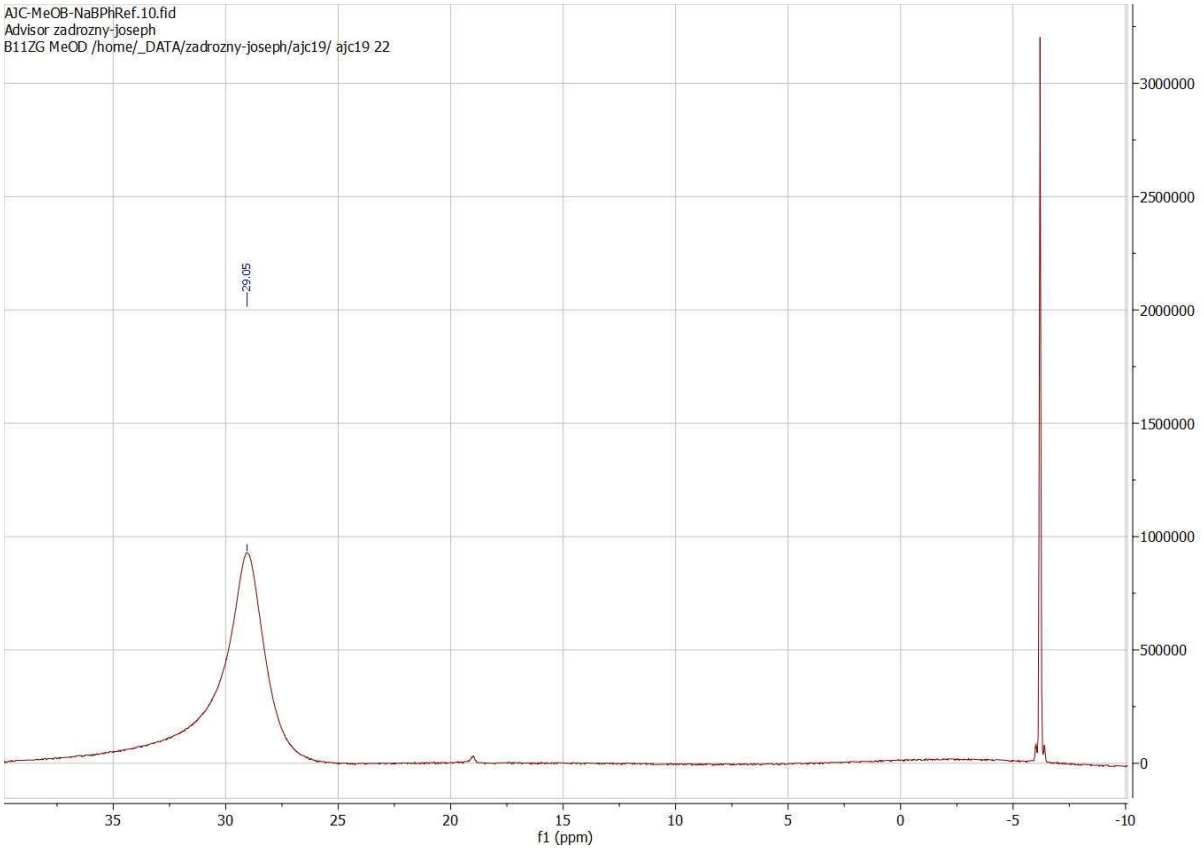

Appendix Figure 3.7. ^{11}B NMR spectra of 3,5-dimethoxyphenylboronic acid referenced to $NaBPh_4$ collected in MeOH-d_4.

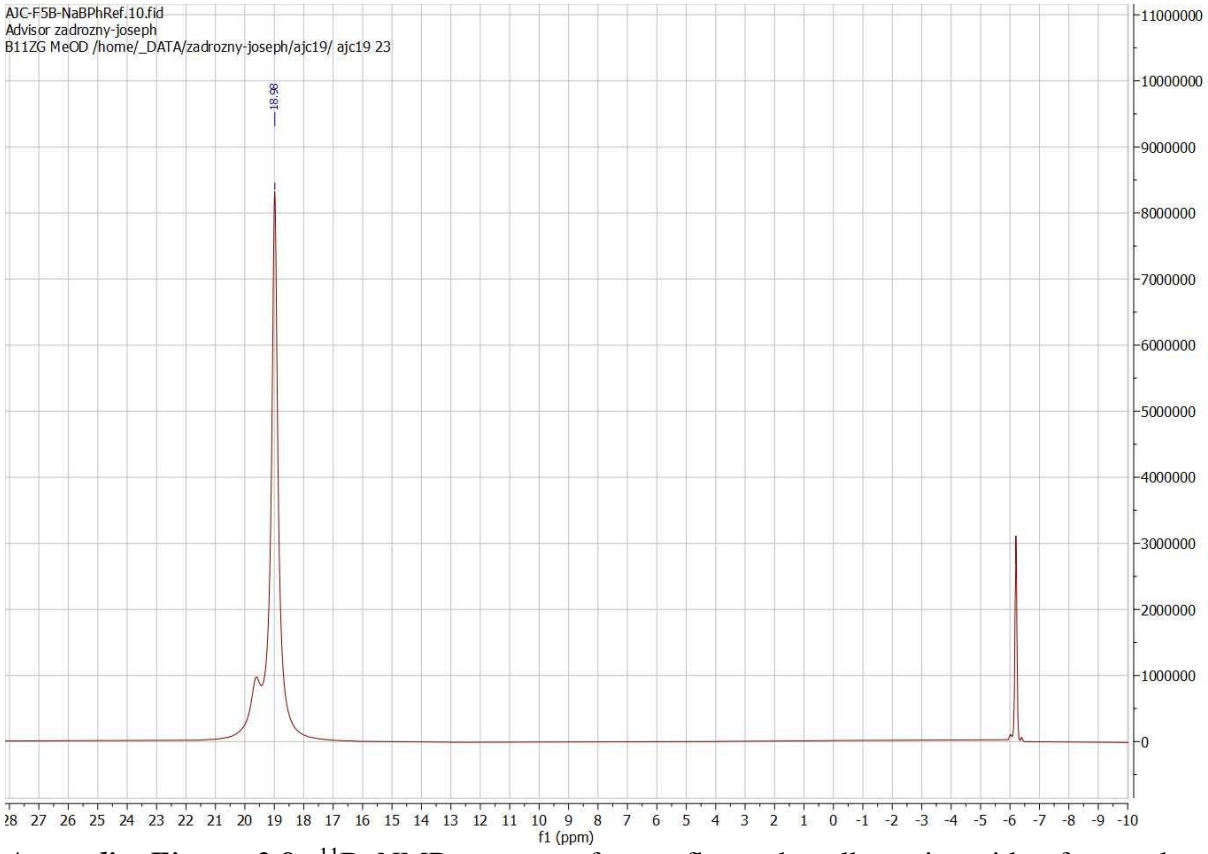

Appendix Figure 3.8. ^{11}B NMR spectra of pentafluorophenylboronic acid referenced to $NaBPh_4$ collected in MeOH-d_4.

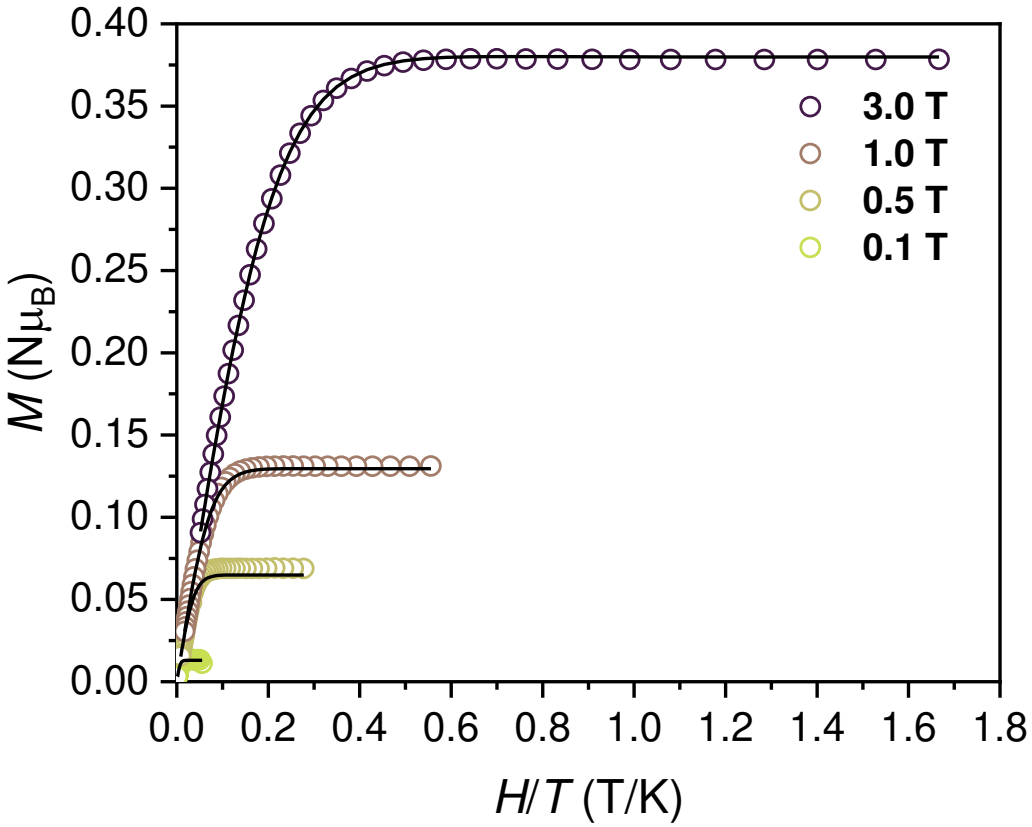

Appendix Figure 3.9. Reduced magnetization data and fits obtained through PHI for complex **1**.

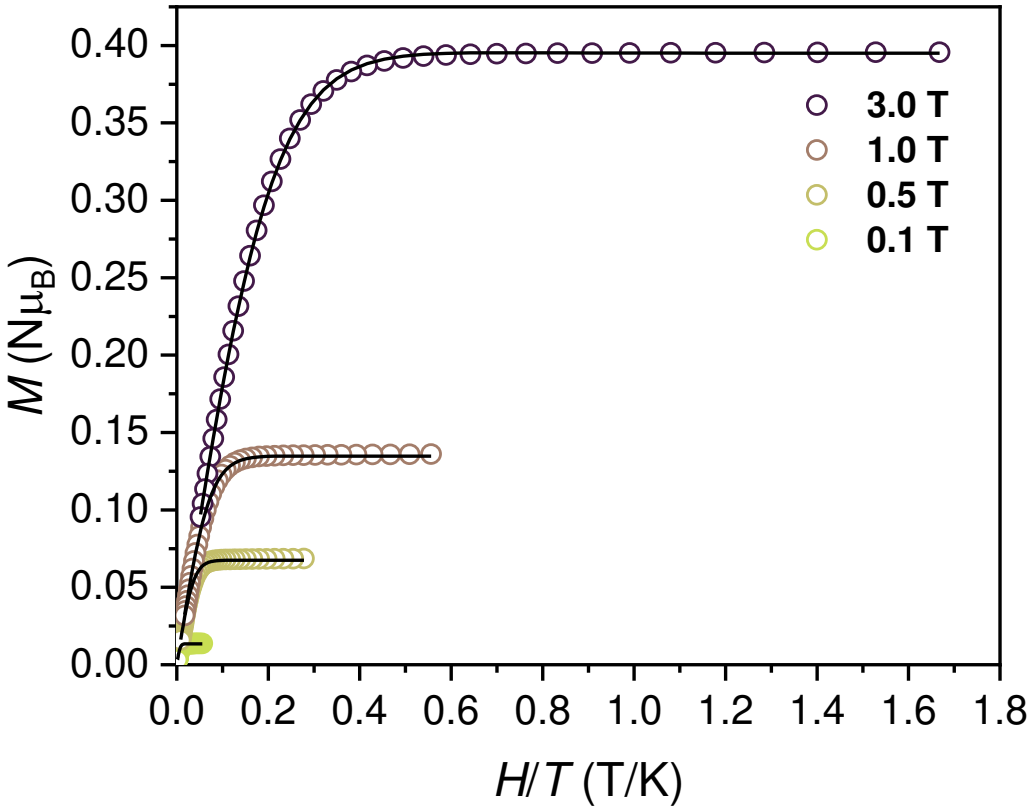

Appendix Figure 3.10. Reduced magnetization data and fits obtained through PHI for complex **2**.

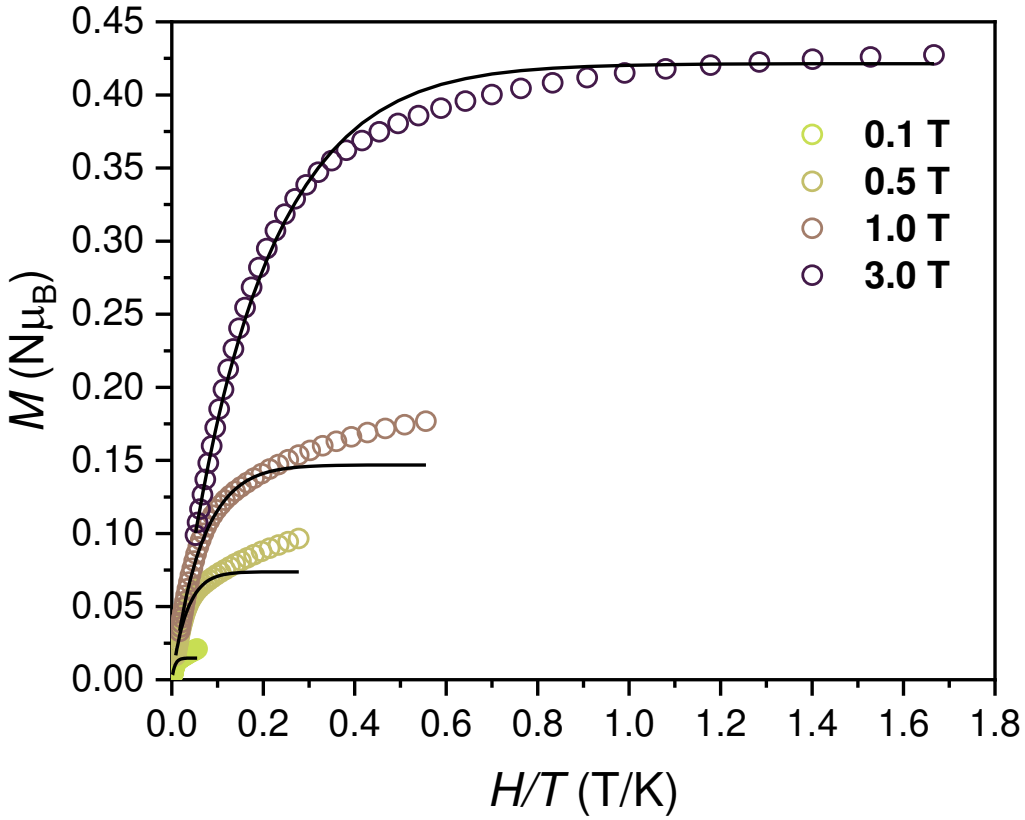

Appendix Figure 3.11. Reduced magnetization data and fits obtained through PHI for complex **4**.

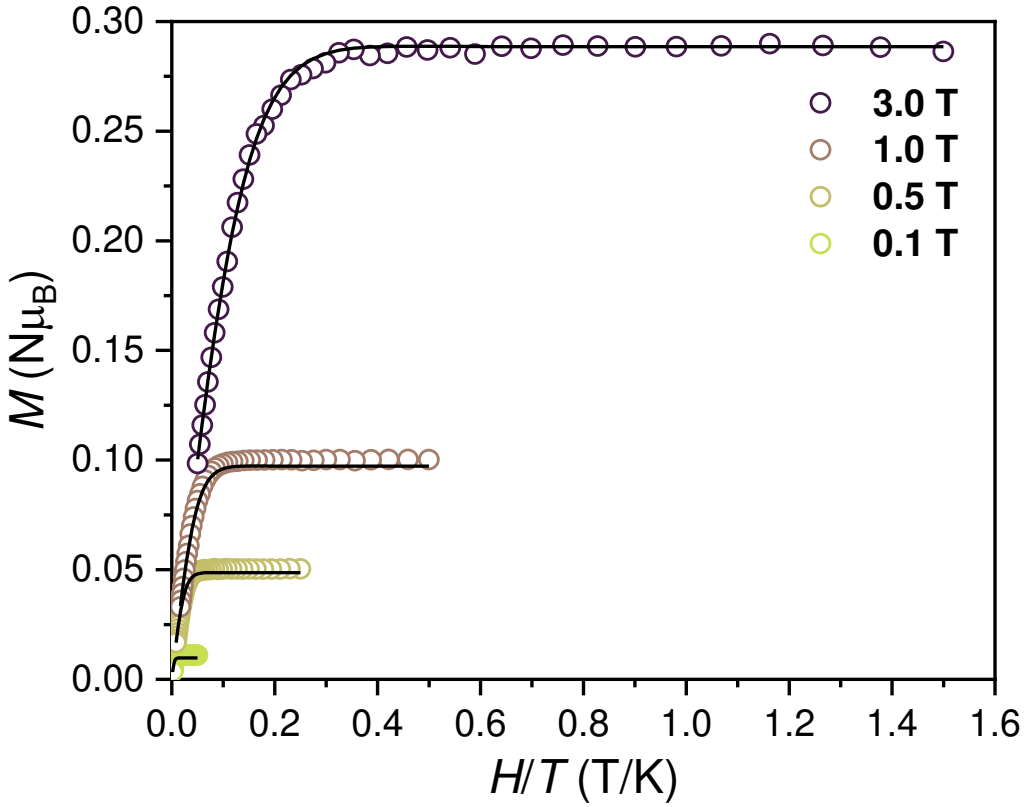

Appendix Figure 3.12. Reduced magnetization data and fits obtained through PHI for complex **5**.

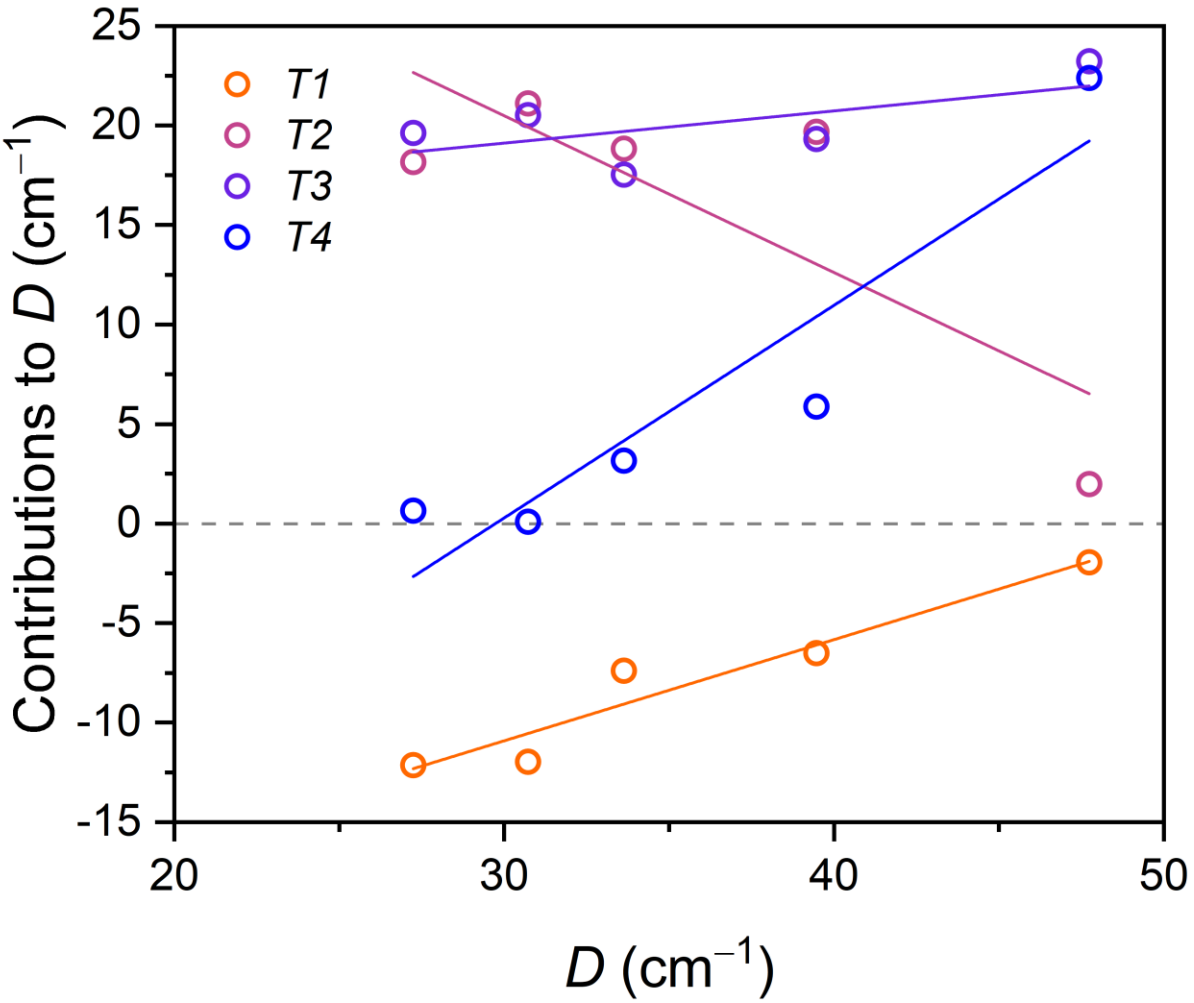

Appendix Figure 3.13. Contributions to *D* respective of triplet (*T*) excited states relative to the predicted total *D* value for each of the five compounds.

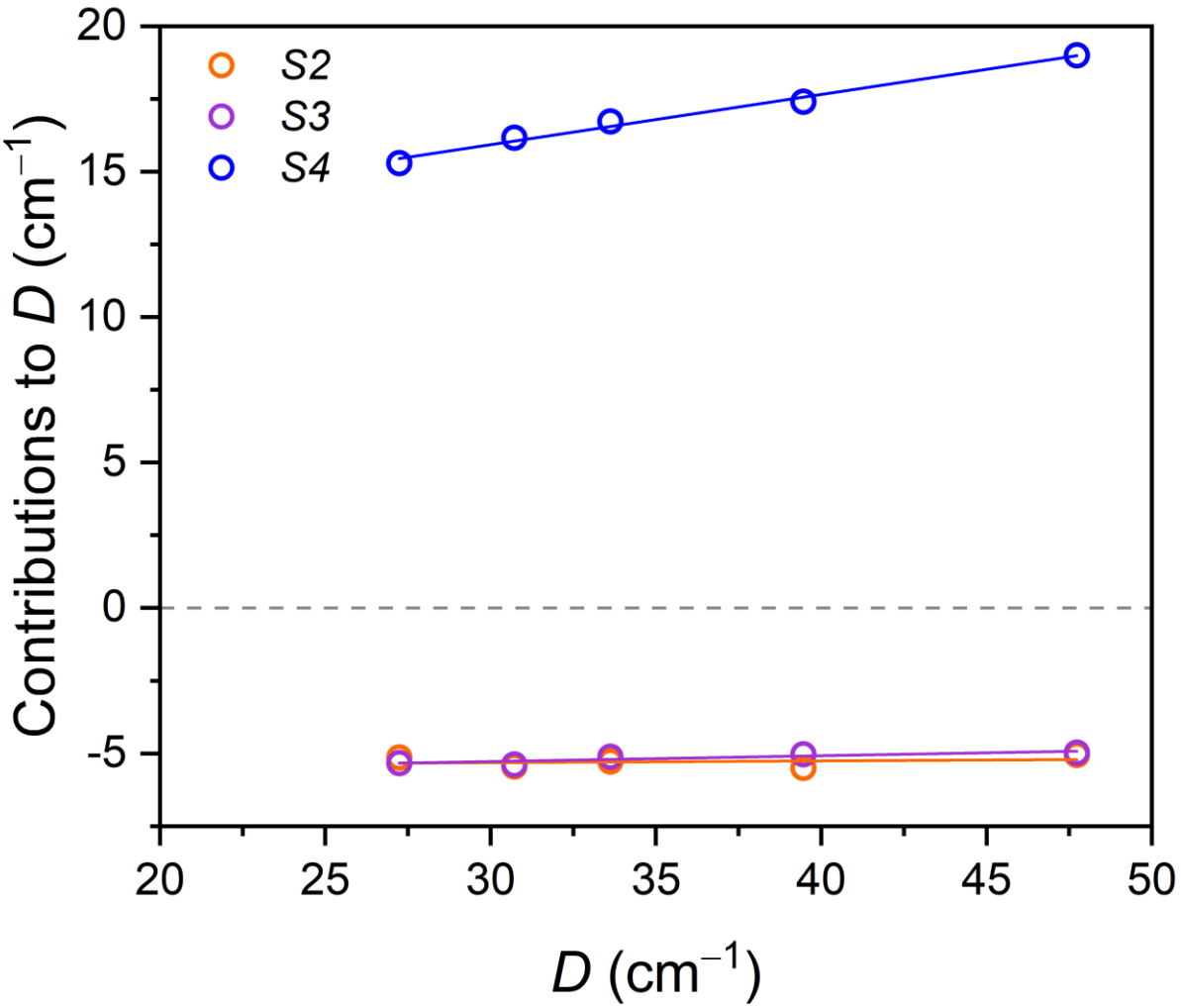

Appendix Figure 3.14. Contributions to *D* respective of singlet (*S*) excited states relative to the predicted total *D* value for each of the five compounds.

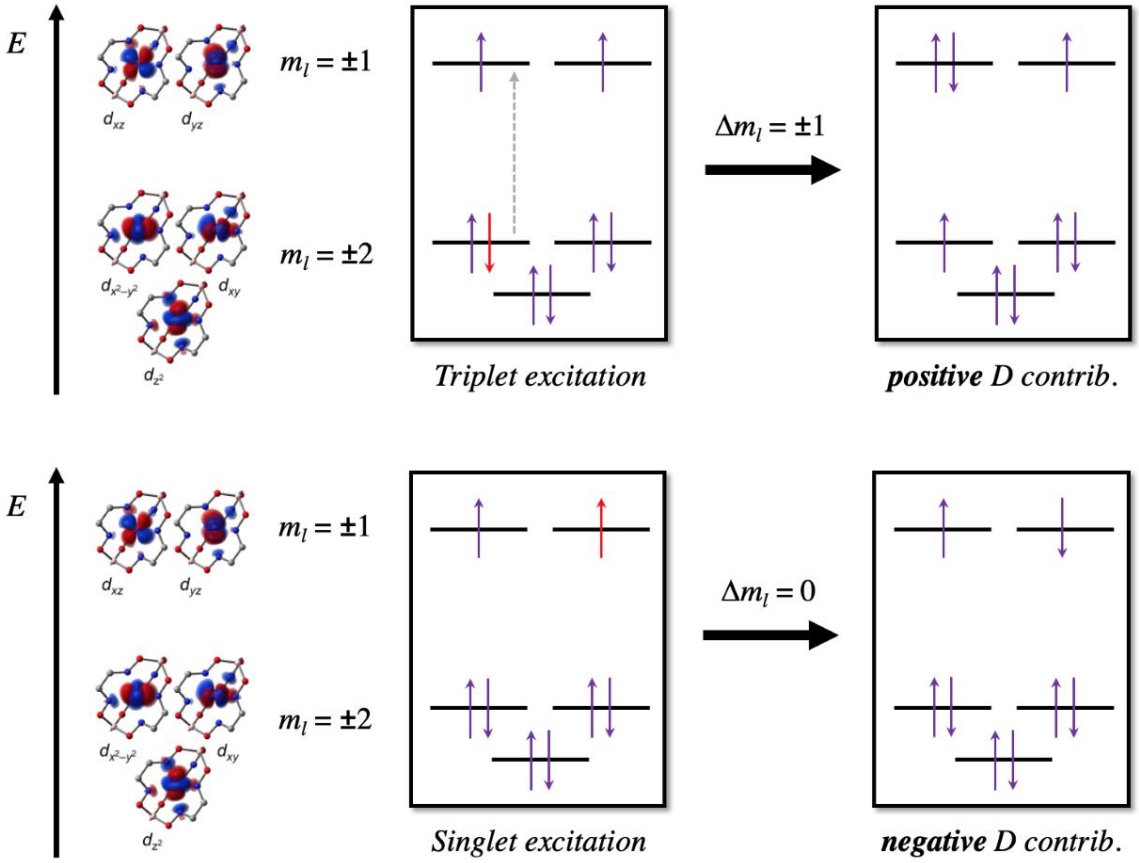

Appendix Figure 3.15. Depiction of some example triplet (top) and singlet (bottom) excitations responsible for positive and negative contributions to *D*, highlighted by the change in Dm_l for the specific excitation.

Appendix 4: Supporting Information for Chapter 5

Appendix Table 4.1. Crystallographic information for the structural refinement of **1**.

Empirical formula	$C_{18}H_{30}F_{12}Mn_2N_8P_2$
Formula weight	703.38 g/mol
Temperature	99.99 K
Crystal system	Trigonal
Space group	$P31c$
a	9.5381(2) Å
b	9.5381(2) Å
c	17.2367(6) Å
α	90°
β	90°
γ	120°
Volume	1358.03(7) $Å^3$
Z	2
ρ_{calc}	1.720 g cm^{-3}
μ	0.713 mm^{-1}
F(000)	714
Crystal color	Orange
Crystal size	0.997 × 0.793 × 0.101 mm^3
Radiation	MoKα (λ = 0.71073 Å)
2θ range for data collection	2.362 to 51.346°
Index ranges	$-11 \leq h \leq 11$, $-11 \leq k \leq 11$, $-21 \leq l \leq 21$
Reflections collected	90018
Independent collections	1728 [R_{int} = 0.0704, R_{sigma} = 0.0127]
Data/restraints/parameters	1728/1/125
Goodness-of-fit on F^2	1.112
Final R indexes [$I \geq 2\sigma(I)$]	R_1 = 0.0260, wR_2 = 0.0679
Final R indexes [all data]	R_1 = 0.0277, wR_2 = 0.0688
Largest diff. peak/hole	0.42/–0.19 e $Å^{-3}$
Flack parameter	0.007(6)

Appendix Table 4.2. Crystallographic information for the structural refinement of **2**.

Empirical formula	$C_{18}H_{42}F_{12}MnN_8P_2$
Formula weight	715.48 g/mol
Temperature	100 K
Crystal system	Trigonal
Space group	*P*–3*c*1
a	9.7469(4) Å
b	9.7469(4) Å
c	16.8886(13) Å
α	90°
β	90°
γ	120°
Volume	1389.50(16) $Å^3$
Z	2
ρ_{calc}	1.710 g cm^{-3}
μ	0.698 mm^{-1}
F(000)	738
Crystal color	Orange
Crystal size	0.178 × 0.114 × 0.111 mm^3
Radiation	MoKα (λ = 0.71073 Å)
2θ range for data collection	4.824 to 62.988°
Index ranges	$-14 \leq h \leq 14$, $-14 \leq k \leq 14$, $-24 \leq l \leq 24$
Reflections collected	154430
Independent collections	1560 [R_{int} = 0.0609, R_{sigma} = 0.0085]
Data/restraints/parameters	1559/0/64
Goodness-of-fit on F^2	1.056
Final R indexes [$I \geq 2\sigma(I)$]	R_1 = 0.0237, wR_2 = 0.0641
Final R indexes [all data]	R_1 = 0.0269, wR_2 = 0.0663
Largest diff. peak/hole	0.44/–0.34 e $Å^{-3}$

Appendix Table 4.3. Crystallographic information for the structural refinement of **3**.

Empirical formula	$C_{26}H_{37}F_{12}MnN_5O_4P_2$
Formula weight	828.49 g/mol
Temperature	99 K
Crystal system	Monoclinic
Space group	$P2_1/c$
a	20.6706(13) Å
b	9.5894(6) Å
c	16.6823(11) Å
α	90°
β	100.993(2)°
γ	90°
Volume	3246.1(4) $Å^3$
Z	4
ρ_{calc}	1.695 g cm^{-3}
μ	0.617 mm^{-1}
F(000)	1692
Crystal color	Orange
Crystal size	0.089 × 0.071 × 0.052 mm^3
Radiation	MoKα (λ = 0.71073 Å)
2θ range for data collection	4.922 to 51.360°
Index ranges	$-25 \leq h \leq 25$, $-11 \leq k \leq 11$, $-20 \leq l \leq 20$
Reflections collected	56128
Independent collections	6172 [R_{int} = 0.1103, R_{sigma} = 0.0536]
Data/restraints/parameters	6172/0/452
Goodness-of-fit on F^2	1.036
Final R indexes [$I \geq 2\sigma(I)$]	R_1 = 0.0411, wR_2 = 0.0744
Final R indexes [all data]	R_1 = 0.0751, wR_2 = 0.0842
Largest diff. peak/hole	0.41/–0.36 e $Å^{-3}$

Appendix Table 4.4. Tabulation of best simulation parameters for the variable-temperature, solid state 390 GHz EPR spectra of **1**. [a]Strains used are *g* strains ordered as strain in [g_x g_y g_z].

T	g_x	g_y	g_z	**Strain**[a]	***D*** **(MHz)**	***E*** **(MHz)**
5	2.008	2.000	2.004	[0.011 0.02 0.01]	800	220
10	2.005	2.001	2.000	[0.01 0.01 0.012]	760	210
20	2.006	2.003	2.002	[0.01 0.008 0.01]	720	210
30	2.006	2.003	2.002	[0.017 0.009 0.014]	700	210
40	2.002	2.0015	2.001	[0.011 0.01 0.01]	700	200
50	2.004	2.002	1.999	[0.009 0.009 0.009]	700	200
60	2.002	2.001	1.995	[0.009 0.009 0.009]	700	200
70	2.003	2.002	1.999	[0.009 0.008 0.009]	700	200
80	2.000	1.999	1.995	[0.009 0.008 0.009]	700	200
100	2.001	2.000	1.995	[0.009 0.008 0.009]	700	200
120	2.003	2.002	1.999	[0.007 0.008 0.008]	700	200
140	2.0015	2.000	1.994	[0.007 0.008 0.008]	700	200
160	2.0035	2.002	1.995	[0.007 0.009 0.009]	700	200
180	2.003	2.001	1.992	[0.007 0.007 0.008]	700	200
200	2.0035	2.0025	2.000	[0.007 0.007 0.008]	650	200
250	2.003	2.001	1.995	[0.007 0.009 0.008]	650	200
300	2.005	2.004	1.999	[0.007 0.009 0.008]	650	200

Appendix Table 4.5. Tabulation of best simulation parameters for the variable-temperature, solid state 390 GHz EPR spectra of **2**. [a]Strains used are *g* strains ordered as strain in [g_x g_y g_z].

T	g_x	g_y	g_z	**Strain**[a]	***D*** **(MHz)**	***E*** **(MHz)**
5	1.998	1.999	1.989	[0.02 0.0025 0.007]	900	220
10	1.998	1.999	1.994	[0.02 0.002 0.006]	1070	220
20	2.000	1.997	1.995	[0.02 0.002 0.007]	1090	260
30	2.004	2.0025	2.000	[0.02 0.003 0.006]	1250	360
40	2.0025	2.001	1.999	[0.015 0.007 0.006]	1290	400
50	2.004	2.0037	2.002	[0.015 0.007 0.006]	1340	400
60	2.002	2.001	2.000	[0.015 0.007 0.006]	1340	400
70	2.004	2.0037	2.002	[0.015 0.007 0.008]	1340	400
80	2.0035	2.003	2.002	[0.013 0.007 0.009]	1300	400
100	2.0035	2.003	2.002	[0.014 0.006 0.009]	1340	410
120	2.001	2.001	2.000	[0.014 0.006 0.009]	1280	400
140	2.0035	2.0035	2.0025	[0.013 0.006 0.01]	1280	400
160	2.0015	2.0005	1.999	[0.013 0.006 0.008]	1280	400
180	2.004	2.0035	2.001	[0.013 0.0065 0.008]	1280	400
200	2.002	2.0015	2.000	[0.013 0.007 0.008]	1280	400
250	2.004	2.003	2.003	[0.013 0.009 0.006]	1280	400
300	2.0015	2.0005	2.000	[0.013 0.007 0.006]	1240	380

Appendix Table 4.6. Tabulation of best simulation parameters for the variable-temperature, solid state 390 GHz EPR spectra of **3**. [a]Strains used are *g* strains ordered as strain in [g_x g_y g_z].

T	g_x	g_y	g_z	**Strain**[a]	***D*** **(MHz)**	***E*** **(MHz)**
5	1.997	2.006	2.001	[0.011 0.009 0.010]	1050	260
10	1.999	2.008	2.003	[0.008 0.008 0.011]	950	230
20	1.996	2.0045	2.001	[0.006 0.006 0.005]	940	200
30	1.996	2.006	2.001	[0.006 0.006 0.005]	940	200
40	1.998	2.008	2.004	[0.006 0.007 0.006]	940	220
50	1.999	2.005	2.001	[0.006 0.006 0.007]	940	220
60	2.000	2.006	2.002	[0.005 0.005 0.006]	940	220
70	1.999	2.0045	2.000	[0.006 0.005 0.006]	940	220
80	2.001	2.0065	2.002	[0.0055 0.005 0.006]	940	220
100	2.001	2.007	2.002	[0.006 0.005 0.006]	940	220
120	2.000	2.005	2.001	[0.006 0.0055 0.006]	940	220
140	2.001	2.006	2.001	[0.006 0.006 0.006]	940	220
160	2.000	2.004	2.000	[0.006 0.006 0.006]	940	220
180	2.001	2.005	2.001	[0.006 0.006 0.006]	940	220
200	2.001	2.005	2.001	[0.006 0.006 0.006]	940	220
250	2.002	2.005	2.002	[0.006 0.006 0.006]	900	220
300	2.000	2.002	2.000	[0.006 0.006 0.006]	900	220

Appendix Table 4.7. Tabulation of best simulation parameters for the variable-temperature, frozen solution state 9.36 GHz EPR spectra of **1** in butyronitrile at 5 mM. Units of *A* and *A*-strain are MHz. [a]Strains used are *g*/*A* strains ordered as strain in [g/A_x g/A_y g/A_z].

T	g_x	g_y	g_z	***g*-strain**[a]	***D*** **(MHz)**	***E*** **(MHz)**
5.5	2.049	2.038	2.034	[0.003 0.035 0.002]	800	225
10	2.049	2.042	2.030	[0.003 0.020 0.002]	790	210
20	2.000	1.990	1.980	[0.001 0.040 0.040]	795	220
30	2.000	1.990	1.980	[0.001 0.035 0.035]	810	220
40	2.000	1.995	1.975	[0.001 0.035 0.035]	790	220
50	2.000	1.995	1.975	[0.001 0.035 0.035]	800	215
60	2.000	1.995	1.975	[0.001 0.025 0.025]	800	215

T	A_x	A_y	A_z	***A*-strain**[a]
5.5	210	255	210	[55 95 95]
10	215	257	215	[55 85 70]
20	230	220	235	[5 95 85]
30	230	220	235	[5 95 85]
40	230	225	230	[5 95 85]
50	230	225	230	[5 95 85]
60	230	225	240	[5 95 85]

Appendix Table 4.8. Tabulation of best simulation parameters for the variable-temperature, frozen solution state 9.36 GHz EPR spectra of **2** in butyronitrile at 5 mM. Units of *A* and *A*-strain are MHz. [a]Strains used are *g*/*A* strains ordered as strain in [g/A_x g/A_y g/A_z].

T	g_x	g_y	g_z	***g*-strain**[a]	***D* (MHz)**	***E* (MHz)**
10	2.007	2.004	2.002	[0.015 0.015 0.015]	1260	220
20	2.007	2.004	2.002	[0.015 0.015 0.015]	1280	220
30	2.007	2.004	2.002	[0.015 0.015 0.015]	1270	215
40	2.007	2.004	2.002	[0.015 0.015 0.015]	1275	210
50	2.007	2.004	2.002	[0.015 0.015 0.015]	1275	210
60	2.007	2.004	2.002	[0.015 0.015 0.015]	1285	210

T	A_x	A_y	A_z	***A*-strain**[a]
10	215	240	220	[75 85 85]
20	210	235	215	[75 85 85]
30	215	240	220	[75 85 85]
40	215	240	220	[75 85 85]
50	215	240	220	[75 85 85]
60	215	240	220	[75 85 85]

Appendix Table 4.9. Tabulation of best simulation parameters for the variable-temperature, frozen solution state 9.36 GHz EPR spectra of **3** in butyronitrile at 5 mM. Units of *A* and *A*-strain are MHz. [a]Strains used are *g*/*A* strains ordered as strain in [g/A_x g/A_y g/A_z].

T	g_x	g_y	g_z	***g*-strain**[a]	***D* (MHz)**	***E* (MHz)**
5.5	2.020	2.015	2.022	[0.002 0.002 0.002]	980	205
10	2.010	2.005	2.012	[0.002 0.002 0.002]	980	220
25	2.010	2.005	2.012	[0.002 0.002 0.002]	975	215
30	2.005	2.005	2.005	[0.002 0.002 0.002]	960	205
40	2.005	2.005	2.005	[0.008 0.008 0.008]	955	210
50	2.005	2.005	2.005	[0.008 0.008 0.008]	945	205
60	2.005	2.005	2.005	[0.008 0.008 0.008]	945	205

T	A_x	A_y	A_z	***A*-strain**[a]
5.5	210	200	240	[25 45 15]
10	240	265	245	[25 45 25]
25	235	255	235	[35 45 35]
30	210	275	240	[15 55 15]
40	235	300	265	[80 85 35]
50	230	295	260	[80 85 35]
60	230	295	260	[80 85 35]

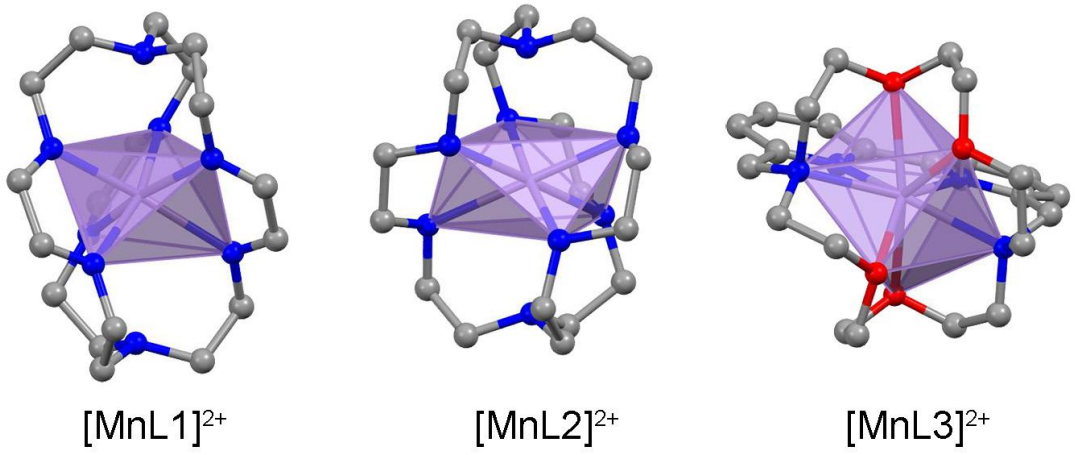

Appendix Figure 4.1. Depictions of the Mn-centered polyhedral in **1-3**.

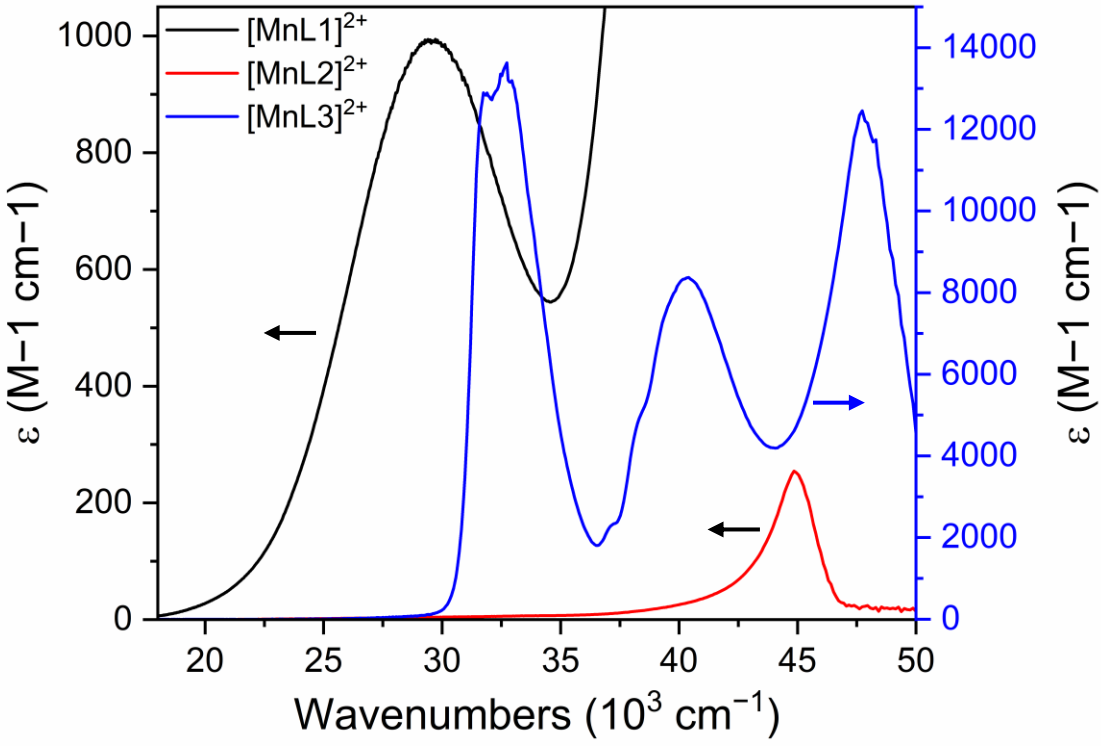

Appendix Figure 4.2. Solution phase, room temperature UV-Vis spectra for **1-3**. Concentrations were *ca*. 0.1 to 10 mM in the complexes. Intensities were normalized to e values from 3-point Beers' law analyses.

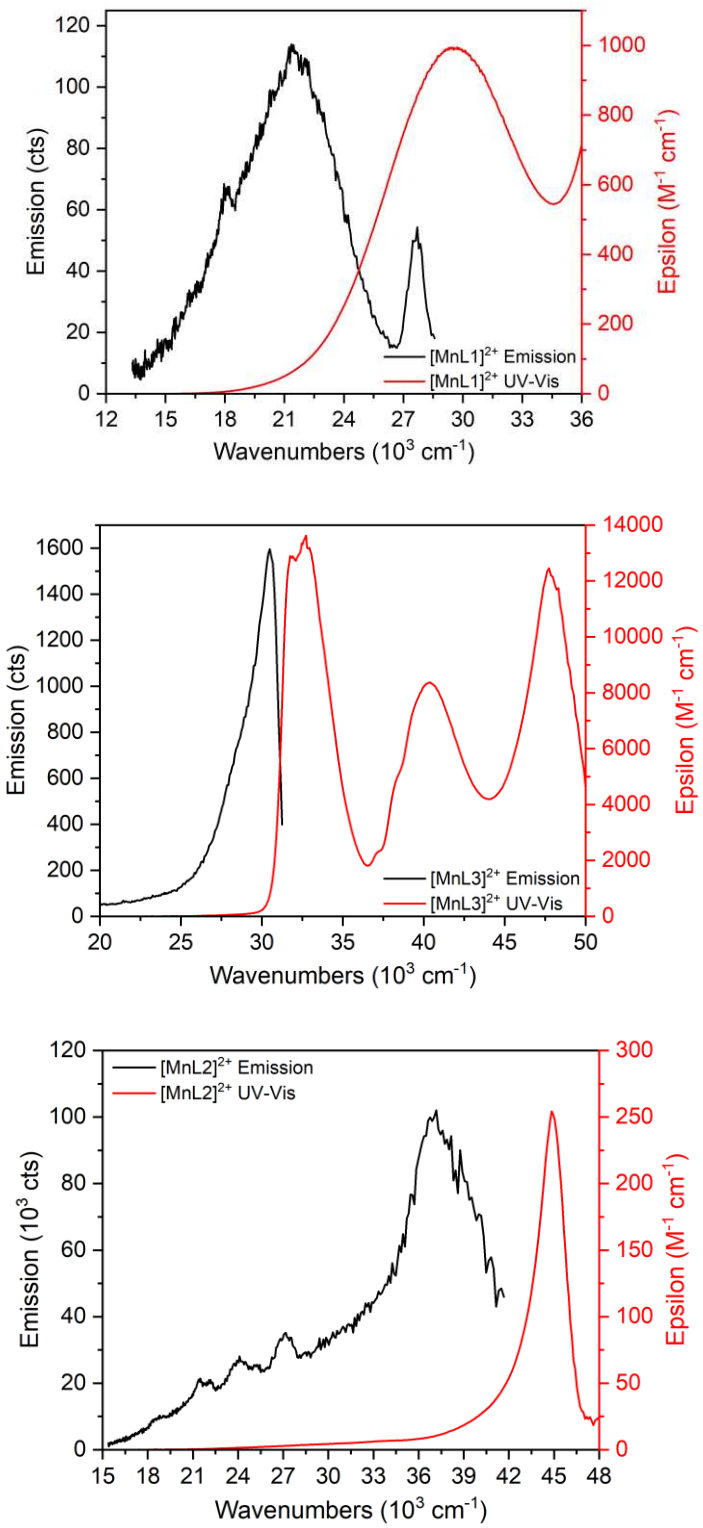

Appendix Figure 4.3. Solution phase, room temperature Emission spectra for **1** (top), **2** (middle), and **3** (bottom). Irradiation wavelengths were 300 m (**1**), 220 nm (**2**), 300 nm (**3**), with integration times of 0.5 s. Concentrations were 0.2 to 12 mM (same as UV-Vis in **Figure A4.2**. the solvent was MeCN and the temperature of measurement was 20 °C.

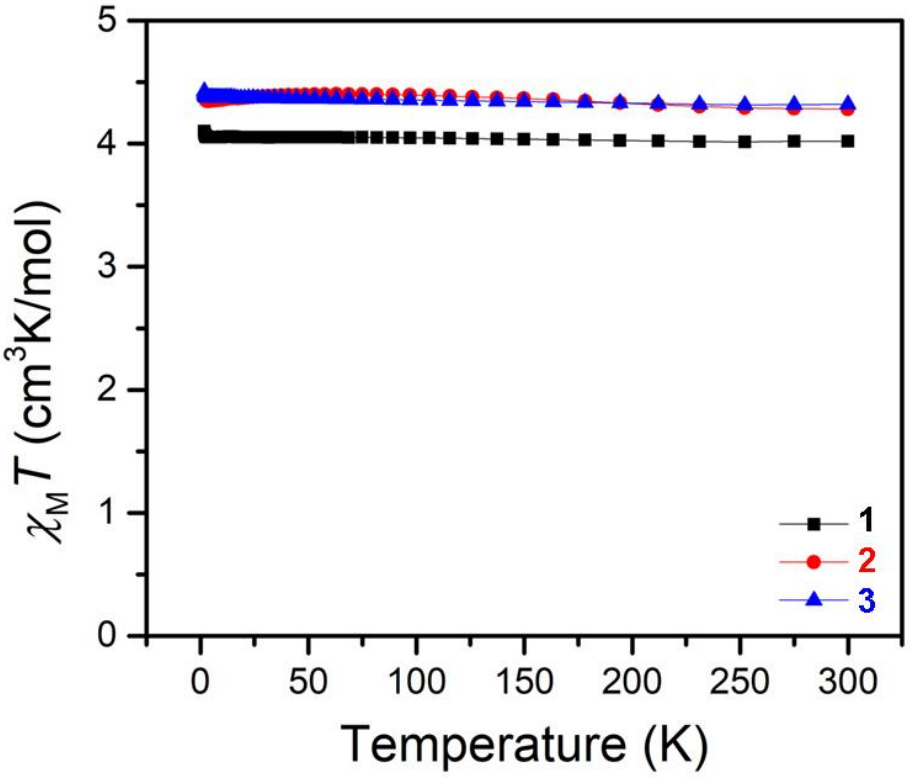

Appendix Figure 4.4. Variable temperature dc magnetometry data collected at 1000 Oe for **1-3**.

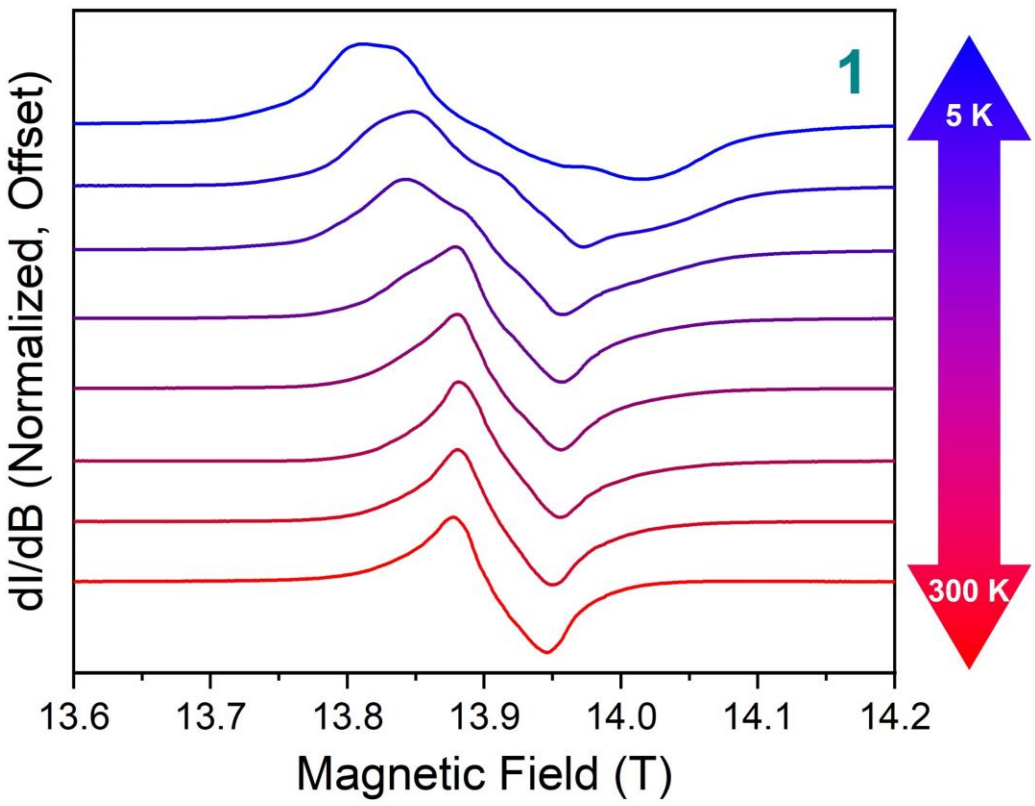

Appendix Figure 4.5. Selected variable temperature EPR spectra of complex **1** collected from 5 K to 300 K at a frequency of 390 GHz. Spectra were collected on sucrose dispersions. Spectra vary considerably in width across this range as a result of the temperature sensitive *D* parameter.

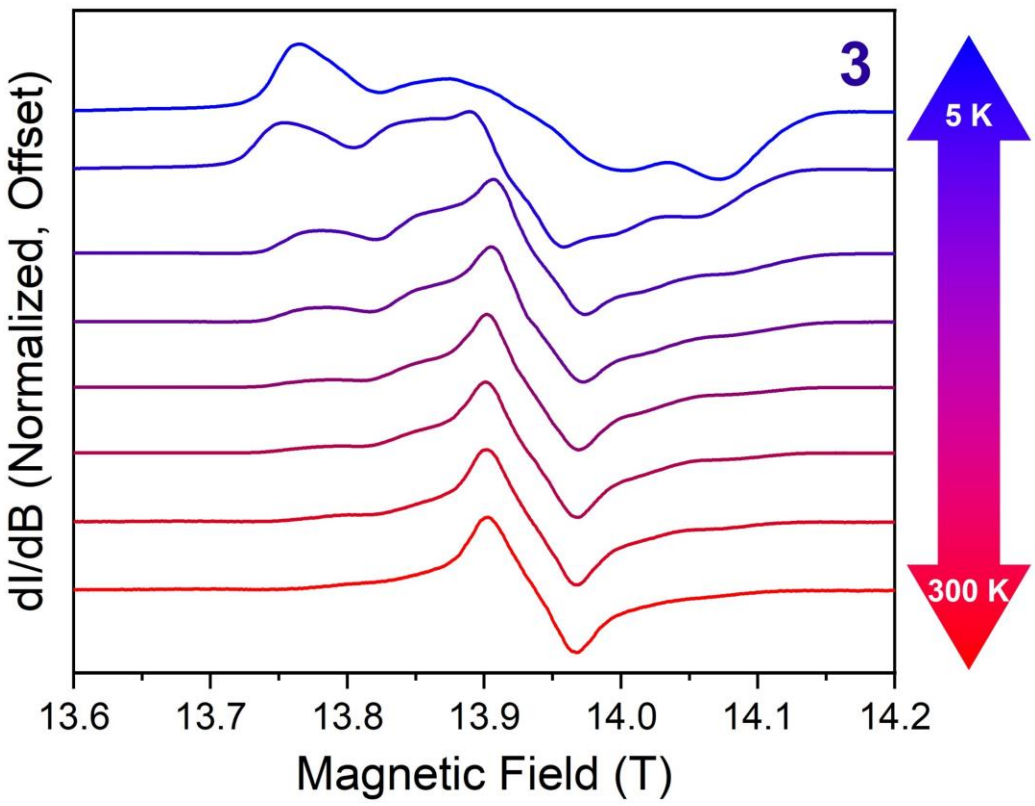

Appendix Figure 4.6. Selected variable temperature EPR spectra of complex **3** collected from 5 K to 300 K at a frequency of 390 GHz. Spectra were collected on sucrose dispersions. Spectra vary considerably in width across this range as a result of the temperature sensitive *D* parameter.

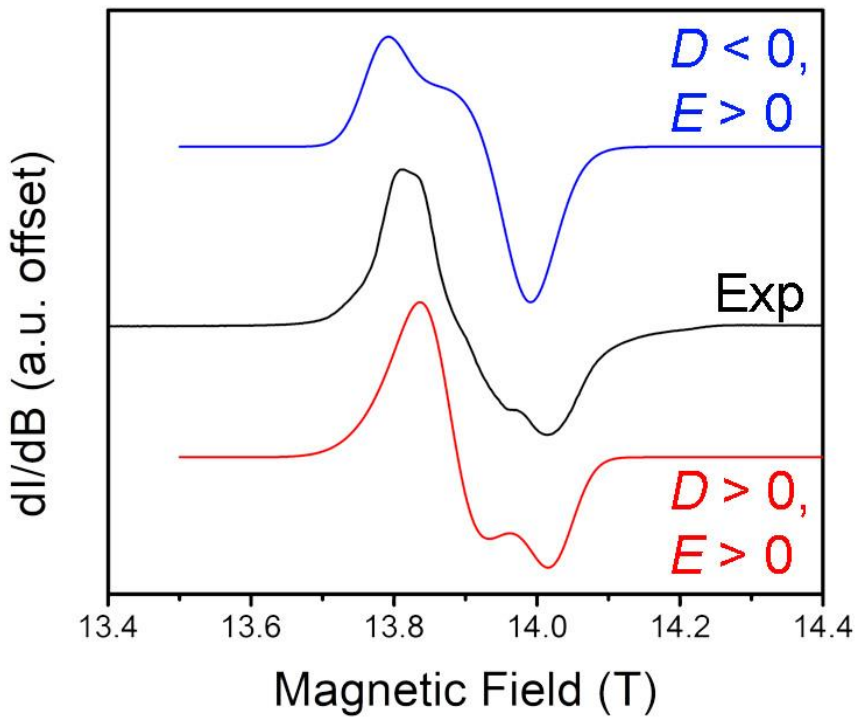

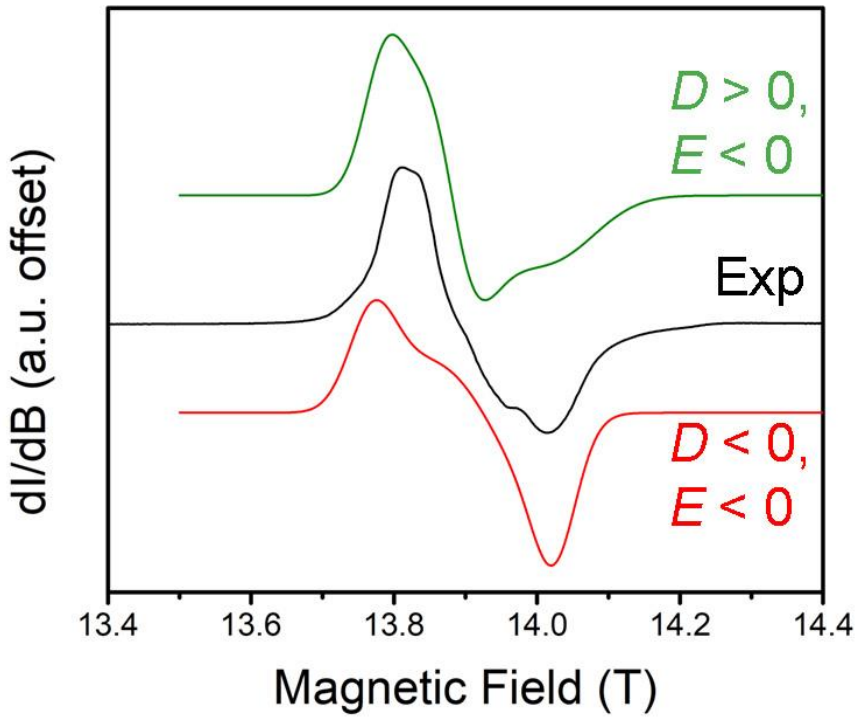

Appendix Figure 4.7. 5 K, 390 GHz EPR spectrum for pure **1** and simulations with opposing signs of *D* and *E*. Spin Hamiltonian parameters and magnitudes used follow the 5 K parameters given in **Appendix Table 4.4**. Closest match between experiment and simulation appears for *D* and *E* > 0 with these measurements.

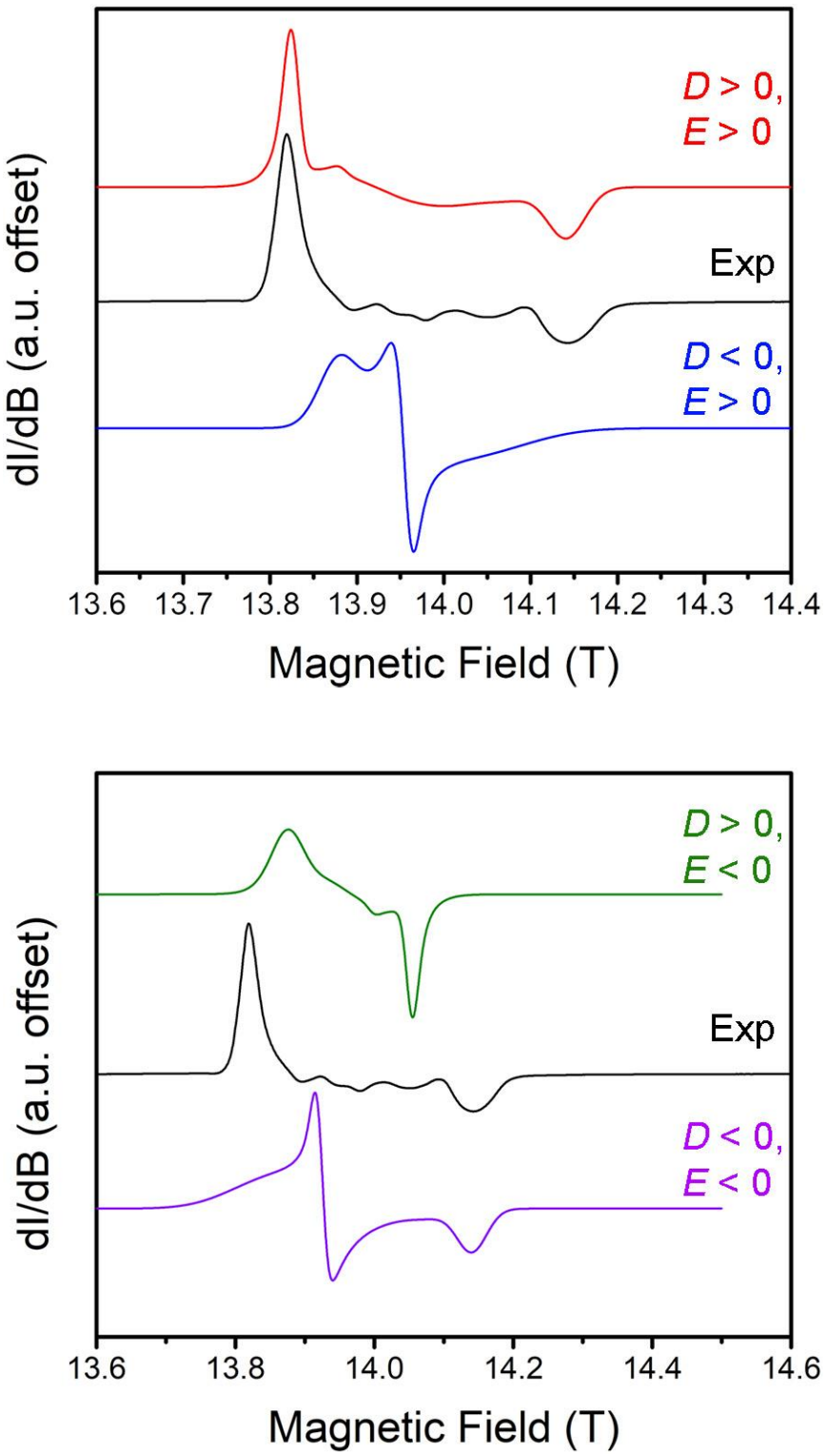

Appendix Figure 4.8. 5 K, 390 GHz EPR spectrum for pure **2** and simulations with opposing signs of *D* and *E*. Spin Hamiltonian parameters and magnitudes used follow the 5 K parameters given in **Table A4.5**. Closest match between experiment and simulation appears for *D* and *E* > 0 with these measurements.

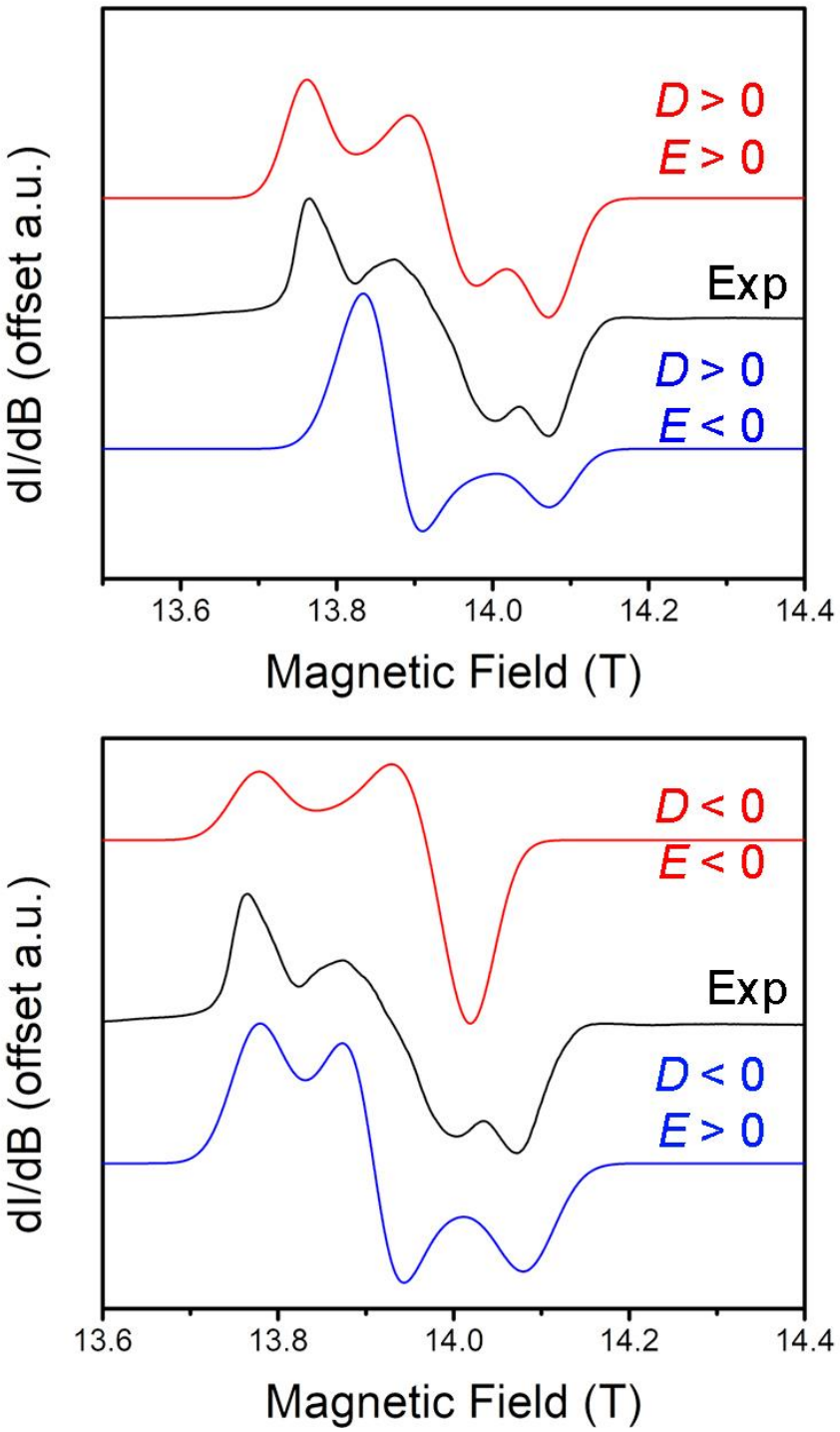

Appendix Figure 4.9. 5 K, 390 GHz EPR spectrum for pure **3** and simulations with opposing signs of *D* and *E*. Spin Hamiltonian parameters and magnitudes used follow the 5 K parameters given in **Table A4.6**. Closest match between experiment and simulation appears for *D* and *E* > 0 with these measurements.

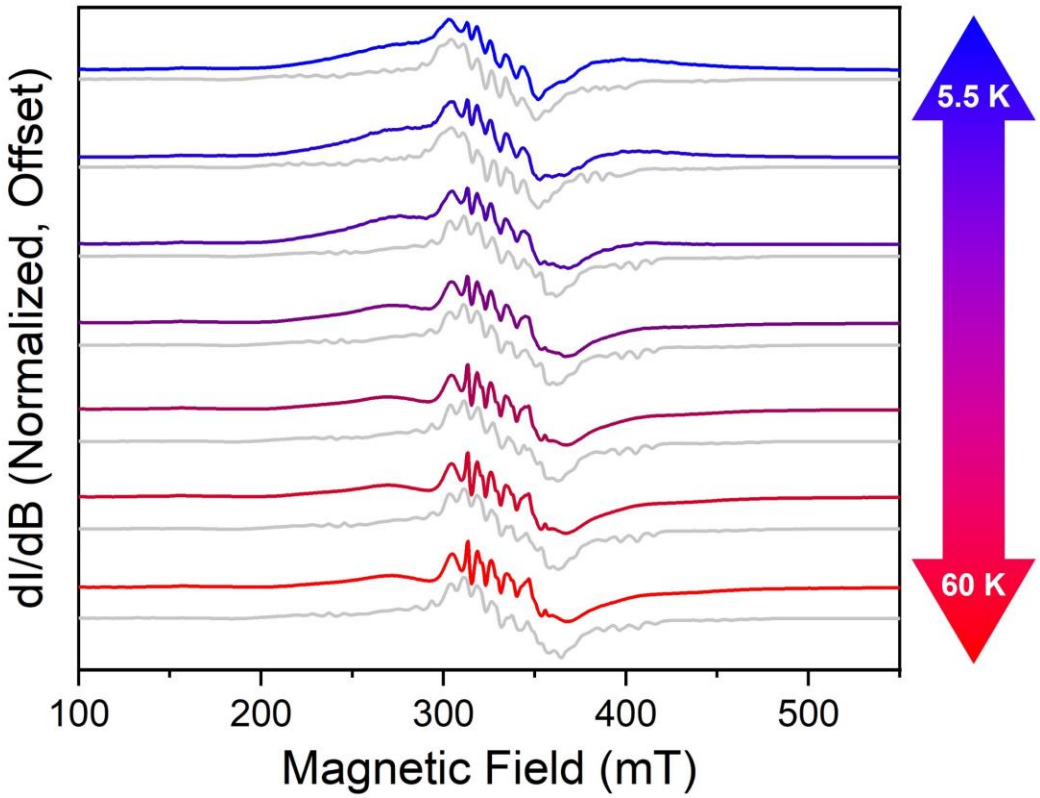

Appendix Figure 4.10. Variable temperature EPR spectra of complex **1** collected from 5.5 K to 60 K at 9.3 GHz. Spectra were collected in 5 mM butryonitrile solutions. Spin-Hamiltonian parameters for the best spectral simulations are found in **Table A4.7**.

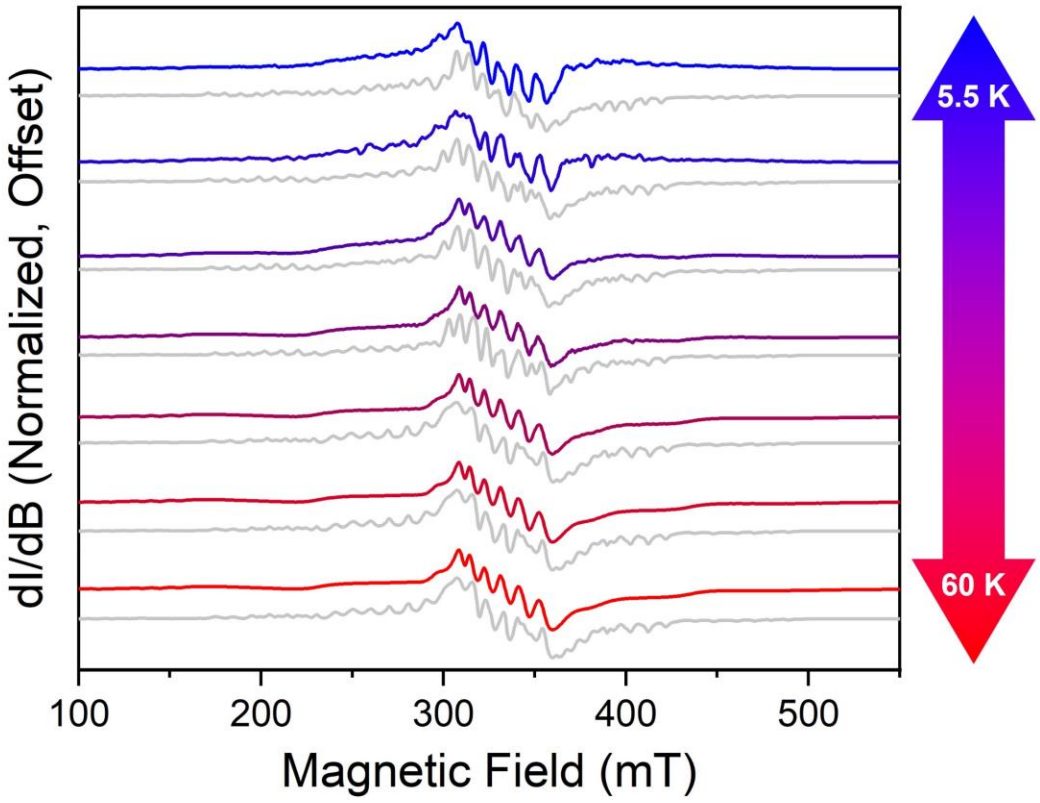

Appendix Figure 4.11. Variable temperature EPR spectra of complex **3** collected from 5.5 K to 60 K at 9.3 GHz. Spectra were collected in 5 mM butryonitrile solutions. Spin-Hamiltonian parameters for the best spectral simulations are found in **Table A4.9**.

Appendix 5: Supporting Information for Chapter 6

Appendix Table 5.1. Crystallographic information for the structural refinement of **2**.

Empirical formula	$C_{24.5}H_{36}Br_2MnN_4O_{4.5}$
Formula weight	673.33 g/mol
Temperature	106.53 K
Crystal system	Monoclinic
Space group	$P2_1/n$
a	10.4063(3) Å
b	13.2785(4) Å
c	19.4079(5) Å
α	90°
β	101.9070(10)°
γ	90°
Volume	2624.08(13) $Å^3$
Z	4
ρ_{calc}	1.704 g cm^{-3}
μ	3.590 mm^{-1}
F(000)	1368.0
Crystal color	Colorless
Crystal size	0.131 × 0.082 × 0.069 mm^3
Radiation	MoKα (λ = 0.71073 Å)
2θ range for data collection	3.742 to 66.564°
Index ranges	$-16 \leq h \leq 16$, $-20 \leq k \leq 20$, $-29 \leq l \leq 29$
Reflections collected	140447
Independent collections	10033 [R_{int} = 0.1440, R_{sigma} = 0.0629]
Data/restraints/parameters	10033/0/344
Goodness-of-fit on F^2	1.014
Final R indexes [$I \geq 2\sigma(I)$]	R_1 = 0.0376, wR_2 = 0.0696
Final R indexes [all data]	R_1 = 0.0771, wR_2 = 0.0793
Largest diff. peak/hole	0.74/–0.54 e $Å^{-3}$

Appendix Table 5.2. Crystallographic information for the structural refinement of **1**.

Empirical formula	$C_{18}H_{30}Br_2MnN_8$
Formula weight	573.26 g/mol
Temperature	100.72 K
Crystal system	Trigonal
Space group	*R*-3
a	8.482 Å
b	8.482 Å
c	26.656 Å
α	90°
β	90
γ	120°
Volume	1660.8 $Å^3$
Z	3
ρ_{calc}	1.719 g cm^{-3}
μ	4.227 mm^{-1}
F(000)	867.0
Crystal color	Orange
Crystal size	0.060 × 0.046 × 0.015 mm^3
Radiation	MoKα (λ = 0.71073 Å)
2θ range for data collection	5.752 to 51.27°
Index ranges	$-10 \leq h \leq 10$, $-10 \leq k \leq 10$, $-32 \leq l \leq 32$
Reflections collected	13922
Independent collections	705 [R_{int} = 0.1210, R_{sigma} = 0.0376]
Data/restraints/parameters	705/0/54
Goodness-of-fit on F^2	1.116
Final R indexes [$I \geq 2\sigma(I)$]	R_1 = 0.0491, wR_2 = 0.1131
Final R indexes [all data]	R_1 = 0.0623, wR_2 = 0.1189
Largest diff. peak/hole	1.73/–0.80 e $Å^{-3}$

Appendix Table 5.3. Tabulation of best simulation parameters for the variable-viscosity, solution state EPR spectra of **1**.

η (cP)	g_{xy}	g_z	***D* (MHz)**	A_{xy} **(MHz)**	A_z **(MHz)**	τ_r **(ns)**
711	2.020	1.955	280	240	200	1000
222	2.015	1.955	280	240	200	316
112	2.010	1.955	270	260	220	126
30.3	2.005	1.945	150	235	230	20.0
11.0	2.002	1.960	180	240	230	6.31
2.46	2.002	1.960	190	255	225	2.00
1.00	2.017	1.960	150	280	230	0.562

Appendix Table 5.4. Tabulation of best simulation parameters for the variable-viscosity, solution state EPR spectra of **2**.

η (cP)	g_{xy}	g_z	***D* (MHz)**	A_{xy} **(MHz)**	A_z **(MHz)**	τ_r **(ns)**
711	2.000	1.950	180	240	220	398
112	2.015	1.960	230	245	245	56.2
30.3	2.015	1.960	230	255	255	22.4
11.0	2.005	1.960	220	235	250	7.08
2.46	2.005	1.960	200	245	250	2.24
1.00	2.010	1.960	180	270	235	0.891

Appendix Table 5.5. Tabulation of best simulation parameters for frozen solution state 9.36 GHz EPR spectra of **1** and **2** a water/glycerol mixture at 5 mM. Units of *A* and *A*-strain are MHz. [a]Strains used are *g*/*A* strains ordered as strain in [g/A_x g/A_y g/A_z].

Complex	g_x	g_y	g_z	***g*-strain**[a]	***D* (MHz)**	***E* (MHz)**
1	1.970	1.990	1.999	[0.005 0.005 0.005]	670	−190
2	2.010	2.005	2.012	[0.0025 0.025 0.0025]	1000	215

Complex	A_x	A_y	A_z	***A*-strain**[a]
1	220	240	210	[5 15 35]
2	235	260	240	[45 65 55]

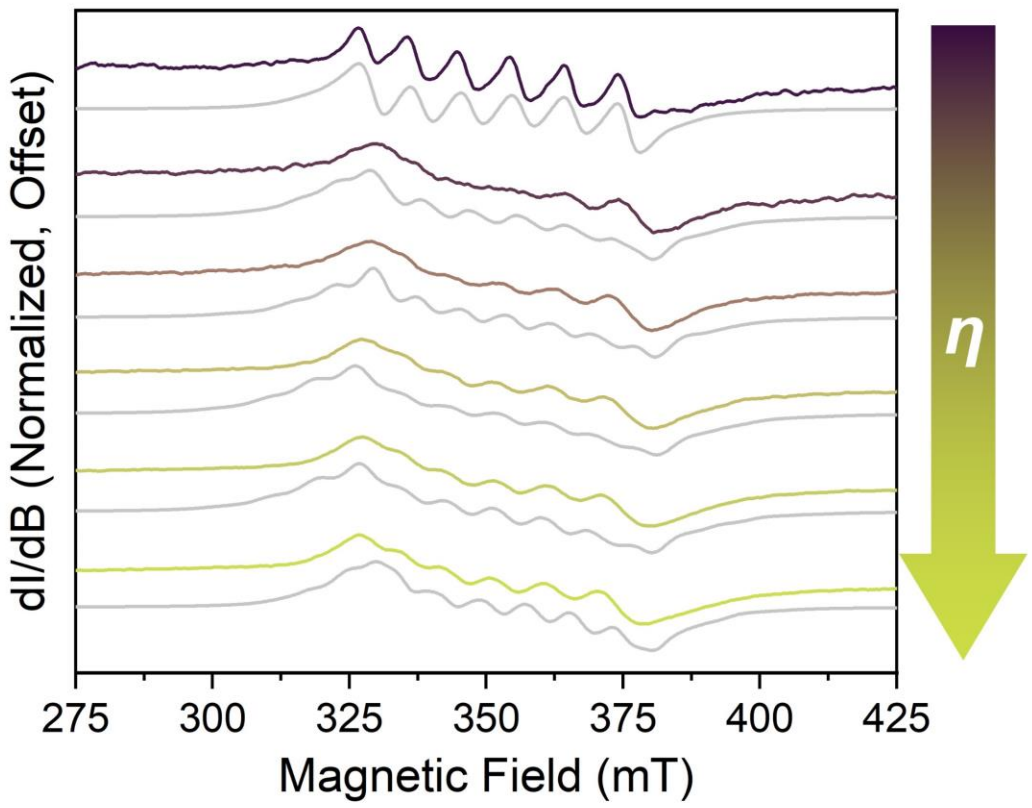

Appendix Figure 5.1. Viscosity dependent EPR spectra of **2** collected at X-band (9.8 GHz). Viscosities varied from 1 cP (top) to 711 cP (bottom). Experimental spectra are colored, and the spectral simulations are in gray. Simulation parameters are found in **Table A5.4**.

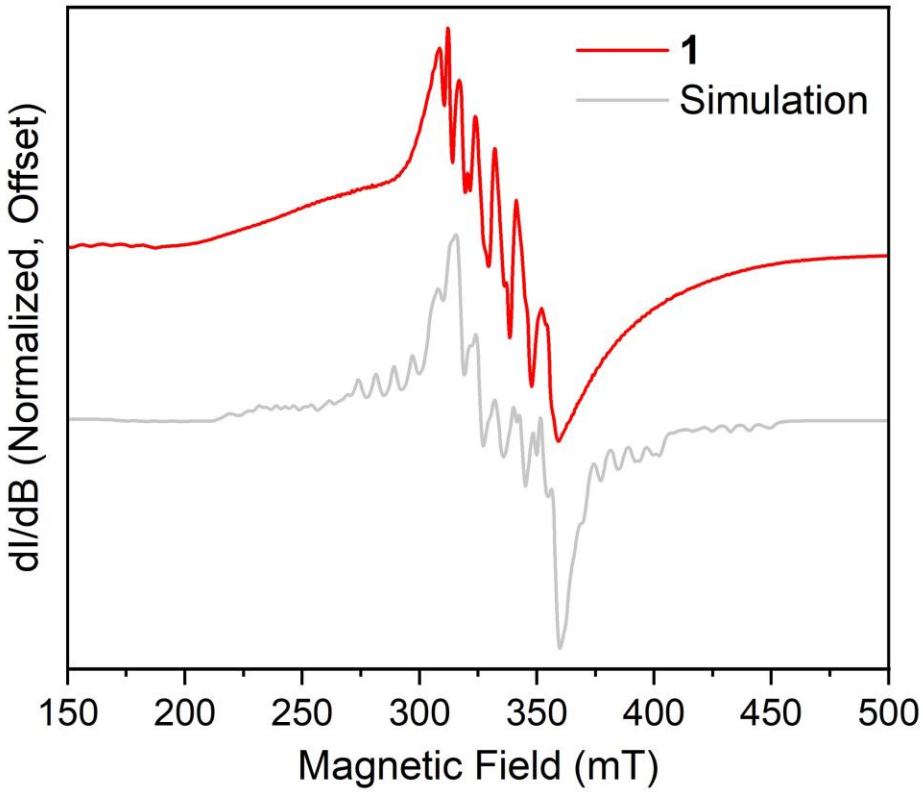

Appendix Figure 5.2. Frozen solution EPR spectra of **1** collected at X-band (9.8 GHz) at 10 K. Experimental spectrum is in red, and the spectral simulation is in gray. Simulation parameters are found in **Table A5.5**.

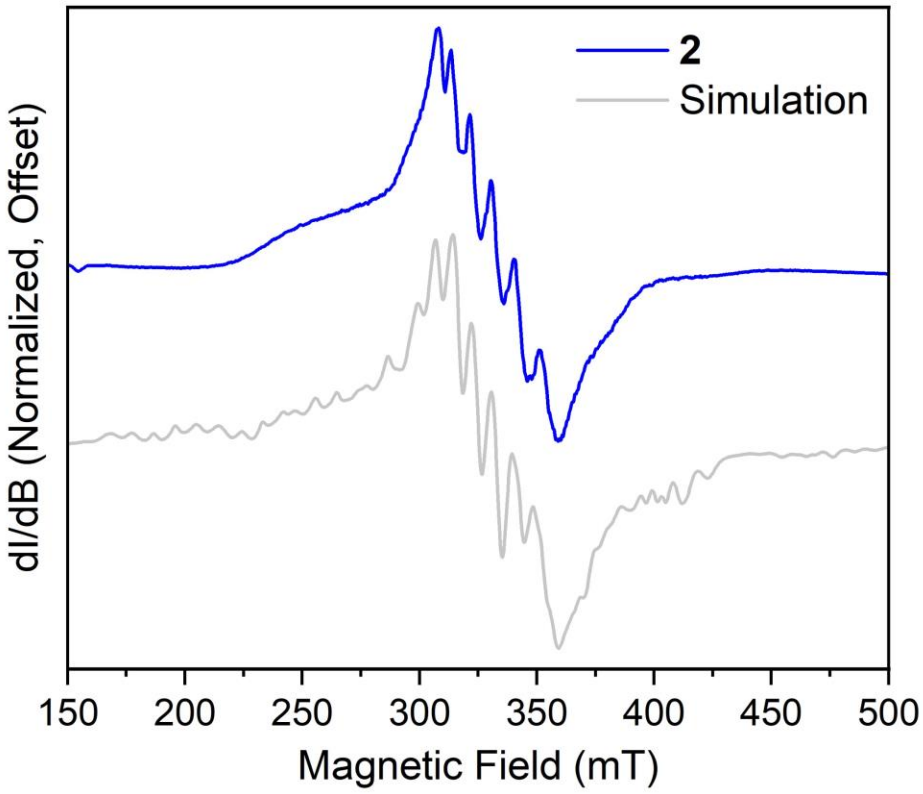

Appendix Figure 5.3. Frozen solution EPR spectra of **2** collected at X-band (9.8 GHz) at 10 K. Experimental spectrum is in blue, and the spectral simulation is in gray. Simulation parameters are found in **Table A5.5**.

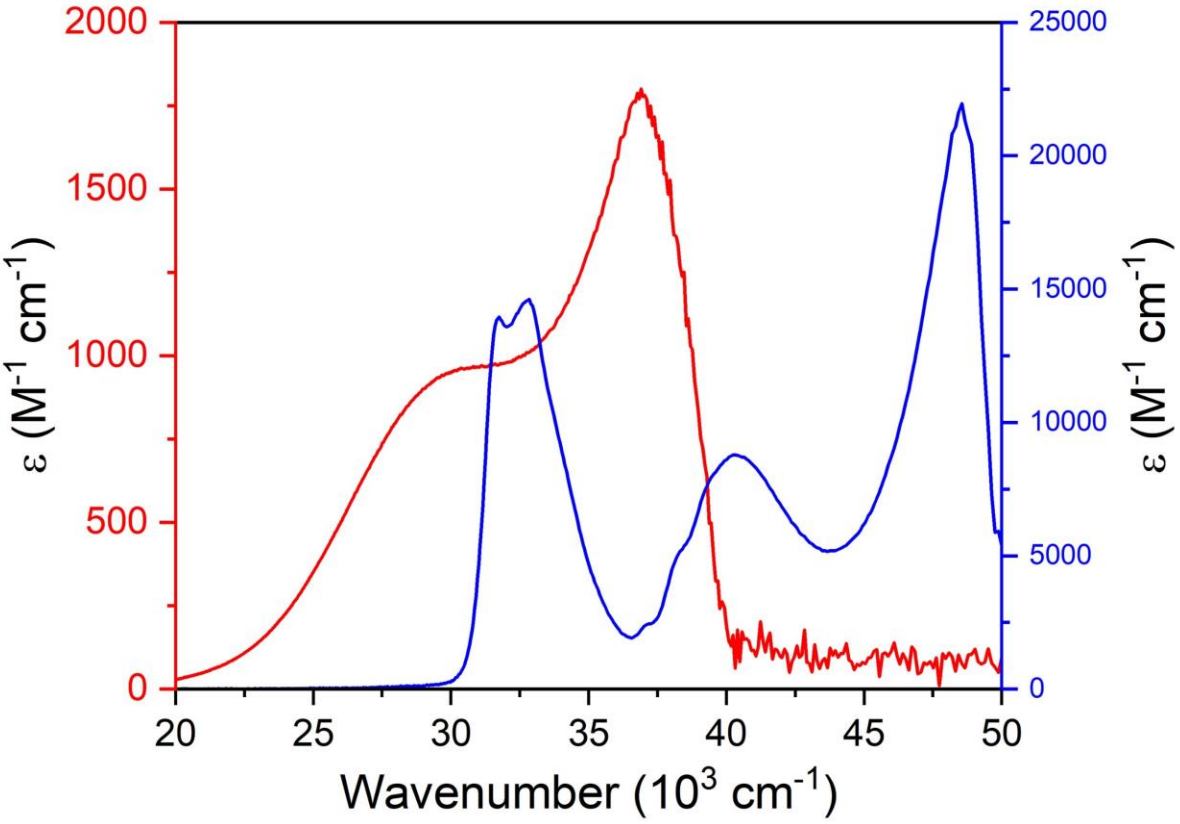

Appendix Figure 5.4. Solution UV-vis spectra of **1** (red), and **2** (blue) collected in methanol.